

Coupling Hydrodynamic and Biokinetic Growth Models in Aerated Wastewater Treatment Processes

Andrew James Oates

SUBMITTED IN ACCORDANCE WITH THE REQUIREMENTS FOR THE DEGREE OF
DOCTOR OF PHILOSOPHY

THE UNIVERSITY OF LEEDS

EPSRC CENTRE FOR DOCTORAL TRAINING IN FLUID DYNAMICS

SEPTEMBER 2021

Declaration

The candidate confirms that the work submitted is his own, except where work which has formed part of jointly authored publications has been included. The contribution of the candidate and the other authors to this work has been explicitly indicated below. The candidate confirms that appropriate credit has been given within the thesis where reference has been made to the work of others.

This copy has been supplied on the understanding that it is copyright material and that no quotation from the thesis may be published without proper acknowledgment.

The right of Andrew James Oates to be identified as Author of this work has been asserted by Andrew James Oates in accordance with the Copyright, Designs and Patents Act 1988.

Acknowledgements

It feels very odd to be writing this after spending all this time working towards the thesis as it means that my time as a PhD student is coming to an end. Nonetheless, it has to come to an end and I would like to thank the people who have helped me reach this point. First of all, I would like to give thanks to my team of supervisors Dr Duncan Borman, Dr Miller Alonso Camargo-Valero, Dr Gareth Keevil and Dr Andrew Sleight, for their guidance in my pursuit of a doctorate of philosophy. Thank you Duncan for imparting just some of your knowledge and wisdom during the PhD, your time and patience with me has been greatly appreciated and you have made the whole experience a lot more enjoyable. Thank you Miller, your immense knowledge of wastewater treatment is immeasurable and for parting just some of that knowledge onto me is invaluable. Thank you Gareth for your time, patience and vast experimental knowledge that has been vital to my work, without it I would still be purchasing wrong pipe fittings. Additionally, I would like to thank Dr Michael Meister who openly welcomed me to his group and provided unique opportunities that have enriched my PhD and helped make some unforgettable memories.

Next, I would like to thank the CDT management for believing in me and providing me the opportunity to study the PhD. Your dedication and commitment to making the CDT program a fulfilling and pleasant experience is appreciated and has made the whole experience that much more enjoyable. I would also like to thank my fellow students who I have come to call friends over these long years. A PhD can be feel like an ordeal at times and these friends have helped me get through these hard times (usually over a good pint) and made the long experience that much more entertaining.

Finally, I am forever thankful to my Mum and Dad whose constant love and support has allowed me to reach the heights I have and I am perpetually grateful to them. Thanks to my brothers for the beers and banter. And thank you to the rest of my family and friends who have supported me and helped make this all possible.

Abstract

In this thesis, a coupled hydrodynamic and wastewater biokinetic finite volume based CFD model for an aeration tank in OpenFOAM has been created to understand the effect of the hydrodynamics on the biological processes. A pilot-scale aeration tank that is aerated using fine membrane diffusers along the base has been designed and manufactured. A procedure for conducting lab experiments using an acoustic Doppler velocimeter to record velocity measurements was outlined. A series of aeration tank experiments with flow rates ranging from 18 – 108 L/min through membrane diffuser setups that involved 1 or 3 diffusers were conducted in which ADV velocity measurements were taken and have been used to validate a CFD model. Additionally, it was found that certain diffuser configurations showed pseudo - 2D behaviour such that the recorded data could be used to validate 2D simulations of the aeration tank. A CFD model using the Eulerian-Eulerian multiphase formulation in OpenFOAM was created to replicate the bubble driven fluid flow and free surface effects in the pilot-scale aeration tank. The influence of the inlet conditions, bubble diameter size and bubble dynamic models on the generated results were investigated and compared with the experimental data to validate the modelling choices. As a result, a 2D and 3D CFD model of the aeration tank was defined and validated against the experimental ADV data.

Using the results, a procedure for coupling the biokinetics into the hydrodynamics was described in OpenFOAM. The difficulties that arose from transferring a two-phase solution with a free surface to a single-phase solver was outlined and solutions to the issues were defined and assessed. The mass transfer of oxygen into the fluid was modelled and compared with experimental results from the membrane diffuser manufactures to confirm the accuracy of the model. The oxygen mass transfer model was used to assess how the membrane diffuser setup and flow rate impacts the oxygenation of the reactor. It was found that increasing the number of aerating diffusers while keeping the total air flow rate the same significantly increased the oxygenation

of the tank in comparison to just increasing the air flow rate which was found to only slightly increase the oxygenation. Additionally, a curve fitting procedure was described to derive a global oxygen transfer rate coefficient and saturation value from the CFD simulation for specific aeration tank setups and assessment of the values found they could give insight to the hydrodynamic behaviour in the reactor. The simulations were further extended to include the biokinetics to describe the biological interactions. A simple biokinetic aeration model was proposed to assess the impact of the hydrodynamics, inlet and outlet locations, and flow rate on the biological processes in tank. It was found that inadequate mixing in the 2D simulation resulted in twice the required amount of time to reach the maximum biomass concentrations compared with the equivalent perfectly mixed reactor. It was shown that the location of the inlet and outlet with the same hydrodynamic flow fields could influence the biological processes. It was found that there was no difference in the biological performance of the 3D reactor with an aerating flow rate of 0.3 and 0.6 L/s such that it would be inefficient to aerate the tank at 0.6 L/s. Finally, the full ASM1 was implemented into the coupled model and compared with the conventional ASM1 model to assess the performance of the aeration tank at producing and removing nitrates and ammonium. It was found that inadequate mixing resulted in reduced efficiency of the reactor at producing and removing nitrates and ammonium, respectively, which would further impact the performance of the sequential reactors.

Contents

Nomenclature	xi
1 Introduction	1
1.1 Wastewater treatment	2
1.2 Aeration basins	5
1.3 Motivation	6
1.4 Objectives	11
2 Biokinetic modelling	13
2.1 Activated sludge models	13
2.1.1 Simplified activated aeration sludge model	15
2.1.2 Activated Sludge Model No.1	19
2.1.3 Activated Sludge Simulation Software (ASIM)	21
2.2 Extending biokinetic models to account for the hydrodynamics	21
3 Aeration tank experiments	25
3.1 Aeration tank model design	26
3.1.1 Membrane diffusers	28
3.2 Instrumentation	29
3.2.1 Acoustic Doppler velocimetry	29
3.2.2 Visualisation	30
3.3 Experimental procedure	31
3.3.1 Membrane diffuser configurations	31
3.3.2 ADV recording locations	32
3.3.3 Aeration flow rates	35

3.3.4	Initial experimental checks	36
3.3.5	Diffuser configuration symmetry	39
3.3.6	ADV recording routine	41
3.3.7	Summary	43
3.4	ADV data post-processing	43
3.4.1	De-spiking algorithm	45
3.4.2	Data evaluation	46
3.5	Error analysis	48
3.6	Experimental results and discussion	49
3.6.1	Configuration “d1d2d3” and “a1a2a3” combined results for flow rate 108 L/min	51
3.6.2	Configuration “d1d2d3” and “a1a2a3” combined results for flow rate 54 L/min	53
3.7	Analysing the 2D behaviour of the velocity data sets	54
3.7.1	Assessment of the 2D behaviour	54
3.8	Chapter summary	58
4	Hydrodynamic modelling	61
4.1	Previous work in using CFD to model wastewater treatment reactors	62
4.1.1	Aeration Basin Modelling	63
4.2	Governing Navier-Stokes equations	65
4.2.1	Steady-state incompressible and isothermal Navier-Stokes equa- tions	66
4.2.2	Reynolds Averaged Navier-Stokes equations	67
4.3	Single phase RANS turbulence modelling	68
4.3.1	Standard $k - \epsilon$ model	68
4.3.2	Realizable $k - \epsilon$ model	70
4.3.3	$k - \omega$ model	73
4.3.4	Shear stress transport $k - \omega$ model	74
4.3.5	Wall functions	74

4.4	Eulerian two-phase modelling	75
4.4.1	Two-phase RANS turbulence modelling	76
4.5	Bubble-fluid modelling	78
4.5.1	Bubble column reactors	79
4.5.2	Bubble property parameters	80
4.5.3	Theoretical bubble rise velocities	81
4.6	Bubble-fluid interaction forces	83
4.6.1	Drag Force	84
4.6.2	Virtual Mass Force	85
4.6.3	Lift Force	86
4.6.4	Turbulent Dispersion Force	87
4.6.5	Wall Lubrication Force	88
4.7	Theoretical oxygen mass transfer	89
4.7.1	Calculating the k_{la} for the experimental aeration tank	91
4.8	Numerical modelling and the finite volume method	92
4.8.1	Discretisation	93
4.8.2	SIMPLE algorithm	96
4.8.3	PISO algorithm	98
4.8.4	PIMPLE algorithm	98
4.9	Chapter summary	99
5	Eulerian two-phase aeration tank modelling	101
5.1	Solver setup - <i>reactingTwoPhaseEulerFoam</i>	102
5.1.1	Solution method and initial conditions	104
5.1.2	Boundary conditions	107
5.2	Assessing CFD modelling approaches and assumptions using the 2D simulations	108
5.2.1	Mesh refinement study	109
5.2.2	Steady-state time analysis	116
5.2.3	Inlet boundary condition sensitivity study	119

5.2.4	Bubble size study	128
5.2.5	Bubble-water dynamic force models	131
5.3	Three-dimensional simulation set up	138
5.3.1	Steady-state analysis	140
5.3.2	Mesh refinement study	144
5.4	Three-dimensional hydrodynamic aeration tank results and discussion	146
5.4.1	Three and two dimensional simulation comparison	147
5.4.2	Three-dimensional reactor hydrodynamic analysis	151
5.4.3	Summary	166
5.5	Chapter summary	167
6	Coupling hydrodynamics, oxygen mass transfer and biokinetic models	171
6.1	Previous work at coupling CFD and biokinetic models	172
6.1.1	Coupling biokinetic model in aeration tanks	177
6.1.2	Coupling using Smooth Particle Hydrodynamics (SPH)	180
6.2	Proof of concept for coupling biokinetic models into CFD simulations	181
6.3	Solver setup - <i>scalarTransportFoam</i>	187
6.3.1	Solution method, initial and boundary conditions	192
6.4	Oxygen mass transfer implementation	195
6.4.1	Water velocity field implementation study	197
6.4.2	Volume fraction filter study	199
6.4.3	Diffuser aeration rate study	200
6.4.4	Deriving volumetric oxygen transfer coefficient, $k_L a$, from simulations	207
6.4.5	Reducing the resolution to improve simulation speed	213
6.5	Simple biokinetic aeration model (SBAM)	216
6.5.1	Comparison of coupled and uncoupled SBAM model	219
6.6	Inlet location case study	224
6.7	Three dimensional flow rate study	230

6.7.1	Oxygen mass transfer	230
6.7.2	Biological processes	234
6.8	Coupled ASM1 reactor	237
6.9	Chapter summary	242
7	Conclusions	245
7.1	Future project	256
8	Appendix	259
8.1	Experimental Results	259
8.1.1	Configuration “c2” and “b2” combined results for flow rate 36 L/min	259
8.1.2	Configuration “c2” and “b2” combined results for flow rate 18 L/min	262
8.1.3	Configuration “c1c2c3” results for flow rate 54 L/min	264
8.1.4	Configuration “d2” results for flow rate 36 L/min	266
8.2	2D assessment	268
8.2.1	Configuration “d1d2d3” and “a1a2a3” combined results for flow rate 108 L/min	268
8.2.2	Configuration “c1c2c3” results for flow rate 54 L/min	269
8.3	Hydrodynamic modelling	270
8.3.1	Turbulent dispersion model	271
8.4	Grid Convergence Index	272
8.4.1	2D Simulations	273
8.4.2	3D Simulations	274

Nomenclature

List of Abbreviations

AD	Anaerobic Digester
AS	Activated Sludge
ASIM	Activated Sludge Simulation Program
ASM	Activated Sludge Model
ASM1	Activated Sludge Model No.1
ASM2	Activated Sludge Model No.2
ASP	Activated Sludge Plant
BOD	Biological Oxygen Demand
CDT	Centre for Doctoral Training
CFD	Computational Fluid Dynamics
COD	Chemical Oxygen Demand
DO	Dissolved Oxygen
FVM	Finite Volume Methods
HRT	Hydraulic Retention Time
MBR	Membrane Bioreactor

MRF	Multiple Reference Frame
N	Nitrogen
P	Phosphorus
PE	Population Equivalent
RANS	Reynolds Navier-Stokes Equations
RRF	Rotational Reference Frame
SPH	Smooth Particle Hydrodynamics
TS	Total Solids
WWTP	Wastewater Treatment Plant

Chapter 1

Introduction

There is an increasing concern of the negative impacts humankind waste has on the environment and, as global population rises, there is a higher demand for infrastructure and agricultural resources which increases the amount of domestic and industrial waste. One form of humankind waste is the production of contaminated water or wastewater. Wastewater contains a large number of harmful compounds which, if left untreated, can lead to serious public health environmental damage, such as eutrophication and oxygen depletion, to ecosystems and lifeforms if discharged straight into the ecological cycle ([Horan, 1989](#); [Wang et al., 2009](#)). Additionally, the use of untreated wastewater by communities can lead to potential risks of water related diseases ([Grant et al., 2012](#)).

Therefore, treatment of wastewater is a crucial part of reducing the impact of humankind's waste on the environment and it is important that there is effective methods to treat wastewater to reduce the amount of pollution and destruction it can cause to the environment. One of the effective solutions to manage and alleviate these risks is to treat the wastewater in a wastewater treatment plant (WWTP) ([Henze et al., 2001](#)).

1.1 Wastewater treatment

Wastewater is generally a multi-phase and multi-species; can be non-Newtonian, (Lei and Ni, 2014; Henze et al., 2001) and cannot be treated all at once. Instead, the wastewater is treated in stages where each stage aims to reduce and remove a portion of the waste from the water efficiently until the water reaches acceptable treatment levels to be released back into the ecological cycle (Horan, 1989). Figure 1.1 illustrates a flow diagram of a cycle in a large wastewater treatment plant.

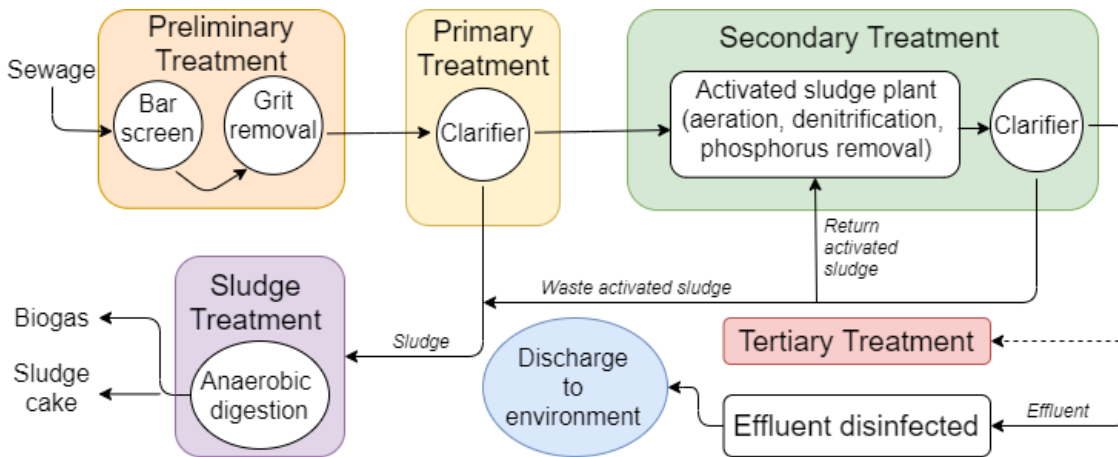


Figure 1.1: Flow diagram summarising the processes in a large WWTP.

The waste is initially pre-treated in the *Preliminary treatment* stage where large inorganic matter; such as egg shells, grit and sand; is removed by fine mesh screens or settled out in long grit removal chambers. The wastewater is further treated in the *Primary treatment* stage where large settling tanks or clarifiers are used to separate the suspended solids in the wastewater via gravitational phase separation. The settled solids or sludge is scraped away and taken to be further treated in the *Sludge Treatment* stage while the rest of the wastewater continues on to the *Secondary treatment* stage (Horan, 1989; Spellman and Drinan, 2003; Turovskiy and Mathai, 2006).

In secondary treatment, a series of bioreactors are used to encourage the growth of bacteria or biomass within the wastewater which feeds on the organic matter and

nutrients present. Active feeding biomass is referred to as activated sludge (AS) and the treatment stage is often referred to as an activated sludge plant (ASP) (Orhon et al., 2009; Wang et al., 2009; WEP, 2002). The ASP aims to reduce phosphorus (P), nitrogen (N) and organic matter levels. The amount of organic matter present is characterised by the biological oxygen demand (BOD) or chemical oxygen demand (COD) concentrations. BOD is the amount of dissolved oxygen needed for the biomass to breakdown the organic matter and COD is the amount of oxygen that is consumed by the chemical reactions in a measured solution; both of which can be related to the levels of organic matter in the wastewater (Horan, 1989; Henze et al., 2001; Orhon et al., 2009). The influent wastewater has a level of BOD, P and N that is needed to be reduced. Some BOD is removed during the primary treatment while BOD, P and N are all reduced in the ASP to the required effluent clean contaminant levels.

One of the bioreactors used in secondary treatment is an aerobic basin which is used to remove BOD and to oxidise N to nitrates (NO_3^-). Air is entrained into the fluid using bubble or mechanical surface aerators and a portion of the entrained air is absorbed into the fluid as dissolved oxygen (DO). The DO and BOD are then consumed during the growth of the bacteria or biomass. Additionally, ammonium, NH_4^+ , is oxidised into nitrates by two groups of autotrophic bacteria known as *Nitrosomonas* and *Nitrobacter*; this process is referred to as nitrification (Horan, 1989).

Another bioreactor in secondary treatment is the anoxic basin which creates the correct conditions for denitrification to occur. In the absence of DO, a series of heterotrophic bacteria, such as *Alcaligenes* and *Pseudomonas* (Wang et al., 2009), can utilise the trapped oxygen inside of nitrates for respiration; creating nitrogen based gasses which are realised into the atmosphere. This process is referred to as denitrification and it removes the nitrogen from the wastewater. Finally, the secondary treatment process tanks can be combined in such a way to stimulate the uptake of P by a bacteria known as *Acinetobacter* (Horan, 1989; Littleton et al.,

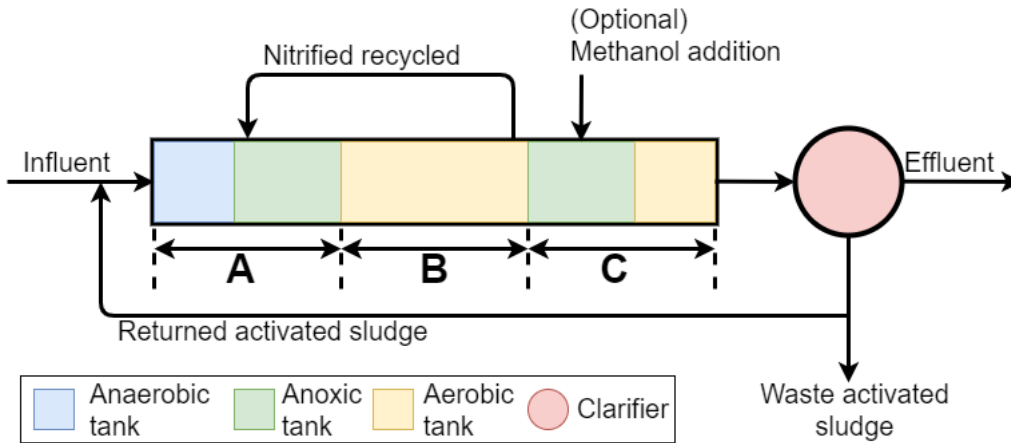


Figure 1.2: The Bardenpho process for removal of P, N and BOD. In section **A**: nitrates are turned into nitrogen based gases through the denitrification process; in section **B**: BOD is removed during biomass growth and ammonium is oxidised to nitrates; and in section **C**: P is removed during biological uptake (Horan, 1989).

2007).

The effluent wastewater from these basins is then pumped to another clarifier to settle out the activated sludge from the treated water. A portion of the settled AS is recycled back into the ASP because an active biomass population takes significant time to increase to appropriate levels and recycling helps to maintain the population at ideal levels (Turovskiy and Mathai, 2006). The rest of the AS is removed and further treated in the *Sludge treatment* stage. The ideal hydraulic retention time of a nitrifying ASP is 10 - 16 hours while the ideal sludge age, the amount of time AS spends in an ASP, is about 8 - 12 days (Horan, 1989). An example of all these processes together is the Bardenpho process (Horan, 1989; WEP, 2002) as illustrated in figure 1.2.

In summary, the main goal of secondary treatment is to encourage the bacteria or AS to consume the various pollutants and then, as the AS is easier to remove than the individual pollutants, to settle the bacteria out of the water to be further treated. The processed wastewater may be further processed in *Tertiary treatment* if additional special treatment is necessarily, otherwise, the effluent treated water is disinfected using chlorine or UV radiation and discharged into the environment

having reached the necessary clean contamination levels (Horan, 1989).

The AS from the *Primary* and *Secondary treatment* is further treated in the *Sludge treatment* stage (Turovskiy and Mathai, 2006). A large treatment works will have a sludge treatment works on site, otherwise, the total removed sludge will be taken to a sludge treatment facility where it is processed in anaerobic digesters to further reduce volume and create biogas for energy production. Afterwards, the processed sludge is dewatered, dried, and burned or recycled into sludge cakes for fertilisation (Wang et al., 2009; Henze et al., 2001; Turovskiy and Mathai, 2006). The main focus of this work is on the aeration basin in secondary treatment. Therefore, additional details will be given on these processes in the next sections.

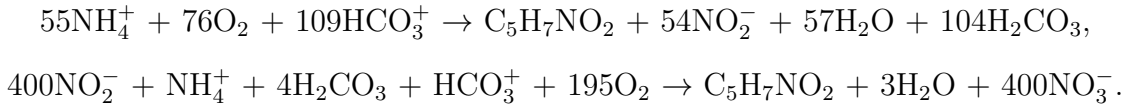
1.2 Aeration basins

The aeration or aerobic basins' main function is to reduce the amount of BOD in the wastewater through the growth of biomass, which also consumes dissolved oxygen, and begin the process of removing nitrogen compounds in the wastewater. Domestic wastewater contains nitrogen compounds in the form ammonium, NH_4^+ , or bound in organic compounds like proteins and nucleic acids which are quickly converted into ammonium during the wastewater treatment process (Horan, 1989; Henze et al., 2001; Wang et al., 2009). The reasons why nitrogen needs to be treated are:

- Ammonium consumes a considerable amount of oxygen and, if left in the water, will disrupt the dissolved oxygen distribution in the water cycle which will greatly affect ecosystems.
- Nitrogen is an important nutrient for plant growth and too much can cause excessive growth, such as algae, which can lead to eutrophication.
- Ammonia is a strong fish poison (Henze et al., 2001; Wang et al., 2009).

During the nitrification process: autotrophic bacteria *Nitrosomonas* converts the

ammonia to nitrite, NO_2^- ; then the bacteria *Nitrobacter* further oxidises the nitrite to nitrates, NO_3^- ; which is further treated in the anoxic basin and converted to nitrogen based gases (Horan, 1989). If we assume the empirical formula for a nitrifying bacteria is $\text{C}_5\text{H}_7\text{NO}_2$, then we can represent the ammonia and nitrite oxidation processes with the chemical formulas below, respectively (Wang et al., 2009),



The chemical reactions above require high amounts of molecular oxygen, every 1 g of ammonium present requires 4.2 g of oxygen (Horan, 1989; Wang et al., 2009), and, therefore, oxygen needs to be dissolved into the wastewater to keep up with this demand. This is achieved in modern plants by pumping air through floor aerators (Rosso et al., 2005); however, this is very costly and improving the efficiency of these processes is consistently an area of interest (Rosso et al., 2008; Leu et al., 2009; Bhuyar et al., 2009; Xu et al., 2010; Gresch et al., 2011; Karpinska, 2013; Terashima et al., 2016; Garrido-Baserba et al., 2017)

1.3 Motivation

The main purpose of WWTPs is to treat and purify the wastewater and return it to the ecological cycle. The big challenge for processing engineers is to optimize these systems to achieve this goal at minimal running costs. The development of the Bardenpho process (figure 1.2) and the creation of the AD reactor to produce a renewable energy source in the form of biogas are examples of effective plant design optimisation. Further research in increasing the efficiency of these systems are an ongoing area of interest to improve wastewater treatments plants capabilities to deal with the increasing wastewater load as population rises.

One example of research into improving wastewater systems was the development of biokinetic models to mathematically describe the biological processes in different

wastewater treatment procedures, for example: aeration basins and anaerobic digesters. These models describe reaction rates of the growth and decay of biomass and the transformation of any targeted pollutants (e.g., biodegradable organic matter, nitrogen compounds, etc.) in wastewater treatment bioreactors. These models are a useful tool for understanding the biological processes occurring in these reactors and can be used to aid and improve design and operating conditions of these systems to increase effectiveness and efficiency (Henze et al., 2007; Orhon et al., 2009). However, one critical assumption made by these models is that the reactors are “well-mixed” such that the parameter concentrations are uniform or homogeneous throughout the reactor. This homogeneity assumption is valid if the reactors are perfectly stirred, which may be the case, but achieving this level of mixing can be costly if done inefficiently.

Aeration basins provide a source of oxygen for bacteria growth, the stabilisation of biodegradable organic carbon, and ammonium oxidation; but also as a mixing mechanism for the reactor. The aeration process is recognised as the highest energy use process in wastewater treatment (Garrido-Baserba et al., 2017). Wastewater treatment can account for about 1 - 3 % of a countries average daily energy consumption (POST, 2007; Capodaglio and Olsson, 2019). Generally, supplying oxygen to the biomass (i.e. the aeration process) is achieved by pumping air at low pressure through the aeration tanks and can account for up to 54 - 75 % of the total operating costs (Rosso et al., 2008; Capodaglio and Olsson, 2019).

The ideal reactor design is one that uses the least amount of energy to mix and operate while not hindering the desired reactions. Due to the difficulty of experimental measurements for these systems, computational fluid dynamics simulations have been developed to describe and investigate the hydrodynamic flow fields created by these various mixing mechanisms in aeration basins and ADs (Karpinska and Bridgeman, 2016; Kariyama et al., 2018). By coupling the hydrodynamics and biokinetic growth models for these systems, we can improve our understanding of the sensitivity between the hydrodynamics and reaction rates. The coupled model

can then be used to aid in improved design and operation of the wastewater bioreactors; leading to more efficient and effective processes and reducing the overall cost of these systems.

Therefore, there is a motive in researching improvements to aeration efficiency to reduce costs of aeration systems in wastewater treatment (Lee et al., 2015; Ozturk et al., 2016; Fan et al., 2017). CFD simulations have been used to investigate the influence of diffuser pattern on the flow field (Gresch et al., 2011) and to analyse the optimal turbulence model choices for simulating an aeration basin (Karpinska and Bridgeman, 2017). The first attempt to couple the biokinetic and hydrodynamics in a CFD simulation was conducted by Gresch et al. (2011) and has been further investigated by Lei and Ni (2014); Rehman et al. (2017) and Sánchez et al. (2018). Lei and Ni (2014) suggested that coupled models can be used as a design tool to investigate optimal arrangements of aeration zones; Rehman et al. (2017) illustrated that incomplete mixing can impact the biological process performances; and Sánchez et al. (2018) showed that intermittent aeration can be implemented to maintain efficiency with lower power consumption.

A key aim of this thesis is to produce a coupled model and illustrate the additional insight the model can provide that would not be possible with conventional biokinetic models. However, to develop this coupled model for a reactor, crucial steps or objectives are required so that we are confident in the predicted solutions. Hydrodynamic CFD simulations need to be run and assessed to confirm their reliability in predicting the fluid flow which requires: a mesh refinement study, analysis of time taken to reach a steady-state, and validation of the CFD modelling choices. To validate the CFD modelling choices, experimental data needs to be obtained which requires an aeration tank to be designed and a procedure outlined for conducting experiments. Once a CFD methodology for simulating the hydrodynamics in an aeration tank is defined and validated, such that there is confidence in the predicted solutions, the model is ready to be coupled with the biokinetic equations. However, this involves a new solving method that requires modification of the original solu-

tion, specifically going from a two-phase to a single-phase solution, to implement the oxygen mass transfer and other biokinetic equations in a computational efficient manner. Once these modifications have been made, the oxygen transfer model needs to be assessed and verified to confirm the oxygenation of the tank is being correctly replicated. Once these steps or objectives have been met, the model can finally be extended to include all the biokinetic processes to complete the coupled model. This coupled model can then be used to investigate how potential changes to the design and operation of the aeration tank can impact the hydrodynamics and, as a result, influence the biological processes which would not be possible if the hydrodynamics had been neglected in the modelling. Having confidence in the predicted solutions of this coupled model is only possible by slowly building up and validating the choices made in the development of the model. A diagram has been created to summarise the steps and procedures required for creating a reliable coupled model, as illustrated in figure 1.3.

[Karpinska and Bridgeman \(2017\)](#) has a detailed description of the CFD simulation and aeration experiments conducted for their lab-scale, fine-pore aerated and impeller stirred reactor which couples and validates the hydrodynamics and oxygen mass transfer model, following a similar framework described in figure 1.3. However, only the oxygen mass transfer model is coupled and they do not include the ASMs. Previous papers have created and used the coupled model to investigate different features of aeration tanks ([Gresch et al., 2011](#); [Lei and Ni, 2014](#); [Rehman et al., 2017](#); [Sánchez et al., 2018](#)); however, they often do not discuss or miss initial steps, like those defined in figure 1.3, describing their modelling choices which is necessary to be confident in the coupling framework and predicted results from these models.

The main aim for this thesis is to define a framework for, and create, a validated coupled CFD model, as described in figure 1.3, for a pilot-scale aeration tank that is aerated by fine membrane diffusers. The coupled model will be used to investigate how various operational features of the aeration tank (e.g. diffuser configuration, aeration flow rates, tank inlet and outlet locations) can influence the biological

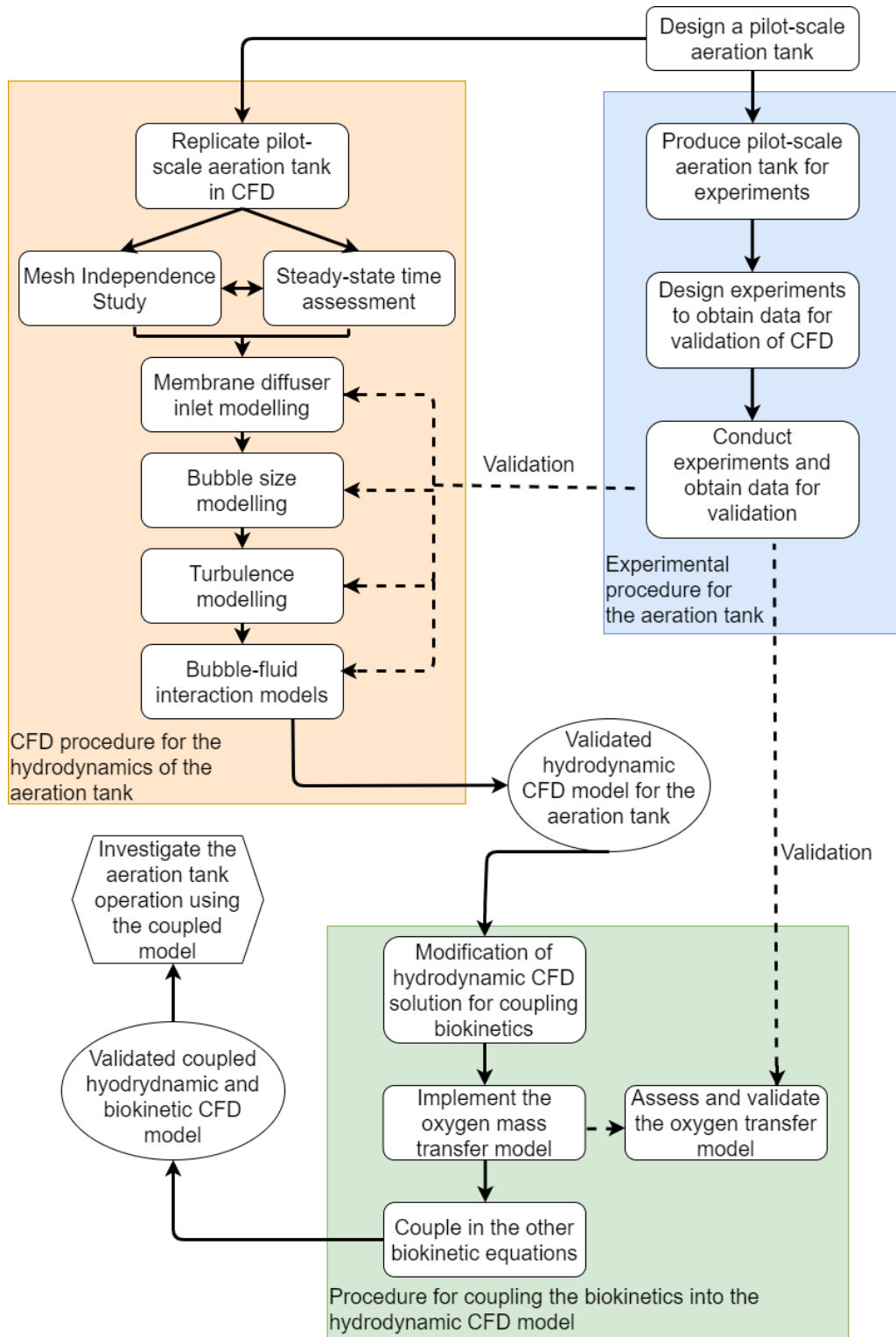


Figure 1.3: Diagram describing the steps and procedures required for creating a reliable coupled hydrodynamic and biokinetic CFD model.

processes to illustrate the benefits of using a coupled model that would not be possible in a conventional biokinetic model; emphasising the benefit of the coupled model. A detailed description for each framework step will be given in this thesis

to allow for other CFD engineers to replicate and create their own coupled models. Finally, this work is conducted in an open source CFD software which increases the accessibility of the coupled model described in this thesis. The framework and attention to detail in the development of the coupled model in this work is what sets this thesis apart from previous work and makes it novel. A list of objectives are described below that will lead us to accomplish the aims set out in this thesis.

1.4 Objectives

1. Investigate and confirm the methodology and procedure for coupling activated sludge models into CFD simulations.
2. Design and manufacture a pilot-scale aeration tank to conduct experiments to obtain measurements for use in validation of the CFD simulations.
3. Develop a CFD model to simulate the hydrodynamics within the pilot-scale aeration tank and assess the modelling approaches using the obtained experimental data to acquire a validated CFD model describing the aeration tank hydrodynamics.
4. Modify the CFD model to allow for coupling of transport equations and analyse these changes to assess their impact on the solution to give confidence in the coupling procedure.
5. Couple the oxygen mass transfer model into the CFD simulations to model the oxygenation in the tank and investigate how different membrane diffuser configurations and flow rates can impact the oxygenation with a comparison of the results against the expected theoretical aeration to verify the oxygen transfer model; resulting in a verified coupled oxygen mass transfer and hydrodynamic CFD model.
6. Implement the additional biokinetic transport equations to complete the cou-

pled model and investigate the impact of the hydrodynamics and changes in the aeration tank operation on the biological processes.

Chapter 2

Biokinetic modelling

The development of mathematical models to represent biological wastewater processes is a powerful tool for assessment of performance and conditions in wastewater treatment plants (Henze et al., 2001; Orhon et al., 2009; Wang et al., 2009). A complete model of the full dynamics and reactions in these bioreactors has still not been fully developed due to its complexity. However, simpler models have been developed by making assumptions to reduce the complexity of the processes in the bioreactors. These models simplify the complex behaviour by grouping and defining key components that are crucial to the biological processes. Modelling techniques are then applied to couple these components together to mathematically describe these process and their reactions rates. The most commonly recognized models to mathematically describe the various wastewater treatment processes in ASPs are called activated sludge models (ASMs).

2.1 Activated sludge models

One of the first recognised models that has become a basis for future wastewater treatment biokinetic models is the Activated Sludge Model No.1 (ASM1) which was developed by the International Association on Water Quality (Henze et al., 1987, 2007). The International Association on Water Pollution Research and Con-

trol (IAWPRC, later known as the International Water Association, IWA) formed a task group in 1983 to produce a practical mathematical model to describe the biological processes in AS systems that could be implemented in every design office. This led to the development of the Activated Sludge Model no.1 (ASM1) in 1987 which was an amalgamation of existing models in their simplest form while still being capable of realistically predicting the processes occurring in these AS systems. This model has been further developed to incorporate additional biokinetic features, for example: Activated Sludge Model no.2 (ASM2) that extends the ASM1 to include biological phosphorus removal; Activated Sludge Model no.2d which is a newer version of ASM2 (Jeppsson, 1996); and Activated Sludge Model no.3 which extends ASM1 to recognise the importance of carbon polymers storage in the biokinetics (Henze et al., 2007); but the ASM1 is still widely used for modelling AS processes and to aid in design (Henze et al., 2007; Orhon et al., 2009). The ASM1 set the standard and framework for ASMs and its most important feature is the simplified matrix form it can be illustrated in, as shown in figure 2.3, where the processes and variables can be quickly read and understood without getting lost in the complex mathematics. To make the model computational efficient, certain crucial assumptions and compromises have been made such as: the reactor is at constant temperature and pH; certain biological processes, unrealistically, occur instantaneously; and the reactor is assumed well-mixed, ignoring the hydrodynamics, such that concentrations are homogeneous throughout the reactor and local concentration variation is not considered. The original ASM1 includes 8 fundamental processes, 13 variables or components and 11 rate equations (Henze et al., 1987) which, for a simplified model, is still quite complex. Therefore, a simplified two species ASM has been derived from the ASM1 that will be introduced in the next section to better explain the general structure and terms in the ASM1 and other ASMs.

Component →		Continuity		Process Rate, ρ_j [ML ⁻³ T ⁻¹]
		1	2	
j	Process ↓	1	2	
		X_B	S_S	
1	Growth	1	$-\frac{1}{Y}$	$\frac{\hat{\mu}S_S}{K_S + S_S} X_B$
2	Decay	-1		bX_B
Observed Conversion Rates ML ⁻³ T ⁻¹		$r_i = \sum_j r_{ij} = \sum_j \nu_{ij}\rho_j$		Kinetic Parameters: Maximum specific growth rate: $\hat{\mu}$ Half-velocity constant: K_S Specific decay rate: b
Stoichiometric Parameters: True growth yield: Y		Biomass [M(COD) L ⁻³]	Substrate [M(COD) L ⁻³]	

Figure 2.1: A simplified two species ASM in matrix form that has been derived from the ASM1 (Henze et al., 2001).

2.1.1 Simplified activated aeration sludge model

A simple two species version of the ASM1 in matrix form is illustrated in figure 2.1 which will be used to explain the ASM equations and matrix structure. The components in this simplified 2 species ASM (denoted by i in figure 2.1) are: X_B ($i = 1$) which is the biomass or bacteria; and S_s ($i = 2$) which is the soluble substrate. The soluble substrate is the dissolved organic matter that can be consumed by the biomass for growth. The two processes (denoted by j) described by this model are growth ($j = 1$) and decay ($j = 2$). The rates of these processes are described in the right column of figure 2.1, denoted as ρ_j . For example,

$$\rho_2 = bX_B,$$

is the rate of decay of the biomass where b is the specific decay rate of the coefficient. Finally, the stoichiometric coefficients, ν_{ij} , which are the constants in the middle of the matrix, are the coefficient dependences each component has on these process rates. For example: $\nu_{21} = -(1/Y)$, is the coefficient dependence of the soluble

substrate component ($i = 2$) on the decay process ($j = 1$) (Henze et al., 1987, 2007; Orhon et al., 2009).

The complete reaction rate equation for a component, denoted r_i , is defined as:

$$r_i = \sum_j \nu_{ij} \rho_j.$$

As an example, the reaction rate for the biomass, X_B or $i = 1$, is,

$$\begin{aligned} r_1 = r_{X_B} &= \frac{dX_B}{dt} = \sum_j \nu_{1j} \rho_j, \\ &= \nu_{11} \rho_1 + \nu_{12} \rho_2, \\ &= (1) \left(\frac{\hat{\mu} S_s}{K_s + S_s} X_B \right) + (-1) (b X_B), \\ &= \frac{\hat{\mu} S_s}{K_s + S_s} X_B - b X_B. \end{aligned}$$

This procedure can be applied for each of the components to get the full system of reaction rate equations which, for the two species ASM model defined in figure 2.1, are presented below,

$$\frac{dX_B}{dt} = \frac{\hat{\mu} S_s}{K_s + S_s} X_B - b X_B, \quad (2.1)$$

$$\frac{dS_s}{dt} = -\frac{1}{Y} \frac{\hat{\mu} S_s}{K_s + S_s} X_B. \quad (2.2)$$

The parameters $Y, \hat{\mu}, K_s, b$ are defined as the: yield, maximum specific growth rate, half-velocity constant, and decay rate, respectively; and are derived from empirical models that follow a Monod relationship describing the substrate consumption and biomass yield which are pre-determined before calculation (Monod, 1949; Henze et al., 1987, 2007).

Monod (1949) found that bacterial cultures that showed exponential growth

rate behaviour, R , could be described by a hyperbolic equation,

$$R = R_K \frac{C}{C_1 + C}, \quad (2.3)$$

where C stands for the concentration of the substrate or component of interest, R_K is the rate limit for increasing concentrations of C , and C_1 is the concentration of the substrate or component when the rate is half the maximum. This hyperbolic form is used to describe the exponential growth rate in the two species ASM by the term,

$$R = \hat{\mu} \frac{S_s}{K_s + S_s}, \quad (2.4)$$

and is commonly used throughout the ASMs. The values of the parameters at 20 °C for the two species model, as defined in Jeppsson (1996), and the initial species concentrations are described in table 2.1. The coupled equations in equations (2.1) and (2.2) were solved over 24 hours using the ordinary differential equation solving function available in a standard *python* package which uses the explicit fourth order Runge-Kutta method. Using the initial condition and parameters defined in table 2.1 produces the graphical results presented in figure 2.2.

K_S (mg/L)	$\hat{\mu}$ (day ⁻¹)	b (day ⁻¹)	Y	Initial S_S (mg/L)	Initial X_B (mg/L)
20	6	0.6	0.67	63	31

Table 2.1: Parameters values at 20 °C, as defined in Jeppsson (1996), and initial species concentrations for the two species ASM to solve the coupled equations.

The problem describes a well-mixed batched reactor such that the concentrations are uniform throughout the reactor. This uniformity implies that if we took a fluid sample from anywhere in the reactor, the component concentrations would be identical and, therefore, the volume of the reactor can be neglected and only the

concentration of each species (milligrams per litre, mg/L) needs to be considered. Analysing the results in figure 2.2, initially there is a surplus of S_S and, more specifically, $K_S \ll S_S$ such that the Monod term for describing the growth rate of the biomass (Monod, 1949),

$$\frac{S_s}{K_s + S_s} \approx \frac{S_s}{S_s} = 1, \quad (2.5)$$

which results in the biomass increasing at a rate proportional to the specific growth rate, $\hat{\mu}$. The specific growth rate is larger than the decay rate, $\hat{\mu} \gg b$, such that the biomass increases linearly at a rate slightly lower than $\hat{\mu}$ while the S_S decreases linearly at a similar rate as it is consumed during the growth process. This behaviour lasts for around 5 hours until the decreasing S_S drops below the K_S value, $S_S < K_S$. This causes the Monod term for the growth of biomass or consumption of S_S ,

$$\frac{S_s}{K_s + S_s} \approx \frac{S_s}{K_s} \rightarrow 0, \quad (2.6)$$

which results in a slow down of the growth rate. At around 8 hours, the S_S has decreased enough such that,

$$\hat{\mu} \frac{S_s}{K_s + S_s} < b, \quad (2.7)$$

and the decaying term dominates the biomass rate equation which results in the decrease of the biomass concentration. At 10 hours, the S_S has all been consumed and only the decay term remains in the biomass rate equation such that the biomass concentration decreases linearly from 10 hours onwards due to bacteria dying. In the full ASM1, there are additional terms that state a portion of the dead biomass becomes potential organic matter to be consumed for growth and acts as a source of S_S such that, in a well-mixed batch reactor, there would be a non-zero equilibrium solution between biomass and S_S . Now that we have a understanding of the biokinetic rate equations describing wastewater treatment processes in this simple

two species ASM, we will introduce the full ASM1 and describe the various defined parameters.

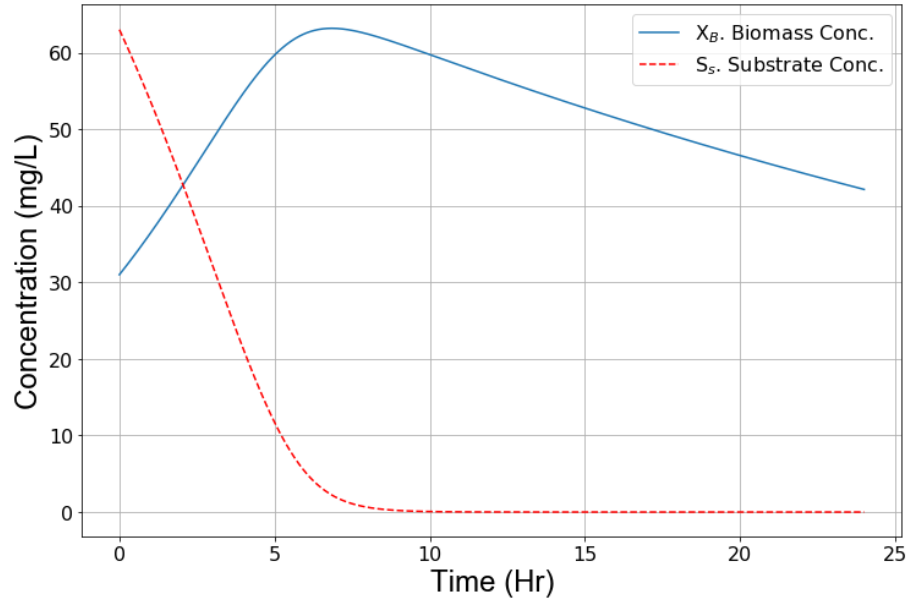


Figure 2.2: The change in concentration over time for the two species ASM using parameters and initial conditions defined in table 2.1.

2.1.2 Activated Sludge Model No.1

The developed ASM1 is for AS systems performing: carbon oxidation, nitrification, and denitrification; and includes 8 fundamental processes, 13 variables or components, and 11 rate or differential equations that describe how the different species concentrations vary over time (Henze et al., 1987, 2007). The matrix form of the ASM1 is presented in figure 2.3, which can be read in the same way as the two species matrix form in figure 2.1 to produce the 11 rate equations, and a brief description of each parameter is given in table 2.2.

As stated previously, certain simplifications and assumptions have been made to produce the ASM1 where some of these are associated with the physical system while others are with the mathematical model. Some of these restrictions are (Jeppsson, 1996; Henze et al., 2007):

- The system operates at constant temperature.

Component \rightarrow	i	1	2	3	4	5	6	7	8	9	10	11	12	13	Process Rate, ρ_j [ML ⁻³ T ⁻¹]	
j	Process \downarrow	S_I	S_S	X_I	X_S	$X_{B,H}$	$X_{B,A}$	X_P	S_O	S_{NO}	S_{NH}	S_{ND}	X_{ND}	S_{ALK}		
1	Aerobic growth of heterotrophs		$\frac{1}{Y_H}$			1			$-\frac{1-Y_H}{Y_H}$						$-\dot{X}_{XB}$	$\dot{\mu}_H \left(\frac{S_S}{K_S + S_S} \right) \left(\frac{S_O}{K_{O,H} + S_O} \right) X_{B,H}$
2	Anoxic growth of heterotrophs		$\frac{1}{Y_H}$			1				$-\frac{1-Y_H}{2.86 Y_H}$					$-\dot{X}_{XB}$	$\dot{\mu}_H \left(\frac{S_S}{K_S + S_S} \right) \left(\frac{K_{O,H}}{K_{O,H} + S_O} \right) \left(\frac{S_{NO}}{K_{NO} + S_{NO}} \right) \eta_g X_{B,H}$
3	Aerobic growth of autotrophs						1		$-\frac{4.57}{Y_A} + 1$	$\frac{1}{Y_A}$					$-\dot{X}_{XB} - \frac{1}{Y_A}$	$\dot{\mu}_A \left(\frac{S_{NH}}{K_{NH} + S_{NH}} \right) \left(\frac{S_O}{K_{O,A} + S_O} \right) X_{B,A}$
4	'Decay' of heterotrophs				$1-f_p$	-1		f_p								$b_H X_{B,H}$
5	'Decay' of autotrophs				$1-f_p$	-1	f_p									$b_A X_{B,A}$
6	Ammonification of soluble organic nitrogen										1	-1		$\frac{1}{14}$		$k_a S_{ND} X_{B,H}$
7	'Hydrolysis' of entrapped organics		1		-1											$k_b \frac{X_S/X_{B,H}}{K_X + (X_S/X_{B,H})} \left[\left(\frac{S_O}{K_{O,H} + S_O} \right) + \eta_h \left(\frac{K_{O,H}}{K_{O,H} + S_O} \right) \left(\frac{S_{NO}}{K_{NO} + S_{NO}} \right) \right] X_{B,H}$
8	'Hydrolysis' of entrapped organic nitrogen											1	-1			$\rho_7 (X_{ND}/X_S)$
Observed Conversion Rates [ML ⁻³ T ⁻¹]		$\dot{\eta}_i = \sum_j V_j \rho_j$									$\dot{\eta}_i = \sum_j V_j \rho_j$					
Stoichiometric Parameters: Heterotrophic yield: Y_H Autotrophic yield: Y_A Fraction of biomass yielding particulate products: f_p Mass N/Mass COD in biomass: k_B Mass N/Mass COD in products from biomass: k_X		Soluble inert organic matter [M(COD)L ⁻³]	Readily biodegradable substrate [M(COD)L ⁻³]	Particulate inert organic matter [M(COD)L ⁻³]	Slowly biodegradable substrate [M(COD)L ⁻³]	Active heterotrophic biomass [M(COD)L ⁻³]	Active autotrophic biomass [M(COD)L ⁻³]	Particulate products arising from biomass decay [M(COD)L ⁻³]	Oxygen (negative COD) [M(-COD)L ⁻³]	Nitrate and nitrite nitrogen [M(N)L ⁻³]	NH ₄ +NH ₃ nitrogen [M(N)L ⁻³]	Soluble biodegradable organic nitrogen [M(N)L ⁻³]	Particulate biodegradable organic nitrogen [M(N)L ⁻³]	Alkalinity - Molar units	Kinetic Parameters: Heterotrophic growth and decay: $\dot{\mu}_H, K_S, K_{O,H}, K_{NO}, b_H$ Autotrophic growth and decay: $\dot{\mu}_A, K_{NH}, K_{O,A}, b_A$ Correction factor for anoxic growth of heterotrophs: η_g Ammonification: k_a Hydrolysis: k_b, K_X Correction factor for anoxic hydrolysis: η_h	

Figure 2.3: The matrix form of the full ASM1 (Henze et al., 2007).

- The pH is constant and near neutrality. The ASM1 includes alkalinity, S_{alk} , which allows the user to detect possible pH problems.
- The rate coefficients have been assumed constant which means that changes to wastewater characteristics cannot be handled by the model; this would involve time varying rate terms that would significantly increase the complexity of the model.
- The effects of limitations in some of the inorganic nutrients (e.g. nitrogen, phosphorus, etc.) have not been considered and, therefore, the model is not accurate in these limitations.
- It is assumed the entrapment of particulate organic matter in the biomass happens instantaneously.
- Hydrolysis of organic matter and nitrogen compounds are coupled and occur at the same time with equal rates.

- The biomass is assumed homogenous and its species diversity is unchanged with time such that the effects of substrate concentration gradients, reactor configuration, etc. on sludge settleability are not considered.
- The reactor is well-stirred such that all the nutrients and components are uniform throughout the reactor.

This last assumption states that the bioreactors are well-mixed so concentrations are uniform throughout such that no consideration needs to be made about the hydrodynamics which is assumed for all the ASMs (Henze et al., 1987). However, the biokinetic equations can be extended to account for the hydrodynamics and how this impacts the biological processes; this extension is further discussed in §2.2.

2.1.3 Activated Sludge Simulation Software (ASIM)

Software is available that solves the ASMs with multiple reactors in an easy to use format and user interface. One of these programs is the Activated Sludge Simulation Program ver.5 (ASIM5). This program allows for up to a series of 10 bioreactors with recirculation for a range of biokinetic models. Alongside this, dynamic simulations are available with supported data analysis for comparison with other observed data. The dynamic series of bioreactors only considers the volume and flow between reactors and the bioreactors are assumed perfectly mixed and uniform in the parameters concentrations.

2.2 Extending biokinetic models to account for the hydrodynamics

The ASMs provide insight into the biological performance of a reactor on the assumption that it is well-mixed. However, if we attempt to save energy during operation by reducing the amount of mixing in a reactor, this impacts the hydrodynamic

Component	Name	Description
S_o	Soluble oxygen	Used in nitrification
S_s	Soluble substrate	Readily available molecules to be absorbed for growth
X_S	Particulate substrate	Organic matter that need enzymatic breakdown prior to absorption
$X_{B,H}$	Heterotrophic Biomass	Bacteria that can grow in anoxic and aerobic conditions
$X_{B,A}$	Autotrophic Biomass	Bacteria that can only grow in aerobic conditions
X_P	Inert Particulates	Products that arise from biomass decay
S_{NH}	Soluble Ammonia	Product from hydrolysis of organic nitrogen and removed during nitrification
S_{NO}	Soluble Nitrates	Product of oxidation of ammonium and removed during denitrification
S_{ND}	Soluble Organic Nitrogen	Soluble organically bound nitrogen
X_{ND}	Particulate Organic Nitrogen	Particulate organically bound nitrogen
S_{ALK}	Alkalinity	Certain bacteria needs specific levels of alkalinity to work (Nitrifiers) and other help to increase alkalinity (denitrifiers)

Table 2.2: Description of the nutrients and components in the ASM1. ([Horan, 1989](#); [Jeppsson et al., 2007](#); [Orhon et al., 2009](#)).

flow field in the tank which can effect the performance of the biological processes. Currently, the ASMs do not consider the hydrodynamics and, therefore, cannot be used to assess how changes in the hydrodynamics impacts the performance of the biological processes. However, the biokinetic equations in the ASMs can be extended to account for the hydrodynamics in a reactor. This can be achieved by modifying

the biokinetic rate equations formulation to incorporate the velocity flow fields in the reactors (Glover et al., 2006; Karpinska and Bridgeman, 2016).

Figure 2.4 illustrates a reactor flow diagram using the simple two species ASM defined in §2.1.1 above to describe the biological processes. This flow diagram describes a system with volume V that has a flow rate, Q_{in} , entering into the reactor that carries a concentration of soluble substrate and biomass defined as $S_{S_{in}}$ and $X_{B_{in}}$, respectively. The compounds that are inside and have entered are moved around the reactor by the hydrodynamic flow field while the biological processes occur. Finally, some of the fluid in the reactor flows out at a rate of Q_{out} , which carries a portion of the soluble substrate and biomass out of the reactor.

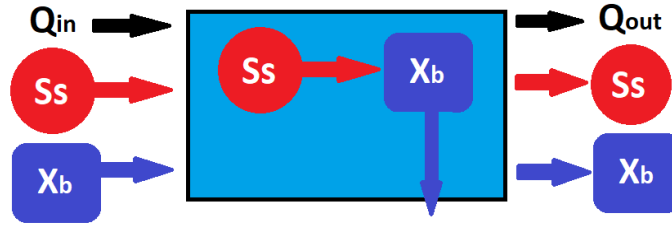


Figure 2.4: Flow diagram of the two species ASM in a reactor with fluid flowing in and out.

The reactor described is a continuous reactor and, therefore, to account for flow moving in and out of the reactor, additional source terms are required to the rate equations in equations (2.1) and (2.2). These modifications are shown below:

$$\frac{dX_B}{dt} = \frac{\hat{\mu}S_s}{K_s + S_s} X_B - bX_B + \frac{Q_{in}}{V} X_{B_{in}} - \frac{Q_{out}}{V} X_B, \quad (2.8)$$

$$\frac{dS_s}{dt} = -\frac{1}{Y} \frac{\hat{\mu}S_s}{K_s + S_s} X_B + \frac{Q_{in}}{V} S_{s_{in}} - \frac{Q_{out}}{V} S_s. \quad (2.9)$$

Furthermore, to account for the generated flow field inside the reactor, equations (2.8)

and (2.9) are extended to advection-diffusion transport equations, as shown below:

$$\frac{dX_B}{dt} + \nabla \cdot (\mathbf{u}X_B) - \nabla \cdot (\Gamma_{X_B} \nabla X_B) = \frac{\hat{\mu}S_s}{K_s + S_s} X_B - bX_B + \frac{Q_{\text{in}}}{V_{\text{in}}} X_{B_{\text{in}}} - \frac{Q_{\text{out}}}{V_{\text{out}}} X_B, \quad (2.10)$$

$$\frac{dS_s}{dt} + \nabla \cdot (\mathbf{u}S_s) - \nabla \cdot (\Gamma_{S_s} \nabla S_s) = -\frac{1}{Y} \frac{\hat{\mu}S_s}{K_s + S_s} X_B + \frac{Q_{\text{in}}}{V_{\text{in}}} S_{s_{\text{in}}} - \frac{Q_{\text{out}}}{V_{\text{out}}} S_s. \quad (2.11)$$

where \mathbf{u} is the fluid velocity in the reactor, Γ_i is the diffusion coefficient for nutrient i , and V_{in} and V_{out} relates to the volume of wastewater entering and leaving through the inlets and outlets, respectively. The extra terms on the left hand side of the equations account for the effect of convection and diffusion, respectively. These equations account for how the compound concentrations change due to the biological processes and reactor hydrodynamics. These equations can be coupled into CFD simulations to investigate and analyse the effects of the hydrodynamics on the biological processes.

Chapter 3

Aeration tank experiments

The large size of WWTP reactors (order 100 m^3) and the unconventional properties of wastewater makes recording experimental measurements on-site difficult. An alternative approach is replicate the reactors at lab-scale to make conducting experiments more manageable. However, the size of lab-scale experiments (order 0.1 m^3) can significantly underestimate the large scale effects observed in full-scale reactors. A pilot-scale reactor (order 1 m^3) is a reactor size that can capture the larger hydrodynamic effects observed in the full-scale WWTP reactors while still being a manageable size to acquire experimental measurements. The University of Newcastle have an operating pilot-scale aeration basin that takes feed from a working wastewater treatment plant in which samples can be taken to conduct biological experiments. In this thesis, a perspex replica of this reactor has been designed and manufactured to conduct hydrodynamic experiments using specialist experimental equipment in a controlled lab environment. These experiments have been conducted in the Civil Engineering water laboratory in the University of Leeds.

In this chapter, a description of the experimental perspex aeration tank design has been given. A detailed explanation of the experimental equipment used to record velocity measurements and the challenges faced when recording in aerated flows has been made. A procedure for recording a series of velocity measurements has been given and a method for post processing the data has been defined. Finally, an

assessment of the experimental results has been conducted and a series of velocity measurements has been obtained that can be used to validate a CFD model of the aeration tank.

3.1 Aeration tank model design

The pilot-scale perspex aeration tank that has been designed for the experiments in this thesis are based on a 2/3 scale of the University of Newcastle pilot-scale aeration tank. The internal dimensions of the perspex tank were: $0.74 \times 0.98 \times 1.20$ m (depth \times width \times height); with a fill height of 1.025 m and fill volume of 0.743 m³ or 743 L (figure 3.1a). Additional structural frame elements were attached to the walls and top to reinforce the sides and stop bowing of the walls, respectively, to further support the reactor. Twelve self-sealing fine bubble membrane diffusers were attached to the base (figure 3.1b) to produce the bubbles when air passes through them. The diffusers have a: membrane diameter of $\cong 0.18$ m (7 inches); a total diameter of 0.23 m; and a height of 0.045 m above the reactor base. The fitted diffusers were spaced equally to the base of the reactor such that the centre placement of the twelve diffusers obey the equation,

$$\text{Centre Placement} = [(2i - 1)R + iL_g] \hat{\mathbf{x}} + [(2j - 1)R + iW_g] \hat{\mathbf{y}}, \quad (3.1)$$

$$\text{for } i = 1, 2, 3 \quad \& \quad j = 1, 2, 3, 4,$$

where $R = 0.115$ m is the diffuser radius, and $L_g = 0.0125$ m and $W_g = 0.012$ m are the space sizes between each diffusers in the depth and width directions, respectively; an illustration of this is provided in figure 3.2.

A manifold system was designed to allow different membrane diffuser configurations setups to be tested, with a maximum of 6 diffusers aerating at one time. A central compressed air system for the lab supplied the air to the reactor. A manual pressure gauge and a gas flow meter (FMA1843A-Mass Flow Meter) were connected

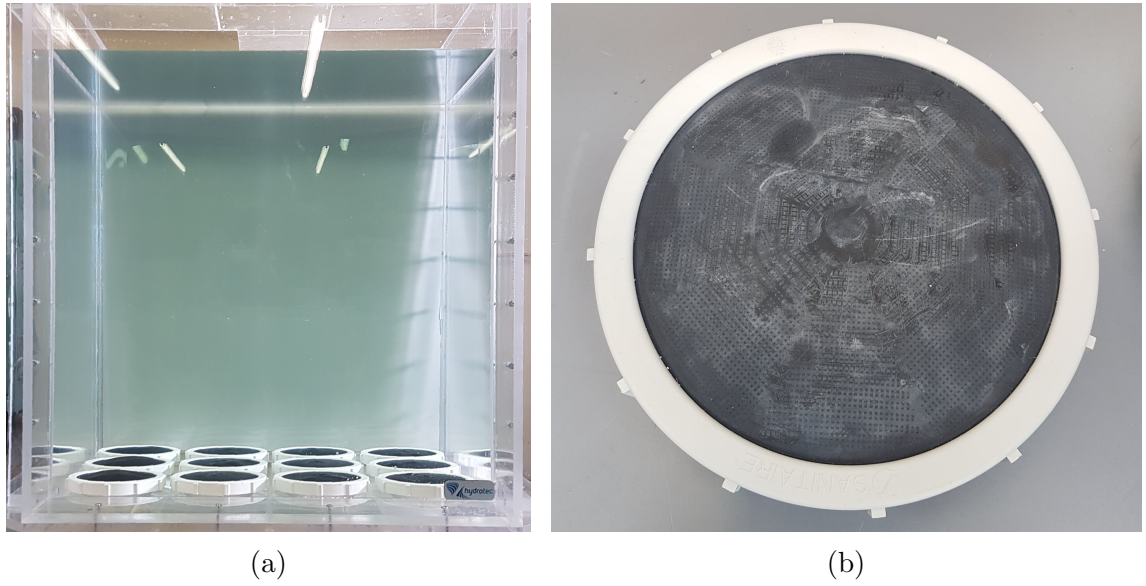


Figure 3.1: Photo of the pilot-scale aeration tank (a) and a fine bubble membrane diffuser (b).

between the central air supply and the perspex tank to allow us to control and measure the amount of air flowing into the tank, respectively. The gas flow meter could measure air flow rates between 0 – 200(± 2) L/min.

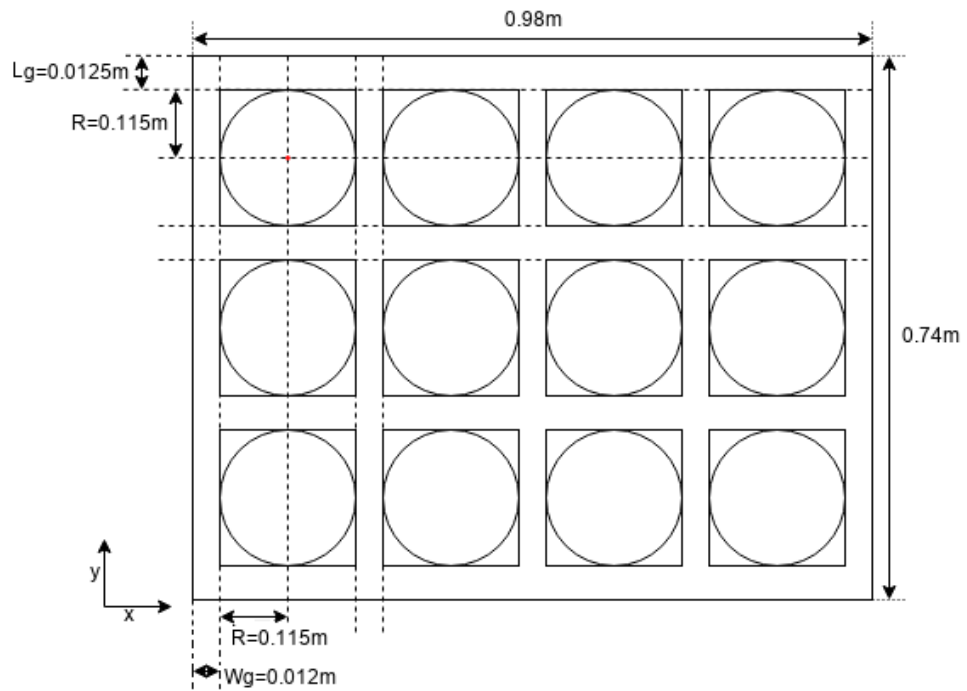


Figure 3.2: Membrane diffuser grid schematic for the base of the aeration tank.

3.1.1 Membrane diffusers

The membranes of the diffusers contain hundreds of tiny holes that are sealed under pressure. As air is pumped into the diffuser, the pressure builds up inside until it is larger than the hydrostatic pressure pushing down on the diffuser. The membrane then begins to bulge under increasing air pressure as it becomes larger than the hydrostatic pressure of the tank. As the membrane bulges, the holes in the membrane begin to stretch until they become wide enough to allow air to escape. As the air escapes, the air pressure drops inside the diffuser and the membrane partially shrinks, sealing the holes in the membrane once more. The releasing and re-sealing of the membrane holes creates bubbles and the process repeats continuously as long as air is being pumped into the diffuser. The manual for the membrane diffusers state the generated bubbles have diameters ranging from 1 - 4 mm ([xylem, 2020](#)).



(a)



(b)

Figure 3.3: A close up of an aerating fine bubble membrane diffuser (a) and an example of the aeration tank running with a specific diffuser configuration setup (b).

3.2 Instrumentation

3.2.1 Acoustic Doppler velocimetry

A Nortek Vectrino Acoustic Doppler Velocimetry (ADV) probe was used to record 3D velocity measurements of the liquid phase in the aeration tank. The ADV has four transducers which can detect and measure the frequency of acoustic waves. A transmitter in the centre of the probe produces a beam of acoustic waves at a fixed frequency. The beam of acoustic waves reflect and scatter off neutrally buoyant particulate seeding (Spherical 110P8, $d_{50} = 10 \mu\text{m}$) that has been mixed into the tank. The four transducers detect the changes in the pulse frequency of the acoustic beam that has been scattered and reflected by the seeding particles. The Doppler shift in the acoustic beam frequency is then used to calculate the velocity of the seeding particle that the beam was reflected off. Finally, because the seeding particulates are neutrally buoyant, the seeding particle velocity is equal to the fluid velocity and, therefore, we find a measurement of fluid velocity at the location the acoustic beam reflected off the seeding particle. An illustration of this process is described in figure [3.4a](#).

The acoustic beam operates at a frequency of 10 MHz with a sampling rate of 100 Hz. The ADV records velocity data in a series of bins below the transmitter. The first bin is located 40 mm below the head of the transmitter, with 1mm spacing between each bin, and the final bin resides 74 mm below the transmitter for a total of 35 bins. A schematic illustration of this is presented in figure [3.4b](#). Full details of how the ADV technology and frequency to velocity calculation can be found in Nortek documentation and [Thomas et al. \(2017\)](#).

The ADV probe is configured to detect velocity measurements in single liquid phase environments and, therefore, the presence of dispersed bubbles in the aeration tank can interfere with recorded velocities. The interface is due to the bubbles travelling at different velocities than the liquid phase as well as changes to the

acoustic pulse as it passes through another phase before being detected. This leads to additional spikes of error appearing in the recorded velocities which need to be removed in post-processing. [Gresch et al. \(2011\)](#); [Lei and Ni \(2014\)](#) and [Karpinska and Bridgeman \(2017\)](#) have all successfully used ADV probes in measuring liquid velocity in aerated systems and, through despiking procedures and algorithms, were able to collect velocity measurements to compare with numerical simulations.

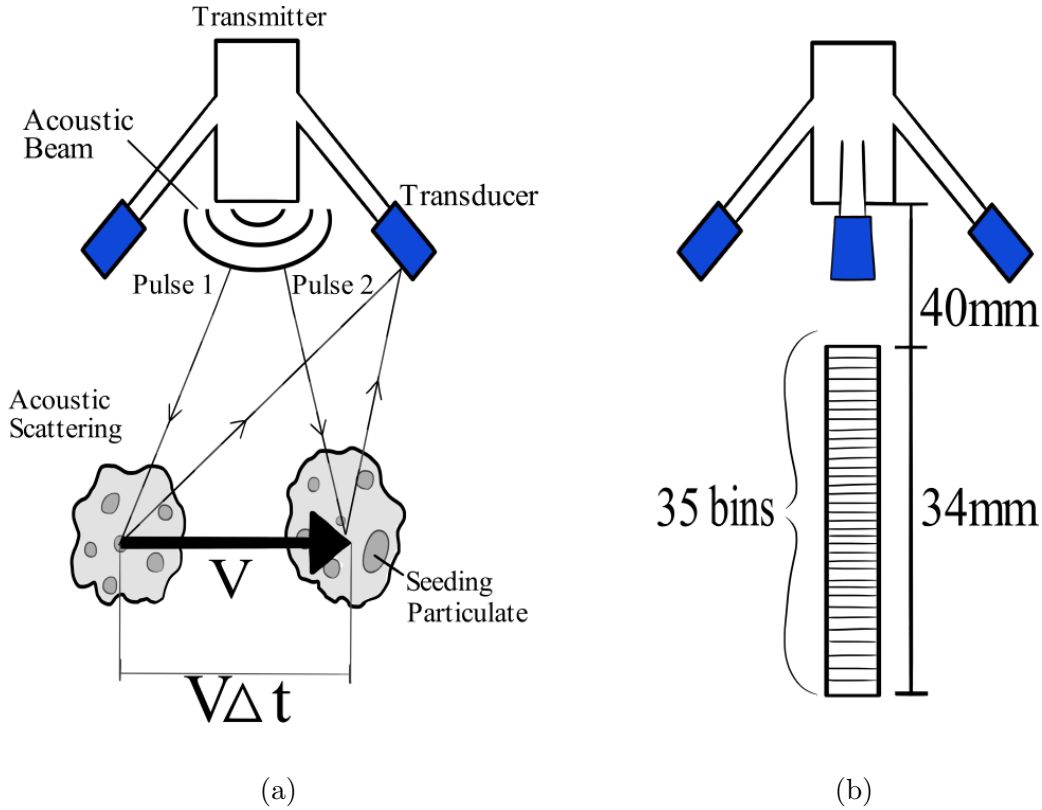


Figure 3.4: An acoustic signal is emitted from central transmitter whose reflection is detected by the 4 outreaching transducers, as shown in (a). The changes in signal frequency can then be used to calculate the fluid velocity in 35 bin locations below the transmitter, as shown in (b). Images are not to scale.

3.2.2 Visualisation

Video capture was used for every ADV recording run to capture the bulk bubble structures in the tank. The video capture was recorded using a GoPro Hero 3 camera at a 1080 HD pixel resolution and a frame rate of 60. The recording was slightly delayed by 10 seconds due to the time taken to begin the ADV recording and travel to initiate the GoPro recording which needs to be considered when matching up the

video recording. The aim was to match the ADV data recording with the video capture such that the video could be cross checked if abnormal velocity data was observed due to significantly more bubble interference near the probe. However, the particulate seeding density required to reach the necessary correlation criteria for good quality ADV velocity measurements resulted in an almost opaque tank and restricted the observations captured by the GoPro. This is illustrated in a later section in figure 3.6. The diffuser configurations setups with high bubble density would often lead to bubbles swarming near the adjacent recording wall that could be captured by the GoPro and provide some qualitative visualisation of the flow structures. However, the location of the ADV was always obscured and, in general, the video capture only provided a qualitative visualisation of the overall bulk flow.

3.3 Experimental procedure

3.3.1 Membrane diffuser configurations

The reactor hydrodynamics is driven by the rising bubbles being released by the membrane diffusers and, therefore, different diffuser configuration setups can create significantly dissimilar flow fields. For the aeration tank, a naming system was introduced to refer to each diffuser which is described in figure 3.5; for example, a configuration “d1d2d3” refers to the 3 diffusers on the far right wall of figure 3.5 aerating.

Having too many diffusers aerating at once would cause a large amount of entrained bubbles, leading to significantly more bubble interference with the ADV. Therefore, the number of bubbles diffusers aerating at one time was limited to 3. The first configuration considered for experiments was “d1d2d3” due to its symmetric and stable generated flow field and is the main configuration considered in this thesis. The sole diffuser “d2” was also considered as another symmetric and reasonable stable configuration with significantly less bubble entrainment but much slower flow

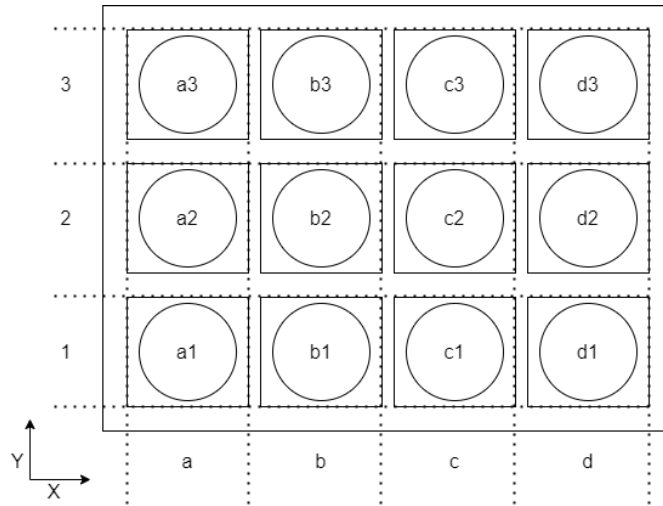


Figure 3.5: A illustration of the naming system to describe each membrane diffuser in the aeration tank.

field. The “c2” configuration was considered to capture an open bubble plume induced flow field; however, due to the asymmetry and near walls of the reactor, this configuration resulted in a less stable bubble plume that increased the error in the ADV recordings. Finally, the “c1c2c3” configuration was also considered as a comparison with “d1d2d3”.

3.3.2 ADV recording locations

The required design for structural stability in the aeration tank when filled was a challenge for the ADV recordings. A perspex cross beam system at the top of the tank, as seen at the top of figure 3.1a, was required to stop the bowing of the side walls under load which obstructed where the ADV probe could reach in the tank. This was improved by upgrading the wide perspex cross beam with two thin m10 steel threaded rods. However, this new system still restricted access to the tank to a quarter of the tank volume from above. A trolley frame was constructed and attached to the top of the tank to allow 3D movement and placement of the ADV inside one quarter of the tank. These features along with the ADV probe are illustrated in figure 3.6.

The ADV probe can only record data at one point at a time and, therefore,

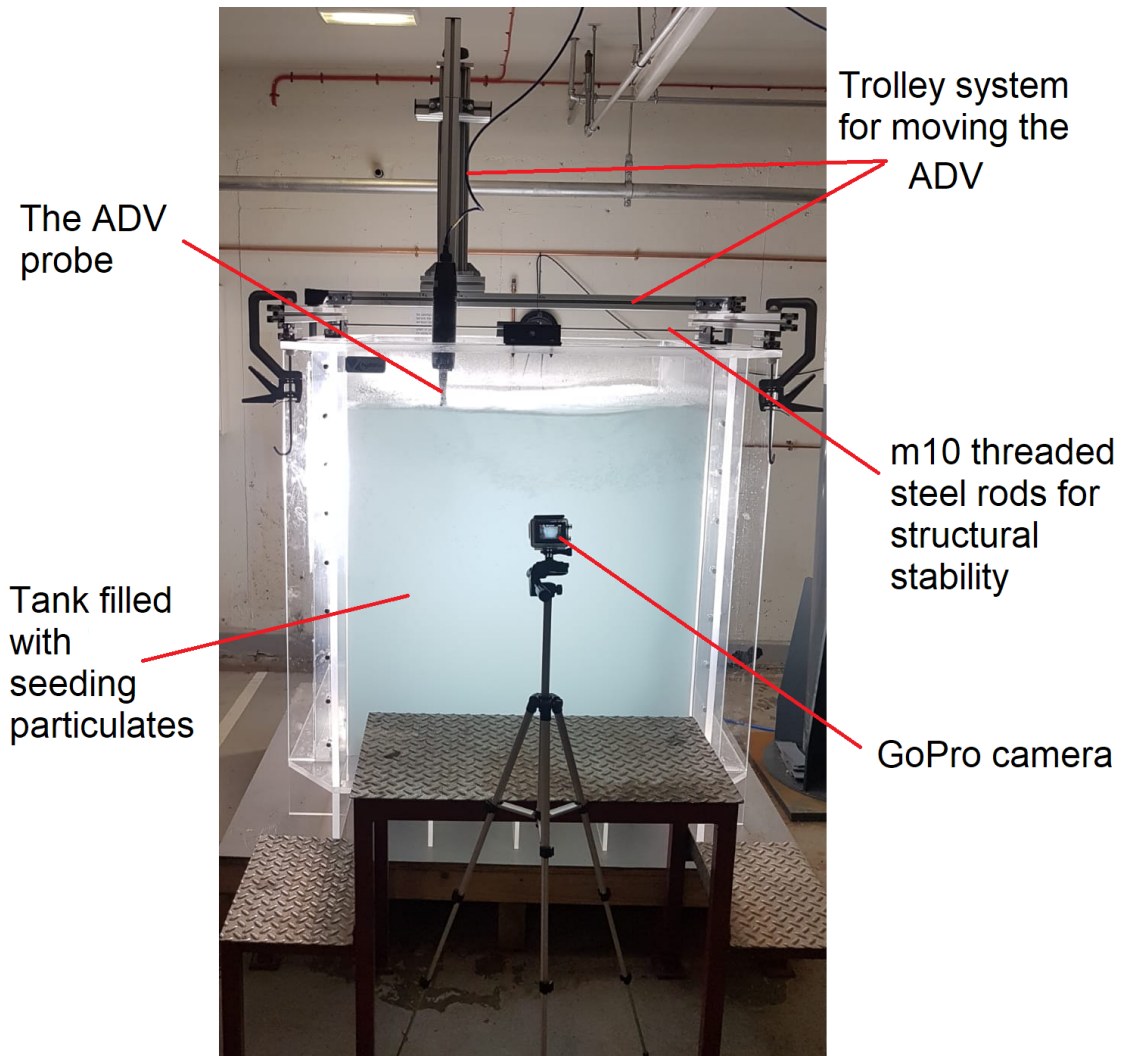


Figure 3.6: The aeration tank with the seeding particulates inside and illustrating the other features of the experimental setup: described above.

it is important to choose optimal locations to get a good spread of velocity data while also choosing points with the least bubble interference. Initial experimental tests found that the produced bubbles swarmed up from the diffusers with a trend to move across towards the near side walls. Once the bubbles reached near the fluid surface, most of the bubbles escaped while a portion of the bubbles would be pulled and driven along the moving liquid surface until reaching the other side wall where the bubbles would then be re-entrained into the reactor with the liquid phase. The higher air flow rates were found to have more bubble entrainment. The entrained bubbles would not travel all way down to the base of the reactor. The rising buoyancy forces would eventually become larger than the entrainment forces

after traversing around half the reactor height. This entrainment along the fluid surface resulted in large amounts of bubbles near surface such that placing ADV probe in this region would result in a lot of bubble interference with the acoustic pulses, making it a poor location for ADV measurements. Furthermore, the flow at the base of the reactor is slow which reduces the accuracy of the ADV measurements such that this would also be a poor location for ADV measurements. Therefore, a 3D region below the fluid surface and above the base has been chosen to record the liquid phase velocities. Three distances in each direction has been chosen to make a total of 27 points for each diffuser configuration. If P_{ijk} describes the recording position, where i, j, k describes the x, y, z direction, respectively, such that: x is the width, y is the depth (figure 3.2 illustrates the x and y axes) and z is the height; then $i, j, k = 1, 2$ or 3 and their values are described in table 3.1.

P_{ijk} Values of i, j, k	Distance (m \pm 0.005m)		
	x_i	y_j	z_k
1	0.127	0.128	0.435
2	0.248	0.249	0.535
3	0.369	0.313	0.635

Table 3.1: The 27 points chosen to record liquid velocity measurements with the ADV probe.

For $k = 1, 2, 3$: $i = 1, 3$ $j = 1$, these correspond to positions above the centre of diffuser “a1” and “b1”, respectively; $i = 1, 3$ $j = 2$ and $i = 2$ $j = 1$ correspond to positions in-between diffusers “a1a2”, “b1b2” and “a1b1”, respectively; and $i = 2$ $j = 2$ correspond to positions in between diffusers “a1a2b1b2”. Due to the restrictions of the cross support bars, the $j = 3$ distance is the deepest the ADV could be placed to be in line with the middle depth of the reactor. The height positions were limited by the trolley height elevator system and the lab ceiling; in general the heights correspond to locations that have the least bubble interference while still capturing key fluid flow features. In an ideal situation, the ADV recording locations would be more spread out in the tank to get larger spread of measurements for a

given flow field; however, due to the limitation of the experimental tank structure, this was not possible. The region volume is approximately 6% of the total reactor volume which is small compared to the total volume of the reactor. However, when we consider that only about 50% of the reactor is appropriate for recording ADV measurements and that we have symmetry down half the reactor for the diffuser configurations considered, the recording volume is approximately more similar to 24% of the available volume for recording which is a more significant percentage of the total recording volume. Additionally, we will illustrate later that, for certain diffuser configurations setups, we are able to combine data sets to further increase to recording volume size, giving an appropriate spread of velocity measurements to validate a CFD simulation. Figure 3.7 is a general illustration of the recording locations for the ADV probe.

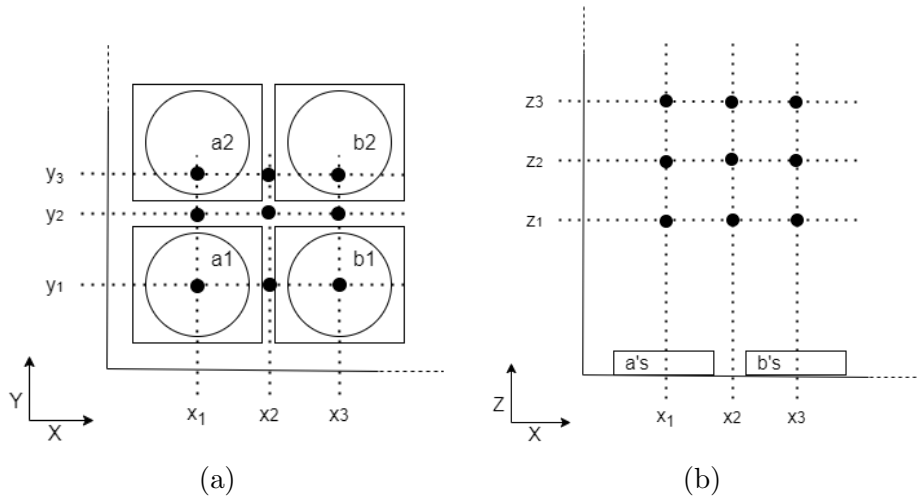


Figure 3.7: An illustration of the ADV recording locations in the x-y plane (a) and x-z plane (b).

3.3.3 Aeration flow rates

The flow meter could measure air flow rates between $0 - 200 \pm 2$ L/min which would be shared between the connected diffusers. The membrane diffusers can operate in a range of 14 - 116 L/min. Gresch et al. (2011) analysed a full-scale aeration tank using ceramic diffusers and found the air flow rates through each diffuser was 0.6 L/s

or 36.7 L/min. The full-scale aeration tank used 1800 diffusers to aerate a 3500 m³ tank such that 0.51 diffusers at 36.7 L/min are required per m³ of wastewater or 18.86 L/min of aeration per m³. This would suggest that for the filled 0.7252 m³ perspex tank, we would require 0.373 diffusers pumping air at 36.7 L/min or 1 diffuser operating at 13.68 L/min. However, a full-scale aeration tank usual has a height of approximately 2 - 6 m (Ovezea, 2009; Roman and Mure, 2015), significantly higher than the our pilot-scale aeration tank, as it allows more time for oxygen to transfer as the bubble rises. A more useful quantity from Gresch et al. (2011) would be the number of diffusers per m² of the reactor base, however, they do not state this. If we assume the height of the reactor is between 2 - 6 m, then there is one diffuser per 0.972 - 0.324 m² of reactor base. The pilot-scale experiments used between 1 or 3 diffusers for a given run which corresponds to one diffuser per 0.725 or 0.242 m² of the reactor base. There are multiple methods to scale the aeration rates for the pilot-scale reactor which all have their own pros and cons. In our case, the aeration rate for the pilot-scale aeration tank was set similar to the rates used in a full-scale reactor. Additionally, the diffuser density at the base of the pilot-scale aeration tank was also similar to a full-scale aeration tank such that the pilot-scale tank is more similar to modelling a segment of a full-scale aeration tank. Therefore, experimental runs were conducted using aeration flow rates rates of 36 and 18 L/min (0.6 and 0.3 L/s, respectively) per diffuser for the diffuser configurations setups described in §3.3.1 which are comparable with the rates described in Gresch et al. (2011).

3.3.4 Initial experimental checks

Initial experiments were conducted to confirm: the time required to average over the data such that we have time averaged steady-state velocity values; the repeatability of the experimental runs for a given probe location; how slight changes in the air flow rate impacted the experimental recorded values; and the symmetry of the tank. To calculate the time required to reach a time averaged steady-state value, the ADV probe recorded data at the same point for a period of: 1, 2, 3 and 4 minutes;

and the time averaged velocity was calculated for each run and compared. The computed values had a variation in the velocity magnitude of 1.5 - 8.5 % from the mean with an average variation of 4.5 % which is relatively small implying that all time periods would be appropriate for averaging. A 2 minute period was chosen for the time averaging period as it is long enough to reach a time averaged steady-state value, would reduce the impact of irregularities from bubble interference over the 1 minute period, and is a relatively shorter time compared with the 3 and 4 minutes period which allows for significant more points of data to be recorded for a given experimental recording session.

A series of tests were conducted to check the repeatability of the experimental runs for a given diffuser configuration setup. After recording a velocity point, these tests involved: turning off the air flow, allowing the tank to reach a rest state, and then starting up the reactor again and recording the same reading; turning off the air, leaving the tank overnight, and testing the same point the next day after turning the air back on; turning off the air, moving the manifold system tubes around and starting up the air again and measuring the same point. The variation from the mean of the calculated velocity magnitude values ranged from 0.5 - 3.5 % with an average of 2.3 % which is small such that we are confident we have repeatability in the measurements.

The central compressed air system in the lab had small fluctuations during operation such that it could cause slight periodic changes in the air flow rates (by ± 1 L/min) over the 2 minute recording periods. The flow rate was controlled by a manual pressure gauge and so different amounts of interaction with the pressure gauge during experimental runs were investigated to assess their impact on the recorded ADV results. It was found there was a 1 % difference in the recorded velocity magnitude between setting the flow rate to the desired value before an experimental recording period and then not manipulating the pressure gauge during the recording period compared with manually keeping the flow rate at the desired flow rate over the whole 2 minute period. While manually changing the pressure

gauge to keep the desired flow rate over the recording period is the more accurate procedure, the gauge is sensitive and takes a certain level of concentration such that, over a long period of recording multiple measurements, the human error will become more significant. In comparison to the 1 % error from the small changes in the central compressed air system over the 2 minute recording period that has no human error, over a series of multiple ADV measurements this procedure will be more accurate. Therefore, the procedure of setting the flow rate to the desired value before an experimental run and not manipulating the system during an experimental run was adopted. The flow rate value at end of each run was recorded to observe if there was a significant change in air flow rate after the two minute period, in which case that run would be neglected and measured again. In total, the average error from all these experimental procedures is about 8 %.

The ADV probe is confined to a quarter of the reactor volume and the only way to move another section would require: draining the tank, removing the cross support beams, shifting the ADV probe across, reattaching the cross support beams, and refilling the tank; all of which takes around a day to complete which significantly increases the time taken to record measurements. However, we can easily change the location of the diffusers that are aerating the tank using the manifold system. These changes could be made such that they would be equivalent to moving the ADV probe to a different quarter segment of the tank (diffuser configuration setup “a1a2a3” is equivalent to “d1d2d3” with a change in the frame of reference, as illustrated in table 3.2). For the diffuser configuration setups considered in this thesis, there is a symmetry planes along the width and depth of the tank. Experimental tests were conducted to confirm if this was the case as, if symmetry planes are shown, data sets from different diffuser configuration setups can be reflected and combined to increase the total size of the data set for a given diffuser configuration. Three pairs of experiments were conducted that involved moving the ADV probe to a new quarter region to assess if this symmetry hypothesis was true. A comparison of the y or depth velocity magnitudes between an “a1a2a3” and “d1d2d3” diffuser

configuration at the same equivalent point was made where 3 runs were conducted for each diffuser configurations. Assuming we are measuring the same y velocity for all 6 experimental runs, the velocities varied between 2 - 7.5 % from the mean value with an average variation of 4.5 %. The other 2 pairs of experiments involved the “b2” and “c2” diffuser configurations which were found to have velocity magnitude average variation of 1.6 and 2 %. These errors are smaller than the experimental procedure error of 8 % so we can assume that the results are the same within experimental procedure error. Therefore, we can assume that we have symmetry in the diffuser configurations such that we can reflect and combine data sets. The implications of this is further discussed in the next section, §3.3.5.

3.3.5 Diffuser configuration symmetry

The pilot-scale tank structural reinforcements restrict the ADV measurements to a quarter of the tank volume. However, due to the symmetry of the tank, for example: the data from running the “d1d2d3” diffuser configuration and measuring above the “a1, a2, b2 and b3” diffusers is identical to the data from the “a1a2a3” diffuser configuration and measuring above the “c1, c2, d2 and d3” diffusers, respectively, with some direction translations to match the coordinate system, as illustrated in figure 3.8. Additionally, through experimental tests discussed in section §3.3.4, we have shown that we have symmetry in the recorded experimental data such that we can reflect the values along these symmetry planes, an example of one of these planes is illustrated in figure 3.8. Therefore, we can combine data from different diffuser configurations to make a larger data set for one diffuser configuration setup.

Additional diffuser configurations: “a1a2a3” and “b2”, were run to be combined with the “d1d2d3” and “c2” configurations, respectively, to increase the size of the original data set. The combining of data sets increases the number of recorded points which can be defined using an updated P_{ijk} form as expressed in table 3.2.

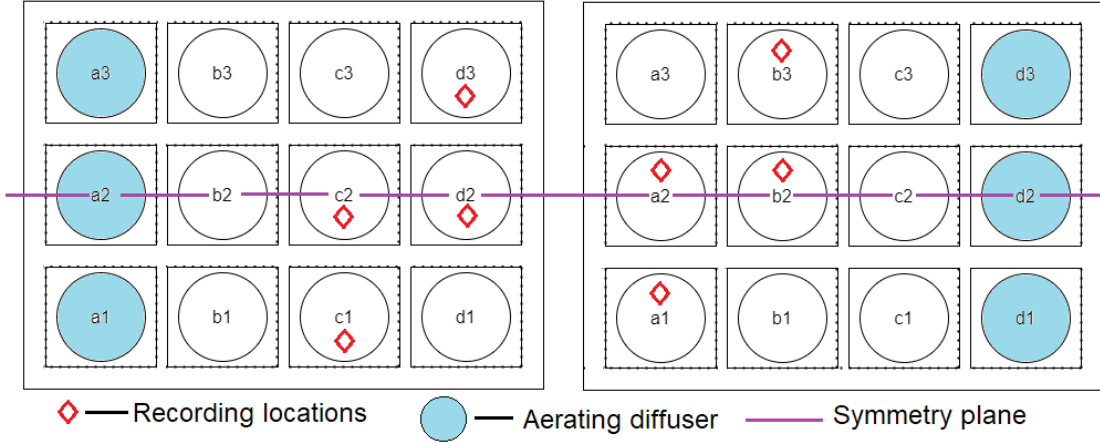


Figure 3.8: In this image, the aerating diffuser setups and recording points of the two scenarios are identical to one another but with different coordinate axes, illustrating the symmetry in the tank for certain diffuser configurations setups. The symmetry plane for this diffuser configuration setup is also illustrated.

P_{ijk} Values of i, j, k	Distance (m \pm 0.005m)		
	x_i	y_j	z_k
1	0.127	0.128	0.435
2	0.248	0.249	0.535
3	0.369	0.313	0.635
4	0.611	-	-
5	0.732	-	-
6	0.853	-	-

Table 3.2: The locations of the 54 points measured by the ADV probe when combing data sets by applying the symmetry condition.

It is important to note, when the mirror diffuser configuration data was recorded, certain positions were not considered as they would lie inside the plume resulting in a lot of bubble interference such that no useful ADV data would be recorded (e.g. points with $i = 1$ for the “a1a2a3” configuration all reside in the plume, this translates to the combined “d1d2d3” data not having any data in the $i = 6$ positions). Therefore, we do not get the total 54 points of data but still obtain a much larger data set compared with the original diffuser configurations considered.

3.3.6 ADV recording routine

In this section, the procedure for recording a series of ADV points for a generic diffuser configuration is outlined. The ADV placement was setup such that the x direction transducer was parallel with the defined x or width direction in figure 3.7 such that the recorded ADV velocities corresponded to the appropriate directions without needing additional post processing afterwards. For a specified diffuser configuration and air flow rate, the designated diffusers would be connected to the manifold and the flow rate would be set and ran for at least 5 minutes to reach a steady-state in the tank which also allowed the seeding particulates to be well mixed into the reactor. Once the tank was observed to have reached a steady-state: the ADV would be placed in the starting recording location; the pressure gauge would be manually moved to set the desired flow rate on the flow meter; and the ADV range settings would be checked to confirm that the data recorded is acceptable. The velocity range defines the range of velocities we expect to be observed at the probe location. Any values above the range gets wrapped around the range and interferes with the recorded data resulting in bad data. However, a range that is too large results in less accuracy in the captured velocities. As the velocities varies with each location, this range needs to be changed to accommodate this. The velocity ranges used for the different diffuser configurations and flow rates are summarised in table 3.3.

Once the velocity range was set, the ADV recording would be initiated for 2 minutes and the GoPro video recoding would be started. After 2 minutes: the ADV would automatically stop recording; the GoPro video recording would be stopped; the flow rate shown on the flow meter would be noted; and the recorded ADV data points Signal-to-Noise Ratio (SNR) and correlation would get an quick inspection to check if the data was acceptable. The SNR is the difference between the recorded signal strength and the background noise and the correlation is a comparison of the energy of the back scattered acoustic signal compared with original to assess the

quality of the recorded data (Thomas et al., 2017). The criteria for good quality ADV measurements are for the SNR and correlation values to be above 20 db and 70 %, respectively (Thomas et al., 2017). The values calculated for these experiments are described in table 3.3 and satisfy the necessary criteria; implying that the data recorded is of good quality.

Once the quality of the ADV data was assessed, the measurement would be repeated at least two more times for the given point with occasional re-runs if required from inspecting the recorded ADV results or if the air flow rate had fluctuated significantly over the 2 minute period. Once the recording of a point was completed, the ADV would be moved using the trolley system to the next location with the priority of y direction first, then x, then z as the trolley system was easiest to move in those directions in that order. The routine above was repeated for the new point and continued until all the desired points for a configuration was completed. Before moving onto the new air flow rate or diffuser configuration, the air was turned off to allow the fluid in the tank to reach a rested state as to not leave any residing fluid structures that could influence the new generated flow field. The above routine was then repeated for the new diffuser configuration or air flow rate; traversing through the same points, but in reverse.

Number of Diffusers	Flow rate (L/min)	Velocity range (m/s)	SNR (db)		Correlation (%)	
			Range	Average	Range	Average
3	108	0.9 - 2.2	23 - 44	38	82 - 94	91
3	54	0.8 - 1.6	28 - 50	40	89 - 95	93
1	36	0.6 - 1.1	26 - 48	38	92 - 96	95
1	18	0.5 - 0.8	22 - 47	36	91 - 96	95

Table 3.3: Summary of the general ADV settings and data quality values obtained from the measurements for the different diffuser configurations and flow rates.

3.3.7 Summary

Overall, a recording of 6 different diffuser configurations was conducted, with 4 of those configurations having two different flow rates measured. A total of 228 different points and 691 runs of data were recorded or 1382 minutes (≈ 23 hours) worth of captured ADV data. A summary of this information is presented in table 3.4.

Diffuser Configuration	Flow Rate (Lmin^{-1})	Number of Points	Total Runs
d1d2d3	108	27	84
d1d2d3	54	27	81
a1a2a3	108	18	54
a1a2a3	54	18	54
c2	36	27	82
c2	18	27	81
b2	36	15	45
b2	18	15	48
c1c2c3	54	27	81
d2	36	27	81

Table 3.4: Summary of the: different diffuser configurations considered, their flow rates, number of point recorded, and total runs for the ADV velocity experiments.

3.4 ADV data post-processing

The ADV records at a sampling rate of 100Hz in 35 bin locations below the transmitter to calculate 4 components of velocity (the z velocity is calculated in two different independent ways) such that, over a two minute recording period, 12000 velocity values are captured for each component at each bin location, making a total of 1.68 million values of data for each measuring point. Therefore, post processing the data effectively is important to get the most worth out of the data. The ADV recording locations have been chosen to reduce the amount of bubble interference, however, bubbles still occasionally reach the recording area and interfere with the acoustic signal. Figure 3.9 illustrates the spatially averaged raw data of the 3 components of velocity and velocity magnitude recorded over a 2 minute period for the “c2” diffuser

configuration; the raw data has been spatially averaged over the 35 bins to make the data more readable. Figure 3.9 plots show a general trend near the calculated mean along the red line but with occasional large spikes in the velocities. These spikes are caused by the bubble interference near the instrument; changes in the acoustic signal speed as it passes through the two mediums causes abnormal frequencies and, thus, velocities to be recorded at the transducers. The data is time averaged to obtain a steady state value; however, these abnormal spikes will impact the final averaged result. A common procedure to reduce the impact of these anomalies is to adopt a de-spiking algorithm to filter and clean the data which will be further discussed in the next section.

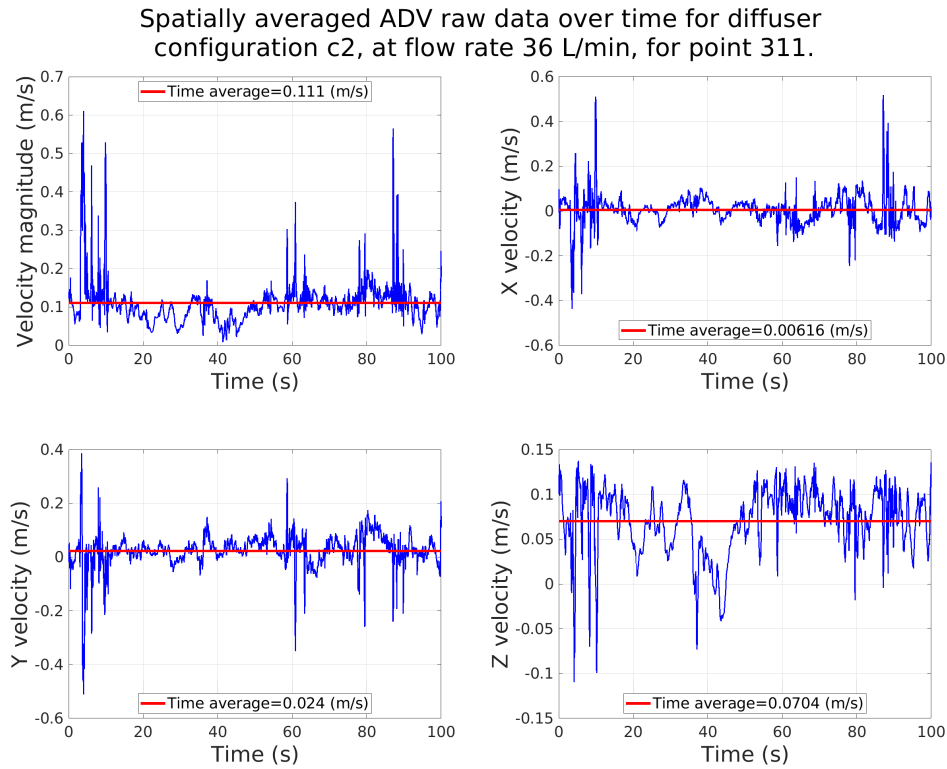


Figure 3.9: Spatially averaged raw ADV data and the time averaged value over a minute recording period for the 3 velocity components and velocity magnitude for diffuser configuration “c2” at flow rate 36 L/min for point P_{311} .

3.4.1 De-spiking algorithm

A de-spiking algorithm finds abnormal data and removes them using statistical methods resulting in a filtered clean data set. In this work, a global averaging filter was applied to de-spike the data. The mean and two standard deviations for each bin over the 2 minute recording for each component of velocity was calculated; any data outside of two standard deviations of the mean was removed. If we assume that the original mean calculation is only partially impacted by the spiked data, then at two standard deviations we should be keeping 95 % of the correct data set. Additionally, this algorithm was only applied once and no interpolation was applied to the removed data such that only the original core data is left for further calculations.

Compared to the global average filter, more complex de-spiking algorithms exist, such as the phase space filter algorithm ([Goring and Nikora, 2002](#); [Wahl, 2003](#)), which have been used on ADV data from bubbly flow experiments ([Mori et al., 2007](#); [Karpinska and Bridgeman, 2017](#)). While these more complex algorithms use more sophisticated statistical methods to remove bad data, they require additional interpolation and iterative steps that can begin to artificially manipulate and replace the data to favour a result. The simpler global average filtering process only manipulates the data once such that the core of the raw data still remains and we can be more confident that the calculated values truly represent the recorded velocities. However, this method is only valid when the majority of the captured data is already clean as we are assuming the global raw mean is very similar to the global clean mean such that the data outside of two standard deviations is only the spiked air bubble data. In the case of these experiments, the ADV recording points have been chosen such that they have minimal bubble interference and, therefore, the majority of the captured data is clean and the global filtering algorithm is appropriate. This algorithm has been applied to the raw data in [figure 3.9](#) and the filtered data is presented in [figure 3.10](#). As illustrated in [figure 3.10](#), the large abnormal data spikes

have been filtered out and we are left with a more structured signal.

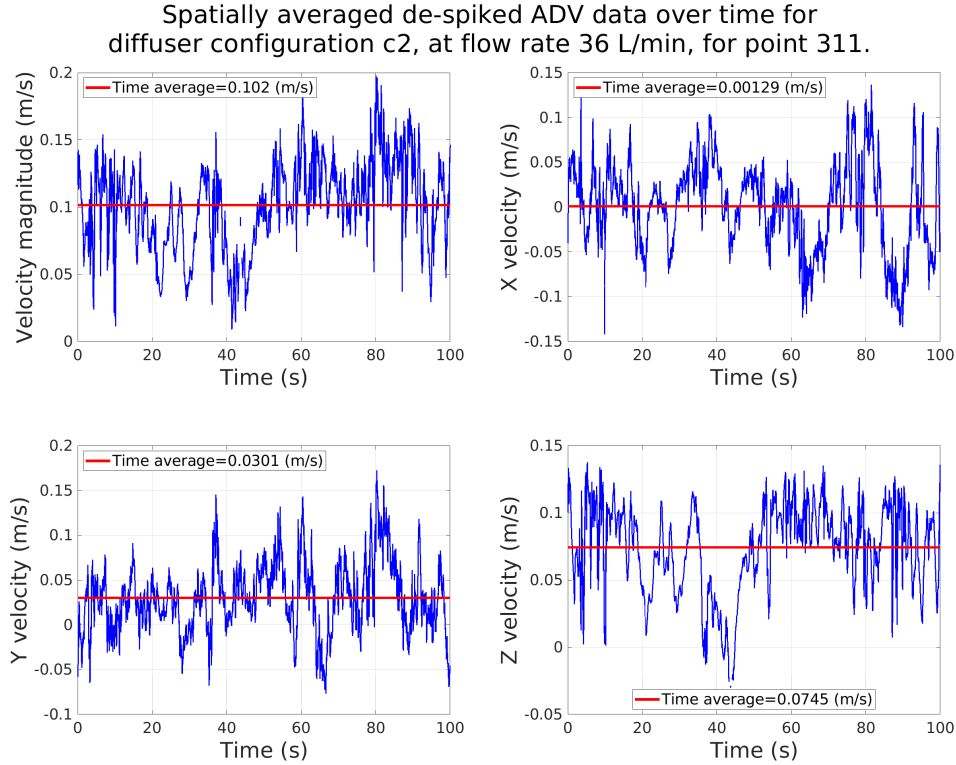


Figure 3.10: Spatially averaged de-spiked ADV data and the time averaged value over a minute recording period for the 3 velocity components and velocity magnitude for diffuser configuration “c2” at flow rate 36 L/min for point P_{311} .

3.4.2 Data evaluation

After applying the despiking procedure the data is ready to be post-processed. The data was time averaged over the 2 minute recorded period for each velocity components; this was done for all runs and bin locations at each point and the standard deviation and error was calculated for each time averaged value. Figure 3.11 is an example of the time averaged data with their standard error for diffuser configuration “d12d2d3” at a total flow rate of 108 L/min for point P_{123} for each run conducted. Additionally, the total spatial average across all bins and runs was calculated and included. The distance on the y axis describes each bin location below the ADV, starting at the first bin that is 35 mm below the acoustic signal transmitter.

To assess the accuracy of the recorded data, the two recorded z velocity com-

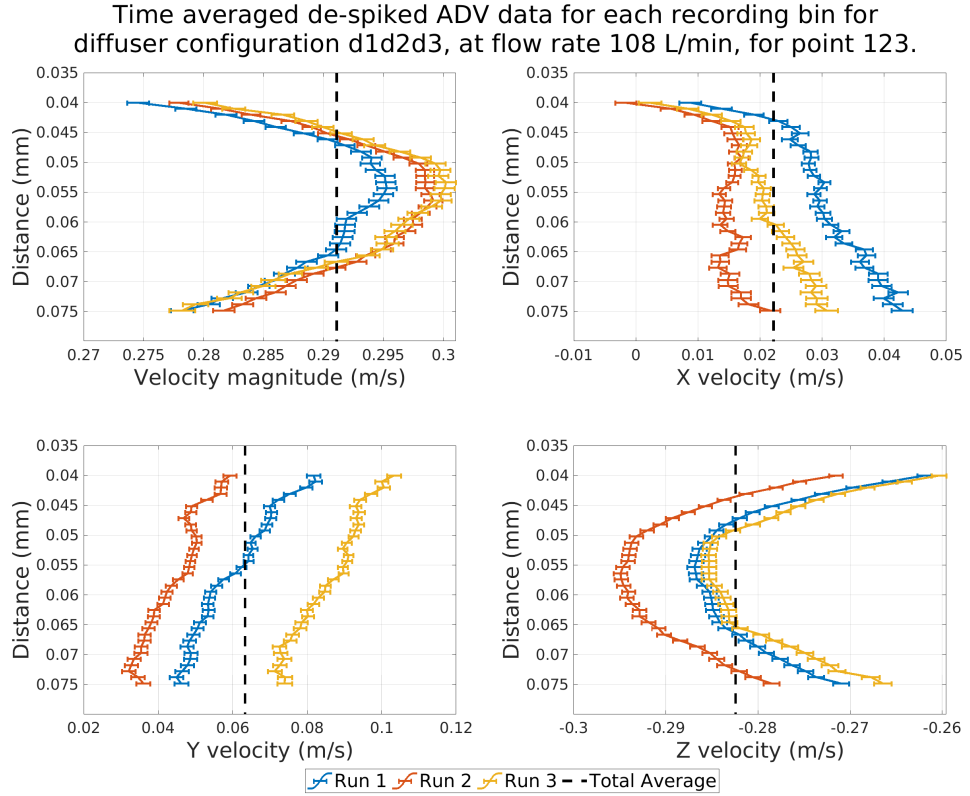


Figure 3.11: The de-spiked time averaged ADV data for the 3 runs recorded with their standard errors for the velocity magnitude and 3 velocity components for: diffuser configuration “d1d2d3”, at flow rate 108 L/min, at point P_{123} .

ponents were compared and the percentage of removed data was calculated. Two independent calculations of z velocity are computed by the ADV which should be identical in smooth well-behaved flow fields. Comparing the z velocity profiles for each run can give us insight if there was any irregularities in the ADV recording. After analysing the recorded points, no irregularities were found in the z profiles giving confidence in the recorded data set. Additionally, the percentage of data removed by the despiking algorithm was found to be around 6 - 8 % on average for each component with an observed maximum of about 10 % for one recording measurement. As 90 % and above of data was still retained after the de-spiking algorithm, it was deemed that there is still enough data remaining that the despiking algorithm was appropriate for these data sets.

The ADV records data at a point in 35 bins in an approximate small volume of $2 \times 2 \times 3.5$ cm which, in comparison to the volume of the tank, is very small.

Comparison of the time averaged Z velocities and percentage of data removed by the de-spiking algorithm for diffuser configuration d1d2d3, at flow rate 108 L/min, for point 123.

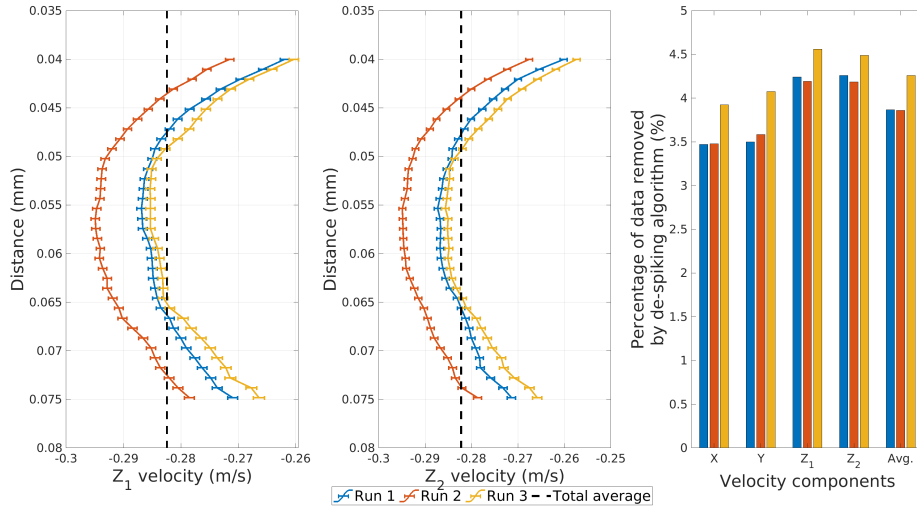


Figure 3.12: The de-spiked time averaged z components for the 3 runs recorded with their standard errors for comparison and the percentage of data removed by the despiking algorithm for each component and run for: diffuser configuration “d1d2d3”, at flow rate 108 L/min, at point P_{123} .

Therefore, instead of considering each bin independently, the spatial average of all the ADV bin locations for all 3 runs is calculated to get one temporal and spatial averaged velocity that represents the whole $2 \times 2 \times 3.5$ cm volume. The temporal standard errors are much smaller than the spatial ones and, therefore, only the spatial errors were considered when calculating the temporal and spatial averaged velocity errors. This was conducted for each diffuser configuration and flow rate and the results are presented in §3.6.

3.5 Error analysis

In this section, we will review the potential uncertainties and errors in the experimental procedure and assess their impact on the experimental results.

- The compressor for the lab would fluctuate during the recording process which could vary the flow rate by ± 1 L/min over the 2 minute recording period. The flow meter value was recorded before and after every run to confirm any abnormal fluctuations. Furthermore, the flow meter has a tolerance of ± 2

L/min initially so the compressor error is smaller than the instrumental error. Additionally, the initial experimental checks found that the slight fluctuations in the flow rates produced a 1 % error in the measurements which is small compared with the other experimental procedure errors.

- The ADV trolley system for setting the probe location had an uncertainty of ± 0.5 cm for the x, y and z directions. However, after spatially averaging the 35 ADV bins locations, the size of uncertainty for the total point volume is larger than the trolley system error; therefore, the error due to the trolley system is minimal.
- Pressure drops across the manifold system outlets can result in lower air flow rates through the neighbouring outlets. However, it was observed that the pressure drops were small enough to not see a change in the air flow rate through neighbouring diffusers.
- The symmetric box shape of the perspex tank and close proximity of walls to the ADV can cause reflection and re-interference of the transmitted ADV acoustic signal. When the ADV emits a beam of acoustic waves, occasionally the signal can be reflected off the tank walls and re-interfere with the original signal and cause irregularities in the detected signal at the transducers. This can cause sudden spikes at specific bins in the data, as illustrated in figure 3.13. However, as illustrated in figure 3.13, if re-interference occurs it only affects one bin location such that the error would be significantly suppressed when we spatially average and, therefore, would not significantly impact the results.

3.6 Experimental results and discussion

A total of 10 different diffuser configurations and flow rate experiments were conducted, as described in table 3.4. When using the symmetry property of the tank, this produces 6 unique sets of velocity data. The work in this thesis focuses on two

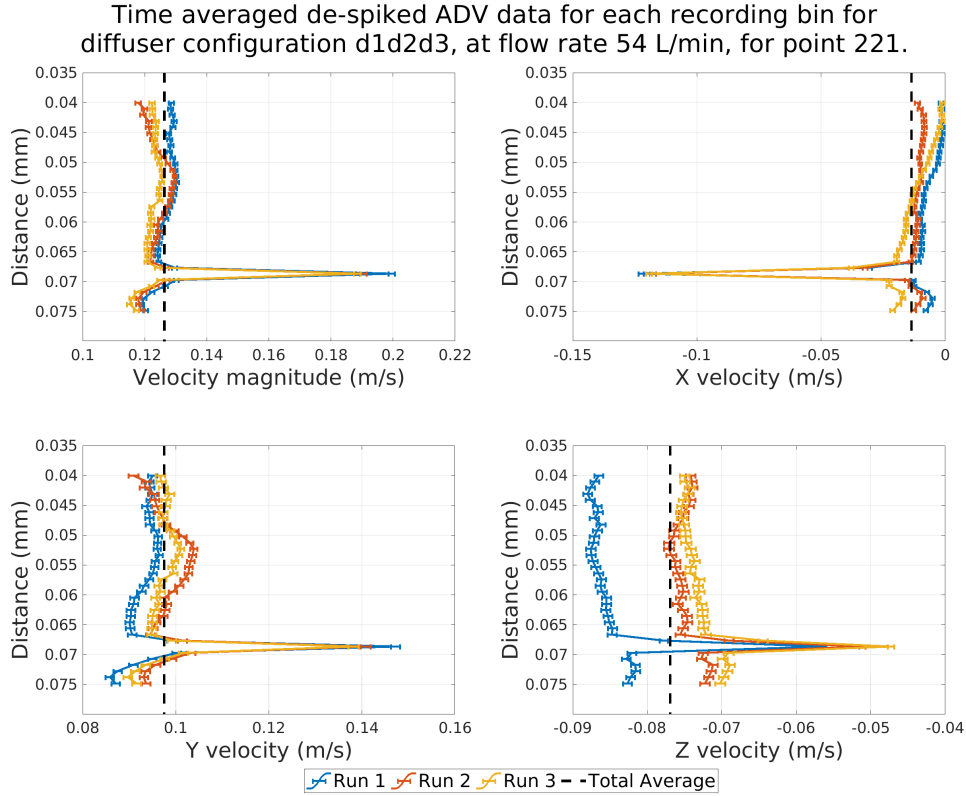


Figure 3.13: The de-spiked time averaged ADV data for the 3 runs recorded with their standard errors for the velocity magnitude and 3 velocity components for: diffuser configuration “d1d2d3”, at flow rate 54 L/min, at point P_{221} .

of those sets: the combined results of the “d1d2d3” and “a1a2a3” configuration at flow rate 108 and 54 L/min; and therefore, only these data sets will be discussed in this section. The other results can be found in the appendix §8.1. A table with all the velocities recorded and their associated standard errors for each configuration will be presented along with 3D vector plot of the data. Along with the table of velocity data, an assessment on the accuracy of the measurements has been made based on the difference of the two recorded z velocities. Ideally, the two independent z velocity measurements are identical; however, with the bubble interference, there can be slight differences from this even after applying the despiking algorithm. The difference between the two z velocities was calculated and divided by the smallest standard deviation of either velocity component to give insight into the magnitude of the difference. If the two z velocities are in the same data set then they should lie within each others standard deviation where, statistically, 68 %, 95 % and 99.7 % of a data set lie within 1, 2 and 3 standard deviations, respectively. These values

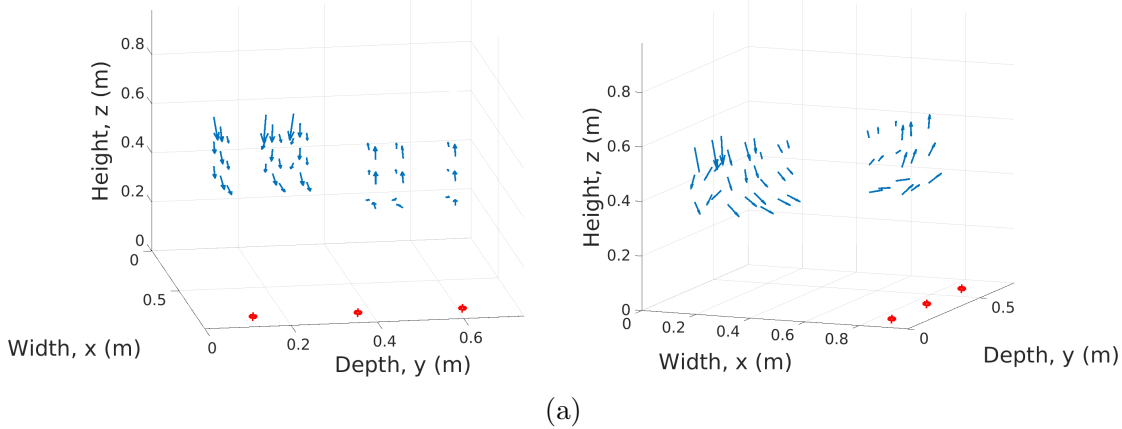
were calculated and presented in table 3.5 and figure 3.16 below with colour codes to represent the accuracy of each point such that: green was if the velocity difference is below 1 standard deviation (good); yellow if the difference below 3 standard deviations (acceptable); and red was if the difference was outside of 3 standard deviations which is an indication of a lot of bubble interference at that point and, therefore, should be further investigated.

3.6.1 Configuration “d1d2d3” and “a1a2a3” combined results for flow rate 108 L/min

This configuration has the highest flow rate and observed the most bubbles entrainment. As a result, it is the data set with the highest amount of points, 6, with the difference between the z velocities outside of 3 standard deviations, as shown in table 3.5. However, evaluating the magnitude of the difference compared with the size of the w_1 velocities finds only about 5 - 20 % difference. This indicates that the data values are close to one another but just have small error bars. When we account for the error in the experimental recording procedure, this difference is reasonable for these 6 points. If we consider the velocity magnitude vector plots in figure 3.14a, the experiments measure a large vortex with a centre of rotation axis down the y direction with an almost 2D flow field along the this direction which was observed qualitatively during the experiments. This 2D flow field behaviour is even more evident when we consider the reflected vector plot in figure 3.14. An unusual result is observed near the $x = 0$ side wall where some of the velocity vectors point towards this wall. This behaviour is seen for 5 points (Pt: 112,122,132,121,131) where they all, except for P_{121} , have green values for accuracy which implies these results are not due to bubble interference. One potential reason is that this is caused by interference from the ADV probe itself. The flow near the side walls goes straight down and then begins to move towards the middle of the tank. The ADV probe can obstruct the flow as it moves towards the middle of the reactor, creating shredding

vortices that interfere with the flow at the recording point which causes this unusual behaviour. Alternatively, this could be a result of entrained bubbles recirculating near the side wall. Bubbles that have been entrained near the wall will begin to rise but then be forced downwards again due to the incoming fluid flow being driven down. This will result in bubbles being trapped which was observed in the experiments. This continuous rise and fall of bubbles could create a recirculation loop near the side wall which is what is being measured at these points by the ADV.

3D velocity vector plots for the "d1d2d3" and "a1a2a3" combined data set for flow rate 108 L/min without assuming symmetry.



3D velocity vector plots for the "d1d2d3" and "a1a2a3" combined data set for flow rate 108 L/min, assuming symmetry.

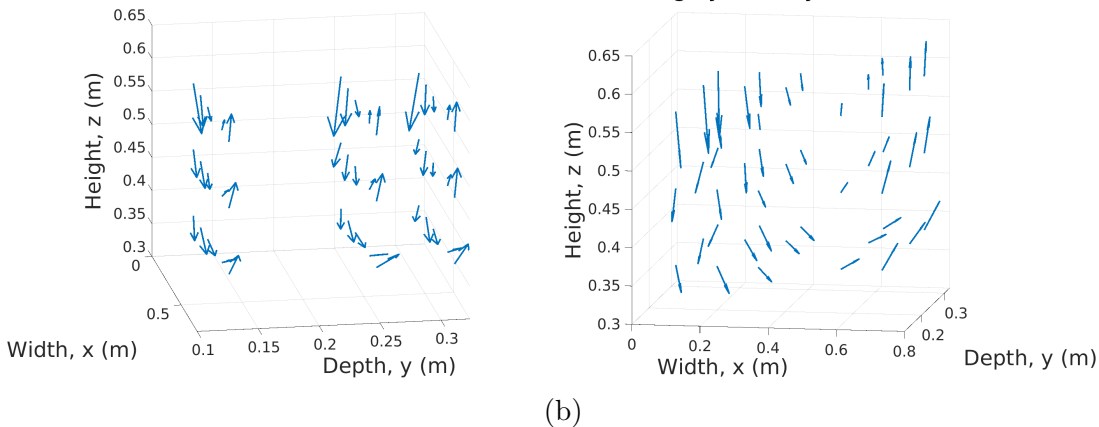
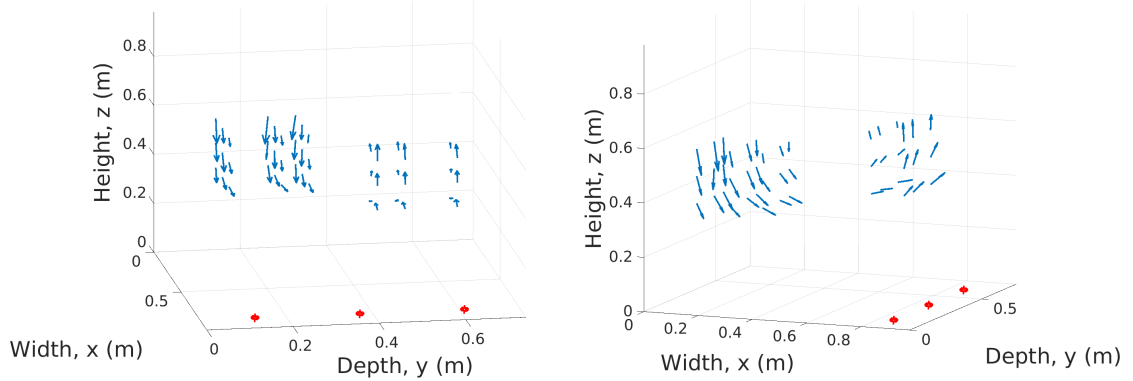


Figure 3.14: 3D vector plots of the diffuser configuration “d1d2d3” and “a1a2a3” combined data set for flow rate 108 L/min: without symmetry (a), and with symmetry where the region with data has been zoomed in on (b). The red dots illustrate the centre locations of the aerating membrane diffusers.

3.6.2 Configuration “d1d2d3” and “a1a2a3” combined results for flow rate 54 L/min

In comparison to the 108 L/min results, the slower 54 L/min air flow rate results only has 4 data points that have their difference in z velocities outside of 3 standard deviations, as illustrated in table 3.6; however, there are more data points that lie between 1 and 3 standard deviations. Similarly with the 108 L/min results, the magnitude of the differences compared with the w_1 lies between 8 - 15 % for the 4 points which is in the same magnitude as the experimental recording procedures; implying the data is reasonable. Additionally, the 3D vector plots in figure 3.15 similarly describe a 2D vortex flow field in the middle of the reactor with a rotational axes along the y direction. For this flow rate, no unusual side wall velocity vectors are observed compared with the 108 L/min. At this slower flow rate there is less bubble entrainment which suggests that the unusual behaviour seen for the 108 L/min flow rate data was a result of trapped bubbles re-circulating near the side wall.

3D velocity vector plots for the "d1d2d3" and "a1a2a3" combined data set for flow rate 54 L/min without assuming symmetry.



(a)

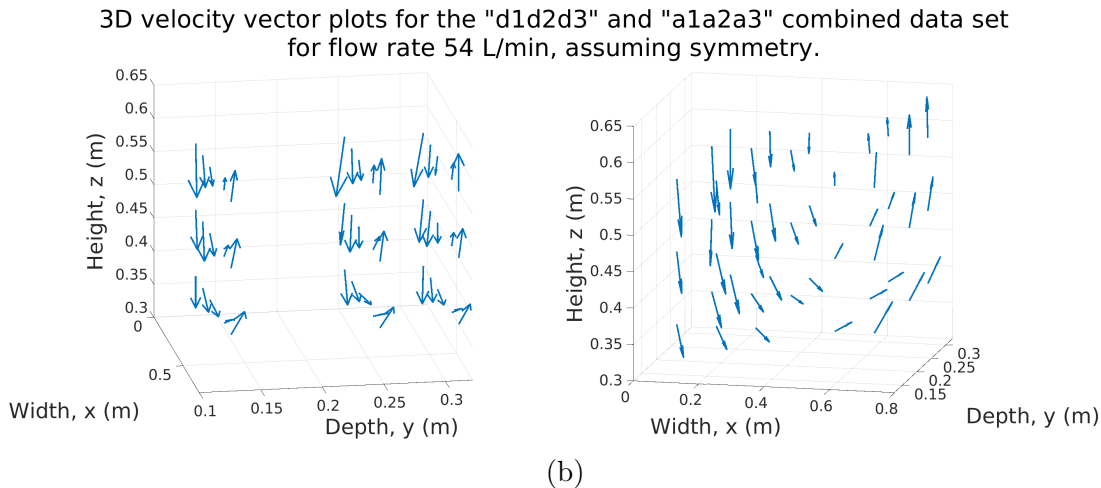


Figure 3.15: 3D vector plots of the diffuser configuration “d1d2d3” and “a1a2a3” combined data set for flow rate 54 L/min: without symmetry (a), and with symmetry where the region with data has been zoomed in on (b). The red dots illustrate the centre locations of the aerating membrane diffusers.

3.7 Analysing the 2D behaviour of the velocity data sets

Analysing the velocities for the “d1d2d3” and “a1a2a3” diffuser configurations, there is strong evidence of 2D behaviour due to the symmetric properties of the reactor. If we obtain quantitative evidence of this 2D behaviour, we can run 2D CFD simulations initially to validate the modelling choices and save significant computation time compared with running 3D simulations. To assess this 2D behaviour, the y plane 2D velocity magnitudes at each point for each plane was calculated and compared and the size of the y velocity compared with the velocity magnitude at each point was assessed.

3.7.1 Assessment of the 2D behaviour

Figure 3.16 illustrate a comparison of the velocity magnitude along each plane and assessment of the magnitude of the depth or y velocities from the combined “d1d2d3” and “a1a2a3” data set for flow rate 54 L/min. The parallel 2D velocity magnitudes

Pt (ijk)	x (m)	y (m)	z (m)	u (m/s)	v (m/s)	w1 (m/s)	w2 (m/s)	u error (m/s)	v error (m/s)	w1 error (m/s)	w2 error (m/s)	w1 & w2 difference assessment
111	0.127	0.128	0.378	0.0523	0.00089	-0.11635	-0.111	0.00138	0.00034	0.00031	0.00018	3.03270286
211	0.248	0.128	0.378	0.108	0.01114	-0.11761	-0.1121	0.00052	0.00043	0.00046	0.00044	1.25458664
311	0.369	0.128	0.378	0.1191	0.01417	-0.06488	-0.0631	0.00027	0.0004	0.00033	0.00032	0.56309497
411	0.611	0.128	0.378	0.154	0.03151	0.036512	0.0357	0.00037	0.00057	0.00056	0.00054	0.17358163
511	0.732	0.128	0.378	0.1372	0.01876	0.111009	0.1093	0.00057	0.00021	0.00086	0.00081	0.24654612
112	0.127	0.128	0.478	-0.043	0.01099	-0.14495	-0.1427	0.00437	0.00074	0.00096	0.00057	0.44646017
212	0.248	0.128	0.478	0.0354	0.0105	-0.12927	-0.117	0.00143	0.00102	0.00061	0.00035	4.00626356
312	0.369	0.128	0.478	0.068	0.00276	-0.07029	-0.066	0.00046	0.00031	0.00056	0.00042	1.18117149
412	0.611	0.128	0.478	0.0554	0.01529	0.038753	0.0388	0.00104	0.00025	0.00077	0.00075	0.00626995
512	0.732	0.128	0.478	0.0739	0.01459	0.135734	0.1359	0.0004	0.0006	0.00036	0.00035	0.04982276
113	0.127	0.128	0.578	0.0348	0.02038	-0.24446	-0.2455	0.00079	0.0008	0.00122	0.00123	0.10168732
213	0.248	0.128	0.578	0.038	0.00572	-0.15151	-0.1518	0.00058	0.00093	0.0009	0.00087	0.04249166
313	0.369	0.128	0.578	0.0119	0.00886	-0.06857	-0.0673	0.00041	0.00043	0.00064	0.00056	0.26812078
413	0.611	0.128	0.578	0.0069	0.00685	0.050984	0.0509	0.00027	0.00034	0.00054	0.00052	0.01950306
513	0.732	0.128	0.578	0.015	0.00602	0.139631	0.1397	0.00039	0.00043	0.00046	0.00045	0.02967671
121	0.127	0.249	0.378	-0.053	0.00184	-0.10777	-0.1026	0.00313	0.00036	0.00068	0.00031	1.65792278
221	0.248	0.249	0.378	0.1093	0.00988	-0.09094	-0.0817	0.00048	0.00074	0.00052	0.0004	2.66760077
321	0.369	0.249	0.378	0.113	0.02068	-0.05993	-0.0516	0.00055	0.00041	0.00032	0.00026	3.70671054
421	0.611	0.249	0.378	0.1402	0.04232	0.025494	0.0247	0.00088	0.00061	0.00039	0.0004	0.24433138
521	0.732	0.249	0.378	0.1116	0.05487	0.077392	0.0772	0.00027	0.00042	0.00094	0.00095	0.01952118
122	0.127	0.249	0.478	-0.066	-0.0166	-0.12808	-0.13	0.00253	0.00059	0.00112	0.00072	0.31381142
222	0.248	0.249	0.478	0.0229	-0.0102	-0.12389	-0.1124	0.00108	0.00122	0.00054	0.00039	3.36750343
322	0.369	0.249	0.478	0.0714	4.90E-05	-8.20E-02	-0.0739	0.00086	0.00075	0.00058	0.00046	2.02085728
422	0.611	0.249	0.478	0.0546	0.01251	0.05949	0.0593	0.00116	0.00036	0.00127	0.00125	0.02193057
522	0.732	0.249	0.478	0.0573	0.0134	0.143817	0.1424	0.00042	0.00041	0.00071	0.00061	0.27083344
123	0.127	0.249	0.578	0.0633	-0.0222	-0.28242	-0.2823	0.0019	0.00088	0.00077	0.00081	0.02519314
223	0.248	0.249	0.578	0.0571	-0.0108	-0.17538	-0.1714	0.0022	0.00096	0.00104	0.00102	0.45062251
323	0.369	0.249	0.578	0.0385	0.00816	-0.07734	-0.076	0.00076	0.00086	0.00048	0.00043	0.36870499
423	0.611	0.249	0.578	-0.002	0.00171	0.06232	0.0625	0.00033	0.00036	0.00122	0.00123	0.01559844
523	0.732	0.249	0.578	0.003	0.00835	0.140644	0.1405	0.00096	0.0004	0.00086	0.00089	0.02344632
131	0.127	0.313	0.378	-0.09	-0.0062	-0.09198	-0.0929	0.0033	0.00103	0.0014	0.00089	0.11681159
231	0.248	0.313	0.378	0.1118	0.00475	-0.10775	-0.0921	0.00155	0.00031	0.00054	0.00043	4.21024466
331	0.369	0.313	0.378	0.1255	0.00608	-0.05905	-0.0476	0.00043	0.00033	0.00035	0.00025	5.31863492
431	0.611	0.313	0.378	0.1496	0.03112	0.040328	0.0391	0.00064	0.0003	0.00014	0.00014	1.00152769
531	0.732	0.313	0.378	0.1265	0.03061	0.114369	0.1101	0.00014	0.00072	0.00018	0.00024	2.81285017
132	0.127	0.313	0.478	-0.062	-0.0063	-0.08248	-0.0906	0.00394	0.00071	0.00191	0.00163	0.57226718
232	0.248	0.313	0.478	0.0454	-0.0102	-0.11334	-0.1072	0.00074	0.00162	0.00079	0.00066	1.08799624
332	0.369	0.313	0.478	0.0581	-0.0039	-0.05825	-0.0553	0.00039	0.0008	0.00079	0.00078	0.43364632
432	0.611	0.313	0.478	0.0531	0.00678	0.063084	0.0629	0.00048	0.00091	0.00056	0.00055	0.0444519
532	0.732	0.313	0.478	0.0501	0.00571	0.153023	0.152	0.00111	0.00028	0.0006	0.00054	0.21078453
133	0.127	0.313	0.578	0.0304	-0.0279	-0.27843	-0.2789	0.00115	0.00071	0.00083	0.00084	0.05161731
233	0.248	0.313	0.578	0.0205	-0.0049	-0.1448	-0.142	0.00082	0.00086	0.00107	0.00095	0.34499875
333	0.369	0.313	0.578	0.019	0.00161	-0.07304	-0.0714	0.00088	0.00073	0.00062	0.00058	0.325929
433	0.611	0.313	0.578	-0.012	0.00664	0.070095	0.0702	0.00039	0.0003	0.00079	0.00079	0.01325721
533	0.732	0.313	0.578	0.014	0.00516	0.147502	0.1474	0.00098	0.0007	0.00104	0.00103	0.01051537

Table 3.5: The ADV velocity results for diffuser configuration “d1d2d3” and “a1a2a3” combined data set for flow rate 108 L/min with the calculated standard errors for each component and an evaluation of the accuracy of each point by dividing the absolute difference in the calculated z velocities by the smallest standard deviation of the z velocity components to quantify the accuracy of the data. Green, yellow and red correspond to the magnitude of the z velocity difference being below 1, in between 1 and 2, and outside of 3 standard deviations.

for each plane in the left of figure 3.16 are very similar to one another such that, for the majority of the points, the velocity magnitude reside within a standard deviation of one another. If we also consider the magnitude of the y velocities in comparison with the velocity magnitude, as presented in the right of figure 3.16, the majority

Pt (ijk)	x (m)	y (m)	z (m)	u (m/s)	v (m/s)	w1 (m/s)	w2 (m/s)	u error (m/s)	v error (m/s)	w1 error (m/s)	w2 error (m/s)	w1 & w2 difference assessment
111	0.127	0.128	0.378	0.063	-0.00306	-0.1297	-0.127	0.00039	0.00097	0.00034	0.00036	1.046248
211	0.248	0.128	0.378	0.085	0.009702	-0.095	-0.087	0.00042	0.0004	9.76E-05	0.00018	9.4811603
311	0.369	0.128	0.378	0.108	0.015455	-0.0597	-0.058	0.00017	0.00066	0.00043	0.00042	0.367057
411	0.611	0.128	0.378	0.138	0.015317	0.03439	0.0325	0.00027	0.0004	0.00063	0.00055	0.3912634
511	0.732	0.128	0.378	0.139	0.025334	0.11922	0.1133	0.0003	0.00022	0.00086	0.00073	0.9235122
112	0.127	0.128	0.478	0.042	0.001749	-0.1674	-0.159	0.00071	0.00077	0.00076	0.00052	1.7598523
212	0.248	0.128	0.478	0.084	-4.33E-05	-0.1611	-0.157	0.00057	0.00064	0.00025	0.00029	1.9533221
312	0.369	0.128	0.478	0.062	0.007857	-0.091	-0.089	0.0002	0.00095	0.0002	0.00018	1.4427051
412	0.611	0.128	0.478	0.065	0.007109	0.05872	0.0583	0.00062	0.00028	0.00073	0.00069	0.0659047
512	0.732	0.128	0.478	0.069	0.01099	0.13802	0.1376	0.00059	0.00026	0.00095	0.0009	0.0491124
113	0.127	0.128	0.578	0.041	0.000725	-0.2309	-0.23	0.0012	0.00092	0.00077	0.00077	0.1921097
213	0.248	0.128	0.578	0.024	0.004942	-0.1387	-0.132	0.0006	0.00055	0.00037	0.00051	2.1251948
313	0.369	0.128	0.578	0.009	0.006274	-0.0831	-0.081	0.00035	0.00054	0.00063	0.0006	0.3854256
413	0.611	0.128	0.578	-0.007	0.003314	0.05323	0.0536	0.00058	0.00026	0.00047	0.00049	0.0832736
513	0.732	0.128	0.578	0.011	0.009053	0.13817	0.1387	0.00065	0.00025	0.00082	0.00081	0.0681543
121	0.127	0.249	0.378	0.084	0.003074	-0.1434	-0.136	0.00069	0.00071	0.00096	0.00106	0.8453832
221	0.248	0.249	0.378	0.097	0.01357	-0.0769	-0.069	0.00084	0.00189	0.00072	0.00066	1.3829192
321	0.369	0.249	0.378	0.088	0.025274	-0.0417	-0.039	0.00028	0.00029	0.00048	0.00042	0.7603769
421	0.611	0.249	0.378	0.123	0.031507	0.02808	0.0277	0.00051	0.00029	0.00101	0.00099	0.0500309
521	0.732	0.249	0.378	0.109	0.02707	0.10442	0.0936	0.0004	0.00039	0.00031	0.00037	4.0814698
122	0.127	0.249	0.478	-0.004	-0.00979	-0.1832	-0.17	0.00477	0.00053	0.00054	0.00058	2.8374692
222	0.248	0.249	0.478	0.071	-0.00745	-0.1523	-0.149	0.0007	0.00094	0.00033	0.00028	1.4324293
322	0.369	0.249	0.478	0.07	-0.00223	-0.0837	-0.082	0.00065	0.00096	0.00028	0.00017	1.143006
422	0.611	0.249	0.478	0.058	0.012971	0.06477	0.0646	0.00053	0.00058	0.00055	0.00052	0.0347621
522	0.732	0.249	0.478	0.047	0.007282	0.13886	0.1386	0.00094	0.00028	0.00104	0.00103	0.0324534
123	0.127	0.249	0.578	0.048	-0.02245	-0.2534	-0.251	0.00174	0.00085	0.00084	0.00078	0.3495528
223	0.248	0.249	0.578	0.04	0.000645	-0.1494	-0.145	0.00061	0.0008	0.0008	0.00091	0.6812106
323	0.369	0.249	0.578	0.028	0.004505	-0.0855	-0.085	0.00031	0.00059	0.00061	0.0006	0.0748376
423	0.611	0.249	0.578	-0.017	0.003797	0.0771	0.0773	0.00053	0.00047	0.00041	0.00041	0.0657249
523	0.732	0.249	0.578	-0.003	0.004105	0.15959	0.1601	0.00032	0.00057	0.00057	0.00054	0.1015879
131	0.127	0.313	0.378	0.088	-0.00678	-0.1528	-0.143	0.00078	0.00035	0.00032	0.00029	3.8681823
231	0.248	0.313	0.378	0.105	0.000616	-0.0931	-0.079	0.00099	0.00059	0.00036	0.00032	5.1564338
331	0.369	0.313	0.378	0.109	0.009712	-0.0539	-0.048	0.00034	0.00051	0.0005	0.00047	1.3408267
431	0.611	0.313	0.378	0.117	0.018015	0.03317	0.0316	0.00085	0.0006	0.00026	0.00025	0.7408699
531	0.732	0.313	0.378	0.09	0.022878	0.09962	0.0878	0.00214	0.00042	0.00062	0.00068	2.1868597
132	0.127	0.313	0.478	0.027	-0.01124	-0.1827	-0.174	0.00098	0.00053	0.00058	0.0006	1.7970668
232	0.248	0.313	0.478	0.06	-0.01134	-0.1448	-0.141	0.00047	0.00068	0.00032	0.00024	1.9144682
332	0.369	0.313	0.478	0.064	-0.0022	-0.0793	-0.077	0.00052	0.00068	0.00068	0.0005	0.5207361
432	0.611	0.313	0.478	0.051	0.002479	0.06634	0.0659	0.00059	0.00025	0.00054	0.00051	0.095306
532	0.732	0.313	0.478	0.039	0.007569	0.13334	0.1263	0.00033	0.00033	0.00029	0.00037	2.806285
133	0.127	0.313	0.578	0.023	-0.02366	-0.23	-0.229	0.00194	0.00064	0.00146	0.00137	0.0875931
233	0.248	0.313	0.578	0.012	-0.00577	-0.141	-0.138	0.00065	0.00075	0.00032	0.0003	0.9988436
333	0.369	0.313	0.578	0.001	-0.00523	-0.0811	-0.081	0.00077	0.00039	0.00078	0.00079	0.0465928
433	0.611	0.313	0.578	-0.015	0.005615	0.07154	0.0719	0.00051	0.00018	0.00081	0.0008	0.0476309
533	0.732	0.313	0.578	-0.008	-0.00026	0.16437	0.1654	0.0007	0.00103	0.0005	0.00041	0.2955648

Table 3.6: The ADV velocity results for diffuser configuration “d1d2d3” and “a1a2a3” combined data set for flow rate 54 L/min with the calculated standard errors for each component and an evaluation of the accuracy of each point by dividing the absolute difference in the calculated z velocities by the smallest standard deviation of the z velocity components to quantify the accuracy of the data. Green, yellow and red correspond to the magnitude of the z velocity difference being below 1, in between 1 and 2, and outside of 3 standard deviations.

of the points have the y velocities contributing 10 % or less towards the velocity magnitude. This implies that either: the x and z velocities are larger than the y velocities; or that the x or z velocity component is significantly larger than the other

two. If we now compare these results to the “c2” and “b2” combined data set at flow rate 36 L/min, where there is no 2D behaviour, we see significant differences in the results. Figure 3.17 shows significant larger difference in the 2D velocity magnitude in different planes compared with the values in figure 3.16. Additionally, the y velocities have a significant larger contribution to the velocity magnitude in figure 3.17 compared with figure 3.16.

From this assessment, there is strong evidence that there is 2D behaviour, or at least pseudo 2D behaviour, for the “d1d2d3” and “a1a2a3” combined configuration at flow rate 54 L/min. The best plane choice to analyse would be the $n = 1$ or $y = 12.8$ cm plane as this crosses straight through the central point of the row 1 diffusers. Therefore from this analysis, we can calculate the 2D velocities, as illustrated in figure 3.18, and compare them to equivalent 2D CFD simulations to validate the CFD modelling choices. This behaviour was also seen for the “d1d2d3” and “a1a2a3” combined data set for flow rate 108 L/min and “c1c2c3” configuration at flow rate 54 L/min where the equivalent plotted results can be found in appendix §8.1.1.

2D assessment of the "d1d2d3" and "a1a2a3" combined data set for flow rate 54 L/min

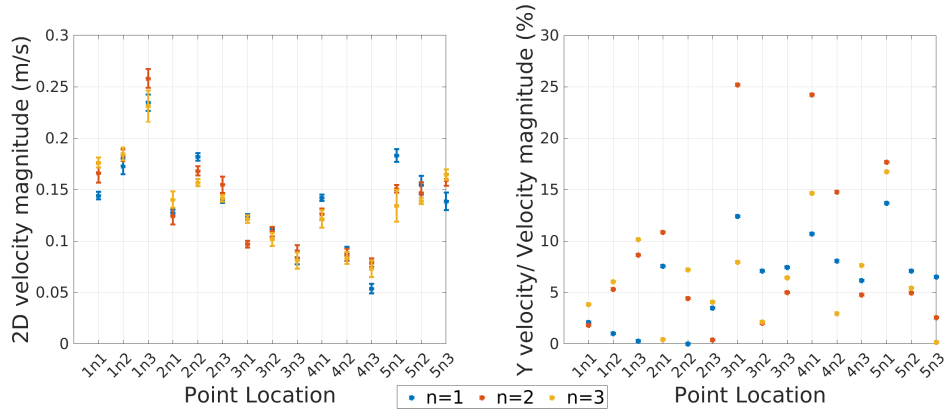


Figure 3.16: An assessment of the 2D behaviour of the “d1d2d3” and “a1a2a3” combined data set for flow rate 54 L/min. A comparison of the 2D velocity magnitude at points along the parallel planes $n = 1, 2, 3$ which correspond to a depth of $y = 0.128, 0.249, 0.313$ m, respectively (a); and an assessment of the y velocity magnitude compared with the 3D velocity magnitude at each parallel plane point.

2D assessment of the "c2" and "b2" combined data set for flow rate 36 L/min

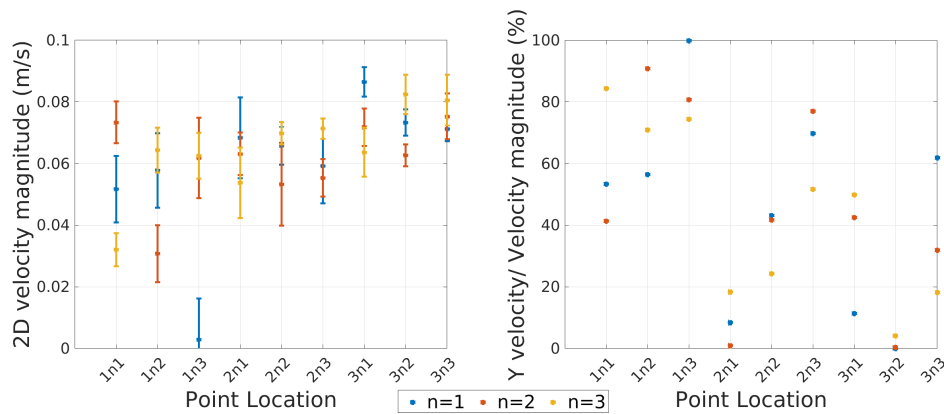


Figure 3.17: An assessment of the 2D behaviour of the “c2” and “b2” combined data set for flow rate 36 L/min. A comparison of the 2D velocity magnitude at points along the parallel planes $n = 1, 2, 3$ which correspond to a depth of $y = 0.128, 0.249, 0.313$ m, respectively (a); and an assessment of the y velocity magnitude compared with the 3D velocity magnitude at each parallel plane point.

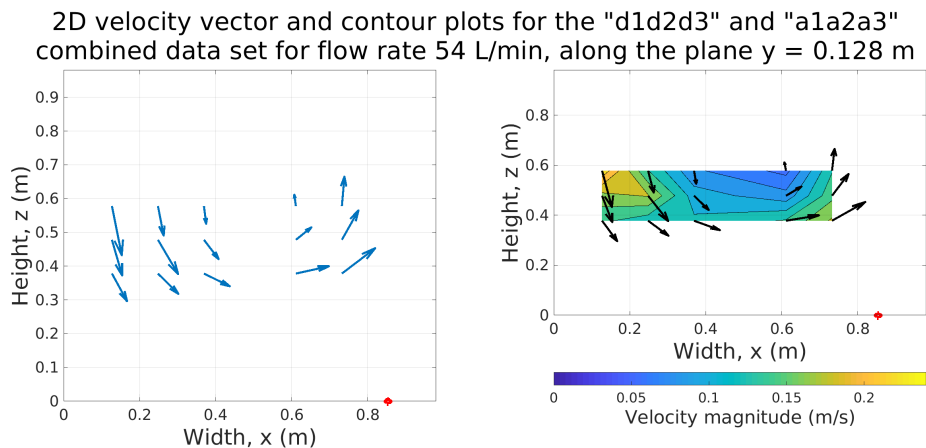


Figure 3.18: 2D vector and contour plots for the “d1d2d3” and “a1a2a3” combined data set for flow rate 54 L/min along the row 1 diffusers at $y = 12.8$ cm. The red dot illustrates the centre location of the air pumping diffuser.

3.8 Chapter summary

In this chapter, an experimental procedure has been described for recording ADV velocity measurements in an experimental pilot-scale aeration tank. This procedure has been used to obtain a large set of velocity measurements for various diffuser configurations and flow rates. This data set can now be used to validate a CFD model of the aeration tank in both 2D and 3D which is conducted in chapter 5.

To obtain this data set of velocity measurements, the chapter first discussed the

background, motivation and procedure for conducting experiments in an aeration tank. Following this, a design for a perspex pilot-scale aeration tank was described which was based on a working pilot-scale aeration tank. This was manufactured to conduct experiments in. An explanation of the tank structure and reasons for it were given along with a description of how the membrane diffusers operate to produce bubbles in the tank, giving an understanding of the tank structural design. In the next section, an explanation of how the ADV equipments works and the difficulties of using the recording technique in aerated flows was given to illustrate the challenges of using an ADV. Initial experiments were completed to confirm the repeatability and symmetry of the ADV measurements in the tank. Finally, a summary of the procedure for conducting the ADV measurements was outlined with illustrations and explanations of the reasons for these choices to allow for the experiments to be repeated. Using the procedure, a series of ADV velocity measurements were recorded for a range of diffuser configurations and flow rates to be used to validate a CFD model.

Once the data had been recorded, it required post-processing to remove bad data as a result of bubble interference with the ADV hardware. A de-spiking algorithm for removing non-physical measurements from bubble interference was defined and an evaluation and discussion of the post-processed data was conducted which confirmed the de-spiking algorithm was operating correctly. A summary of the potential errors and uncertainties during the whole experimental procedure was outlined and discussed to evaluate the accuracy of the measurements. The experimental results for a series of diffuser configurations and flow rates were illustrated. An assessment of the accuracy of the data was conducted which found the results were all reasonable in comparison with the experimental procedure errors. Finally, an assessment of the 2D behaviour observed for specific diffuser configurations was conducted and it was found that there was strong 2D or pseudo 2D behaviour in the measurements which implied that 2D CFD simulations can be conducted and compared with this data for validation.

Chapter 4

Hydrodynamic modelling

Traditional wastewater treatment plant design is based on empirical data and tried-and-true tested solutions to specific pollution problems (Wang et al., 2009); however, the ever increasing complexity of environmental problems demands more intelligent planning and greater understanding of wastewater treatment to improve operations (WEP, 2002). The fluid flow in bioreactors is non-trivial and depends on: vessel geometry; operating conditions, and physical properties of its contents such as: phase, density and viscosity. These all influence the local components, concentrations, phase collisions and mass transfer. The typical dynamics of AS system dynamics involve: multi-phase flow comprising of suspended solids, activated sludge and air; a range of length scales between sludge flocs, bubbles and tank geometry; and different velocity scales for the phases from the mixer and aerators (Horan, 1989; Henze et al., 2001). Local flow velocities and mixing can be found using experimental methods, such as tracer techniques, but these are not feasible for full scale units which make simulations a more attractive option. Factors such as reduced cost, improved time efficiency and prediction before implementation all contribute to the attraction of simulating wastewater treatment processes (Orhon et al., 2009).

Mathematical models have been developed to predict and understand the hydrodynamics in wastewater treatment reactors which capture the crucial physics that describe the dynamics of the system. The complexity of fluid dynamics is such

that the fundamental equations that describe their motion can not be solved analytically and must be solved numerically. Computational fluid dynamics (CFD) is the general term used to describe the process of creating numerical simulations computationally that solve fluid dynamics equations. In this chapter, the fundamental equations that describe the movement of fluids has been defined and the numerical techniques used in CFD software to model the hydrodynamics in aeration tanks has been described.

4.1 Previous work in using CFD to model wastewater treatment reactors

[Karpinska and Bridgeman \(2016\)](#) and [Samstag et al. \(2016\)](#) have both reviewed applications and capabilities of CFD in modelling different wastewater treatment cycle unit processes. CFD of ASP creates opportunities for analysis of the multiphase flow behaviour and operating conditions impact on the local scale phenomena. Studies on modelling preliminary treatment have been done to evaluate three different types of grit removal tanks by [McNamara et al. \(2012\)](#) to confirm claims made by the grit chambers manufacturers. [GriBORIO et al. \(2014\)](#) produced 2D and 3D CFD models of two primary sedimentation tanks to evaluate their geometries and suggest improvements from the results. [Karpinska and Bridgeman \(2016\)](#) provides a summary of the multiphase and turbulence models used in CFD simulations of activated sludge reactors. [Karpinska and Bridgeman \(2016\)](#) and [Samstag et al. \(2016\)](#) reviews conclude further work is needed on: evaluating and improving current flocculation and rheology models that are used for modelling sedimentation tanks; the development of a full 3D sedimentation tank model incorporating all these together; the inclusion of more models in digester simulations; and to couple the ASM with these improved CFD models.

4.1.1 Aeration Basin Modelling

Aeration supplies oxygen and plays an important role in the mixing of aeration tanks and accounts for a large portion of energy demand in wastewater treatment. A major challenge of wastewater treatment is complying with effluent quality criteria while keeping investment and operating costs as low as possible (Rosso et al., 2008). Lee et al. (2015); Ozturk et al. (2016) and Fan et al. (2017) have all shown ways to optimise the aeration systems to reduce operational costs while still achieving safe effluent levels. This can be achieved by reducing the aeration flow rates or using intermittent aeration zones. However, the aeration has an impact on the mixing which can also affect the tanks efficiency and further work needs to be done to investigate this impact.

Computational fluid dynamics has been used to investigate and improve aeration efficiency in aeration tanks. Bhuyar et al. (2009) used CFD models to design an efficient curved-blade-surface mechanical aerators for oxidations ditches, a treatment process used to treat domestic sewage, by optimising six parameters. An optimal aerator efficiency was found and a full 3D simulation of the oxidation ditch and mechanical aerator was developed to compare simulation results with experimental data. Xu et al. (2010) developed a CFD model for a new type of oxidation ditch, an airlift oxidation ditch (ALOD), that uses floor aeration instead of mechanical aerators to achieve all three desired functions of mixing, propulsion and oxygenation. The simulations found the new design allowed for an increase in depth for the oxidation ditches; these results were verified using a bench-scale ALOD and they demonstrated that the ALOD design is an attractive alternative choice for the oxidation ditch if capital costs are not an issue.

Gresch et al. (2011) used an Eulerian-Eulerian CFD modelling approach to replicate a full-scale 3500 m³ nitrification zone and analysed how the aeration pattern impacted the flow field, aeration efficiency, and plant operation. Additionally, a simple one species Monod-type biokinetic equation (Monod, 1949) for ammonia was

integrated into the model. The unsteady simulation captured a period of 5 hours and the results were validated against experimental ADV and ammonia measurements. They found that the flow field is very sensitive to the aeration pattern such that the diffuser layout can lead to oscillations in the flow field. The CFD simulation was able to reproduce the flow field and complex interactions but highlighted more experimental data is required for full validation. It was concluded that the measurements of ammonia were a valuable method for validation; however, their biokinetic model was extremely simple and did not take into account the oxygen demand during nitrification. More accurate results could be obtained using a more complex biokinetic models along with the inclusion of oxygen mass transfer of oxygen from the aeration.

[Terashima et al. \(2016\)](#) performed CFD studies to match the measured oxygen transfer coefficient, k_l , to appropriate bubble sizes for different single diffusers in clean water and activated sludge CFD simulations. Additional simulations were run to investigate the affect of an extra diffuser on simulation results. It was concluded that, for fine diffusers, a 5 - 6 mm bubble diameter was required when using the Higbie's penetration theory ([Higbie, 1935](#)) to get expected oxygen transfer results; and that inclusion of extra diffusers causes reduction in the efficiency of an individual diffuser such that careful consideration should be considered when including multiple diffusers in CFD models.

[Karpinska and Bridgeman \(2017\)](#) reviewed models used in CFD to simulate the hydrodynamics and oxygen mass transfer in a lab-scale aeration tank to develop a robust framework for modelling activated sludge systems. Experimental velocity and dissolved oxygen data was collected in a lab-scale aeration tank using an ADV and PIV methods, and dissolved oxygen probes, respectively. This data was used to validate a transient CFD model that predicts the correct hydrodynamics and mass transfer in their lab-scale aeration tank. Their research concluded that accurate simulations of the fluid flow is crucial for correct predictions of the mass transfer coefficient and the SST $k - \omega$ turbulence model was the most accurate model in

reproducing the experimental results.

In this work, a CFD model will be developed to replicate the dynamics observed in the experimental aeration tank. The tank aerates via fine membrane diffusers. An approach to modelling the membrane behaviour, which has to our knowledge not been proposed in previous work, will be outlined, assessed, and validated against experimental data. Furthermore, the two-phase approach adopted will model the free surface with the inclusion of an air layer on top which will incorporate the effects of the fluid surface on the generated flow fields which has been neglected in previous work. In addition, a detailed study of the available bubble-fluid interaction models and how they influence the hydrodynamics will be conducted and compared with experimental data to find the optimal choices for replicating the bubble dynamics in the fine membrane aerated tank which has not been seen in previous literature. The results of these studies will be used to develop a robust and validated procedure for modelling the experimental aeration tank in CFD. This procedure will then be used to replicate the 2D and 3D experimental aeration tank hydrodynamics which will be validated once more against the ADV measurements to confirm accuracy of the CFD simulation results for various flow rates and diffuser configurations. These validated hydrodynamic results can then be used to couple in the biokinetic models to investigate how the hydrodynamics effects the biological processes. However, before the CFD simulations can be run, the governing equations and available modelling choices to replicate the fundamental physics in the aeration tank need to be defined. In this chapter, the governing fluids equations and available CFD modelling choices will be outlined as well as the fundamental numerical methods and schemes used in the CFD software.

4.2 Governing Navier-Stokes equations

The governing equations that are the basis for all hydrodynamic modelling are the Navier-Stokes equations. These equations describe the motion of fluids and can

be solved to derive a velocity field for a hydrodynamic system. The Navier-Stokes equations for an unsteady and compressible fluid is given by the conservation of mass or continuity equation,

$$\frac{\partial \rho}{\partial t} + \nabla \cdot (\rho \mathbf{u}) = 0, \quad (4.1)$$

where ρ and \mathbf{u} are the fluid density and velocity, respectively, and the momentum equations,

$$\rho \left(\frac{\partial \mathbf{u}}{\partial t} + \mathbf{u} \cdot \nabla \mathbf{u} \right) = -\nabla p + \nabla \cdot \bar{\boldsymbol{\tau}} + \mathbf{F}, \quad (4.2)$$

where p , ρ , $\bar{\boldsymbol{\tau}}$ and \mathbf{F} are the fluids pressure, density, viscous stress tensor and body forces acting on the fluid, respectively. The viscous stress tensor, $\bar{\boldsymbol{\tau}}$, is given by,

$$\bar{\boldsymbol{\tau}} = \mu \left(\nabla \mathbf{u} + (\nabla \mathbf{u})^T - \frac{2}{3} (\nabla \cdot \mathbf{u}) \bar{\mathbf{I}} \right), \quad (4.3)$$

where μ is the local dynamic viscosity of the fluid and $\bar{\mathbf{I}}$ is the identity matrix.

4.2.1 Steady-state incompressible and isothermal Navier-Stokes equations

If we assume the fluid flow being modelled by the Navier-Stokes equations is in a steady state, such that $d\mathbf{u}/dt = 0$, and the fluid is incompressible, such that ρ is constant, then the continuity equation in equation (4.1) simplifies to,

$$\nabla \cdot \mathbf{u} = 0, \quad (4.4)$$

which ensures the velocity field is divergence free everywhere, and the momentum equations in equation (4.2) simplifies to,

$$\mathbf{u} \cdot \nabla \mathbf{u} = -\frac{\nabla p}{\rho} + \frac{1}{\rho} \nabla \cdot \bar{\boldsymbol{\tau}} + \frac{\mathbf{F}}{\rho}, \quad (4.5)$$

where \mathbf{u} , p , ρ , $\bar{\boldsymbol{\tau}}$ and \mathbf{F} are the fluids velocity pressure, density, viscous stress tensor and the body forces, respectively, as described in §4.2.

4.2.2 Reynolds Averaged Navier-Stokes equations

The Reynolds Averaged Navier-Stokes (RANS) equations are the Reynolds averaged continuity and momentum equations for the fluid flow motion. The velocity field vector components, u_i , are decomposed into their averaged and fluctuation components, $u_i = \bar{u}_i + u'_i$, such that, when we average the fluid velocity vector components, the fluctuations average to zero and we are only left with the averaged components. These velocity component decompositions are substituted into the Navier-Stokes equations and each term is averaged yielding the RANS formulation of the Navier-Stokes equations which, in Einstein notation, is presented below,

$$\frac{\partial \rho}{\partial t} + \frac{\partial}{\partial x_i} (\rho \bar{u}_i) = 0, \quad (4.6)$$

$$\frac{\partial}{\partial t} (\rho \bar{u}_i) + \frac{\partial}{\partial x_j} (\rho \bar{u}_i \bar{u}_j) = -\frac{\partial \bar{p}}{\partial x_i} + \frac{\partial}{\partial x_i} \left[\mu \left(\frac{\partial \bar{u}_i}{\partial x_j} + \frac{\partial \bar{u}_j}{\partial x_i} - \frac{2}{3} \delta_{ij} \frac{\partial \bar{u}_k}{\partial x_k} \right) - \overline{\rho u'_i u'_j} \right] + F_i, \quad (4.7)$$

where $-\overline{\rho u'_i u'_j}$ are the Reynolds stresses. In this form, the RANS equations are not closed because of the Reynolds stress term. To close the equations we need to empirically model the Reynolds stresses which are referred to as turbulence models; these will be discussed in §4.3.

4.3 Single phase RANS turbulence modelling

In the RANS formulation, additional modelling is required for the Reynolds stresses for closure. A common approach is to relate the Reynolds stresses to the mean velocity gradients using the Boussinesq hypothesis,

$$-\overline{\rho u'_i u'_j} = \mu_t \left(\frac{\partial \bar{u}_i}{\partial x_j} + \frac{\partial \bar{u}_j}{\partial x_i} \right) - \frac{2}{3} \left(\rho k + \mu_t \frac{\partial \bar{u}_k}{\partial x_k} \right) \delta_{ij}, \quad (4.8)$$

where k is the turbulence kinetic energy, μ_t is turbulent viscosity and δ_{ij} is the Kronecker delta function. This relation assumes the turbulent viscosity is an isotropic scalar quantity such that it is uniform in all ordinations. This modelling approach has been adopted in almost all RANS turbulence models; however, two more variables have been introduced, k and μ_t , that require further modelling which will be discussed in the next sections.

4.3.1 Standard $k - \epsilon$ model

In the standard $k - \epsilon$ turbulence model, and in general, the turbulent viscosity, μ_t , is defined as,

$$\mu_t = \rho C_\mu \frac{k^2}{\epsilon} \quad (4.9)$$

where k is the turbulence kinetic energy, ϵ is the dissipation rate and C_μ is a constant coefficient. While the turbulent viscosity has been defined, another variable, ϵ , that describes the dissipation rate of the turbulence has been introduced which needs to be modelled along with the turbulence kinetic energy, k . In the standard $k - \epsilon$ turbulence model, two more transport equations are defined to describe these

variables which take the forms,

$$\frac{\partial}{\partial t}(\rho k) + \frac{\partial}{\partial x_i}(\rho k \bar{u}_i) = \frac{\partial}{\partial x_j} \left[\left(\mu + \frac{\mu_t}{\sigma_k} \frac{\partial k}{\partial x_j} \right) \right] + G_k + G_b - \rho \epsilon - Y_M + S_k, \quad (4.10)$$

$$\frac{\partial}{\partial t}(\rho \epsilon) + \frac{\partial}{\partial x_i}(\rho \epsilon \bar{u}_i) = \frac{\partial}{\partial x_j} \left[\left(\mu + \frac{\mu_t}{\sigma_\epsilon} \frac{\partial \epsilon}{\partial x_j} \right) \right] + C_{1\epsilon} \frac{\epsilon}{k} (G_k + C_{3\epsilon} G_b) - C_{2\epsilon} \rho \frac{\epsilon^2}{k} + S_\epsilon, \quad (4.11)$$

for the k and ϵ variables, respectively, where the source and sink terms on the right hand side of the equations describe the rate of production or destruction, respectively, for each variable and are well defined in the literature (Ansys, 2018). In the k and ϵ transport equations, the first three terms describe the transport of these variables due to time, convection, and diffusion, respectively. The first source term, G_k , in the k equation describes the production of turbulence kinetic energy due to the mean velocity gradients and, from the exact equations, is defined as,

$$G_k = -\overline{\rho u'_i u'_j} \frac{\partial \bar{u}_j}{\partial x_i}. \quad (4.12)$$

However, this contains the Reynolds stresses which we are trying to solve for. Therefore, this is modelled in a similar manner to the Boussinesq approach and is defined as,

$$G_k = \mu_t S_{ij} S_{ij}, \quad (4.13)$$

where,

$$S_{ij} = \frac{1}{2} \left(\frac{\partial \bar{u}_j}{\partial x_i} + \frac{\partial \bar{u}_i}{\partial x_j} \right), \quad (4.14)$$

is the strain-rate tensor or the gradient of the flow velocity. The rate of dissipation, ϵ , appears in the k equation as a destructive term as it acts to dissipate the turbulence kinetic energy. The other terms in two equations are: G_b which describes the generation of k due to buoyancy which is applied when there is a non-zero gravity

field and temperature gradient; Y_M which represents the reduction of k due to compressible turbulence; and S_k and S_ϵ which are user defined source terms. In the ϵ equation, dissipation is generated with the generation of k in the fourth term but the rate of generation is controlled by ϵ/k . In parts of the flow where the k is large, the rate of generation of ϵ is small until k is of the order of ϵ at which point ϵ will begin to dominate the source terms, replicating the small scale turbulence decaying faster due to the viscous dampening. Moreover, the fifth term in the ϵ equation is regulated by a ϵ^2/k term which reduces the production of ϵ when k tends to zero so the overall dissipation rate does not grow uncontrollably. Additionally, upper limits on the size of ϵ are usually applied as well. In the case of: steady-state, incompressible, isothermal, sub-sonic flows with no additional source terms; a lot of these terms are zero or can be neglected such that the standard $k - \epsilon$ model simplifies to,

$$\frac{\partial}{\partial x_i}(\rho k \bar{u}_i) = \frac{\partial}{\partial x_j} \left[\left(\mu + \frac{\mu_t}{\sigma_k} \frac{\partial k}{\partial x_j} \right) \right] + G_k - \rho \epsilon, \quad (4.15)$$

$$\frac{\partial}{\partial x_i}(\rho \epsilon \bar{u}_i) = \frac{\partial}{\partial x_j} \left[\left(\mu + \frac{\mu_t}{\sigma_\epsilon} \frac{\partial \epsilon}{\partial x_j} \right) \right] + C_{1\epsilon} \frac{\epsilon}{k} G_k - C_{2\epsilon} \rho \frac{\epsilon^2}{k}. \quad (4.16)$$

4.3.2 Realizable $k - \epsilon$ model

If we consider the normal Reynolds stresses from the Boussinesq hypothesis in equation (4.8); for an incompressible fluid, $\partial u_i / \partial x_i = 0$, the Reynolds stresses components for $i = j$ simplifies to,

$$-\rho \overline{u'_i u'_i} = -\rho \overline{(u'_i)^2} = 2\mu_t \left(\frac{\partial \bar{u}_i}{\partial x_i} \right) - \frac{2}{3} \rho k \quad (4.17)$$

which rearranges to,

$$\overline{(u'_i)^2} = \frac{2}{3} k - \frac{2\mu_t}{\rho} \left(\frac{\partial \bar{u}_i}{\partial x_i} \right). \quad (4.18)$$

There is a squared velocity on the left hand side and, therefore, mathematically the normal stresses need to be a positive quantity. If they become negative then that

is non-realizable. Substituting the equation for turbulent viscosity, we find that the equation becomes non-realizable when,

$$\frac{k}{\epsilon} \left(\frac{\partial \bar{u}_i}{\partial x_i} \right) > \frac{1}{3C_\mu} \simeq 3.7, \quad (4.19)$$

which also violates the Schwarz inequality, $(\overline{u_\alpha u_\beta})^2 \leq \overline{u_\alpha^2 u_\beta^2}$. To ensure realizability, C_μ must not be constant but related to the mean strain rate. The realizable $k - \epsilon$ model recertifies this by providing an alternative formulation for the turbulent viscosity; specifically allowing C_μ to vary. The model has an identical k transport equation structure as the standard $k - \epsilon$ in equation (4.10) (or equation (4.15) when the same fluid assumptions are applied) but with different modelling constants. Additionally, a different dissipation equation is derived from the transport of the mean-square vorticity fluctuations (Shih et al., 1995). The new dissipation equation formulations is,

$$\begin{aligned} \frac{\partial}{\partial t}(\rho\epsilon) + \frac{\partial}{\partial x_i}(\rho\epsilon\bar{u}_i) = & \frac{\partial}{\partial x_j} \left[\left(\mu + \frac{\mu_t}{\sigma_\epsilon} \frac{\partial \epsilon}{\partial x_j} \right) \right] + \rho C_1 S_\epsilon \\ & - \rho C_2 \frac{\epsilon^2}{k + \sqrt{\nu\epsilon}} + C_{1\epsilon} \frac{\epsilon}{k} C_{3\epsilon} G_b + S_\epsilon, \end{aligned} \quad (4.20)$$

which, under the same fluid assumptions that were applied to equations (4.15) and (4.16), simplifies to,

$$\frac{\partial}{\partial x_i}(\rho\epsilon\bar{u}_i) = \frac{\partial}{\partial x_j} \left[\left(\mu + \frac{\mu_t}{\sigma_\epsilon} \frac{\partial \epsilon}{\partial x_j} \right) \right] + \rho C_1 S_\epsilon - \rho C_2 \frac{\epsilon^2}{k + \sqrt{\nu\epsilon}}, \quad (4.21)$$

where,

$$C_1 = \max \left[0.43, \frac{\nu}{\nu + 5} \right], \quad \nu = S \frac{K}{\epsilon}, \quad \text{and} \quad S = \sqrt{2S_{ij}S_{ij}}. \quad (4.22)$$

The differences in equation (4.20) are the second and third terms on the right hand side which better represent the spectral energy transfer and to remove a singularity when k goes to zero, respectively. In the turbulent viscosity formulation, C_μ is

computed from,

$$C_\mu = \frac{1}{A_o + A_s \frac{kU^*}{\epsilon}}, \quad (4.23)$$

where in [Ansys \(2018\)](#),

$$U^* = \sqrt{S_{ij}S_{ij} + \overline{\Omega_{ij}\Omega_{ij}}}, \quad (4.24)$$

$$\overline{\Omega_{ij}} = \overline{\Omega_{ij}} - \epsilon_{ijk}\omega_k, \quad (4.25)$$

where $\overline{\Omega_{ij}}$ is the mean rate-of-rotation tensor viewed in the moving reference frame with angular velocity ω_k . The model constants are defined as,

$$A_o = 4.04, \quad A_s = \sqrt{6} \cos(\phi), \quad (4.26)$$

where,

$$\phi = \frac{1}{3} \cos^{-1}(\sqrt{6}W), \quad W = \frac{S_{ij}S_{jk}S_{ki}}{\tilde{S}^3},$$

$$\tilde{S} = \sqrt{S_{ij}S_{ij}}, \quad \text{and} \quad S_{ij} = \frac{1}{2} \left(\frac{\partial u_i}{\partial x_j} + \frac{\partial u_j}{\partial x_i} \right).$$

In summary, the realizable $k - \epsilon$ model considers extra mathematical constraints, consistent with physics of turbulent flows, on the Reynolds stresses in comparison with standard $k - \epsilon$ model; improving its robustness. This results in a new function for the C_μ coefficient such that it depends on the mean strain and rotation rates in the eddy viscosity definition. Additionally, the derivation of the dissipation transport equation is based on the dynamics equation for the mean-square vorticity fluctuations. This formulation has been shown to have substantial improvements over the standard $k - \epsilon$ model for flows with strong rotation ([Shih et al., 1995](#); [Ansys, 2018](#)).

4.3.3 $k - \omega$ model

Another two equation method for closing the RANS equations is the standard $k - \omega$ turbulence model. The model solves transport equations for the turbulent kinetic energy, k , and the specific dissipation rate, ω , which is a ratio of ϵ and k (Wilcox, 1993). The k and ω equations are defined as,

$$\frac{\partial}{\partial t}(\rho k) + \frac{\partial}{\partial x_i}(\rho k \bar{u}_i) = \frac{\partial}{\partial x_j} \left[\left(\mu + \frac{\mu_t}{\sigma_k} \frac{\partial k}{\partial x_j} \right) \right] + G_k - Y_k + S_k, \quad (4.27)$$

$$\frac{\partial}{\partial t}(\rho \omega) + \frac{\partial}{\partial x_i}(\rho \omega \bar{u}_i) = \frac{\partial}{\partial x_j} \left[\left(\mu + \frac{\mu_t}{\sigma_\omega} \frac{\partial \omega}{\partial x_j} \right) \right] + G_\omega - Y_\omega + S_\omega, \quad (4.28)$$

and the turbulent viscosity, μ_t , is defined as,

$$\mu_t = \alpha^* \frac{\rho k}{\omega}, \quad (4.29)$$

where α^* is a damping correction coefficient for low Reynolds number systems and $\alpha^* = 1$ for high Reynolds number systems. The terms in the equations are: G_k which describes the generation of turbulence kinetic energy, similarly to the $k - \epsilon$ formulation, and is defined in the same way as shown in equation (4.13); G_ω describes the generation of ω and is defined as,

$$G_\omega = \alpha^* \frac{\omega}{k} G_k; \quad (4.30)$$

Y_k and Y_ω describes the dissipation of k and ω due to turbulence, respectively; and S_k and S_ω are the user defined source terms. The standard $k - \omega$ model has been found to correctly predict shear flow rate spreading for problems with: far wakes, mixing layers, and plane, round and radial jets; and is, therefore, applicable to wall-bounded and free shear flows. The model constants can be found in Ansys (2018).

4.3.4 Shear stress transport $k - \omega$ model

The shear stress transport (SST) $k - \omega$ model is another alternative two equation turbulence model. The standard $k - \epsilon$ model is more accurate in the free stream regions but its near wall predictions underperforms for boundary layers with adverse pressure gradients (Versteeg and Malalasekera, 2007). This led Menter (1994) to the derivation of a hybrid model, the SST $k - \omega$ model, that uses the standard $k - \epsilon$ model in the fully turbulent region far from the walls and transitions to the standard $k - \omega$ model in the near-wall region where the $k - \epsilon$ accuracy suffers and the $k - \omega$ performs better. To achieve this, Menter (1994) transforms the $k - \epsilon$ equations into a $k - \omega$ formulation and introduces a blending function that is one in the boundary layer and zero in the outer free stream regions to transition between the two models. These features make the SST $k - \omega$ model more accurate and reliable than the standard $k - \epsilon$ and $k - \omega$ models (Menter, 1994; Versteeg and Malalasekera, 2007).

4.3.5 Wall functions

The presence of walls in turbulent flows can significantly change the flow in non-trivial ways. In the near wall regions, viscous damping reduces the tangential velocity fluctuations while the presence of the wall reduces normal fluctuations. However, these fluctuations cause large mean velocity gradients to appear which results in increased production of turbulence kinetic energy in the outer part of the near-wall regions. Correctly predicting the flow near the walls can determine the accuracy of the simulations in wall-bounded turbulent flows. The near wall region can be split into three layers: the innermost viscous sub-layer where viscosity dominates and the flow acts in an almost laminar regime; the outer layer where the mean velocity gradients are dominating the generation of k and the turbulence plays an important role; and the buffer layer or transition region between these two layers where the effects of the viscous forces and turbulence are equally important (Ansys, 2018). An illustration of these layers is presented in figure 4.1 using the relationship between

the dimensionless velocity and wall distance, y^+ . The $k - \epsilon$ turbulence model formulation requires wall functions as they are inaccurate in near wall regions where the wall function choice is dependent on the problem and mesh resolution. The simplest one is the standard wall function that models all three near wall turbulent layers while more complex functions, such as enhanced wall treatment, assesses the resolution near the wall and applies a model that is appropriate for the calculated wall distance (Ansys, 2018).

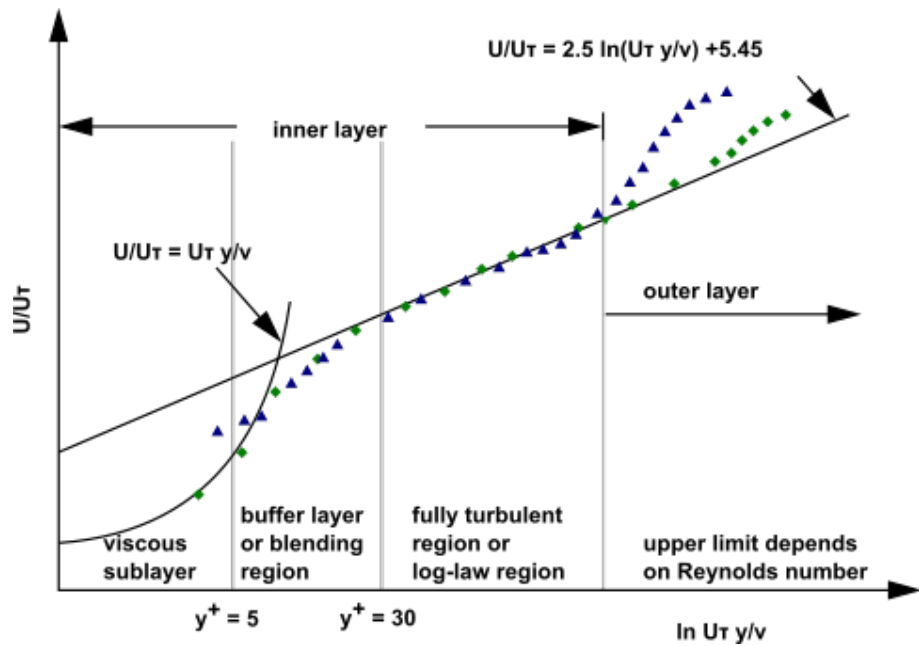


Figure 4.1: An illustration of the three different layers in the near wall region through the plotting of the dimensionless velocity, u/u_T , against the dimensionless wall distance, y^+ . u_T is the friction velocity and $y^+ = \rho u_T y / \mu$ (Ansys, 2018).

4.4 Eulerian two-phase modelling

The aeration tank involves water and air and is, therefore, a two phase problem which means that the normal governing fluid equations presented in §4.2 need to be modified to include the interaction between the two phases. There are a range of methods to model the interaction of the two phases; in this work the Eulerian-Eulerian approach has been used. This approach introduces the volume fraction for

each phase, α_p , into the governing equations which represents the fraction of a cell that is made up of a certain phase and obeys the equation, $\sum_p \alpha_p = 1$. Taking these phases into account, assuming we have no mass transfer between phases, and both fluids are compressible; the Eulerian-Eulerian modified continuity equation becomes,

$$\frac{\partial \alpha_p \rho_p}{\partial t} + \nabla \cdot (\alpha_p \rho_p \mathbf{u}_p) = 0, \quad (4.31)$$

where ρ_p is the density of phase p and \mathbf{u}_p is the velocity of phase p . In a similar manner, the Eulerian-Eulerian modified momentum equations are,

$$\frac{\partial \alpha_p \rho_p \mathbf{u}_p}{\partial t} + \nabla \cdot (\alpha_p \rho_p \mathbf{u}_p \mathbf{u}_p) = -\alpha_p \nabla p + \alpha_p \rho_p \mathbf{g} + \nabla \cdot (\alpha_p \bar{\bar{\boldsymbol{\tau}}}_p) + \mathbf{I}_q \quad (4.32)$$

where p is the pressure, \mathbf{g} is the gravitational vector, $\bar{\bar{\boldsymbol{\tau}}}_p$ is the viscous stress tensor and \mathbf{I}_q contains all the momentum exchange forces between the phases. The stress tensor is defined as,

$$\bar{\bar{\boldsymbol{\tau}}}_p = \mu_p (\nabla \mathbf{u}_p + \nabla \mathbf{u}_p^T) - \frac{2}{3} \mu_p (\nabla \cdot \mathbf{u}_p) \bar{\mathbf{I}} \quad (4.33)$$

where μ_p is the viscosity of phase p and $\bar{\mathbf{I}}$ is the identity matrix. In the case of two-phase bubbly flow, α_l and α_g are the volume fraction of the liquid and gas phase, respectively, and are related by the equation, $\alpha_l = 1 - \alpha_g$, such that, by calculating one phase volume fraction, we can derive the other.

4.4.1 Two-phase RANS turbulence modelling

In a similar procedure to RANS modelling for single-phase flow defined above §4.2.2, the Reynolds averaging method can be applied to the two-phase governing equations. The velocities of each phase can be decomposed into their mean and fluctuating components, $\mathbf{u}_p = \widetilde{\mathbf{u}}_p + \mathbf{u}'_p$, and all scalars can be decomposed similarly as, $q = \tilde{q} + q'$. These obey the averaging definitions: $\overline{\alpha \mathbf{u}'_p} = 0$, $\overline{q'} = 0$, $\overline{\alpha \mathbf{u}_p} = \overline{\alpha} \widetilde{\mathbf{u}}_p$. Applying these definitions to the two sets of RANS equations for each phase results in two sets of

Reynolds stresses that require closure. A range of methods of varying complexity exist to close these equations; the most commonly used approach is to use the two-equation turbulence method (such as the $k - \epsilon$ model) for the continuous phase Reynolds stresses and then relate these results to the dispersed phase Reynolds stresses. Applying the Boussinesq hypothesis for the continuous liquid phase and re-defining \mathbf{u}_p as the Reynolds-averaged phase velocity, $\widetilde{u}_{p,i} = u_{p,i}$, then the Reynolds stresses for the continuous liquid phase are defined as,

$$-\overline{\rho_l \alpha_l u'_{l,i} u'_{l,j}} = \mu_t \left(\frac{\partial u_{l,i}}{\partial x_j} + \frac{\partial u_{l,j}}{\partial x_i} \right) - \frac{2}{3} \left(\rho_l k + \mu_t \frac{\partial u_{l,k}}{\partial x_k} \right) \delta_{ij}, \quad (4.34)$$

where k is the turbulent kinetic energy of the continuous phase and μ_t is the turbulent viscosity defined as,

$$\mu_t = \overline{\alpha_l} C_\mu \rho_l \frac{k^2}{\epsilon}, \quad (4.35)$$

where ϵ is the dissipation rate of the continuous phase and both k and ϵ satisfies the $k - \epsilon$ transport equations defined in equations (4.10) and (4.11), respectively. The continuous liquid phase Reynolds-stresses are related to the dispersed gas phase Reynolds-stresses through a turbulence response coefficient, C_t , which is defined as the ratio of the root mean squared velocity fluctuations of the dispersed gas and continuous liquid phase, \mathbf{u}'_g and \mathbf{u}'_l , respectively (Gosman et al., 1992), such that,

$$C_t = \frac{u'_{g,i}}{u'_{l,i}},$$

$$u'_{g,i} = C_t u'_{l,i}. \quad (4.36)$$

Applying this relation, we get a formula for the dispersed phase Reynolds stresses,

$$-\overline{\rho_g \alpha_g u'_{g,i} u'_{g,j}} = -C_t^2 \left(\frac{\overline{\rho_g \alpha_g}}{\overline{\rho_l \alpha_l}} \right) \overline{\rho_l \alpha_l u'_{l,i} u'_{l,j}}, \quad (4.37)$$

$$= -C_t^2 \left(\frac{\overline{\rho_g \alpha_g}}{\overline{\rho_l \alpha_l}} \right) \left[\mu_t \left(\frac{\partial u_{l,i}}{\partial x_j} + \frac{\partial u_{l,j}}{\partial x_i} \right) - \frac{2}{3} \left(\rho_l k + \mu_t \frac{\partial u_{l,k}}{\partial x_k} \right) \delta_{ij} \right]. \quad (4.38)$$

This method for turbulence modelling the two-phase governing equations is an attractive approach due to its simplicity; requiring only two equations to model the turbulence for both phases and has been used in multiple studies to model the turbulence in bubble-water flows (Gosman et al., 1992; Rusche, 2002; Lei and Ni, 2014; Karpinska and Bridgeman, 2017). One drawback of this method is that the derivation of the turbulence response coefficient, C_t , assumes the ratio between phase velocity fluctuations is invariant in space (coefficient values are the same in all directions) which may not be the case for all flows.

4.5 Bubble-fluid modelling

There are a range of industries that utilise bubbly flow such as steel, nuclear and wastewater industries. A bubble plume is the shape that a swarm of bubbles will form rising through a large fluid tank. A bubble column is a specific case where the plume is more restricted by the volume of the tank such that it behaves differently. In our system, the tank is larger than a conventional bubble column; however, the walls of our tank are still close enough to impede on the bubble plume. Therefore, a brief description of the dynamics of bubble columns and plumes will be made to better understand the expected dynamics in our aeration tank.

4.5.1 Bubble column reactors

Bubble column reactors are multiphase reactors where gas is introduced into a continuous fluid phase as bubble structures through gas spargers. They are widely used in petrochemical, biochemical, chemical and metallurgy industries (Besagni et al., 2018; Li et al., 2015; Colombo and Fairweather, 2015) and the desired results differ for each industrial process. In chemical related industries: hydrogenation, oxidation, chlorination etc. may be desired; while in metallurgy, aeration is used to keep the molten steel well-mixed and to assist in removing impurities. In wastewater treatment the aeration basins introduce air to induce new flow regimes and influence chemical reactions. In a bubble column the vessel shape impacts the dynamics within the reactor, which is observed in the experimental aeration tank; however, in a full-scale aeration tank the fill volume is so large that the walls impede less on the flow.

When considering the dynamics inside of a bubble column, it is important to consider the length scales of each associated phenomena. The three important scales are the: molecular, bubble and reactor scales. At the molecular scale, the chemical reactions are required to formulate mass transfer models (Besagni et al., 2018); at the bubble scale, the important characteristics are the bubble-fluid interaction forces (Amaral et al., 2018); and at the reactor scale, the hydraulic regimes, vortices and the gas residence time are all important characteristics (Besagni et al., 2018).

It is important to note that the bubble scale dynamics has an effect on the characteristics of the other scales. The bubbles drive the hydrodynamics at the reactor scale, dragging fluid along as they rise, while at the molecular scale the mass transfer only occurs along the bubble surface. Therefore, correctly understanding the bubble scale forces is crucial for accurately modelling the dynamics at all scales in the reactor.

4.5.2 Bubble property parameters

The dynamics of a rising swarm of bubbles are affected by the bubbles: fluid properties, size distributions, shapes and rising velocities; which all have an impact on the bulk hydrodynamics and mass transfer in the reactor. Bubble size distributions and shape are important characteristics as they determine the available bubble surface area which affects the heat and mass transfer rates. The shape of the bubble depends on bubble rise velocity, u_b , bubble diameter, d_b , phase density difference, $\Delta\rho = \rho_l - \rho_g$, liquid viscosity, μ_l , surface tension, σ , and gravitational acceleration, g (Haberman and Morton, 1953). These variables can be represented in a series of non-dimensional numbers:

the Eotvos Number,

$$Eo = \frac{g(\rho_l - \rho_g)d_b^2}{\sigma};$$

the Morton Number,

$$Mo = \frac{g(\rho_l - \rho_g)\mu_l^4}{\rho_l^2\sigma^3};$$

and the Reynolds Number,

$$Re = \frac{\rho_l u_b d_b}{\mu_l}.$$

These non-dimensional numbers relate the bubble properties to bubbles rising in an infinitely high medium (Clift et al., 1978). If Morton number is fixed then the bubble shape changes with increasing bubble diameter from spherical to ellipsoidal to cap-shaped, as illustrated by the bubble phase regime diagram in figure 4.2. Bubbles are spherical when the surface tension and viscous forces are larger than the inertial forces which generally occurs for $Re = 400$ and below.

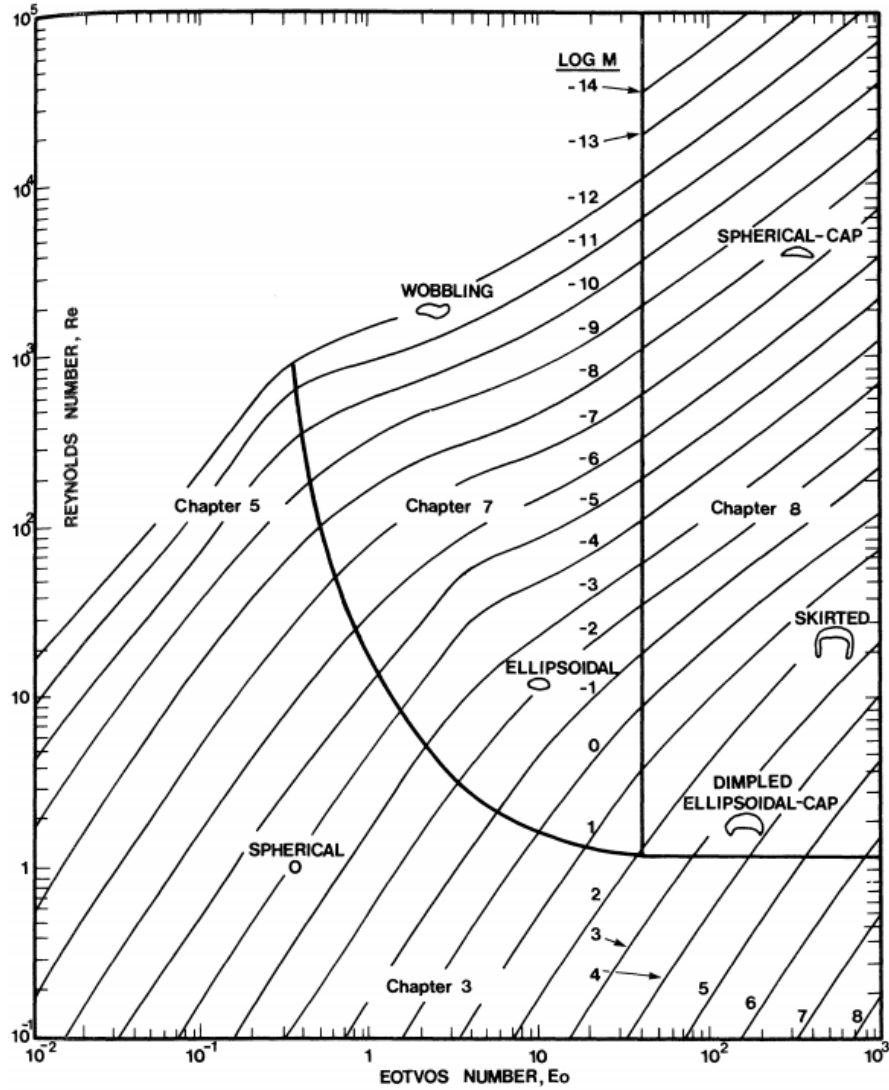


Figure 4.2: Shape regimes for bubbles and drops in unimpeded gravitational motion through liquids (Clift et al., 1978).

4.5.3 Theoretical bubble rise velocities

The bubble rise velocities are known to be dependent on the bubble shape which are further dependent on the E_o , M_o and Re numbers (Park et al., 2017). Wallis (1974) found that for spherical bubbles in highly viscous flows with a $Re < 1$, $\mu_g \ll \mu_l$, and $\rho_g \ll \rho_l$, which is common for most liquid-gas systems, the bubble rise velocity can be defined as,

$$v_{b,\text{visc}} = \frac{g\rho_l d_b^2}{12\mu_l}, \quad (4.39)$$

where: μ_g and μ_l are the gas and liquid viscosities, respectively; ρ_g and ρ_l are the gas and liquid densities, respectively; g is gravitational acceleration; and d_b is the volume equivalent bubble diameter. For larger Re numbers where the inertial forces are important, Wallis (1974) and Grace et al. (1976) found that, in a Re range of $1 < Re < 100$, the rise bubble velocity for spherical, ellipsoid and spherical-cap bubbles: $v_{b,\text{sph}}$, $v_{b,\text{ellip}}$ and $v_{b,\text{cap}}$, respectively; can be described by the formulae,

$$v_{b,\text{sph}} = 0.14425g^{5/6} \left(\frac{\rho_l}{\mu_l} \right)^{2/3} d_b^{3/2}, \quad (4.40)$$

$$v_{b,\text{ellip}} = \sqrt{\frac{2.14\sigma}{\rho_l d_b} + 0.505gd_b}, \quad (4.41)$$

$$v_{b,\text{cap}} = 0.721\sqrt{gd_b}, \quad (4.42)$$

respectively; where σ is the surface tension between the liquid and gas medium. It was found that the rise velocities increase with bubble size because of larger buoyancy forces which dominate over the increase in frictional forces due to the increase in surface area, as described in the $v_{b,\text{sph}}$ formulation. However, as the diameter increases, the shape of the bubbles shifts in the phase diagram (figure 4.2) to a more ellipsoid shape which greatly increases the surface area and, therefore, the frictional forces. This results in a decrease in the rise velocity with increasing bubble size as the frictional forces are increasing faster than the buoyancy forces. As the bubble size increases further, the bubble aspect ratio of long axis against short axis reaches a maximum such that the bubble cannot get any flatter and the surface area stops increasing significantly. This results in the rise velocity increasing again with bubble size, as described in the $v_{b,\text{ellip}}$ formulation. Finally, at even higher bubble diameters, they become so large that they start to deform into spherical cap shapes and follow the $v_{b,\text{cap}}$ formulation.

Park et al. (2017) found that the $v_{b,\text{ellip}}$ approximately converges to the $v_{b,\text{cap}}$ formulation as the bubble size increase such that the $v_{b,\text{ellip}}$ formulation can be used for ellipsoid and non-spherical bubbles. After further analysis of the bubble rise velocity formulation, Park et al. (2017) derived a general formula for the rise

velocities for any bubble shape defined as,

$$v_b = \min(v_{b,\text{visc}}, v_{b,\text{sph}}, v_{b,\text{ellip}}). \quad (4.43)$$

Additionally, this can be used to identify a bubble shape if the bubble rise velocity is already known. Therefore, using the data provided in the membrane diffuser manual (xylem, 2020), we can calculate the theoretical bubble features for the experimental aeration tank. The manual for the fine membrane diffusers describe a bubble range between 1 - 4 mm. If we assume the bubbles have a Sauter mean bubble diameter, $d_b = 2.5$ mm, and, at 5°C, the properties of water and air are (Potter et al., 2016):

$$\sigma = 0.075 \text{N/m}, \quad \mu_l = 1.519 \text{mPa s}, \quad \rho_l = 1000 \text{kg/m}^3, \quad \rho_g = 1.269 \text{kg/m}^3,$$

and with gravitational acceleration, $g = 9.81 \text{m/s}^2$, then we can derive the theoretical bubble parameters. The theoretical bubble rise velocity formula from equation (4.43) finds that,

$$v_b = \min(3.364, 0.915, 0.277) = 0.277 \text{ m/s},$$

which gives us parameter numbers:

$$E_o = 0.816, \quad M_o = 1.24 \times 10^{-10}, \quad Re = 456.$$

These values of Re and M_o imply that the bubbles lie close to the wobbling regime in the phase diagram in figure 4.2.

4.6 Bubble-fluid interaction forces

When modelling the flow field generated by bubbles, we need to consider how the bubble and reactor scale dynamics interact with one another. A difficulty with

this is that the bubble scale is a lot smaller than the reactor scale and resolving both scales simultaneously would be very computationally expensive. However, by extensively studying the bubble scale dynamics (by considering a single or a few bubbles) it is possible to quantify the bubble-fluid forces and make models that simulate their effects at large scales (Roghair et al., 2011; Baltussen et al., 2017). The important forces that have been found to accurately replicate the bubble-fluid interactions are: drag, virtual mass, lift, turbulent dispersion and wall lubrication forces (Dhotre et al., 2009; Colombo and Fairweather, 2015; Vik et al., 2018). The momentum exchanges terms on the liquid phase, $I_l = -I_g$, due to the bubble-fluid forces are,

$$I_l = -I_g = F_d + F_{vm} + F_l + F_{td} + F_w,$$

where F_d is the drag force, F_l is the lift force, F_w is the wall lubrication forces, F_{vm} is the virtual mass force and F_{td} is the turbulent dispersion force. The paper by Wang and Yao (2016) discuss, compare and review the different force models and consider their relevance for varying flow regimes. Wang and Yao (2016) compared bubble force models against three different experiments and found that there was no set of standard models that could be applied universally for all flow conditions. The model forces and their corresponding coefficient models are dependent on the bubble regimes and flow patterns for the varying bubble Reynolds numbers considered.

4.6.1 Drag Force

The drag force expresses the resistance experienced by a bubble as it moves relative to the surrounding liquid. Viscous stresses from friction with the bubble surface causes skin drag while a pressure distribution from a build up of fluid particles around the bubble causes form drag (Colombo and Fairweather, 2015). The model for the drag force is defined as,

$$F_d = \frac{3}{4} \frac{C_D}{d_b} \alpha \rho_l |U_r| U_r,$$

where C_D is the drag coefficient, d_B is the bubble diameter, α is the volume fraction, ρ_l is the liquid density and U_r is the relative bubble velocity, $U_r = U_g - U_l$. The drag coefficient is unknown and needs to be modelled empirically. A number of papers have proposed correlations for the drag coefficient; the simplest correlation relates C_D to the Reynolds number. These types of correlations to model the coefficient have been used in [Smith \(1998\)](#); [Dhotre and Smith \(2007\)](#); [Dhotre et al. \(2009\)](#) and [Colombo and Fairweather \(2015\)](#).

One of the first empirical models for the drag coefficient was developed by [Schiller and Naumann \(1935\)](#) for laminar flow and is defined as,

$$C_D = \begin{cases} \frac{24}{Re}(1 + 0.15Re^{0.687}) & \text{for } Re \leq 1000, \\ 0.44 & \text{for } Re \geq 1000, \end{cases} \quad (4.44)$$

which has been adopted in [Chen et al. \(2004\)](#) and [Kim et al. \(2007\)](#).

[Tomiya et al. \(2002\)](#) have produced a great deal of work in investigating and improving models for the drag coefficients for bubbly flow. They found a drag coefficient correlation with the bubble Reynolds and Eotvos numbers which is defined as,

$$C_D = \beta \max \left[\min \left(\frac{16}{Re}(1 + 0.15Re^{0.687}), \frac{48}{Re} \right), \frac{8}{3} \frac{E_o}{E_o + 4} \right] \quad (4.45)$$

where Re is the bubble Reynolds number, E_o is the Eotvos number and β is a tuning factor ([Tomiya et al., 2002](#)) which has been used in [Lubchenko et al. \(2018\)](#).

4.6.2 Virtual Mass Force

The virtual mass force models the work required by the bubbles to accelerate the surrounding liquid as it rises and is defined as,

$$F_{vm} = \alpha \rho_l C_{vm} \left(\frac{d}{dt} U_r + (\mathbf{u} \cdot \nabla) U_r \right),$$

where C_{vm} is the virtual mass coefficient in which $C_{vm} = 0.5$ is commonly used for spherical bubbles [Colombo and Fairweather \(2015\)](#). [Smith \(1998\)](#); [Dhotre and Smith \(2007\)](#) and [Dhotre et al. \(2009\)](#) found the virtual mass force can be useful for stabilising the problem initially by limiting bubble acceleration; however, it has been found to be negligible once the system has reached pseudo-steady conditions. [Colombo and Fairweather \(2015\)](#) also reported previous studies that have found the virtual mass has little effect on the dynamics and can be neglected.

4.6.3 Lift Force

A bubble travelling through a shearing flow will experience a lift force perpendicular to the direction of motion. The lift force models the contribution shearing motion has on the momentum and is defined as,

$$F_L = \alpha \rho_l C_L U_r \times \nabla \times U_l,$$

where C_L is the lift coefficient and U_l is the liquid velocity.

The lift force has a strong impact on the outward movement of the bubbles and, therefore, the volume fraction distribution. The simplest model for the lift coefficient is to use a constant value such as $C_L = 0.1$ as used in [Dhotre and Smith \(2007\)](#); [Dhotre et al. \(2009\)](#); [Colombo and Fairweather \(2015\)](#).

The lift coefficient is assumed to depend strongly on bubble size and [Tomiyama et al. \(2002\)](#) found a lift coefficient correlation to the Eotvos number defined as,

$$C_L = \begin{cases} \min [0.288 \tanh(0.121, Re), f(E_o)] & \text{for } E_o < 4, \\ f(E_o) & \text{for } 4 \leq E_o \leq 10.7, \\ 0.288 & \text{for } 10.7 < E_o, \end{cases} \quad (4.46)$$

where,

$$f(E_o) = 0.00105E_o^3 - 0.0159E_o^2 - 0.0204E_o + 0.474. \quad (4.47)$$

A positive lift coefficient is used for small spherical bubbles (low Eotvos number) which results in plume spreading while negative coefficients are used for large bubbles (larger Eotvos number) which causes a centre-peaked bubble distribution. In the small bubble case, the positive lift coefficient results in a volume fraction peak near the wall which can be unphysical. To account for this, a wall lubrication force can be applied that stops the volume fraction peak as the bubbles get closer to the wall. [Shaver and Podowski \(2015\)](#) neglected the dependence on bubble size and proposed a simplified lift coefficient correction that damped the lift force when within one bubble diameter of a wall. The proposed model is given by,

$$C_L = \begin{cases} 0, & \text{for } y_w/d_b < 0.5, \\ C_{L_0} \left(3\left(\frac{2y_w}{d_b} - 1\right)^2 - 2\left(\frac{2y_w}{d_b} - 1\right)^3 \right), & \text{for } 0.5 < y_w/d_b < 1, \\ C_{L_0}, & \text{for } 1 < y_w/d_b, \end{cases}$$

where y_w is the distance from the wall and C_{L_0} is the normal constant lift coefficient value. This lift model has been used in [Lubchenko et al. \(2018\)](#) and [Ma et al. \(2016\)](#) in which they proposed that this damping approach could provide a substitute for the physical wall lubrication models.

4.6.4 Turbulent Dispersion Force

The drag and lift forces are related to the relative velocity between phases. When using the RANS equations for two phases, the mean velocity for both phases is found. The turbulent dispersion force was created to model the influence of random turbulent eddies from the rising bubbles on the fluid which have been averaged out when deriving the RANS formulation. [Davidson \(1990\)](#) proposed the force is proportional to the volume fraction gradient, the drag force, and a dispersion coefficient that is equal to the turbulent dynamic viscosity, μ_t , which is set equal for

both phases as defined below,

$$F_{td} = \frac{3}{4} \frac{C_D}{d_b} \mu_t \alpha \rho_l |U_r| \nabla \alpha,$$

This force acts to diffuse the bubbles away from the plume centre axis to correctly model the plume spreading and has been used in [Dhotre and Smith \(2007\)](#) and [Dhotre et al. \(2009\)](#). [Burns et al. \(2004\)](#) derived an alternative force model by applying Favre averaging to the drag force such that,

$$F_{td} = \frac{3}{4} \frac{C_D \alpha \rho_l |U_r|}{d_b} \frac{\mu_{t,l}}{\sigma_\alpha} \left[\frac{1}{\alpha} + \frac{1}{1-\alpha} \right] \nabla \alpha,$$

where $\mu_{t,l}$ is the turbulent kinematic viscosity of the liquid and σ_α ($\sigma_\alpha = 1.0$) is the turbulent Prandtl number for the volume fraction. This force model has been used in [Rzehak and Krepper \(2013b\)](#); [Colombo and Fairweather \(2015\)](#) and [Lubchenko et al. \(2018\)](#).

4.6.5 Wall Lubrication Force

The presence of walls affects the flow field around bubbles when in close proximity. The flow field in the region between the bubbles and the wall is slower than the region between the bubbles and ambient fluid. This creates a pressure difference on the bubble surface that pushes the bubbles away from the wall. The lift and turbulent dispersion forces cannot correctly predict this behaviour and the wall force is required to overcome the problem of peaked volume fraction distribution near the walls. [Antal et al. \(1991\)](#) derived a model by considering a rising bubble in laminar flow and proposed the wall force has the form,

$$F_W = \max \left[0, C_{w,1} + C_{w,2} \frac{d_b}{y_w} \right] \alpha \rho_l \frac{|U_r|^2}{d_b} n_w,$$

where y_w is the wall distance, $C_{w,1}$ and $C_{w,2}$ dictates the strength of the wall effects and n_w is the vector normal to the wall. This model has been used in [Rzehak](#)

and Krepper (2013b) and Colombo and Fairweather (2015) with fixed coefficients, $C_{w,1} = -0.055$ and $C_{w,2} = 0.09$, which were found after optimising the values against experimental data.

4.7 Theoretical oxygen mass transfer

In the experimental aeration tank, as bubbles rise through the liquid, some of the air transfers and is dissolved along the bubble surface into the water. An ODE can be derived that describes the amount of oxygen that is transferred into the liquid. We first define the concentration of oxygen in the liquid, C , and the oxygen saturation concentration, C_s , which is the maximum amount of oxygen that can be dissolved into the liquid. Additionally, if we assume that the volumetric mass transfer of oxygen from the bubbles to the liquid is proportional to some rate constant, $k_l a$, and that the aeration tank is well mixed; then an ODE to describe the rate transfer of oxygen into the liquid can be derived as presented below (ASCE, 2007),

$$\frac{dC}{dt} = k_l a (C_s - C).$$

The oxygen concentration inside the tank changes at a rate proportional to $k_l a$ that is regulated by the difference between the current and oxygen saturation concentration of the liquid. It is important to note that we have not defined bubble size, air flow rate, liquid volume, temperature and other environmental parameters. These parameters are all captured in the rate constant $k_l a$ and, therefore, for each system the $k_l a$ will be different.

The ODE above can be solved using separable methods as shown below,

$$\int \frac{1}{(C_s - C)} dC = \int k_l a t dt,$$

which, using the initial condition $C = C_0$ at time $t = 0$ where C_0 , can be solved and gives the solution,

$$C = C_s - (C_s - C_0)e^{-k_l a t}.$$

This is the theoretical oxygen mass transfer equation for a batch reactor such that the solution would be different if there was fluid coming in and out of the reactor carrying oxygen.

Before we calculate the theoretical oxygen mass transfer rate for the experimental aeration tank, two new tank aeration parameters need to be introduced. The first of which is the:

SOTR - Standard Oxygen Transfer Rate ($\text{kg O}_2 \text{ hr}^{-1}$);

which describes the amount of oxygen that is transferred per hour under standard conditions. Under standard conditions of 20°C , the SOTR is found to have the relation ([ASCE, 2007](#)),

$$SOTR = k_l a_{20} C_{s_{20}} V,$$

where V is the volume of the vessel, $k_l a_{20}$ is the oxygen mass transfer rate (mass of O_2 per second) at 20°C and $C_{s_{20}}$ is the saturation of the liquid in the tank (mass per volume) at 20°C . The second parameter is the:

SOTE - Standard Oxygen Transfer Efficiency (%)

which refers to the fraction of oxygen in an inputted airflow that is dissolved into the reactor under standard conditions and is a useful variable for expressing the efficiency of a diffuser for comparison with other products. The SOTE is calculated by the formula ([ASCE, 2007](#)),

$$SOTE = 100 \frac{SOTR}{W_{\text{O}_2}} = 100 \frac{SOTR}{O_f \rho_a Q_s},$$

where $W_{\text{O}_2} = O_f \rho_a Q_s$ refers to the mass flow of oxygen in the input airflow ($O_f \approx$

20%, fraction of oxygen in air; ρ_a is the air density; Q_s is the air flow rate and the 100 is to convert the value to a percentage).

4.7.1 Calculating the $k_{l a}$ for the experimental aeration tank

Combining the two definitions for SOTE and SOTR and rearranging for $k_{l a_{20}}$ leads to the formula,

$$k_{l a_{20}} = \frac{SOTE O_f \rho_a Q_s}{100 C_{s_{20}} V}.$$

The xylem diffusers state that their diffusers have an approximate SOTE of 6.5 % per m of height (xylem, 2020). Using this we can calculate the $k_{l a_{20}}$ value for the aeration tank (assuming everything is under standard conditions). Using the values: $Q_s = 1.8$ L/s or 0.0018 m³/s (3 diffusers at 0.6 L/s each), $V = 0.7252$ m³, $C_{s_{20}} = 10$ mg/L = 0.01 kg/m³, $O_f = 0.20946$, and $\rho_a = 1.225$ kg/m³; we calculate a $k_{l a_{20}}$ value of:

$$k_{l a_{20}} = 4.057 \times 10^{-3} \text{ s}^{-1}.$$

Finally, the experimental aeration tank is operated at a temperature 6 °C such that the $k_{l a_{20}}$ value needs to be converted to represent the rate at 6 °C. The formula for the conversion is given by (ASCE, 2007),

$$k_{l a_{20}} = k_{l a} \Theta^{(20-T)},$$

where $\Theta = 1.024$ is a relation constant and T is the operating temperature in degrees Celsius. Using this formula, the final calculation of $k_{l a}$ for the experimental aeration tank is,

$$k_{l a} = 5.654 \times 10^{-3} \text{ s}^{-1}.$$

If we insert this value into the concentration equation,

$$C = C_s - (C_s - C_0)e^{-k_{l a} t}.$$

and set the initial concentration as $C_0 = 0$ mg/L and use a saturation concentration $C_s = 10$ mg/L, which has been derived from Wang et al. (1978) for a fluid of temperature 15 °C, then we produce the plot in figure 4.3. This give us insight into the rate of oxygenation in the experimental tank and can be used to compare with the results we obtain from the coupled model.

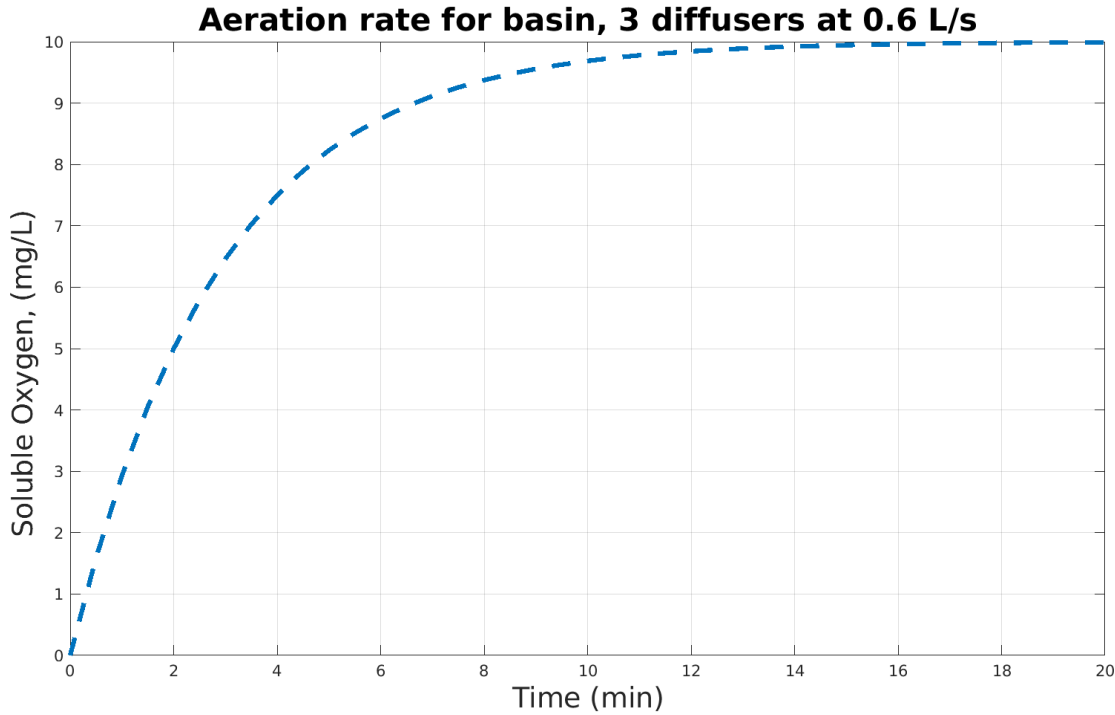


Figure 4.3: Average soluble oxygen profile for the experimental aeration tank with 3 aerating diffusers at 0.6 L/s each under the assumption the tank is completely mixed.

4.8 Numerical modelling and the finite volume method

The RANS equations discussed above are too complex to be solved analytically and require numerical methods to find a solution. The finite volume method (FVM) is an example of a numerical method and is the most commonly adopted in CFD software due to its conservation of physical properties. In the FVM, the problem domain is broken up into a mesh of volume cells and the solutions for each physical

quantity are found at the centre of each cell along with the flux through each cell face. The derivation of the FVM formulations is presented below.

Consider a simple steady convection-diffusion equation for a property ϕ ,

$$\nabla \cdot (\rho \mathbf{u} \phi) = \nabla \cdot (\Gamma \nabla \phi) + S_\phi, \quad (4.48)$$

where ρ and \mathbf{u} are the fluid density and velocity, respectively, Γ is the diffusion coefficient and S_ϕ designates the source or sink terms for ϕ . If we integrate these terms over some control volume, V , with a boundary, A , and apply the divergence theorem we get,

$$\int_A (\rho \mathbf{u} \phi) \cdot \mathbf{n} \, dA = \int_A (\Gamma \nabla \phi) \cdot \mathbf{n} \, dA + \int_V S_\phi \, dV, \quad (4.49)$$

where the divergence theorem states,

$$\int_V \nabla \cdot \mathbf{F} \, dV = \int_A \mathbf{F} \cdot \mathbf{n} \, dA, \quad (4.50)$$

where \mathbf{F} is a continuously differentiable vector field, V is closed and bounded with a piece-wise smooth boundary A and normal vector \mathbf{n} (Versteeg and Malalasekera, 2007). Equation (4.49) represents a flux balance in the control volume where, from the left, the terms describe the convective flux, diffusive flux, and generation or destruction of ϕ within the volume.

4.8.1 Discretisation

The convection-diffusion equation in 1D is governed by,

$$\frac{d}{dx}(\rho u \phi) = \frac{d}{dx} \left(\Gamma \frac{d\phi}{dx} \right) + S_\phi, \quad (4.51)$$

which also satisfies the continuity equation,

$$\frac{d}{dx}(\rho u) = 0. \quad (4.52)$$

Consider a one-dimensional control volume, ΔV , with a central node P and neighbouring central nodes W and E with w and e referring to the faces connecting the volumes W and E , respectively, as illustrated in figure 4.4. The distances between

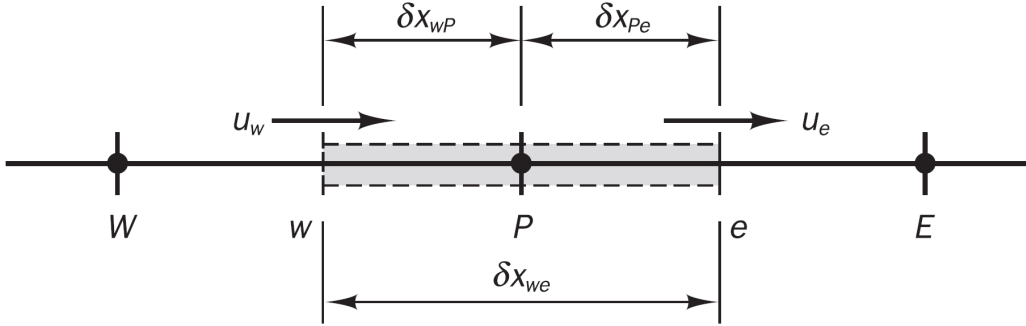


Figure 4.4: Illustration of the 1-D control volume (Versteeg and Malalasekera, 2007).

W and P and P and E are denoted as δx_{WP} and δx_{PE} , respectively. Similarly, the distances between face w and node P , and node P and face e are denoted as δx_{wP} and δx_{Pe} , respectively. Finally, the width of volume P is defined as $\Delta x = \delta x_{we}$.

If we integrate the 1D convection diffusion equation (4.51) over the central volume P we get,

$$\int_{\Delta V} \frac{d}{dx}(\rho u \phi) dV = \int_{\Delta V} \frac{d}{dx}(\Gamma \nabla \phi) dV + \int_{\Delta V} S_\phi dV, \quad (4.53)$$

applying divergence theorem,

$$\int_A (\rho u \phi) \cdot n dA = \int_A \left(\Gamma \frac{d\phi}{dx} \right) \cdot n dA + \bar{S}_\phi \Delta V, \quad (4.54)$$

$$(\rho u A \phi)_e - (\rho u A \phi)_w = \left(A \Gamma \frac{d\phi}{dx} \right)_e - \left(A \Gamma \frac{d\phi}{dx} \right)_w + \bar{S}_\phi \Delta V, \quad (4.55)$$

where A is the cross-sectional area of the control volume faces and \bar{S}_ϕ is the average

value of S_ϕ over the control volume. Similarly, integrating the continuity equations yields,

$$(\rho u A)_e - (\rho u A)_w = 0. \quad (4.56)$$

Considering equation (4.55), the physical interpretation is that the convective fluxes of ϕ entering or leaving through the faces must be balanced by the diffusive fluxes of ϕ entering and leaving the faces and the generation or destruction of ϕ in the control volume.

To obtain the discretised equations, we must approximate the terms in equation (4.55). Defining the variables F and D , to represent the mass fluxes and diffusive conductances, respectively, such that,

$$F_f = (\rho u)_f, \quad D_f = \frac{\Gamma_f}{\delta x_{LR}}, \quad (4.57)$$

where f is the face of interest and L and R represents the central nodes to the left and right of the face, respectively, or the central nodes in the negative and positive x direction from the faces, respectively. In the case of the P control volume faces we have,

$$F_e = (\rho u)_e, \quad F_w = (\rho u)_w, \quad (4.58)$$

$$D_e = \frac{\Gamma_e}{\delta x_{PE}}, \quad D_w = \frac{\Gamma_e}{\delta x_{WP}}. \quad (4.59)$$

Additionally, if we assume the distances between the control volumes are small, we can approximate the ϕ gradients at a face f as,

$$\left(\frac{d\phi}{dx}\right)_f = \frac{\phi_R - \phi_L}{\delta x_{LR}}. \quad (4.60)$$

Combining all these and assuming the velocity field is known, we can write the

integrated 1-D convection-diffusion equation as,

$$F_e A_e \phi_e - F_w A_w \phi_w = D_e A_e (\phi_E - \phi_P) - D_w A_w (\phi_P - \phi_W) + S_P \quad (4.61)$$

where $S_P = \bar{S}_\phi \Delta V$, and the integrated continuity equation as,

$$F_e A_e - F_w A_w = 0. \quad (4.62)$$

This has been derived for 1D but the same derivation can be applied for the other dimensions for the full 3D derivation. In order to solve these equations the face values, ϕ_w and ϕ_e , need to be calculated. To calculate these face values, a Gaussian approach is often adopted which assumes,

$$\phi_e = g_{PE} \phi_P + (1 - g_{PE}) \phi_E, \quad (4.63)$$

$$\phi_w = g_{WP} \phi_W + (1 - g_{WP}) \phi_P, \quad (4.64)$$

where $g_{PE} = \delta x_{eE} / \delta x_{PE}$ and $g_{WP} = \delta x_{wP} / \delta x_{WP}$ are the distances between the face of interest and one of the adjacent cell centres and these act as distance weighting for the face values. This approach is accurate for hexahedral meshes where there is cell uniformity but loses accuracy with tetrahedral meshes with large cell skewness. This approach can include further complexity by interpolation schemes, such as the upwind differencing or central differencing schemes, that include more cells in the weighting calculation. Once this has been done for each term in the equation, an algorithm is run that solves these discretised equations to find how the velocity field and pressure changes.

4.8.2 SIMPLE algorithm

The Semi-Implicit Method for Pressure Linked Equations (SIMPLE) algorithm is a numerical procedure for solving the Navier-Stokes equations for steady-state sys-

tems. The SIMPLE algorithm is a segregated approach that solves the equations iteratively. After computing the velocity gradient and pressure from the previous step or initial guess, the algorithm solves the discretised momentum equations. Assuming that all the other variables are constant or frozen while solving each momentum equation iteratively, we find a system of equations for the u component of the velocity field and compute a new value, \tilde{u} . This is repeated for each momentum equation, using the most recent updated available variable, for example \tilde{u} will be used and frozen for the solving the v momentum equation, to produce an intermediate new velocity field which is also used to compute the mass fluxes at the cell faces. However, this new field most likely will not satisfy the continuity equation and needs to be corrected, for example,

$$u_{i,c} = \tilde{u}_i + u'_i,$$

where $u_{i,c}$ are the correct velocity components that satisfies the continuity equation, \tilde{u}_i is the intermediate velocity field initially found and u'_i are the corrections to the intermediate field. It is assumed that these velocity corrections can be derived from suitable pressure corrections such that, in a similar way,

$$p_c = \tilde{p} + p',$$

where p_c is the desired pressure in the cell centres to satisfy the continuity equation and p' is the correction needed to the current pressure \tilde{p} , which is the value of pressure from the previous global iteration. An equation for the pressure corrections can be derived and solved using the newly obtained intermediate velocity field to find p' . The pressure correction term is used to correct the pressure field and velocity components which is then used to correct the mass fluxes at the faces as well. Additionally, any updates to density etc. due to pressure changes is made. Finally, this repeated until the velocity and pressure fields have stop changing significantly such that the result has converged or the residual changes are below some set criteria.

4.8.3 PISO algorithm

The Pressure Implicit with Splitting of Operator (PISO) algorithm is another numerical procedure for solving the Navier-Stokes equations that is an extension of the SIMPLE algorithm which was developed for non-iterative computation of unsteady compressible flow but has been adapted for steady-state problems. The PISO algorithm follows a similar procedure as the SIMPLE algorithm but, by default, has one predictor and two corrector steps. For a given iteration, the initial predictor step follows the same procedure as SIMPLE for finding the new corrected velocity and pressure fields with corrected mass fluxes. However, it returns back to the predictor step again with the new corrected velocity and pressure fields as the initial guess and repeats the whole correction procedure which is referred to as the first corrector step. This procedure is repeated again for the second and final corrector steps to obtain the final solution for this iteration. The time step is then increased for the next iteration and the whole process is repeated again. The number of corrector steps, by default, is two but this can be increased to the amount required.

4.8.4 PIMPLE algorithm

The PIMPLE algorithm is a combination of the PISO and SIMPLE algorithm. The PIMPLE runs the PISO algorithm, for a given time step and correction loops but runs it in a SIMPLE algorithm such that it runs the PISO algorithm for n iterations until the solution has converged or reached some designated residual criteria before moving onto the next step. It is similar to running the PISO algorithm with n correction loops but the n changes each time step and is dependent on how fast the solution converges.

4.9 Chapter summary

In this chapter, we have defined the governing hydrodynamic equations and outlined the additional important models required for replicating the fluid motion in wastewater treatment reactors, specifically, the features required for modelling the two-phase aeration tank using a Eulerian-Eulerian approach. The various bubble-fluid interactions have been described and defined for modelling the bubble dynamics. A theoretical oxygen mass transfer model was derived and used to estimate the oxygen mass transfer rate for the experimental aeration tank with 3 diffusers aerating at a total flow rate of 1.8 L/s. Finally, the finite volume method was described along with the discretisation procedure and an outline of the various algorithms available for solving the discretised system of equations. In the next chapter, we will discuss how these models have been implemented in the CFD software and the solutions from these simulations.

Chapter 5

Eulerian two-phase aeration tank modelling

The previous chapter has discussed the fundamental equations, models and finite volume techniques required to numerically solve and simulate bubble driven hydrodynamic flow. There is a range of CFD software available that implement these tools to solve the Navier-Stokes equations for these systems. In this work, a finite volume open source CFD software called *OpenFOAM* (foundation version 4.1, [OpenFOAM \(2020\)](#)) has been used to solve the Eulerian-Eulerian RANS equations to simulate the bubble induced hydrodynamics in the aeration tank. In the first section of this chapter, a description of the solver used in OpenFOAM to solve the Eulerian-Eulerian RANS equations will be made along with the solution methods, initial conditions, and boundary conditions required for modelling the aeration tank. In the next section, a mesh refinement and steady-state analysis study will be conducted for the 2D representation of the aeration tank. An assessment of the accuracy of the bubble force models on replicating the bubble-fluid interactions in the aeration tank will be made by comparing the simulation and experimental results, where these findings will be used to model the aeration tank in 3D. The next section will conduct a mesh refinement and time analysis study for the 3D simulation setup. Finally, an analysis of the hydrodynamic results from the 3D simulations will be conducted, comparing

the solutions with the experimental results for validation, with the 2D results for comparison, and comparing the findings for two different aeration flow rates.

5.1 Solver setup - *reactingTwoPhaseEulerFoam*

OpenFOAM is an open source CFD software written in C++ ([OpenFOAM, 2020](#)) that uses the FVM to solve the Navier-Stokes equations, as described in §4.2, similarly to other CFD software such as ANSYS Fluent ([Ansys, 2018](#)). The benefit of OpenFOAM over other CFD software is that, due to it being open source, the user is able to easily access and manipulate the source code to suit their specialist needs. This access to the source code is crucial later on in this thesis when the biokinetic models are coupled into the hydrodynamic two-phase solutions. In this section, the procedures for modelling the aeration tank hydrodynamics in OpenFOAM are described. While explaining the full inner workings of OpenFOAM is out of scope for this thesis, a brief description of each OpenFOAM process will be given.

There exist various multiphase approaches that describe and model the interactions between two or more phases. Two approaches that are applicable to the aeration tank is the Eulerian-Eulerian approach, which has been described in §4.4, and the Eulerian-Lagrangian approach. In the Eulerian-Lagrangian approach, the water phase is modelled in the usual FVM that is consistent in CFD simulations while the air bubbles are modelled as discrete particles and tracked as they rise through the domain. The interactions between the particles and fluid are applied as force terms in the corresponding cells the bubble particles reside in. Initial simulations were conducted using both methods and it was found that both were suitable for modelling the aeration tank dynamics. However, a key goal of this thesis is to include the free surface in the hydrodynamic modelling which is not possible in the Eulerian-Lagrangian approach by default. The volume of fluid method, a numerical technique that can capture the free surface between two phases, can be included in the Eulerian-Lagrangian approach to model the free surface but this would increase

the computational resources needed for the simulations which is already computationally demanding. Additionally, to our understanding, all previous work has only used the Eulerian-Eulerian approach for modelling an aeration tank. It is for these reasons that only the Eulerian-Eulerian approach has been considered in this work.

OpenFOAM has a series of pre-defined scripts that have been written to solve specific fluid problems, referred to as *solvers* (OpenFOAM, 2020). One of these is the transient Eulerian-Eulerian based multiphase solver, *reactingTwoPhaseEulerFoam*, which solves the two-phase RANS equations (as described in §4.4) and has been modified and used to model the bubble driven aeration tank for both the 2D and 3D simulations. To utilise these solvers, OpenFOAM has pre-defined case files to be used as templates that describe fluids problems related to the solved equations in these solvers. In this work, the *bubbleColumn* case file template has been used which describes a rectangular bubble column. This template has been modified to replicate the experimental aeration tank described in chapter 3.

The first modification to the solver was to neglect the effects of temperature as it was approximately constant at 7 °C in the aeration tank such that it has no influence on the flow field. To remove the effects of temperature, the solving tolerance was set to zero in the temperature solver settings and the properties of each phase was set to Isothermal. This results in the energy equation not being solved per iteration which reduces the computational cost of the simulation. The density in the solver setup is initially compressible and models the air and water phase as a perfect gas and fluid, respectively. This models the effect bubble expansion has on the flow field as the bubbles rise up through the reactor. However, we are assuming the water is incompressible and, therefore, the density model for the water has been modified. Initially, the density of water was modified to constant; however, this led to stability issues in the solver. This is probably a result of the equations for the two phases not being compatible when one phase is compressible while the other is not; resulting in convergence issues for the continuity equation. The formula for a

perfect fluid used to describe the water density in *OpenFOAM* is defined as,

$$\rho = \frac{1}{RT}p + \rho_0,$$

where ρ_0 and ρ are the initial and new fluid density, respectively, T is temperature, p is the pressure and R is a constant [OpenFOAM \(2020\)](#). To replicate an incompressible fluid, the default value of R was increased from 3000 to 10000 such that it effectively suppresses the density changes due to changes in pressure. This formulation results in a pseudo incompressible fluid being modelled for the water while solving the stability issues found using the constant density model.

5.1.1 Solution method and initial conditions

The *PIMPLE* algorithm (as described in §4.8.4) was used to couple and solve the pressure and velocity in the RANS equations where the system of equations is looped over 3 times per time step to ensure convergence. In OpenFOAM, the discretisation of each term in the equations can be chosen. The schemes used for the hydrodynamic simulations are described below with a summary presented in table 5.1. The bounded first order implicit Euler method has been used for the discretisation of the time derivative. The Gaussian approach (as described in §4.8.1) has been used to calculate the face values for all the terms. The gradient and Laplacian terms use the second order unbounded central differencing scheme for the interpolation. The divergence term for the volume fraction uses the *vanLeer* scheme that switches from the second order central differencing to first order upwind schemes in regions of rapidly changing gradient for the variable of interest to improve stability. The divergence of the pressure and turbulence quantities use the *limitedLinear* scheme that works the same as *vanleer*, but with a stricter switching coefficient. Finally, the velocity divergence term uses the *LimitedLinearV* scheme which switches from central differencing to upwind, similar to the *limitedLinear*, but the switch coefficient value is based on the velocity component that has the largest changing gradient

which is applied to all three components. A tolerance of 10^{-8} and 10^{-7} was set for the pressure and the rest of the variables, respectively.

Terms	Schemes
Time derivative	Bounded first order Implicit Euler method
Face values	Gaussian approach
Gradient	Second order unbounded central differencing scheme
Laplacian	Second order unbounded central differencing scheme
Divergence - α	vanLeer scheme
Divergence - velocity	limitedLinearV scheme
Divergence - others	limitedLinear scheme

Table 5.1: Summary of the schemes used to solve the discretised terms in the two-phase RANS equations.

The membrane diffusers create air bubbles with diameters in a range of 1 - 4 mm (as described in §3.1.1) and so a Sauter mean diameter of 2.5 mm was defined initially in the simulations; the impact of bubble size is further investigated in §5.2.4. In the two-phase Eulerian-Eulerian setup, a continuous phase is defined which corresponds to the dominant phase in the problem; the other phase is referred to as the discrete phase. This can dictate how the equations are implemented in the solver, for example, if using the two-phase mixture $k - \epsilon$ turbulence model described in §4.4.1, the turbulence is solved for the continuous phase only and the results of this are extrapolated and applied to the discrete phase. Usually in bubbly flow, the liquid is defined as the continuous phase and is unchanged throughout the problem. However, in our case where the free surface is modelled, there is a layer of air on top of the domain where the gas is the continuous phase in this region. In our case, while we assume the water is the continuous phase for the majority of the simulation, OpenFOAM offers a blending function that can switch which phase is the continuous phase based on the volume fraction ratio of the two phases in a cell during the run time (OpenFOAM, 2020). This allows for forces like drag to be applied when we have bubbles rising through the tank but not included when there

are significant changes to the water-air volume fraction ratios, for example, when there is equal or more air in a cell than water such as at the free surface, which can affect the dynamics of the problem.

The blending function was setup such that if the volume fraction reaches 0.7 for either phase, that phase is then defined as the continuous phase. Additionally, there is a blending switch value at a volume fraction of 0.5 where both phases are assumed partly continuous. Once a switch is made, it will not change until it reaches another switching value, for example, if the water volume fraction reached 0.8, it would be defined as the continuous phase and the relevant forces for when the water is a continuous phase would be applied. If the volume fraction were to decrease to 0.6, the water phase will still be defined as the continuous phase as it has not passed one of the limits. It would have to decrease to 0.5 to reach the partly continuous limit value before a change occurred. After reaching 0.5, the water volume fraction would have to increase to 0.7 again to switch from a partly continuous to the continuous phase. The surface tension between water and air was set at 0.07 N/m and the effect of gravity was included. The default bubble force models used were the Schiller-Naumann drag model (Schiller and Naumann, 1935) and the virtual mass force with coefficient, $C_{VM} = 0.5$, as described in §4.6. These are further investigated in this chapter in §5.2.5.

The density of water was set at $\rho_{0,w} = 1000 \text{ kg/m}^3$ and the air density is described by the perfect gas formulation,

$$\rho_a = \frac{1}{RT}p,$$

where R is the specific gas constant, T is the temperature, and p is pressure. The mixture $k - \epsilon$ turbulence model, as defined in §4.4.1, has been used to close the two-phase RANS equations. Finally, the time step was allowed to vary during runtime to ensure that the max Courant number did not exceed 0.5 for each time step to improve stability. The goal of the simulation were to run till a steady-state was

reached.

5.1.2 Boundary conditions

A velocity inlet was used for the air inlet condition. The nature of the diffuser membrane means that the velocity inlet value is dependent on the air flow rate and volume fraction. This is further investigated in a later study (§5.2.3). The top wall or outlet is set as an *inletOutlet* condition that allows air and water to escape (OpenFOAM, 2020). It is defined such that if continuity issues arise when fluid leaves through the outlet, it is replaced with air. The membrane diffusers in the experimental rig are raised above the base, as illustrated in figure 3.1a, such that there is a region of volume around and below the diffusers. The extra meshing complexity required to model and resolve the fluid flow in this lower space would take computational resources away from the core hydrodynamics being solved in the bulk of the reactor. Additionally, the volume of space below the diffusers is less than 5 % of the total volume which is small. Therefore, the lower volume has been neglected and the base of the tank is assumed to start at the top of the membrane diffusers. The fill height of the experiments was 1.03 m and so, when removing the space below the diffusers, the fill height of the simulations will be 0.98 m.

The membrane of the diffusers expand and bulge under pressure creating a 3D dome shape, as illustrated by the close left diffuser in figure 3.1b. The amount the membrane expands is proportional to the flow rate which adds an additional level of complexity to the meshing. It is assumed that the bulging dome shape does not impact the flow field and only the bubbles being produced are important. Therefore, the simulations will assume the membrane does not expand such that it can modelled as a flat circular inlet.

The other walls of the tank are defined with a no slip condition. The total mesh height is set higher than the fluid surface to allow for the water free surface to move freely without being confined by the outlet which stops water from escaping

through the outlet. However, it was not set “too high” to avoid mesh cells being wasted on a region of the tank that was of little interest. The fill height was set at 0.98 m and the total height of the domain was 1.13 m and 1.08 m for the 2D and 3D simulations, respectively, which was found to be appropriate from initial simulations. The larger space was given for the 2D simulations as the fluid surface rose higher in these simulations due to the confined nature of 2D simulations. Finally, the volume fraction for water was set at 1 and zero for regions below and above the fill height, respectively, and the free surface was resolved by the Eulerian formulation without additional models. These simulations were run on the University of Leeds’ high performance computer clusters, ARC3 and ARC4, using between 36 cores to 150 cores with 4.6 GB of ram for each core for the 2D and 3D simulations, respectively, which would require between 3 - 10 days to run to reach a steady-state.

5.2 Assessing CFD modelling approaches and assumptions using the 2D simulations

In §3.6, the experimental results showed that two of the diffuser configurations had pseudo 2D behaviour, as such these results can be used to compare and validate 2D model simulations. The benefit of running 2D simulations is that they are computationally cheaper than 3D and can be used to efficiently investigate and verify the modelling choices for the aeration tank CFD model. The diffuser configuration that demonstrated the pseudo 2D behaviour was the “d1d2d3” configuration, as described in §3.3.1. A 2D slice through the “d1” diffuser was modelled, as illustrated in figure 5.1a, where the plane aligns with 15 velocity measurements recorded by the ADV, as illustrated in figure 3.7. A mesh refinement study and a study to assess the time taken to reach steady-state needs to be conducted prior to the CFD being validated.

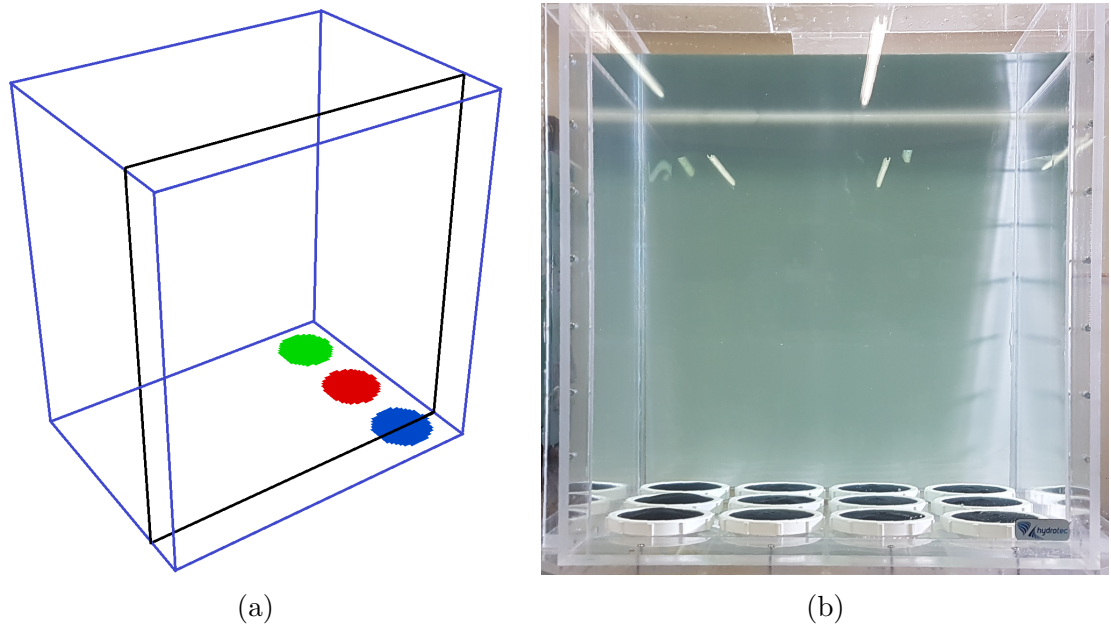


Figure 5.1: Illustration of the 2D slice made through the “d1” diffuser in the aeration tank for running the 2D model simulations (a) with an illustration of the experimental aeration tank for context (b).

5.2.1 Mesh refinement study

A detailed mesh refinement study has been conducted using a uniform hexahedral structured mesh. This was programmatically generated using the OpenFOAM meshing tool *blockMesh* which has been analysed to confirm mesh independence (OpenFOAM, 2020). The number of cells along the height and width of the mesh were kept the same, as illustrated in figure 5.2a. The inlet was imprinted on the generated mesh using the *topoSet* and *createPatch* utilities (OpenFOAM, 2020). An initial inspection of the generated flow field in the 2D simulations found that it calculated a counter-clockwise vortex in the centre of the reactor, as illustrated in figure 5.2b, which was qualitatively observed in the experiments. This gave us confidence that the simulation setup is reasonable and allowed us to move forward with the mesh refinement study. The mesh resolutions assessed for independency are described in table 5.2. The mesh independence simulations were recreating the “d1d2d3” diffuser experiments where each diffuser is aerating at a flow rate of 36 L/min or 0.6 L/s.

To assess if these simulations have reached a pseudo steady-state, an evaluation

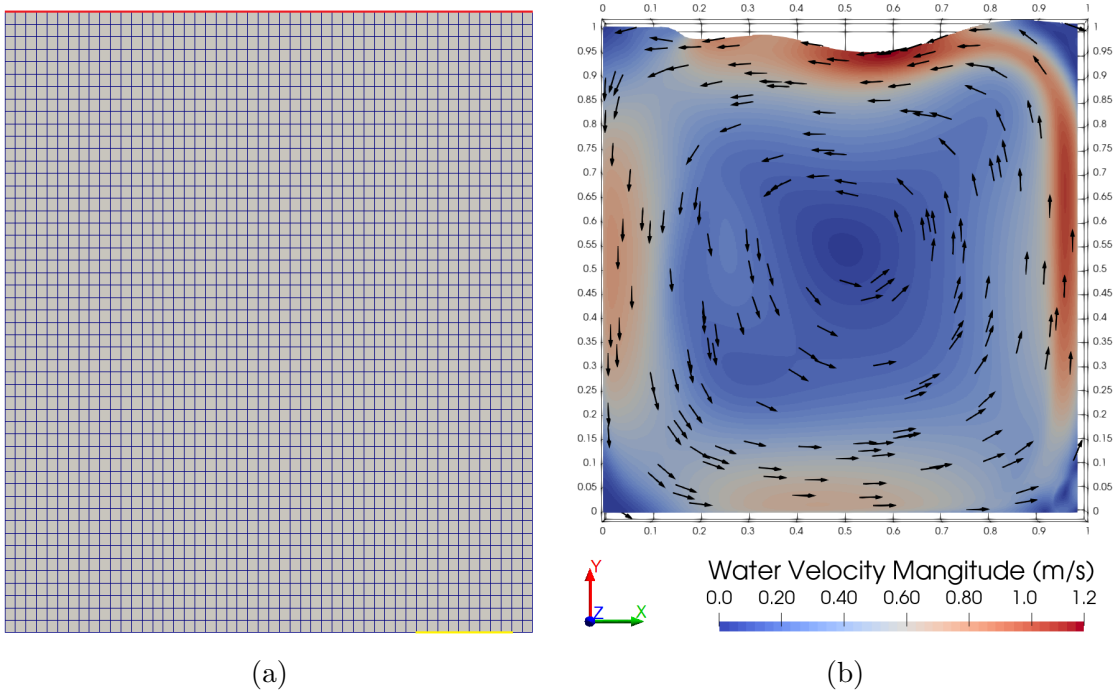


Figure 5.2: An example of the two dimensional aeration tank mesh with the inlet, marked as yellow, in the bottom right corner and outlet, marked as red, at the top (a) (This mesh is coarser than those used in the mesh refinement study for illustration purposes) and a water velocity magnitude contour and normalised vector plot for the 2D simulation at 0.6 L/s aeration flow rate (b).

Mesh number	Cell numbers
# 1	121 801
# 2	252 004
# 3	502 681
# 4	659 344

Table 5.2: Mesh resolutions assessed for independence of the 2D slice of the aeration tank.

of the average kinetic energy throughout the domain was made. As bubbles are released and rise up through the tank, energy is passed from the bubbles into the fluid through bubble-fluid interactions. This transfers energy to the fluid which eventually dissipates away due to resistance forces. If a steady-state has been reached in the fluid, then an equilibrium has been found between the induced and dissipated

energy in the system. The equation for the kinetic energy of the fluid is,

$$\frac{1}{2}m(\mathbf{u} \cdot \mathbf{u}) \approx \mathbf{u} \cdot \mathbf{u}. \quad (5.1)$$

As we are only interested in the change of energy, we only need to consider the fluid velocity as the kinetic energy only varies due to the velocity. Therefore, if we calculate $\mathbf{u} \cdot \mathbf{u}$ for the fluid in each cell and average over the cells throughout the domain, we can assess how the energy in the system changes over time for each simulation to provide an indication if a steady-state has been reached. The average $\mathbf{u} \cdot \mathbf{u}$ calculation was made at intervals of 20 seconds for the first 100 seconds and then every second from 100 to 220 seconds. The results for each mesh resolution are illustrated in Figure 5.3.

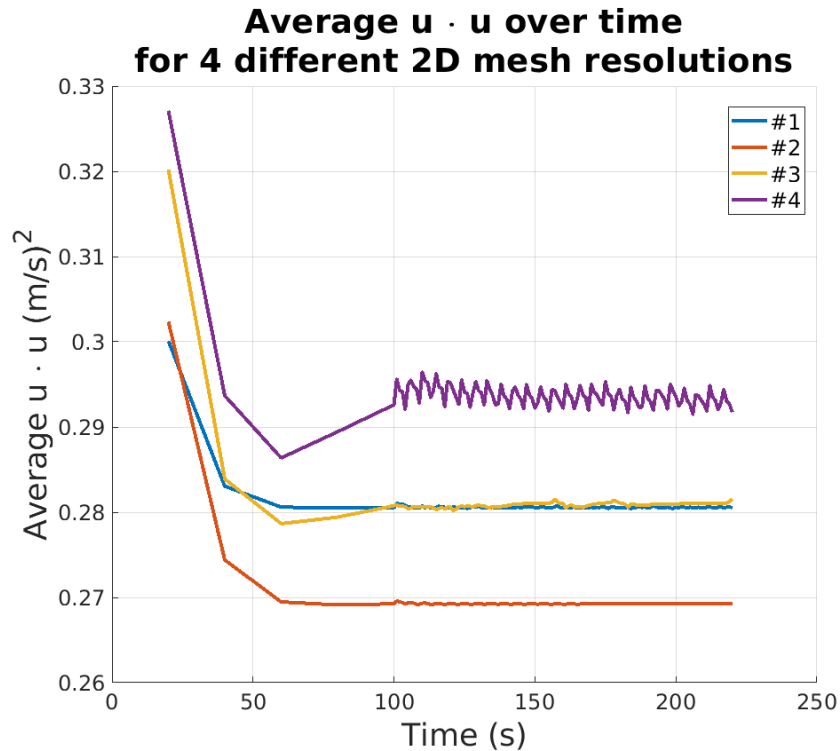


Figure 5.3: The average $\mathbf{u} \cdot \mathbf{u}$ for the four meshes over time.

After 100 seconds, the average $\mathbf{u} \cdot \mathbf{u}$ has reached an equilibrium between energy being induced and dissipated away for all four mesh resolutions. The flow is transient and so there can be smaller fluctuations at a local cell level which is the reason for the small periodic fluctuations at the later times in figure 5.3. However, we can

observe that the total energy in the water is not changing such that we can expect the fluid to be in a pseudo steady-state after ≈ 100 seconds. Therefore, a mesh refinement study can be conducted with confidence that the transient effects of the system are having minimal effects on the solutions. The study was conducted using the results obtained after 220 seconds to further minimise the transient effects (which was confirmed to be acceptable in §5.2.2). The velocity profiles for each mesh resolution along the reactor width and height at various heights and widths were calculated. Additionally, the “mesh error”, which is defined as the average of the differences between the velocity components along a profile for increasing mesh resolutions as described by the formula,

$$\text{Mesh error}_{ij} = \text{mean}(|\mathbf{u}_i - \mathbf{u}_j|), \quad (5.2)$$

where u is the designated velocity component profile being considered and i and j are the mesh numbers being compared where $i = j + 1$, was calculated to assess mesh independency, as illustrated in figures 5.4 to 5.6.

For the width profiles in figures 5.4 and 5.5, the rising y velocities profiles have very good agreement between all four meshes, with mesh number 3 and 4 having the best agreement. The rising y velocities are, on average, over a magnitude larger than the x velocities; therefore, the y velocities dominate the velocity magnitude profiles. As a result, the velocity magnitude profiles visually show the same agreement between the meshes as the y velocities. Analysing the mesh error plot in figure 5.4, the largest errors are calculated from the y velocity comparisons which implies that the y velocities see the largest difference between meshes. If we consider the mesh error between mesh 3 and 4, it approximately has the same mesh error as those comparing 3 to 2. This implies that the accuracy of the simulations is not improving with the increase in mesh resolution from 3 to 4; suggesting that mesh 3 can be used without loss of accuracy. If we consider the plots for the 63.5 cm height profiles in figure 5.5, the same analysis above applies for this profile as well.

If we consider the height profiles in figure 5.6, qualitatively the profiles match well with one another and better than the previous plots. The x velocities are, on average, of similar magnitude as the y velocities along the height profiles. If we consider the mesh error plot in figure 5.6, they do not converge to an error value as with the previous plots. This is due to the inclusion of the fluid surface and cells above. If we look at the figure 5.6 plots, the values near and above the fluid surface (at 1m) are very different for each mesh. This region of the simulation is highly dependent on the mesh resolution and simulation time due to it being an interface between phases. As a result, this will influence the mesh error calculation. However, for the majority of the bulk fluid, which is the region of most interest, there is qualitatively good agreement which is further backed up by the quantitative analysis from figures 5.4 and 5.5.

The aeration tank being modelled is a complex two-phase transient problem such that we expect the modelling choices to have a more dominant effect on the solution than the mesh at these resolutions. The 2D simulations are to be used as a testing case for comparing various modelling approaches against experimental data which requires multiple simulations to be run. At 500 000 cells, the simulation is already computational demanding for a 2D problem. Therefore, mesh 3 is a good compromise between a well resolved mesh whose resolution has minimal effect on the hydrodynamic solution that is still at a computational efficient resolution. As a result, mesh 3 at $\approx 500\,000$ cells has been adopted as the resolved mesh for the following 2D simulations.

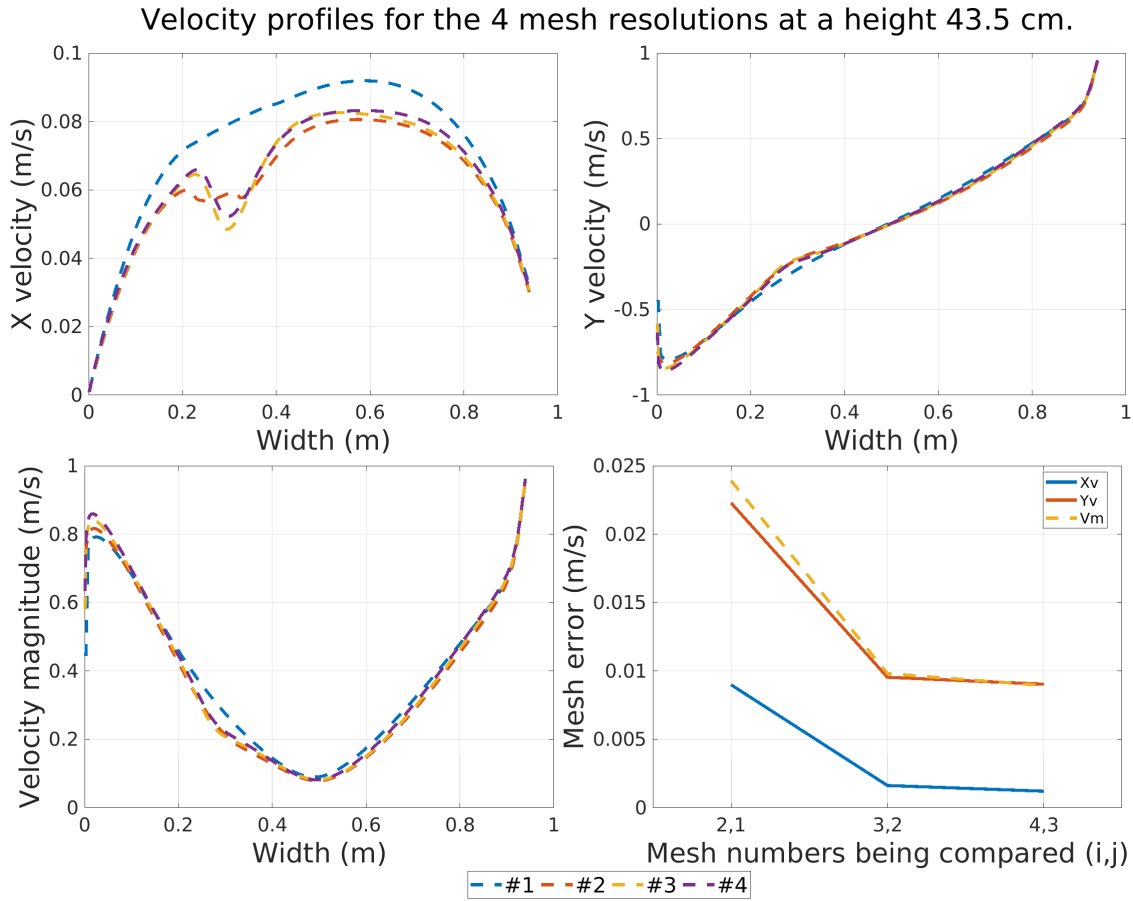


Figure 5.4: The velocity component profiles for the four meshes considered along the width at a height of 43.5 cm and a calculation of the mesh error, as described by equation (5.2).

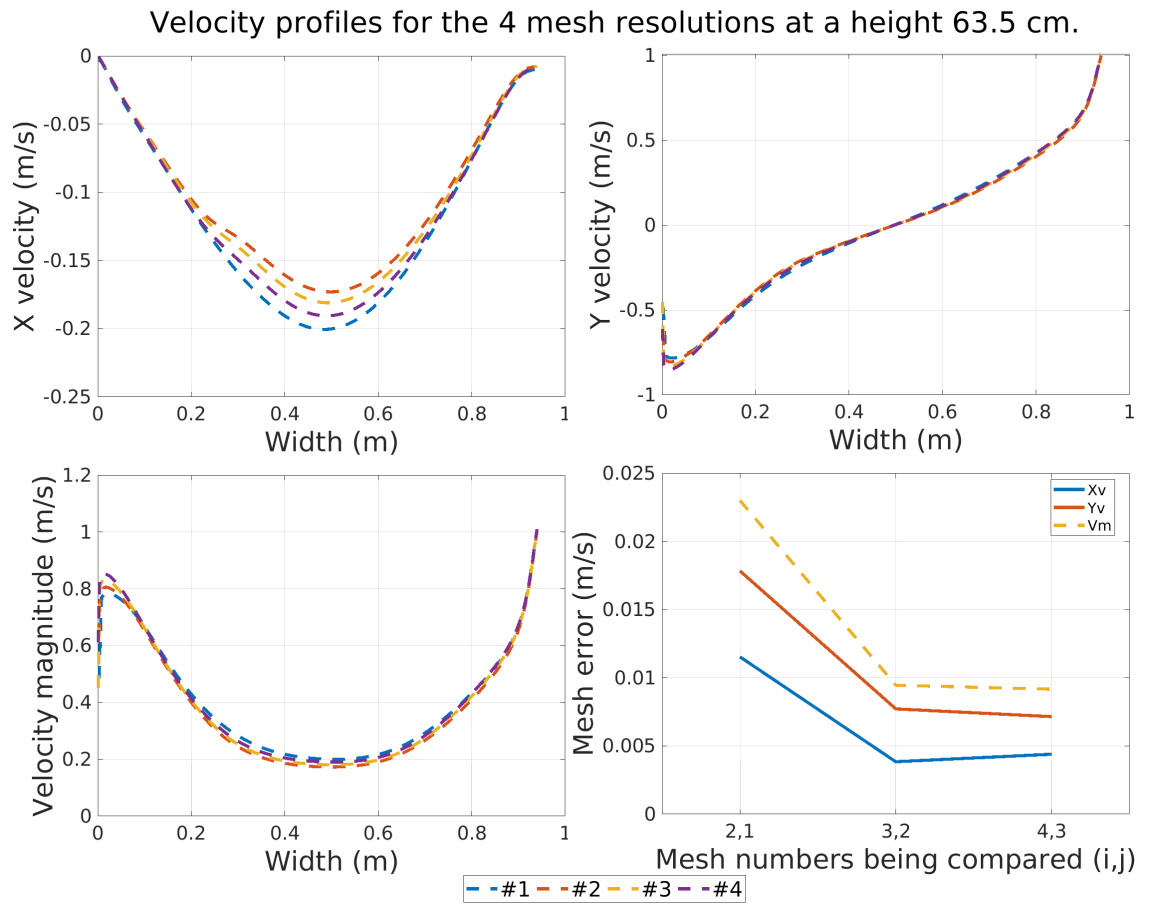


Figure 5.5: The velocity component profiles for the four meshes considered along the width at a height of 63.5 cm and a calculation of the mesh error, as described by equation (5.2).

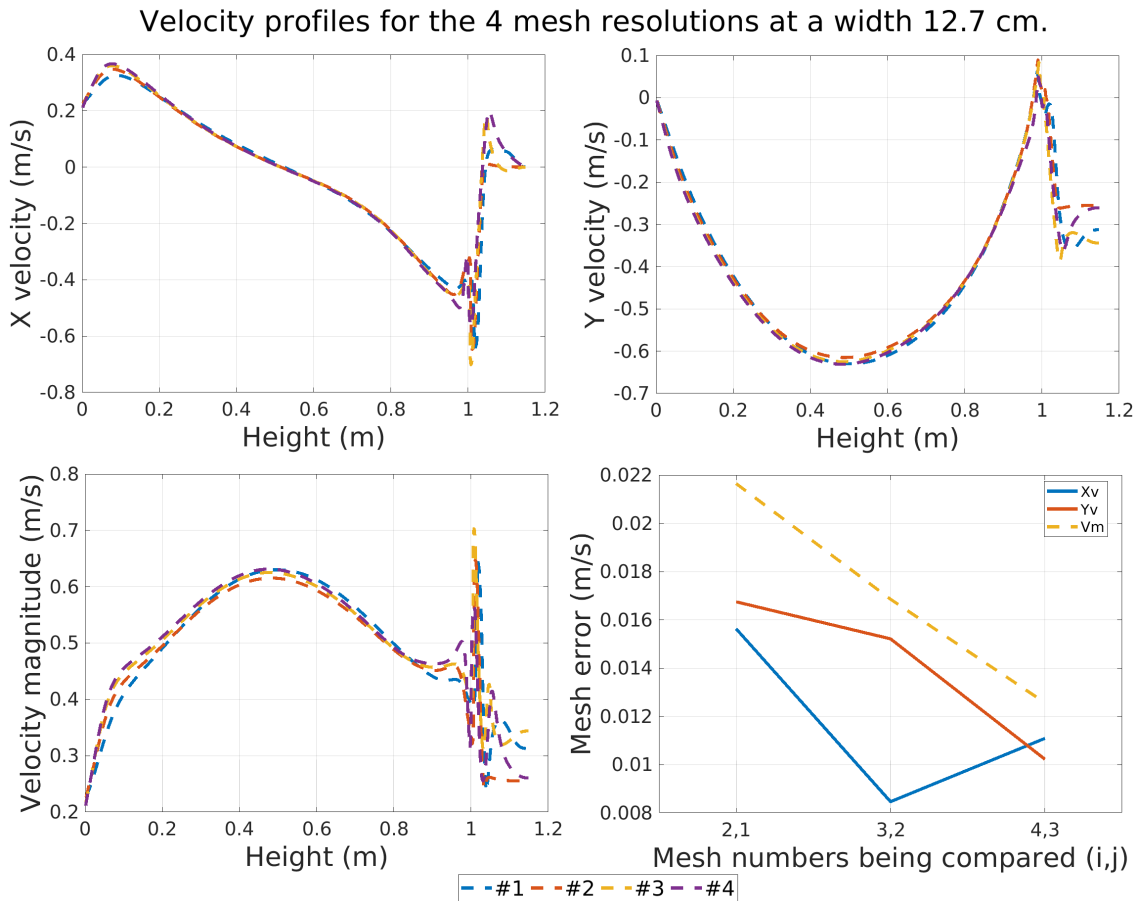


Figure 5.6: The velocity component profiles for the four meshes considered along the height at a width of 12.7 cm and a calculation of the mesh error, as described by equation (5.2).

5.2.2 Steady-state time analysis

The solver is transient and we want to find the time required for the hydrodynamics to reach a steady-state field in the 2D simulations so that we can compare the results to the experimental measured velocities. The analysis of the kinetic energy in figure 5.3 suggested that after 100 seconds, the 2D system is likely to be at a steady-state (or at a pseudo steady-state). To further assess this, a comparison was made of the simulation results for increasing time to fully verify if the simulations reach a steady-state after 100 seconds. Velocity component profiles were taken along the width of the tank at a height of 53.5 cm as well as up the height of the tank at a width of 85.3 cm for various run times. Additionally, the “time step error”, which is defined as the average of the difference between the velocity profiles of the

current time step solution and the final time solution at 220 seconds as described by the formula,

$$\text{Time step error}_{220,j} = \text{mean}(|\mathbf{u}_{220} - \mathbf{u}_j|), \quad (5.3)$$

where u is the designated velocity component profile being considered and j is the current time step being compared with the final 220 second time step, was calculated and plotted on a semi-log plot along the y axis to assess the error between the solutions. These results are presented in figures 5.7 and 5.8.

If we consider the large scale rising y velocities and velocity magnitude profiles in figures 5.7 and 5.8, we observe that they are qualitatively identical for all time periods. If we consider the x velocities in figure 5.7, these results are not qualitatively the same for all time periods. However, if we consider the time step error in figure 5.7, the error between time steps is larger for the y velocities which implies the qualitative visual differences between the x velocities are quantitatively smaller than the difference for the y velocities. The straight line in the time step error semi-log plot in figure 5.7 implies the time step error is converging. After 130 seconds the magnitude of the error is smaller than 10^{-3} , and after 160 seconds the error is close to 10^{-4} . When we consider the size of x and y velocities in figure 5.7, the majority of the velocities are of order 10^{-2} or above which implies the errors are between 1 and 2 magnitude smaller.

If we consider the plots in figure 5.8, each profile visually looks identical which qualitatively informs us that the solutions is not changing much. If we consider the time step error for the figure 5.8 profiles, after 100s, they have an average size of 10^{-3} and they are all smaller than 10^{-2} . The larger time step errors for these plots can be accounted for by the inclusion of the fluid surface and above as the fluid surface is more influence by the transient behaviour of the simulations compared with the bulk fluid. Overall, the magnitude of the x and y velocities are around 10^{-1} which are between 1 and 2 magnitudes larger than the time step errors. As the time step error are between one and two magnitudes below the predicted velocities, this

implies that the predictions are not changing in value after 160 seconds such that we can assume the simulations have reached a steady-state after this time period. This study only considered the fastest aeration flow rate at 0.6 L/s. It is assumed that the faster flow rate creates more turbulence and so takes longer to reach a steady-state such that this calculated length of time for a steady-state to be reached is valid for the slower 0.3 L/s flow rate. Mesh independence has been shown and a time period for the simulation to reach a steady-state has been found. Therefore, the 2D simulations can be used to investigate the modelling choices for replicating the experimental aeration tank.

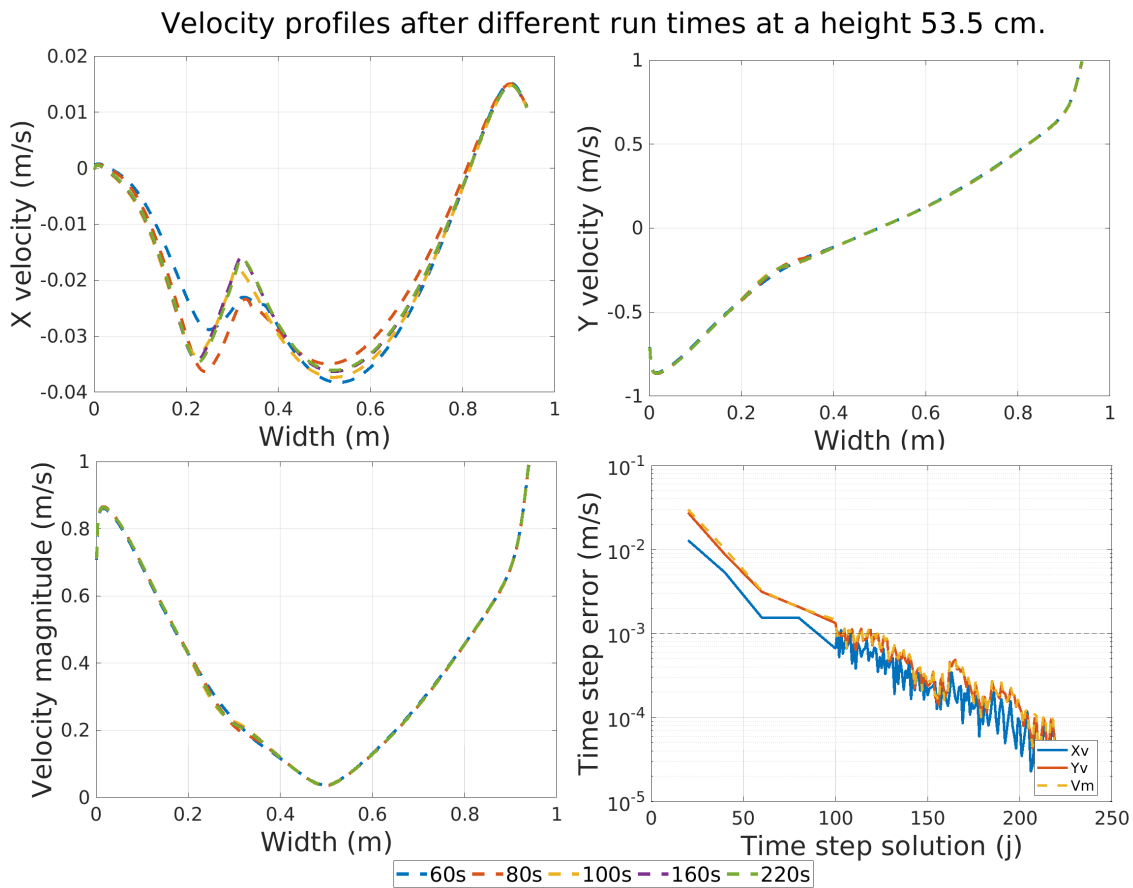


Figure 5.7: The velocity component profiles solutions after different run times along the width at a height of 53.5 cm with a calculation of the time step error as described in equation (5.3).

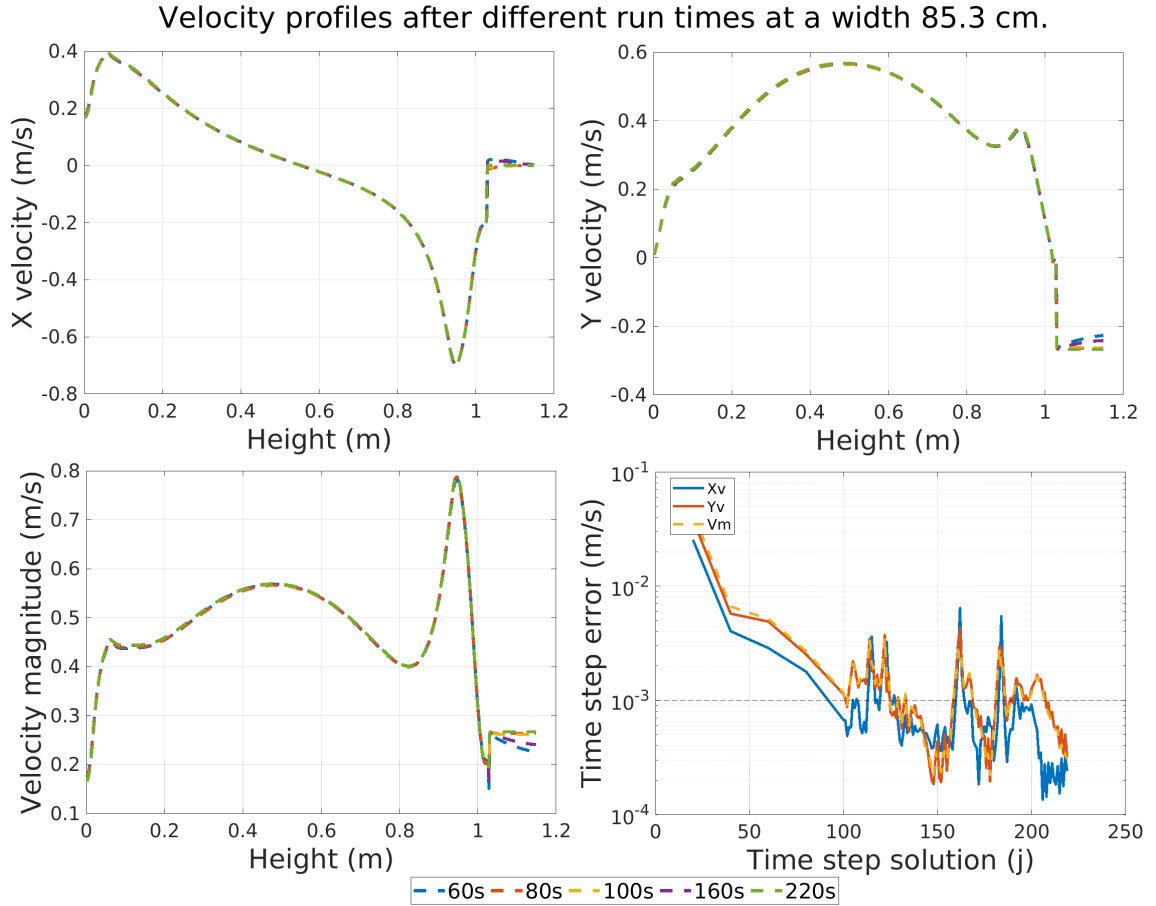


Figure 5.8: The velocity component profiles solutions after different run times along the height at a width of 85.3 cm, the centre of the pumping diffuser, with a calculation of the time step error as described in equation (5.3).

5.2.3 Inlet boundary condition sensitivity study

The experimental rig pumps air through membrane diffusers to create a continuous stream of bubbles into the reactor. The bulging of the membrane under pressure has been neglected and a horizontal velocity inlet has been used in the model to reduce the problem complexity. As the membrane bulges under air pressure, the holes in the membrane expand and open up to allow air to pass through, but, it is not known how many holes expand and by how much. However, we can assume that sum of all the holes add up to a fraction of the total diffuser area. To replicate this in our simulations, the air volume fraction entering through the inlet can be varied, for example an air volume fraction of 1 entering would be equivalent to having no

membrane while an air volume fraction 0.5 would imply 50 % of the membrane surface area is occupied by holes. However, to conserve the air flow rate entering through the inlet, the horizontal velocity applied at the inlet needs to be increased as the air volume fraction is decreased. The relationship between the inlet velocity and the membrane area, and air volume fraction is described in figure 5.9 for the 0.6 L/s flow rate with a membrane area, $A = 0.0254 \text{ m}^2$, as used in the experiments.

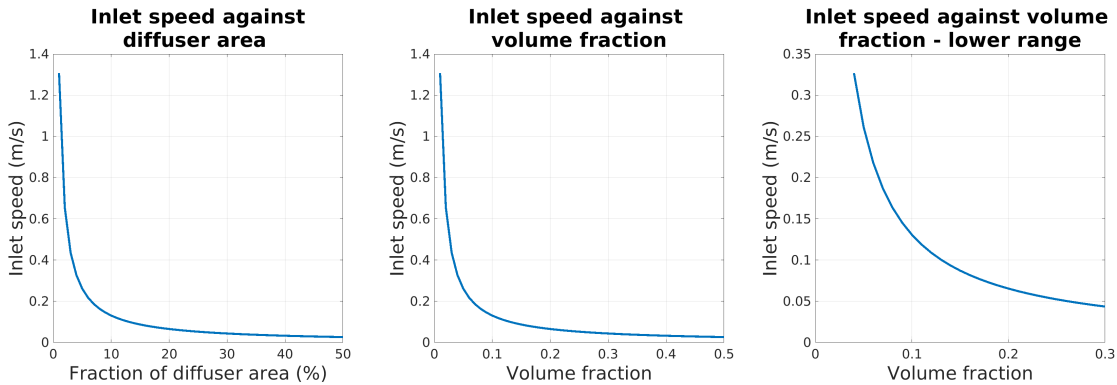


Figure 5.9: The relationships between the inlet speed and the membrane diffuser area and air volume fraction for a diffuser membrane of surface area $A = 0.0254 \text{ m}^2$ and air flow rate of 0.6 L/s or $6 \times 10^{-4} \text{ m}^3/\text{s}$.

The correct area fraction required to account for the holes is not known; therefore, an investigation into how the inlet velocity-volume fraction coupled boundary condition effects the simulation results needs to be conducted. Additionally, there are two approaches for modelling the inlet condition in the 2D simulations. First, if we assume that the 3 aerating diffuser tank can be simplified, for modelling purposes, to 1/3 of the tank with a single diffuser when considering the 2D case, as shown in figure 5.10a, then the inlet condition of the 2D reactor can be modelled in two ways as described below.

The 2D simulations are attempting to replicate the 2D flow field in a slice through the centre of a diffuser in the 3D geometry, as illustrated by figure 5.10b. This is achieved by applying a symmetry wall condition on either side of the 2D geometry which implies that the actual geometry being modelled in the 2D simulation is illustrated by figure 5.10c. In this case, the rectangle diffuser has a greater surface area than that of the circular diffuser in figure 5.10b such that, if we apply

the same flow rate through the rectangular inlet, the velocity at the inlet is slower. Therefore, a choice for the inlet velocity needs to be made between: conserving the flow rate such that inlet speed is slower compared with the inlet speed in the 3D simulations, which will be referred to as the *conserved flow rate approach*; or to conserve the inlet speed such that the horizontal inlet speed matches those applied in the 3D simulation, which will be referred to as the *conserved inlet velocity approach*; however, this results in a higher aeration flow rate being modelled when we consider that the rectangular diffuser is being modelled in the 2D simulations, as illustrated in figure 5.10c.

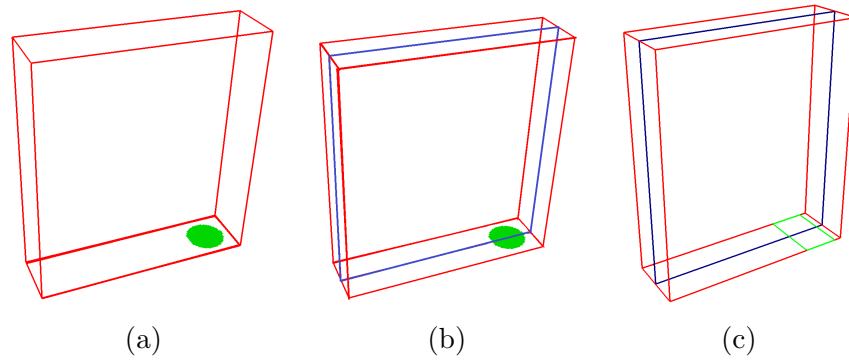


Figure 5.10: Illustration of how the 2D simulation are derived and to show and explain the two modelling approaches: *Conserved inlet velocity approach* (b) and the *conserved flow rate approach* (c), for the 2D inlet condition.

An inlet condition study was conducted to investigate the coupled behaviour of the inlet velocity and volume fraction and the impact of choosing the *conserved flow rate* or *conserved inlet velocity* approach for modelling the 2D velocity inlet to find an optimal procedure for modelling the inlet condition. The range of velocities and volume fraction ratios considered for the two “conserved” approaches are presented below in table 5.3 for a 0.6 L/s aeration setup. The results from this study are compared with the 2D experimental data, as described in §3.6, for both conserved approaches which are presented in figures 5.11 and 5.13, respectively. The plotted experimental data also included an error bar which is the standard deviation from the 2 minute time averaging of the measured velocities to provide context to how much the velocities varied over the measuring period.

Area Fraction (%)	Air Volume Fraction	Inlet Velocity (m/s)	
		<i>Conserved inlet velocity approach</i>	<i>Conserved flow rate approach</i>
40	0.4	0.0589	-
30	0.3	0.0786	-
20	0.2	0.118	0.0654
10	0.1	0.236	0.131
5	0.05	-	0.261
4	0.04	0.589	-
1	0.01	2.36	1.31

Table 5.3: The inlet velocity and volume fraction ratios investigated for the two inlet modelling approaches for a flow rate of 0.6 L/s.

We will first consider the results from the *conserved inlet velocity approach* in figure 5.11. The error bars for the experimental data are the standard deviation from the 2 minutes time averaging. The first thing to observe in figure 5.11 are that the plots are all different which implies that the velocity-volume fraction ratios do impact the generated flow field for the *conserved inlet velocity approach*. There is a pattern in the behaviour of the profiles where the 1 % ratio profile moves towards the 20 % profile as the percentage increases. Then, as the ratio increases pass 20 %, the 30 and 40 % profiles shift back towards the 1 % profile. This results in the 10 and 30 % ratio values producing very similar behaviour. This behaviour may be due to the amount of entrained air for the different ratio values as the amount of entrained air can influence the velocity field. If we analyse the air volume fraction plots for the different ratio values in figure 5.12, all simulations predict a portion of air entrainment into the bulk fluid flow, as was observed in the aeration experiments. The size of the entrainment region for the 1 and 40 % and the 10 and 30 % ratio values are similar which explains why those profiles are similar to one another. Comparing all the plots, the 20 % ratio value produces the largest region of air entrainment. An assessment of the velocity profiles against the experimental data in figure 5.11 finds that the 20 % ratio value matches best compared with the others which implies the large region of air entrainment is an important feature

of the experimental aeration tank. Additionally, this transitional behaviour over the 1 - 40 % ratio values implies that, around the 20 % ratio value, there is a unique equilibrium between the strength of the flow field driving bubbles down and the buoyancy of the entrained bubbles trying to rise back up such that this ratio value produces the largest region of air entrainment. The difference in the amount of entrained air may be because, at lower ratio values, the bubbles will be forced down lower into the tank due to the higher velocity values which results in larger buoyancy forces because they are deeper in the tank. This results in the entrained bubbles rising faster which reduces the chances of them staying entrained. In the larger ratio values, the velocities are too low to drive the bubbles down low enough to stay entrained and most just escape instead.

Further inspecting how the profiles in figure 5.11 match with the experimental data, the y velocities and velocity magnitudes profiles follow and lie within most of the experiments measured points, especially for the 10, 20 and 30 % ratio values. These ratio values correctly predict the large vortex flow field with negative and positive velocities on the left and right sides of the reactor, respectively. It is important to note that the y velocities dominate the velocity magnitude calculation as they are larger than the x velocities such that if the y velocities match well so do the velocity magnitude plots. The simulations calculate large y velocities near the left wall of the reactor, around -0.8 m/s; larger than the nearby measured experimental data points. This is expected due to the 2D nature of the simulations and the fluid surface. As the simulations are confined to a 2D slice of the reactor, the fluid flow can not disperse along the third dimension which results in the fluid surface being forced downwards along the left wall as it moves from the right to left, causing a large spike in the y velocities which is not seen in the experimental data. This is a flaw in the 2D methodology when comparing with pseudo-2D experimental data as the extra dimension plays an important role in dispersing and dissipating the energy in the reactor. However, the profiles do match reasonably well with the other experimental points.

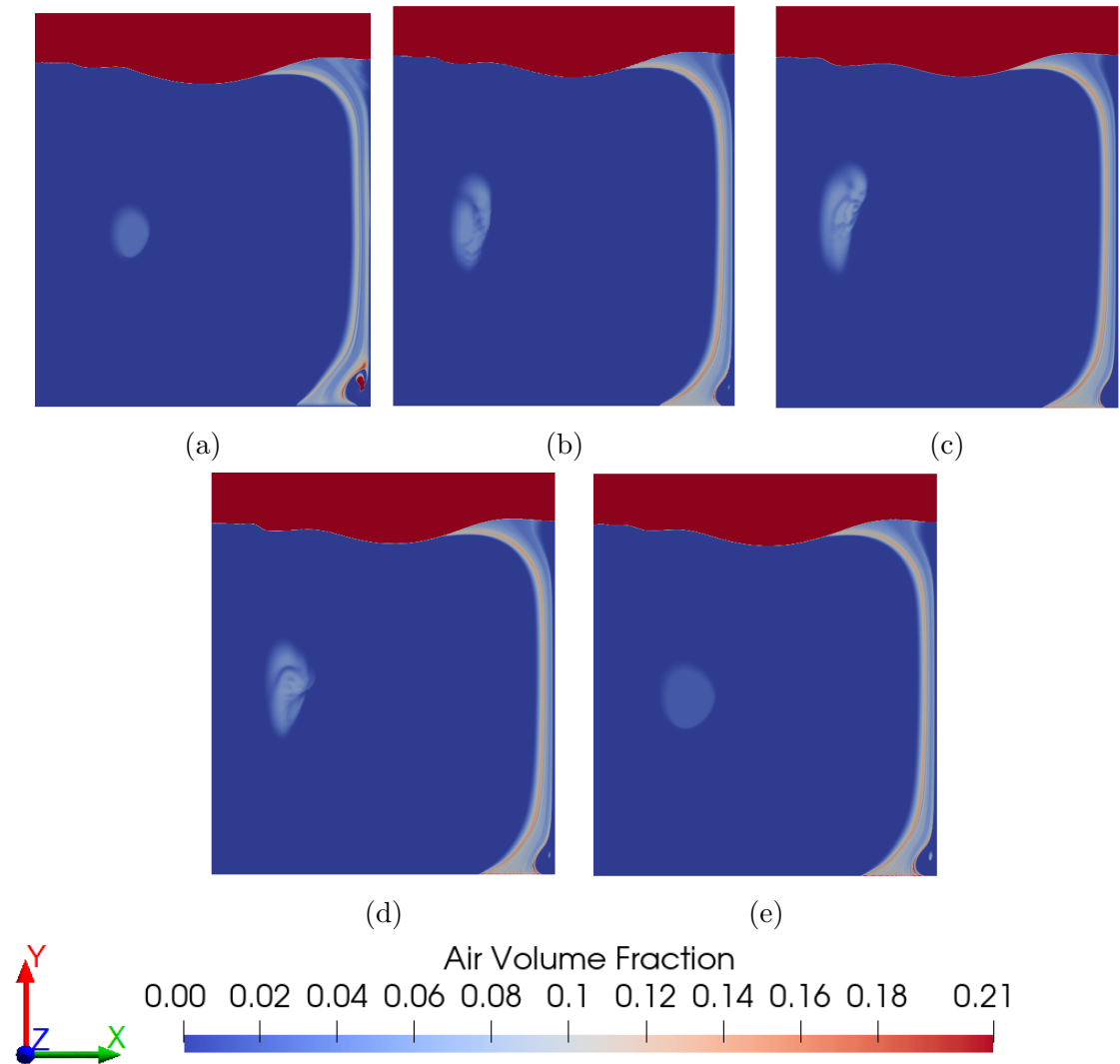


Figure 5.12: Air volume fraction profile after 160 seconds for the *conserved inlet velocity approach* with velocity-volume fraction ratios of 1 % (a), 10 % (b), 20 % (c), 30 % (d) and 40 % (e).

If we consider the smaller x velocities profiles, the simulations predictions pass through the error range of most of the experimental data points. The large error size of the x experimental velocity values suggest that the vortex centre in the flow field shifts around over the two minute period. However, what is most important are if the velocities are positive or negative for each height profile as these can inform us of where the vortex centre approximately lies. At heights 43.5 and 53.5 cm, the simulation calculates a smaller velocity compared with the experimental mean x velocities. At height 63.5 cm, the simulations calculate negative x velocities which implies the flow is moving from right to left; in comparison the experiments still

predict mostly positive x velocities implying the fluid is still moving to the right. This difference suggests that the centre location of the vortex loop in the simulations is lower compared with the experiments. The simulations predict the loop centre is between 53.5 - 63.5 cm due to changes in the sign of the x velocities which is approximately the region of height where the entrained aired was observed for the different ratio values in figure 5.12. In comparison, the experimental results suggest the vortex centre is higher than 63.5 cm.

Overall, the simulation predictions match reasonably well with the measured velocities and does predict a vortex structure in the reactor. The predictions suggest a lower centre position for the vortex than the experiments data suggests but most of the values lie within the error bars of the experimental data. Additionally, the 20 % ratio value for the *conserved inlet velocity approach* matches the best with the experimental data.

If we now consider the *conserved flow rate approach* in figure 5.13, the ratio values have very little impact on the calculated fluid velocities. The profiles are all very similar to the *conserved inlet velocity approaches* 1 and 4 % profiles in figure 5.11. The *conserved flow rate approach* calculates a more linear y velocity profile which does not match well with the experimental data which is, therefore, also the case for velocity magnitude profiles.

In conclusion, the *conserved velocity inlet approach* matches much better with the experimental data compared with the *conserved flow rate approach* and, therefore, is recommended for modelling the 2D velocity inlet. Additionally, the 20 % ratio value is found to match best with the experimental data and, therefore, is chosen as the velocity-volume fraction ratio value to be used for the concurrent and future 2D and 3D simulations.

Inlet boundary condition analysis for the conserved flow rate approach at various heights.

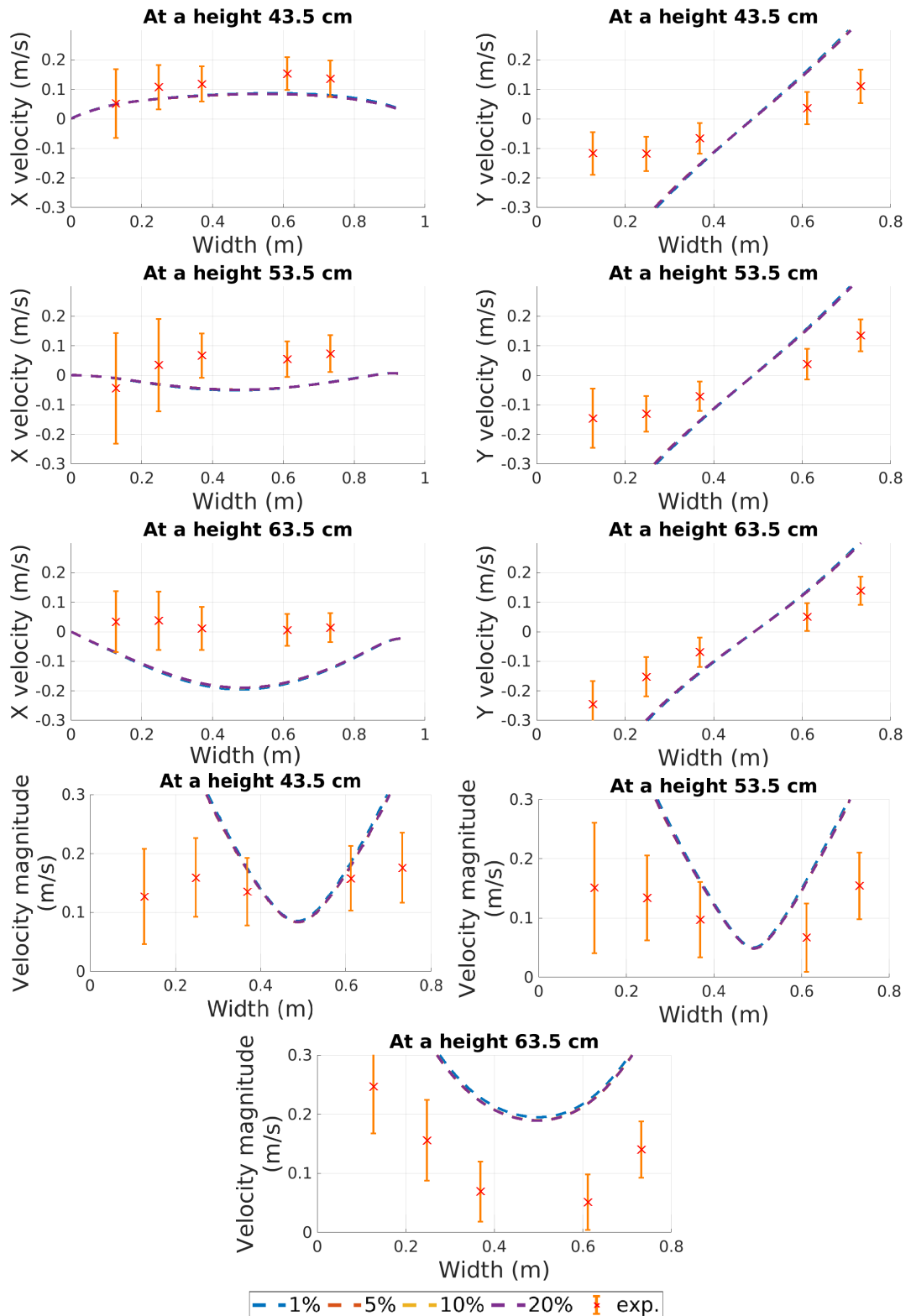


Figure 5.13: Velocity plots for different velocity-volume fraction ratios, as defined in table 5.3, for the *conserved flow rate approach*.

5.2.4 Bubble size study

The bubbles produced by the membrane diffuser are created with diameters in a range of 1 - 4 mm. The bubbles drive the fluid to generate the flow field and the momentum transfer between air and water for a given flow rate is dependent on the bubble size. Generally, larger bubbles will reach a higher rise velocity compared with smaller ones due to larger buoyancy forces (as described in §4.5.3) and, therefore, should provide a larger momentum transfer to the fluid and increase the fluid velocities and rate of mixing. However, for a given flow rate, producing smaller bubbles increases the total bubble surface area available. Oxygen mass transfer into the fluid only occurs at the interface between air and water. Therefore, larger bubble surface area improves the rate of oxygen transfer into the liquid which is important for the biological processes. Additionally, momentum transfer between the air and water only occurs at the bubble's surface. While larger bubbles have a greater potential momentum transfer due the higher rise velocities, smaller bubbles will transfer their momentum faster and more uniformly. Furthermore, the lower rise velocities results in the bubbles spending longer in the fluid which provides them more time to transfer their momentum and mass ([Zimmerman et al., 2008](#)).

In general, using smaller bubbles does not significantly reduce the momentum transfer and, if both momentum and mass transfer are of interest; which is the case in aeration tank, the smaller bubbles are the more desired operation condition. The creation of fine membrane diffusers, as used in this aeration tank, is an example of an engineering technique to create bubbles at the milli-scale that is optimising the momentum and mass transfer potential for a given volume of air. However, producing bubbles efficiently at these scales or lower is significantly more difficult and costly, although, recent engineering techniques have been developed to create bubbles at the micro-scales at an efficiency rate that is potentially suitable for full-scale use ([Zimmerman et al., 2009](#)).

The initial simulations have used a Sauter mean diameter value of 2.5 mm which

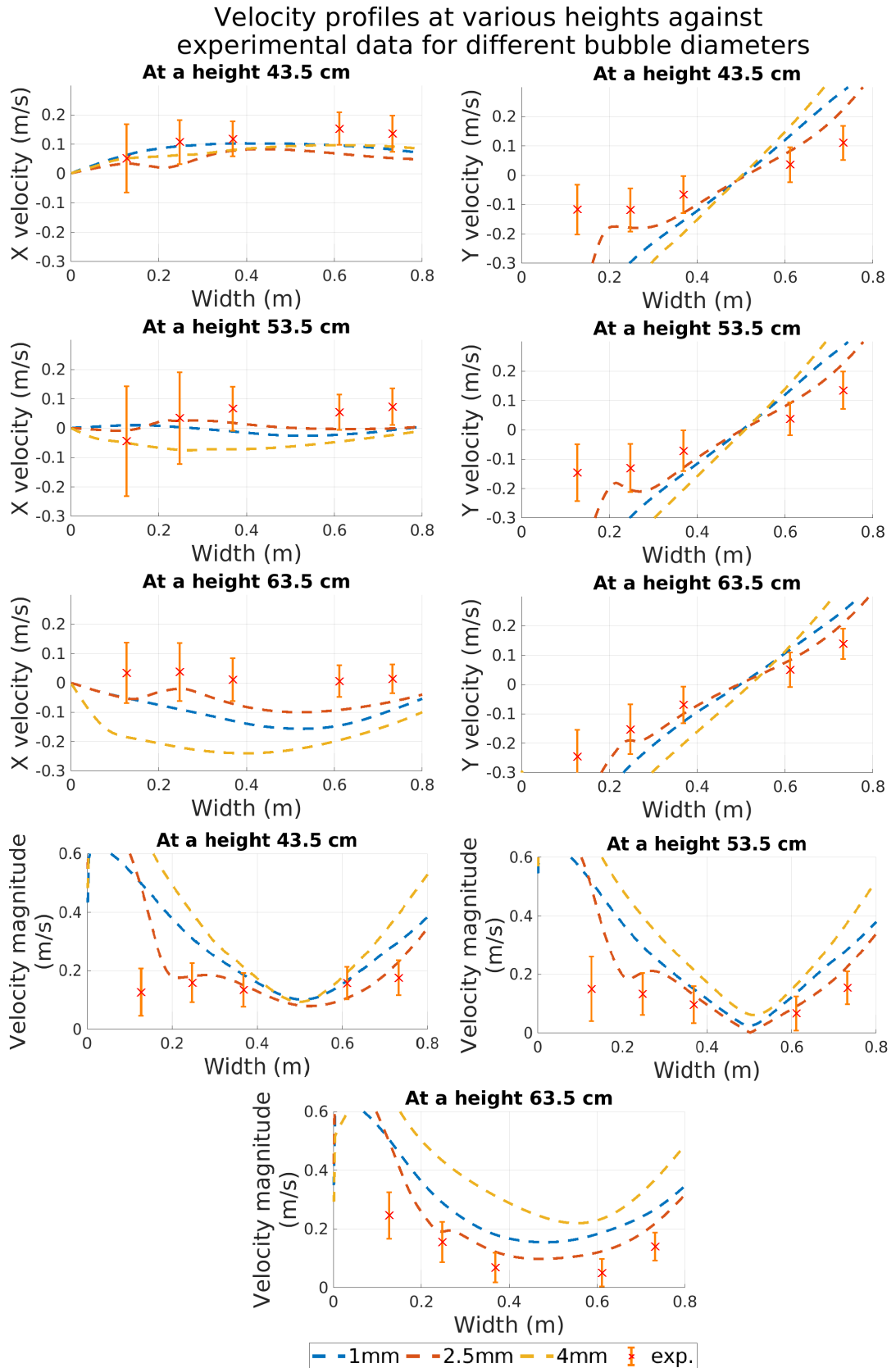


Figure 5.14: Analysis of the impact of bubble size on simulation results alongside experimental data to evaluate the bubble size modelling approach.

lies in the middle of the described 1 - 4 mm range defined in the membrane diffuser manual (xylem, 2020). To investigate the effects of bubble size on the calculated flow field, simulations with a Sauter mean diameter of 1 and 4mm, the upper and lower limits of the range, were also run along with the 2.5 mm simulation and compared with experimental data to find the optimal diameter value. The 2D simulations were run with the Schiller-Naumann drag model, which assumes the bubbles are spherical, and the virtual mass model for an air flow rate of 0.6 L/s. The results are presented in figure 5.14.

It is found that the three different bubble diameters create slightly different flow fields. The y velocities and velocity magnitude profiles for the 1 mm diameter simulation are smaller and more linear compared with the other two diameters. The profiles are more linear because the smaller bubble diameters have a more uniform momentum transfer and the maximum velocities near the right wall are smaller because the maximum rise velocity is lower for the smaller bubbles. The 4 mm diameter simulation has the largest rise velocities near the right wall due to the increased buoyancy forces from their larger size. Near the left wall, the 2.5 and 4 mm diameter simulations have very similar maximum velocities which implies that the momentum being transferred across the fluid surface and into the reactor is the same for both the diameters, even though the velocities are higher along the right wall for the 4 mm diameter simulation. The x velocity profiles for all three diameter simulations differ. The difference implies that the centre location of the vortex loop is not the same for each simulation. If we compare the results with the experimental data, all the y velocities and velocity magnitude profiles as well as the x velocities profiles at height 53.3 and 63.5 cm for the 2.5 mm diameter simulation are most compatible with the experimental data, while x velocities at a height of 43.5 cm match more closely with the 1 mm diameter simulation. Overall, these results imply that the 2.5 mm diameter is the better choice for modelling the bubble diameters which is predictable as 2.5 mm is the middle value from the potential range of diameters created by the membrane diffusers from the manufactures (xylem, 2020)

and qualitatively matches with the observations in the aeration tank. Therefore, a bubble diameter of 2.5 mm has been used for the diameter in the future simulations.

5.2.5 Bubble-water dynamic force models

The bubbles are the main driver for generating the flow field in the aeration tank as they interact and rise through the fluid. To correctly model the bubble effects in the fluid, micro-scale bubble-water dynamic force models are required to re-create the physical behaviour observed. These models include the drag, lift, virtual mass, wall lubrication and turbulent dispersion models, as described in §4.6. Studies of each of these models were conducted and compared with the experimental data to assess their influence on the simulation results and evaluate if they improve the solution. The goal of these studies is to conclude the best modelling choices for modelling the bubble-fluid interactions and to exclude forces that are negligible or reduce the accuracy of the simulations in the aeration tank. The experimental data points incorporated in these studies included a standard deviation error from the time averaging to give insight into the distribution of velocities measured during the 2 minute recording period.

Virtual mass

The virtual mass force accounts for work done by the bubbles to accelerate the surrounding liquid. The default simulation setup used the Schiller and Naumann drag model and virtual mass force with coefficient $C_{VM} = 0.5$ which is the base setup that has been used for the previous studies above. [Dhotre and Smith \(2007\)](#) found that the virtual mass model was useful for simulation stability by limiting the bubble acceleration while [Colombo and Fairweather \(2015\)](#) stated that it has little effect on the simulation dynamics and can be neglected. A comparison of the velocity results from simulations using the Schiller and Naumann drag model with and without the virtual mass force is presented in figure 5.15 along with the experimental data. The

difference between the two modelling choices for all the velocity profiles is small but they are not zero which implies the virtual mass force does impact the results. The simulation that included the virtual mass model matched the experimental data better, especially for the velocity magnitude profile at a height of 63.5 cm, in almost all the velocity profiles compared to the simulation without the virtual mass model. While the differences between the two models are small for each plot and individually could be seen as negligible, the total combination of all these improvements sums to an amount that is not negligible and implies that the virtual mass model is likely improving the reliability of the simulations. Therefore, future simulations will include the virtual mass force.

Drag model

The drag model describes the resistance a bubble feels as it rises through a fluid and is important for describing the dynamics of rising bubbles and modelling the transfer of momentum between bubbles (Roghair et al., 2011). The different drag models describe the definition used to model the coefficient of drag in the drag force formulation. In this study, the default Schiller-Naumann drag model, which assumes spherical bubbles and relates the drag coefficient to the Reynolds number §4.6, and the Tomiyama drag model, which also relates the coefficient to the Reynolds number but also accounts for bubble deformity in the coefficient formulation by including the Eotvos number §4.6, are compared with one another and the experimental data to assess the drag coefficient modelling approach, as illustrated in figure 5.16.

There is very little difference between the results of the two drag models. The y velocities and velocity magnitude are almost identical, with only minor differences in the size of the velocities near the left wall. The x velocities are also very similar with the biggest difference at a height of the 63.5 cm. This suggests that, when comparing the formulation of the drag coefficient for the two models in §4.6, they have similar values. The calculated Reynolds number in the bubble plume where the drag force is most important was calculated to be around $Re = 2200$. This implies

Virtual mass force analysis for flow rate 0.6 L/s
at various heights against experimental data

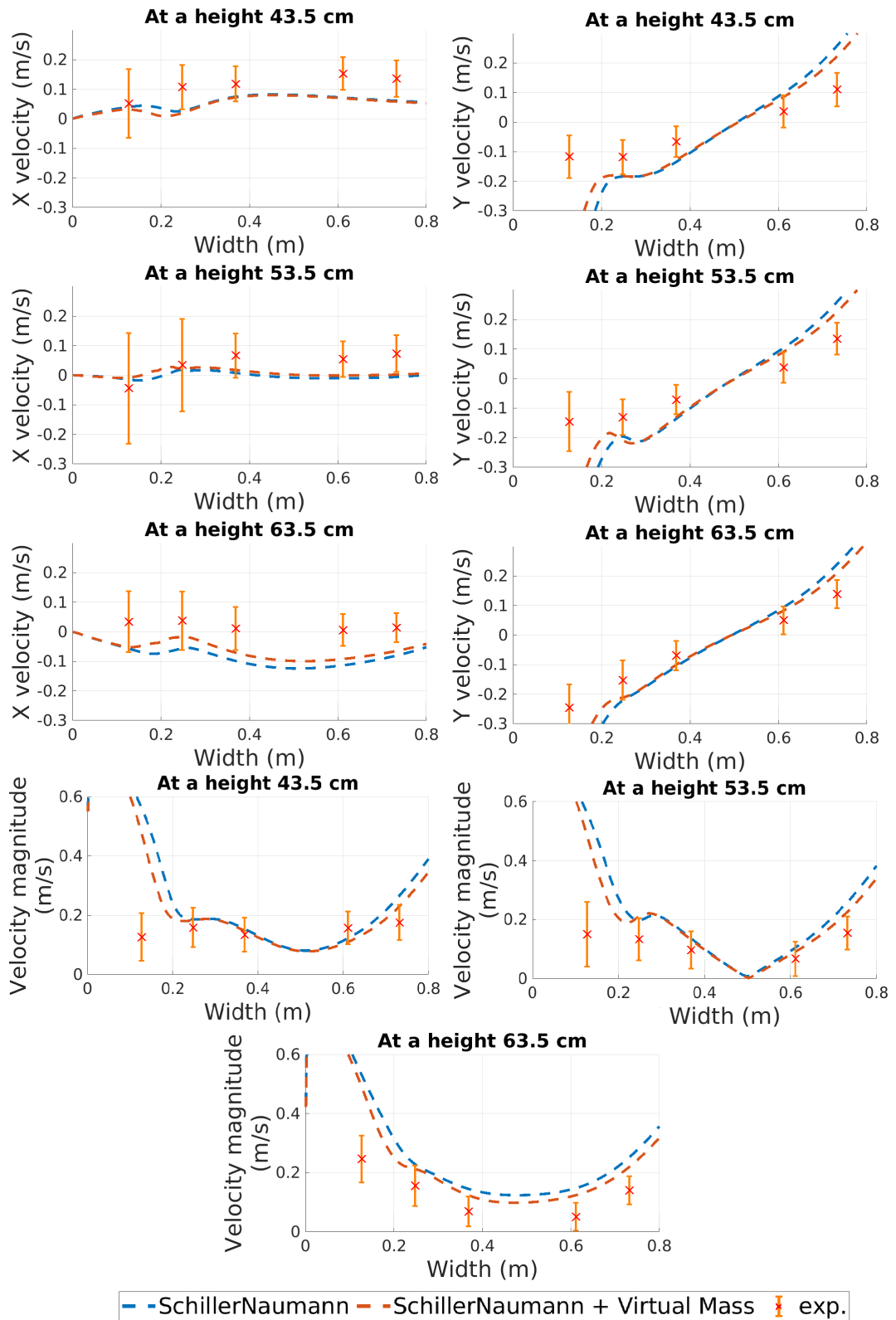


Figure 5.15: Analysis of the virtual mass force model against experimental data to assess the modelling choice.

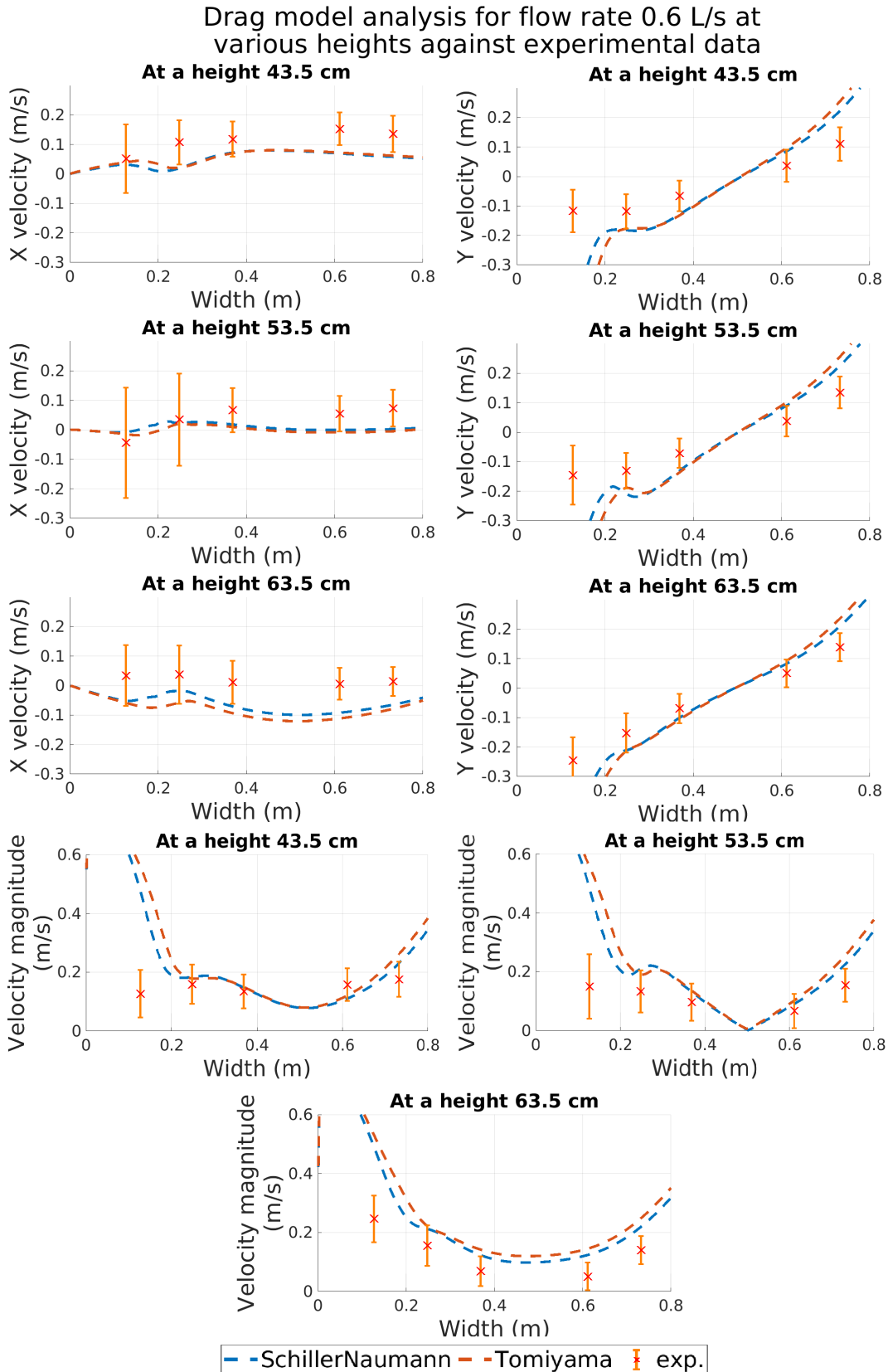


Figure 5.16: Velocity plots of Schiller-Naumann and Tomiyama drag models against experimental data to assess the modelling choice.

a constant coefficient of 0.44 for the Schniller-Naumann drag model. In comparison, for the same Reynolds number the Tomiyama drag model coefficient formulation, with a turning factor of $\beta = 1.0$ and calculated $E_o = 0.872$ for the bubbles in the aeration tank, simplifies to,

$$C_D = \frac{8}{3} \frac{E_o}{E_o + 4} = 0.477,$$

which is almost identical to the Schniller-Naumann coefficient value and explains why the two models are almost identical. Additionally, this slight change in the coefficient for the Tomiyama model results in the simulation not matching as well with the experimental data compared with the Schniller-Naumann model. Therefore, as the Schniller-Naumann model is more accurate and computationally less expensive compared with the Tomiyama formulation, the Schniller-Naumann drag model is recommended and has been adopted as the drag model for future simulations.

Wall lubrication model

As bubbles pass near side walls, the fluid between the wall and the bubbles moves slower than the fluid region between the bubbles and ambient fluid. This causes a pressure difference that pushes bubbles away from the walls and reduces the problem of a peaked volume fraction near the side wall. The [Antal et al. \(1991\)](#) wall lubrication force with fixed constant coefficients, $C_{w,1} = -0.055$ and $C_{w,2} = 0.09$, which has been used in [Rzehak and Krepper \(2013a\)](#) and [Colombo and Fairweather \(2015\)](#), and described in §4.6 was implemented into the Schniller-Naumann drag and virtual mass model simulation to investigate the wall force effects on the results. These findings are presented in figure 5.17 along with the experimental data.

In the y velocities and velocity magnitudes profiles, the effects of the wall force on these velocities is small with minor differences between the simulation results near the left wall. In the x velocities, the wall force causes slightly more positive x

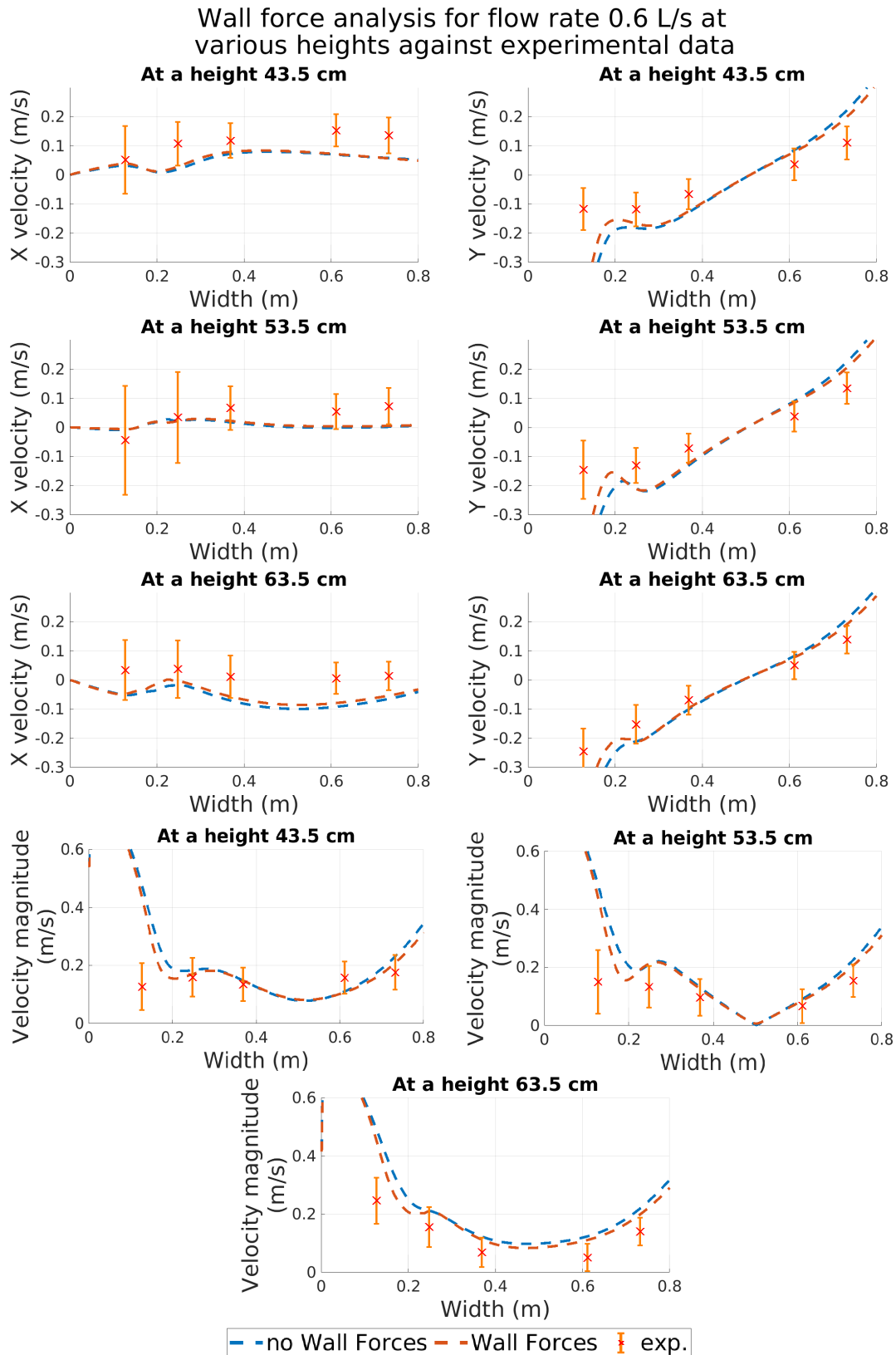


Figure 5.17: Analysis of the wall lubrication model against experimental data to assess the modelling choice.

velocities for all heights. While the differences between the results are smaller than previous models, if we compare the wall force model results to the experimental data, the wall force simulation matches better with the experimental data than without the model. The aeration tank design has the bubble diffusers near the side walls which has been observed to influence the bubble plume behaviour. The wall force aims to model the physical behaviour a bubble would experience when near a wall. When comparing the two simulation results, this has a very small effect on the calculated hydrodynamics; however, it does result in the velocities matching better with the experimental data for all 9 velocity profiles. Therefore, although the difference is small, the wall force will be included in future simulations.

In this study the wall force has had a positive effect on the results because the rising bubbles in this aeration tank are near the side walls and, therefore, the wall effects are important in the calculation of the hydrodynamics. However, in another aeration tank where the diffusers are away from the walls, the wall force may have no effect on the results. Therefore, the geometry of the aeration tank should be considered to assess if the side walls would impede on the hydrodynamics before deciding to include the wall force model.

Summary

Additional studies were conducted for the lift and turbulent dispersion force. The non-lift simulation matched the experimental data significantly better than the lift model cases where the lift model over-predicted the magnitude of the velocities throughout the domain. As a result, the lift model was not included in the simulations. Additionally, the turbulent dispersion force model created stability issues and matched the experimental significantly worse such that it was not included as a result. These findings can be found in the appendix in sections 8.3 and 8.3.1, respectively. In conclusion from this bubble-water dynamic force study, for modelling the bubble forces in this aeration tank it is recommended to use the the Schiller-Naumann drag model ([Schiller and Naumann, 1935](#)), the virtual mass force

with coefficient $C_{VM} = 0.5$ and the wall force model with constant coefficients of $C_{w,1} = -0.055$ and $C_{w,2} = 0.09$ (Antal et al., 1991). These models have been incorporated into all the future simulation unless stated otherwise.

5.3 Three-dimensional simulation set up

The 2D simulations have been conducted to investigate the impact of the inlet condition and the bubble-water dynamic force models to validate the modelling approaches. However, the aeration tank is 3D and, therefore, the extra dimension needs to be modelled to capture the complete hydrodynamics in the aeration tank. These results can then be compared with the 3D velocity measurements recorded by the ADV for validation. However, before these simulation can be run, time and mesh resolution studies need to be conducted again to confirm the time required to reach a steady-state and mesh independence for the 3D simulation, respectively. The symmetry in the 3 diffuser reactor geometry is such that 1/3 of the reactor can be modelled instead of the full reactor, as illustrated in figure 5.18a, to save on computational costs while still capturing the important hydrodynamic features.

These studies were conducted alongside the 2D mesh studies such that they were run with the default simulation setup of the Schiller-Naumann drag model and virtual mass force only, which is deemed acceptable for the mesh and time analysis as this was a verification study only. The diffuser included in the 1/3 geometry was the one that was closest to the $x = 0$ wall which was in the plane of the recorded experimental data. The far wall in the 1/3 geometry, where the reactor has been sliced, was defined with a symmetry boundary condition while the rest of the walls and base are modelled with the no slip condition. The top wall or outlet is defined using the *inletOutlet* boundary condition, identical to the outlet in the 2D simulations. In these studies, an air flow rate of 0.6 L/s was used which was modelled using a velocity inlet condition with velocity, $v_{in} = 0.118$ m/s, and an inlet air volume fraction, $\alpha_{air, in} = 0.2$, in accordance with the results in §5.2.3.

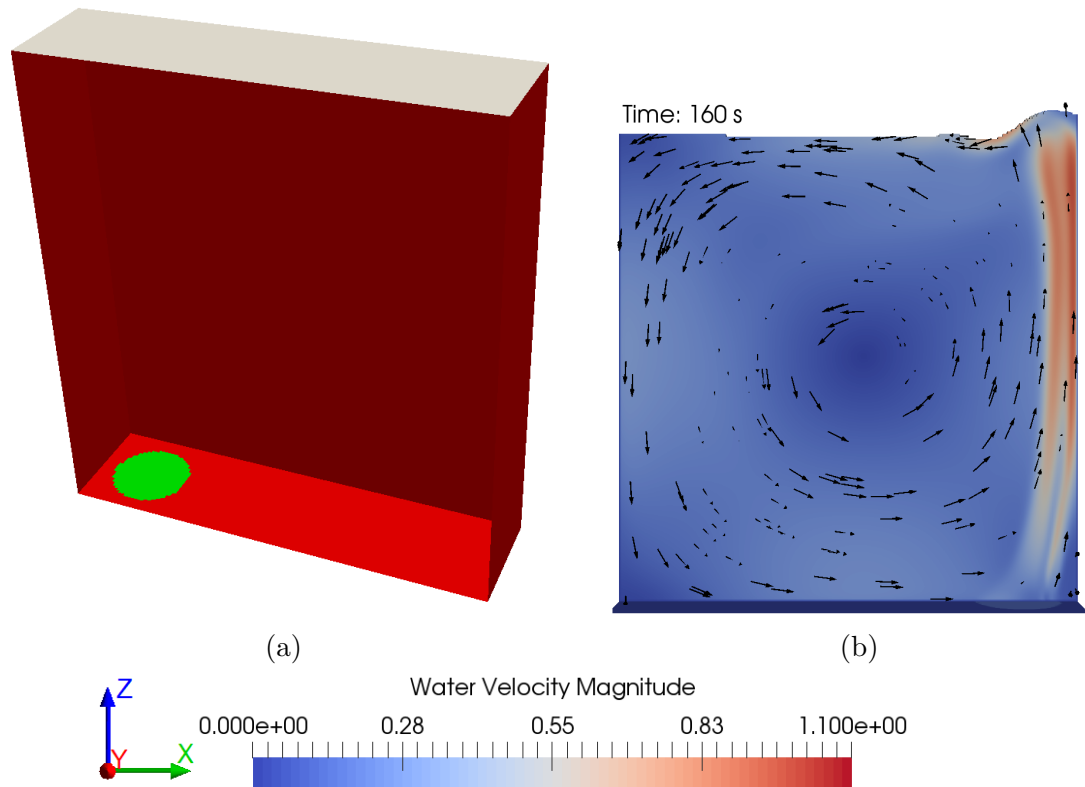


Figure 5.18: Illustration of the 1/3 reactor geometry with a single diffuser that was modelled in the 3D simulations (a) and the velocity magnitude contour and normalised vector plot for the 0.6 L/s aeration flow rate after 160s seconds (b). The colour bar and axes are with respect to (b)

The 3D meshes were created in OpenFOAM using *blockMesh* (OpenFOAM, 2020), to create a uniform hexahedron mesh. The mesh was generated uniformly and the two utilities: *topoSet* and *createPatch* (OpenFOAM, 2020); were used to patch in a circular shape to the base for the inlet. The cells inside and on the boundary of the circular patched inlet are converted into inlet cells which approximates the circular inlet. To accurately model a circular shape with hexahedral cells would require an o-grid. However, this restricts the use of a uniform hexahedron mesh as well as causes large skewness in the cells which can cause stability issues. The circular shape is only important at the inlet such that conserving the circular shape in the mesh cells accurately has negligible effects on the results. Additionally, adding a new inlet into the hexahedron mesh with the *topoSet* and *createPatch* utilities is trivial compared to using the o-grid method which would require a completely new mesh. Therefore, the circular shape patching method was assessed to be the best

approach for creating the inlet in the 3D geometry. An initial inspection of the generated flow field in the 3D simulations after 160 seconds found that it calculated a counter-clockwise vortex in the centre of the reactor, as illustrated in figure 5.18b, which was qualitatively observed in the experiments. This gave us confidence that the 3D simulations were behaving similarly to the 2D simulations and allowed us to move forward with the mesh refinement and time analysis studies.

5.3.1 Steady-state analysis

The solver is transient and we want to find the time required for the hydrodynamics to reach a steady-state field in the 3D simulations so that we can compare the results to the experimental measured velocities. An initial mesh resolution of 2.9 million cells was used in this study which was later confirmed as acceptable. It was assumed initially that 160 seconds would be the time required to reach a steady-state as this was the case for the 2D simulations; however, it was found that the results had not reached a steady-state after 160 seconds, as illustrated in figure 5.19. The velocity magnitude plots for all 6 locations continue to change after 160 seconds and have not stopped changing after 420 seconds. Observing the plots in figure 5.19, there is periodic behaviour appearing over a 260 second period. The plots approximately repeat themselves every 120 seconds. This is further confirmed by the series of velocity magnitude contour and vector plots in figure 5.21. The 160 and 300 second plots look identical in both the velocities magnitude contour and vector profiles. This is true for each paired image after each 20 second interval. The velocities do not settle into a steady-state but oscillate over a 120 second period. Therefore, the time average can be taken over a 120 second period to get a time-average steady-state result.

To confirm this, the simulations were run again and the velocities were time-averaged over a 120 second period after the initial 160 seconds had passed. The velocity profiles results after averaging for intervals of increasing 20 second are pre-

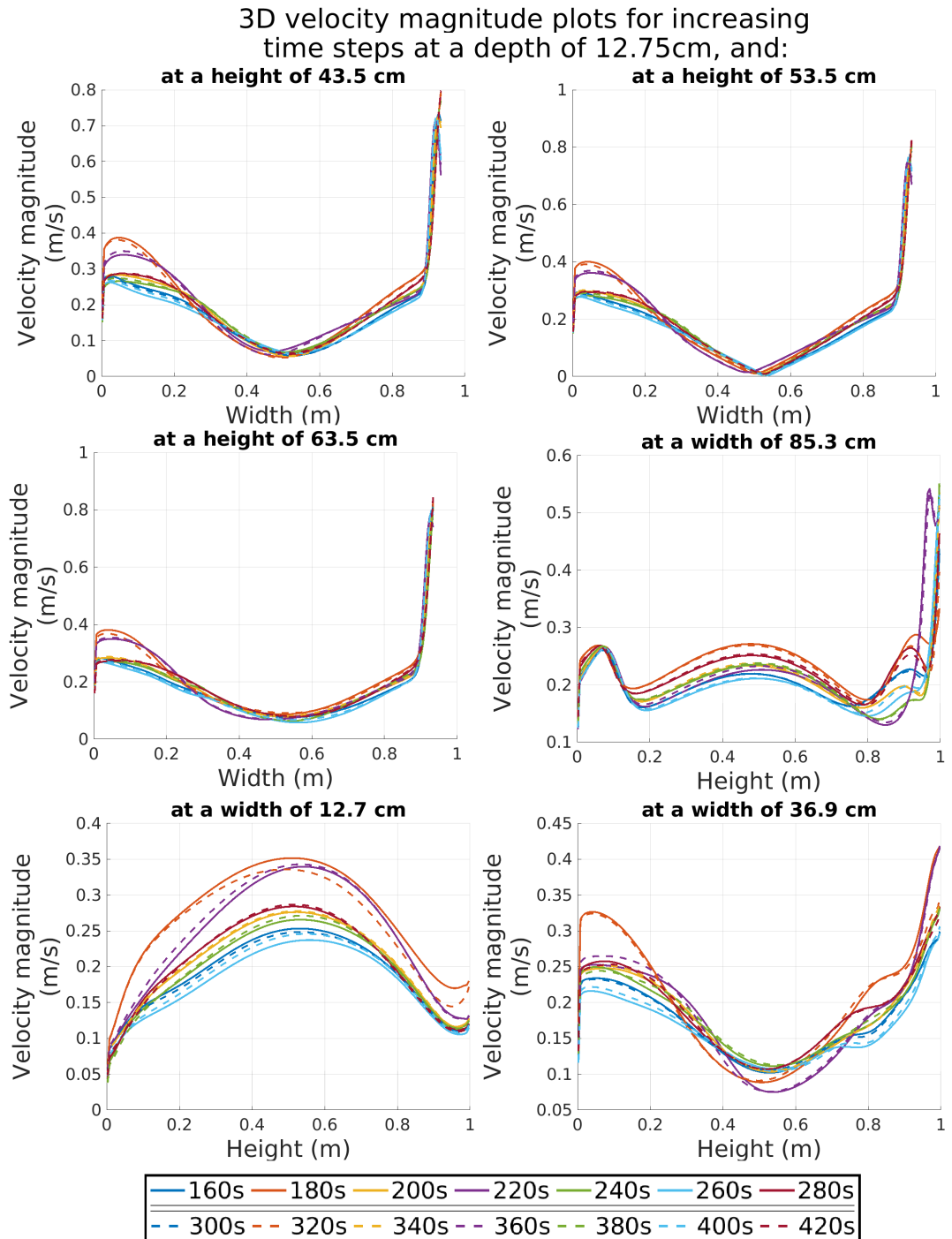


Figure 5.19: Analysis of the periodic behaviour of the 3D 1/3 reactor simulation over 200 seconds after an initial 160 seconds for an air flow rate of 0.6 L/s.

sented in figure 5.20. The results are closer together than the plots in figure 5.19. Additionally, it was found that the time averaged results after 180 and 240 seconds were identical to the 120 second averaged results. This implies that both the simulations and experimental both agree that 120 seconds is an appropriate length of time for averaging data. As a result of this analysis, the 3D simulations will be run

for 160 seconds and then run for a further 120 seconds where the results will be time averaged over the 120 second period.

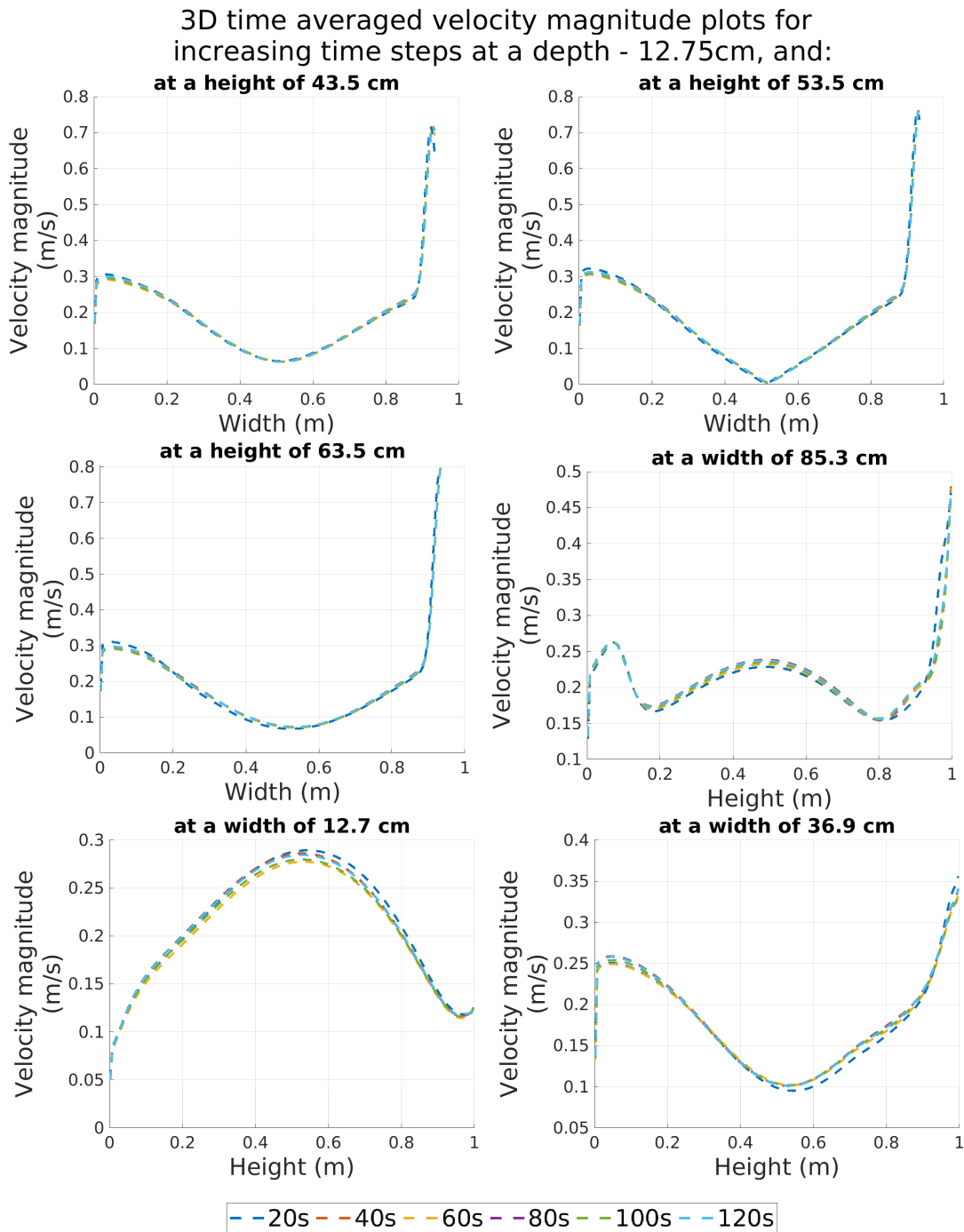


Figure 5.20: The time averaged results for range of time periods after an initial 160 seconds has passed.

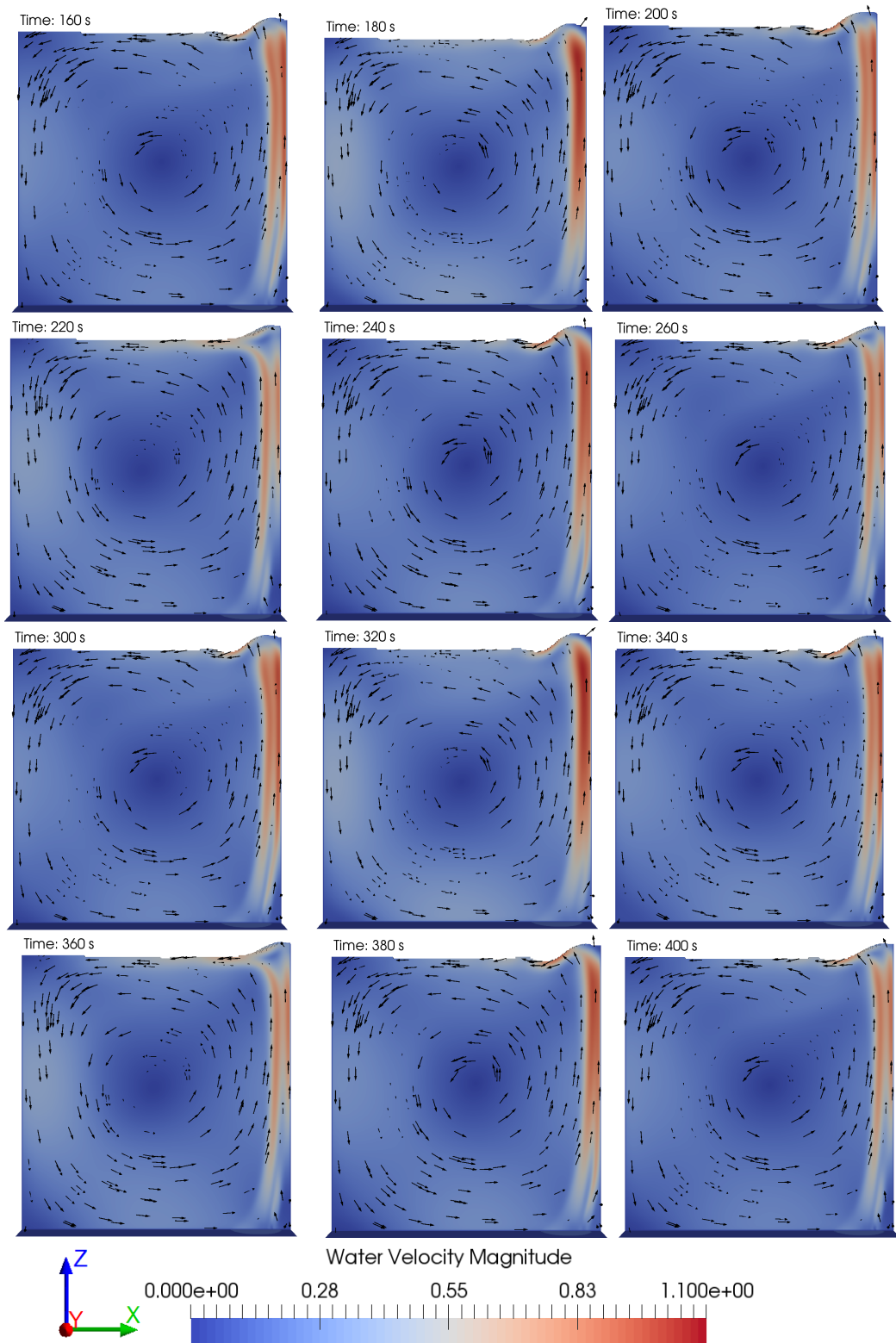


Figure 5.21: Analysis of the velocity magnitude contour and normalised vector plots at specific times to illustrate the periodic behaviour seen in the 3D 1/3 reactor simulations after an initial 160 seconds of running.

5.3.2 Mesh refinement study

An mesh refinement study has been conducted to confirm mesh independence for the 3D 1/3 geometry aeration tank with a uniform hexahedral structured grid that has been generated using OpenFOAM's *blockMesh* utility. An illustration of the outline one of the meshes is presented in figure 5.22. The mesh resolutions investigated

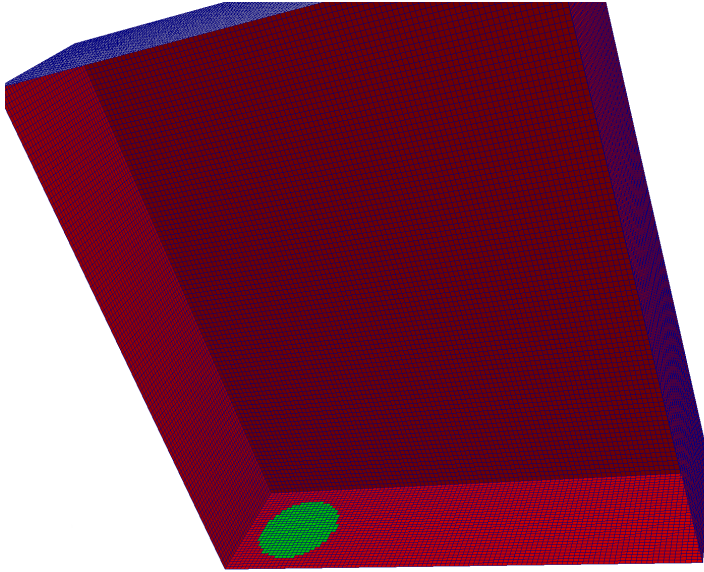


Figure 5.22: An example of the mesh for the 3D 1/3 aeration reactor with a single diffuser. This is coarser than the meshes assessed for illustration purposes.

are defined in table 5.4 where the number of cells along each axis was chosen such that each cell was approximately cubic in shape and the increases in resolution were proportional to one another. The simulations were conducted with an air flow rate of 0.6 L/s.

Time averaged velocity magnitude profiles were found along various heights and widths at a depth of 12.75 cm for the 5 different mesh resolutions. The results of these simulations are found in figure 5.23. All 5 mesh resolutions look very similar to one another which implies the bulk fluid motions are being captured by all the resolutions. The largest differences are seen along the the width profiles near the middle of the reactor and the fluid surface. This is a result of the vortex in the centre being resolved better in the higher resolution simulation.

The three highest mesh resolutions have a maximum difference of approximately

Mesh number	Cell numbers (mil)
# 1	0.53
# 2	1.80
# 3	2.86
# 4	4.23
# 5	6.04

Table 5.4: Mesh cell resolutions for the 3D 1/3 aeration tank investigated in the mesh independence study.

± 0.02 m/s, with mesh 3 and 4 are almost identical to one another, based on the plots in figure 5.23. The variation of 0.02 m/s for the highest three mesh resolutions is under 10% of the maximum velocity observed in the profiles in figure 5.23 which suggest a 10% error in the predictions from the mesh resolution.

Solving a two-phase flow with a mesh of 4.23 million cells is already computationally expensive. Additionally, only 1/3 of the full reactor is being modelled such that, if the full sized reactor was modelled, this would require at least 3 times the mesh resolution of the 1/3 geometry which will be even more computationally expensive. From the analysis above, choosing mesh 3 or 4 over 5 implies that we would have a potential maximum 10% error in the predictions. The errors are a magnitude smaller than the larger velocity values which is deemed an acceptable error. The differences in the velocity profiles between the mesh 3 and 4 resolutions are very small which implies that mesh resolutions between 2.86 and 4.23 million cells are both resolving the same hydrodynamic features. Using mesh 4 over mesh 3 would only be increasing the computational costs with very little impact on the results. Therefore, mesh 3 will be used for the 3D 1/3 reactor simulations with a potential maximum error of 10%. Furthermore, if the full 3D aeration tank was modelled, it will be assumed that that 3 times the mesh resolution of mesh 3 (8.58 million cells) is an appropriate resolution.

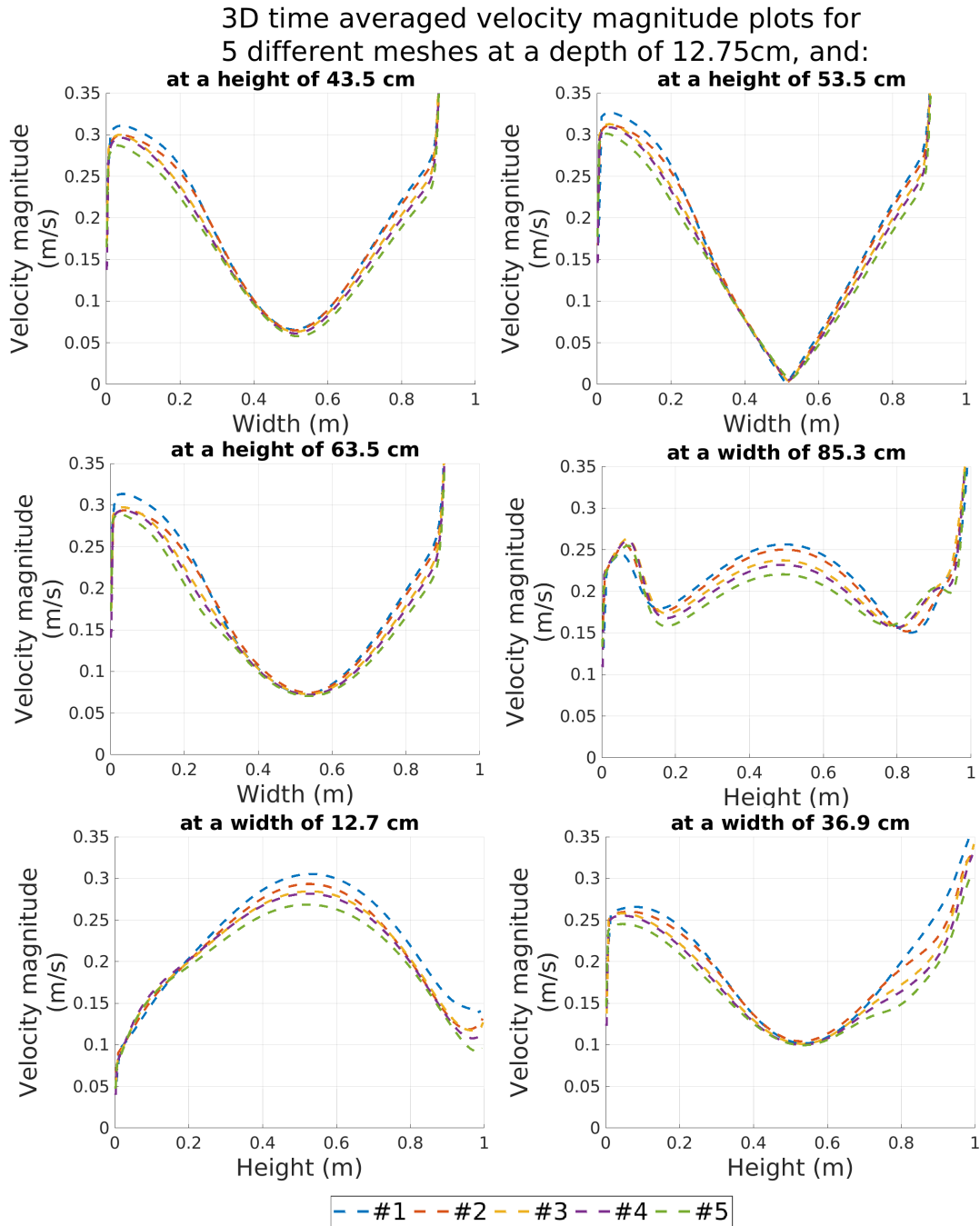


Figure 5.23: The 120 second time averaged velocity magnitude results for the 5 mesh resolutions considered in the mesh independence study.

5.4 Three-dimensional hydrodynamic aeration tank results and discussion

In this section, we will assess the 3D 1/3 reactor simulation results for an air flow rate of 0.6 and 0.3 L/s. These will be compared with the 2D simulations to assess

the effect of including an additional dimension. The results will also be compared with the experimental data to validate the CFD for the 3D simulations. Finally, the results for the two flow rates will be compared to assess how the flow impacts the hydrodynamic solutions.

5.4.1 Three and two dimensional simulation comparison

In this section, we will compare the 3D results with the 2D results from above for the two flow rates. A slice through the 3D geometry was made through the centre of the diffuser to match with the 2D simulations. To match the coordinates of the simulation, the directions (x, y, z) will correspond to the (width, depth, height) dimensions. Therefore, the y direction originally defined in §5.2 as the height velocities will now defined be in z direction. Additionally, the 2D velocity magnitude will only consider the velocities in the x and z directions such that the results can be directly compared. The solutions from this comparison are presented below in figures 5.24 and 5.25 for flow rates 0.6 and 0.3 L/s, respectively.

If we first consider the 0.6 L/s flow rate results in figure 5.24, there is a difference between the 2D and 3D solutions. The biggest difference between them is observed in the z and 2D velocity magnitude profiles for all heights. The velocities near the left and right walls are significantly less in the 3D simulations. This is a result of having the extra depth dimension in the 3D simulations for dispersion of the energy. In the 2D simulations, the fluid was confined to 2D which results in fast moving fluid moving upwards from the rising bubble plume being forced along the fluid surface to the left and back down into the bulk fluid. This causes the large velocities on the left side of the reactor in the 2D simulations. In the 3D simulations, the fluid is not confined and can disperse along the y depth dimension which results in lower velocities along the 2D slice. Additionally, a lower max velocity is observed in the fluid directly driven by the bubble plume in the 3D simulation compared with 2D simulation which is also due to the dispersion of energy and momentum along the

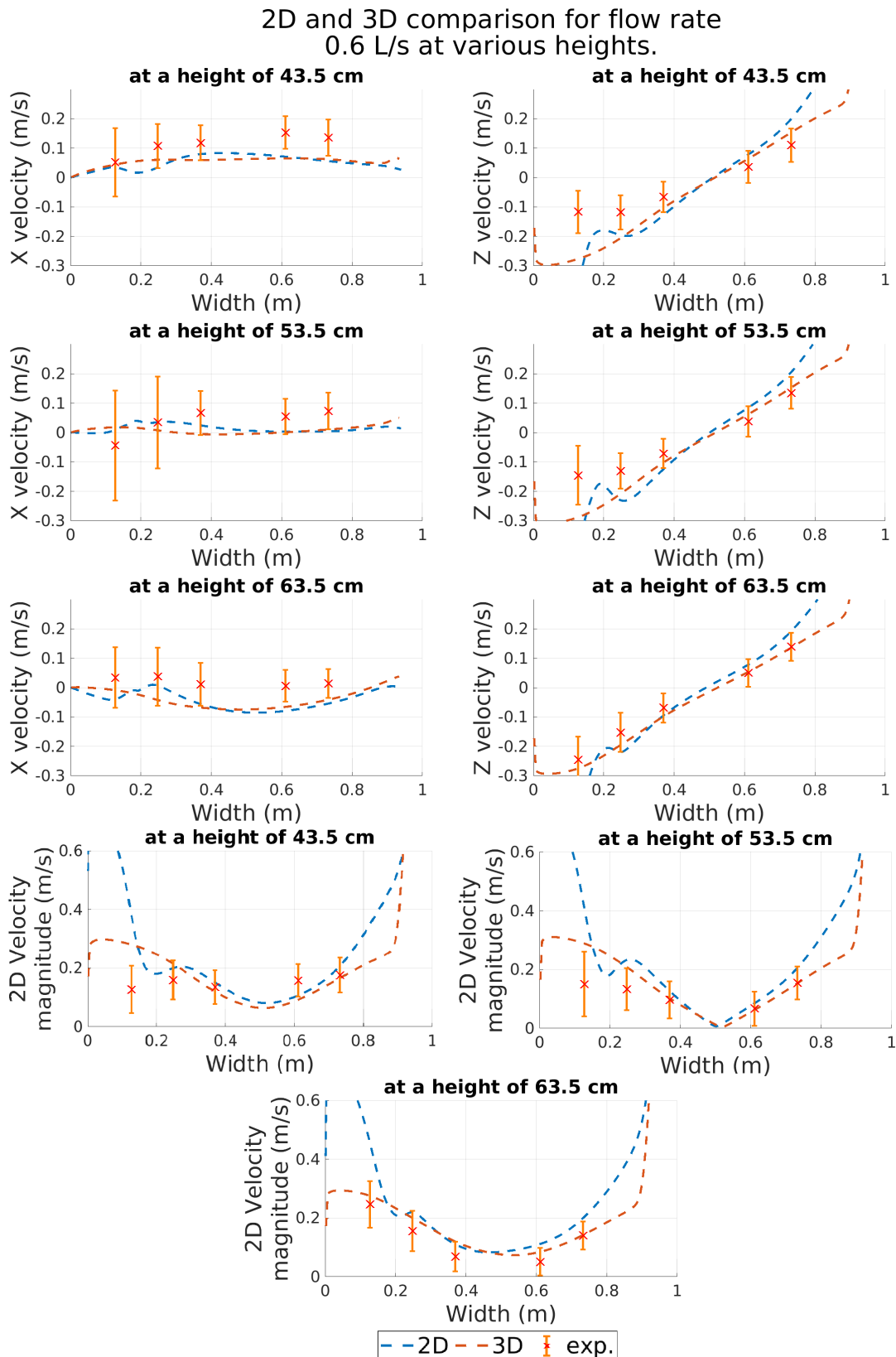


Figure 5.24: Comparison of the 2D results of the 1/3 3D reactor simulations and the 2D reactor solutions and experimental data for and aeration flow rate of 0.6 L/s.

depth direction.

If we compare the 2D and 3D z velocities and velocity magnitude profiles with the experimental data, the 3D simulations fit a lot better compared with the 2D simulations. The z velocities profiles match much better, especially at height 63.5 cm. This is also true for the 2D velocity magnitude profiles. The experimental data was taken in a 3D aeration tank and, though we have shown that the data is pseudo 2D in §3.6, the dynamics are still 3D; therefore, it is expected that the 3D simulations will perform better.

Comparing the x velocity profiles for the 2D and 3D simulations, it is found that they are very similar with only slight differences. The size of the x velocities are closer to zero at height 53.5 cm for the 3D results which implies the 3D simulations calculates the centre of the vortex loop to be approximately around a height of 53.5 cm while the 2D simulations calculate the centre of the vortex to be higher. The 3D simulation results overall match the experimental data well and better compared with the 2D simulations.

If we consider the results from the 0.3 L/s simulations in figure 5.25, the differences between the z velocities and 2D velocity magnitude profiles for the two simulations are similar to what is observed for 0.6 L/s case but with the 3D simulations matching significantly better with the experimental data. With the exception of the velocities near the left wall at height 43.5 cm, the 0.3 L/s 3D profiles are all very close to the mean experimental values while the 2D simulations significantly over-predict the magnitude of the experimental velocities. Assessing the x velocity profiles, the 3D simulations perform well with matching the experimental data for all heights except at a height 43.5 cm. In summary, the 2D simulation are acceptable but the 3D simulations better match the experimental data for both flow rates, especially for the 0.3 L/s case, compared with the 2D results which is due to the additional dimension being modelled in the 3D simulations to allow for dispersion of the fluid momentum and energy.

2D and 3D comparison for flow rate
0.3 L/s at various heights.

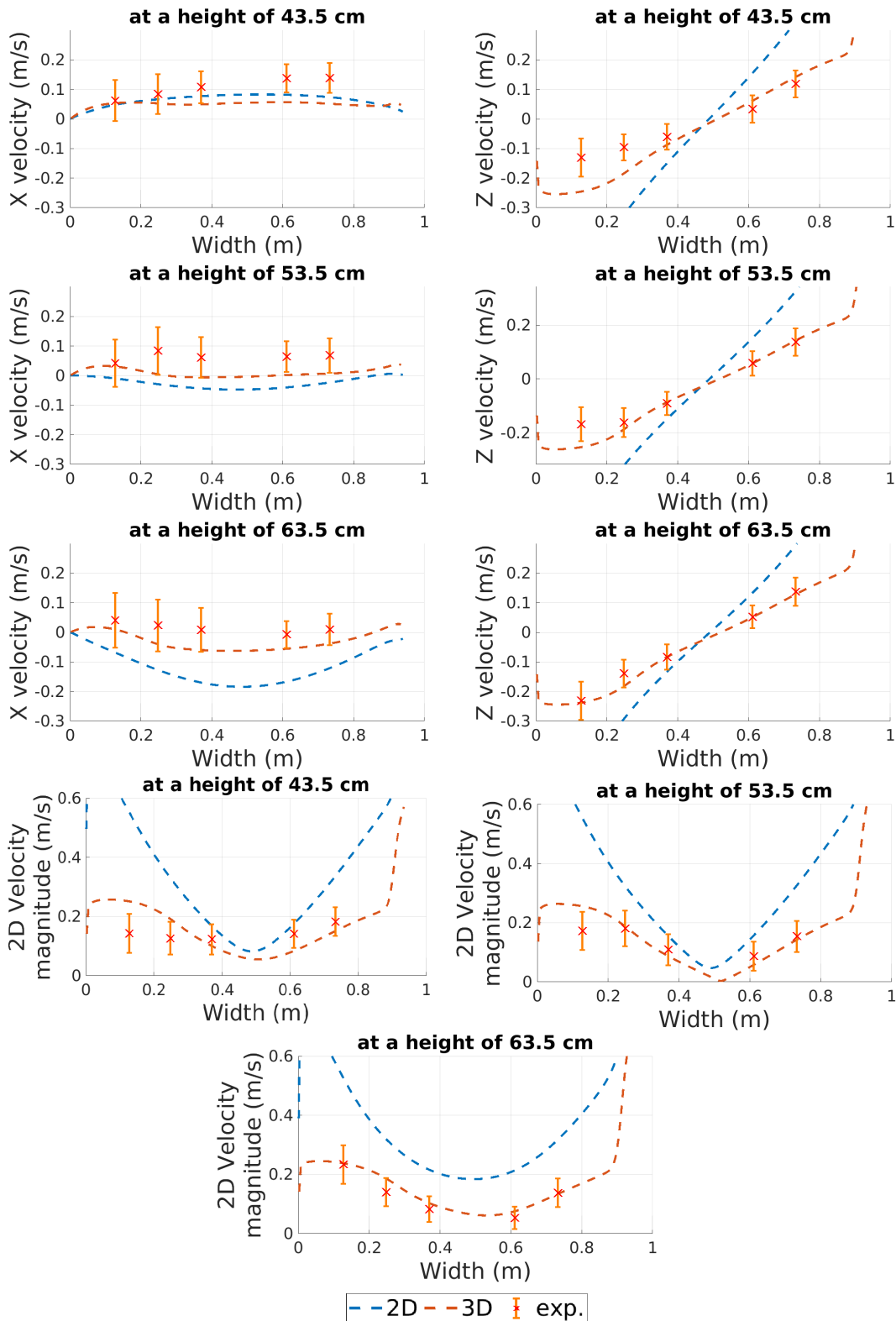


Figure 5.25: Comparison of the 2D results of the 1/3 3D reactor simulations against the 2D simulations and experimental data for an aeration flow rate of 0.3 L/s.

5.4.2 Three-dimensional reactor hydrodynamic analysis

In this section, we will further analyse the full 3D hydrodynamics of the 1/3 reactor for both 0.6 and 0.3 L/s aeration rate simulations. The results will be assessed against all the relevant experimental data to validate the 3D CFD methodology and further investigations will be conducted to improve our understanding of the generated flow field in the reactor.

The 0.6 L/s flow rate 3D results

The faster 0.6 L/s aeration flow rate will be investigated first. The results in figure 5.26 illustrate a comparison of the one third reactor velocities against the experimental data along width profiles at 3 different heights at a depth of $y = 12.8$ cm which intersects the centre of the membrane diffuser. Some of these plots are identical to those presented above in §5.4.1; however, as these are 3D results, we can also compare the y velocities and the full 3D velocity magnitudes with the corresponding experimental velocities. If we consider the x velocities in figure 5.26, these are the same profiles as shown in figure 5.24 such that the observations are the same.

The simulations predict that the centre of the vortex resides approximately at a height of 53.5 cm by the sign change of the x velocities and the velocity magnitude profile reaching 0 m/s at this height. In comparison, the experimental data implies the vortex centre is closer to a height of the 63.5 cm. The experimental mean y velocities are all approximately around 0 m/s which is expected as we have previously shown in §3.6 that this experimental setup is pseudo two dimensional. Similarly, the CFD simulations approximately calculate 0 m/s y velocities along the majority of the profile which matches well with the experimental data. However, we find a slight decrease and then increase from 0 m/s in the y velocities near the left wall implying, if looking down the negative z axis, a slight anti-clockwise rotation in the CFD simulation. Assessing the y water velocity contour plot at a height $z = 0.5$ m, as illustrated in figure 5.27, it is found that there is a slow anticlockwise rotation

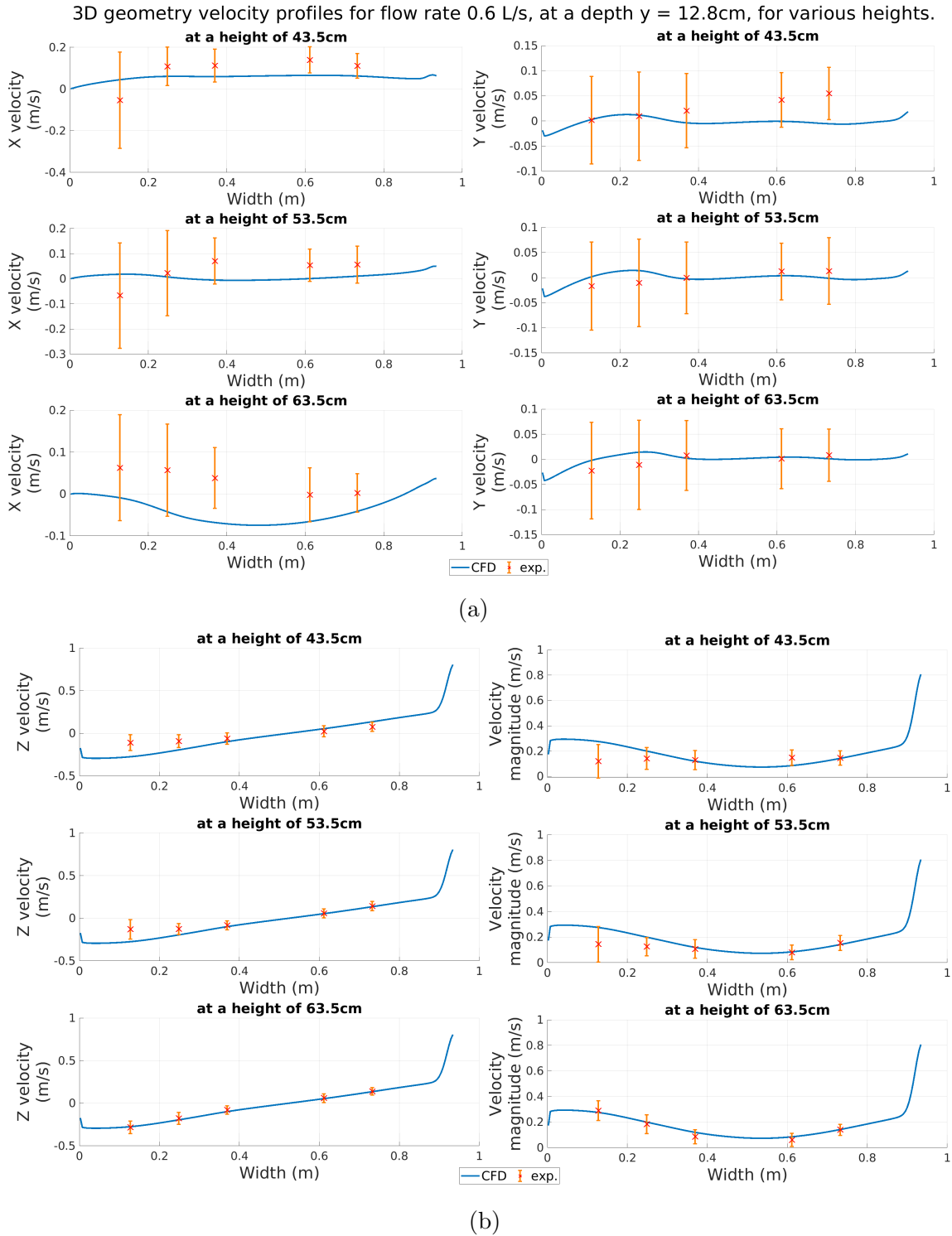


Figure 5.26: Comparison of the one third reactor 3D velocity results and experimental data along width profiles at heights: 43.5, 54.5 64.5 cm, at a depth of 12.8 cm for an aeration flow rate of 0.6 L/s. The x and y velocities are shown in (a) and the z velocities and 3D velocity magnitudes are shown in (b).

near the left wall. Additionally, there is another rotational profile, but at a much slower velocity, near the right wall and in the middle of the reactor.

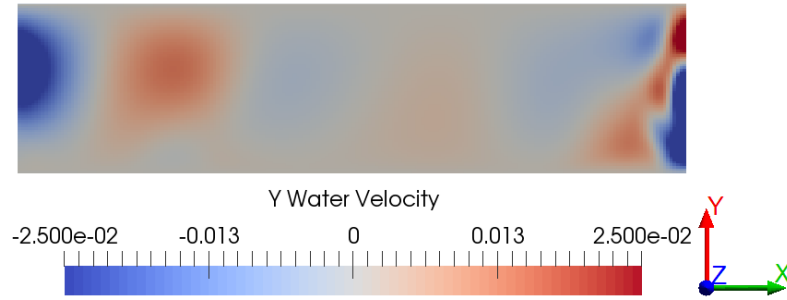


Figure 5.27: The y water velocity (m/s) contour plot on a slice made at a height $z = 0.5\text{m}$.

As previously stated in the comparison of the 2D and 3D results in §5.4.1, the z velocities in figure 5.26 match well with the experimental data with a slight over calculation of the velocity size near the left wall. The 3D velocity magnitude profiles are almost identical to the 2D profiles in figure 5.24 due to the small y velocities contributing very little towards the calculation. The profiles in general match well with the experimental data, especially the 63.5 cm height profiles.

The direct impact of the rising bubble plume on the fluid can be seen to start at around 0.9 m along the width in all 3 z velocity profiles which implies the bubble plume has a diameter of 0.1 m. Figure 5.28a illustrates the z rise velocities contours near the bubble plume at a height of $z = 63$ cm. The presence of the side wall near the diffuser draws the bubbles towards the walls due to the pressure difference between the bubbles and the wall and bubbles and bulk ambient fluid. This causes the bubble plume to lose its circular shape as it rises and become compressed, as illustrated in figure 5.28a, which results in the plume losing the usual circular structure. The diameter along the x axis is about 0.1 m while along the y axis the diameter is around 0.15m which are smaller than the diffuser diameter of 0.23 m. This compressed behaviour in the bubble plume is also seen for 0.3 L/s flow rate, as illustrated in figure 5.28b, with a similar shape and size to the 0.6 L/s flow rate simulation. However, the maximum rise velocity is lower in the 0.3 L/s compared with the 0.6 L/s results at this height which is predictable as the bubbles rise faster in the higher flow rate reactor which means the maximum amount of momentum that can be transferred to the fluid is higher.

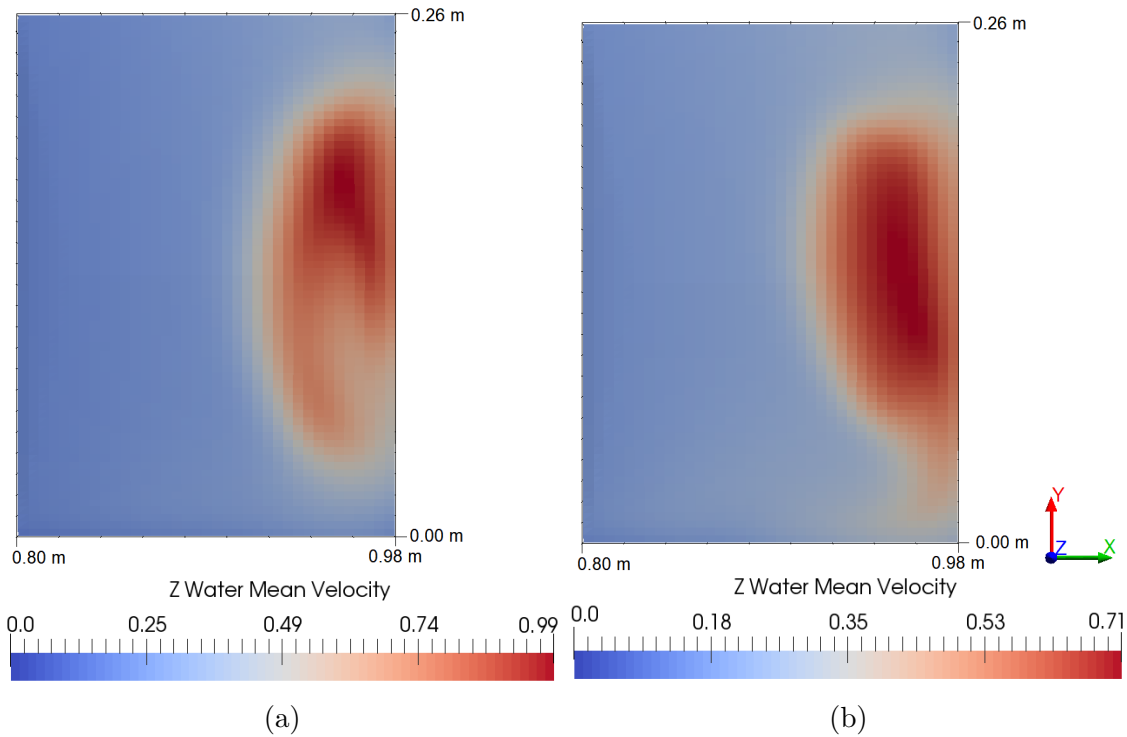


Figure 5.28: The z rise velocity (m/s) near the bubble plume at a height of $z = 63$ cm for flow rate 0.6 L/s (a) and 0.3 L/s (b).

Analysing the water velocity magnitude vector and contour plot in figure 5.29 can provide a better understanding of the general flow field through the reactor. The z rise velocities increase from 0.7 to 0.8 m/s from height 43.5 to 63.5 cm, respectively, in figure 5.26 and reaches a maximum of 1 m/s at approximately a height of 0.9 m from figure 5.29b. The contour plots also illustrate the impact on the fluid flow as the bubble plume transition towards the wall away from being directly above the diffuser due to the influence of the reactor geometry. Figure 5.29 illustrates the vortex loop that we have observed in the velocity profiles and experimental aeration tank. The centre of the vortex loop is approximately at a (x,z) coordinate of $(0.53,0.5)$ metres which agrees with the results seen in the velocity profiles in figure 5.26. The slowest moving fluid regions reside in the top and bottom left corners of the reactor and in the centre of the vortex loop. These are regions of interest for assessing the impact of the hydrodynamic mixing on the biological processes in the coupled model.

If we consider the air velocity magnitudes in the bubble plume, as illustrated in figure 5.30, we can compare the difference between the air and water velocities to

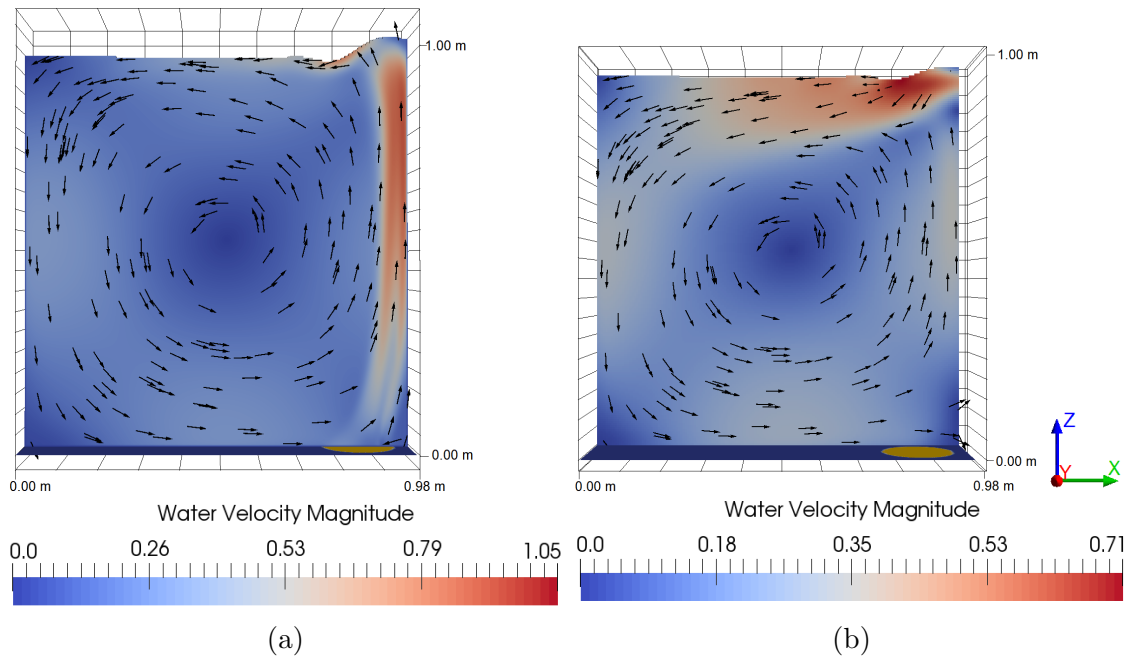


Figure 5.29: The water velocity magnitude (m/s) contour and normalised vector plot for an aeration flow rate of 0.6 L/s at a depth of $y = 12.8$ cm (a) and $y = 24.8$ cm (b). The yellow circle at the base illustrates the location of the aerating diffuser.

assess how much momentum is being transferred as the bubbles rise. The air rise velocities reach a maximum velocity of 1.3 m/s, as shown in figure 5.30a, for the 0.6 L/s flow rate simulation which is higher than the maximum 1.0 m/s water velocity observed in figure 5.29a. This is also the case for the 0.3 L/s flow rate where the maximum air and water velocity is found to be 1.0 and 0.75 m/s, respectively, as illustrated in figure 5.30b and figure 5.34a, respectively. Furthermore, the rising air velocities never stop increasing along the height of the tank before reaching the fluid surface for both flow rates which implies that a terminal velocity was not reached and suggests that, to get the most benefit out of the rising bubbles, the tank needs to be taller. Additionally, this lower height means that there is less time for the bubbles to transfer their momentum into the tank. This explains why the water velocity is also significantly slower than the air velocity, where they should be more similar if an equilibrium has been reached. This is to be expected as aeration tanks are usually around 3 m high (Meister et al., 2017) which would allow more space for the rising bubbles to reach terminal velocities and provide more time for the bubbles to transfer their momentum.

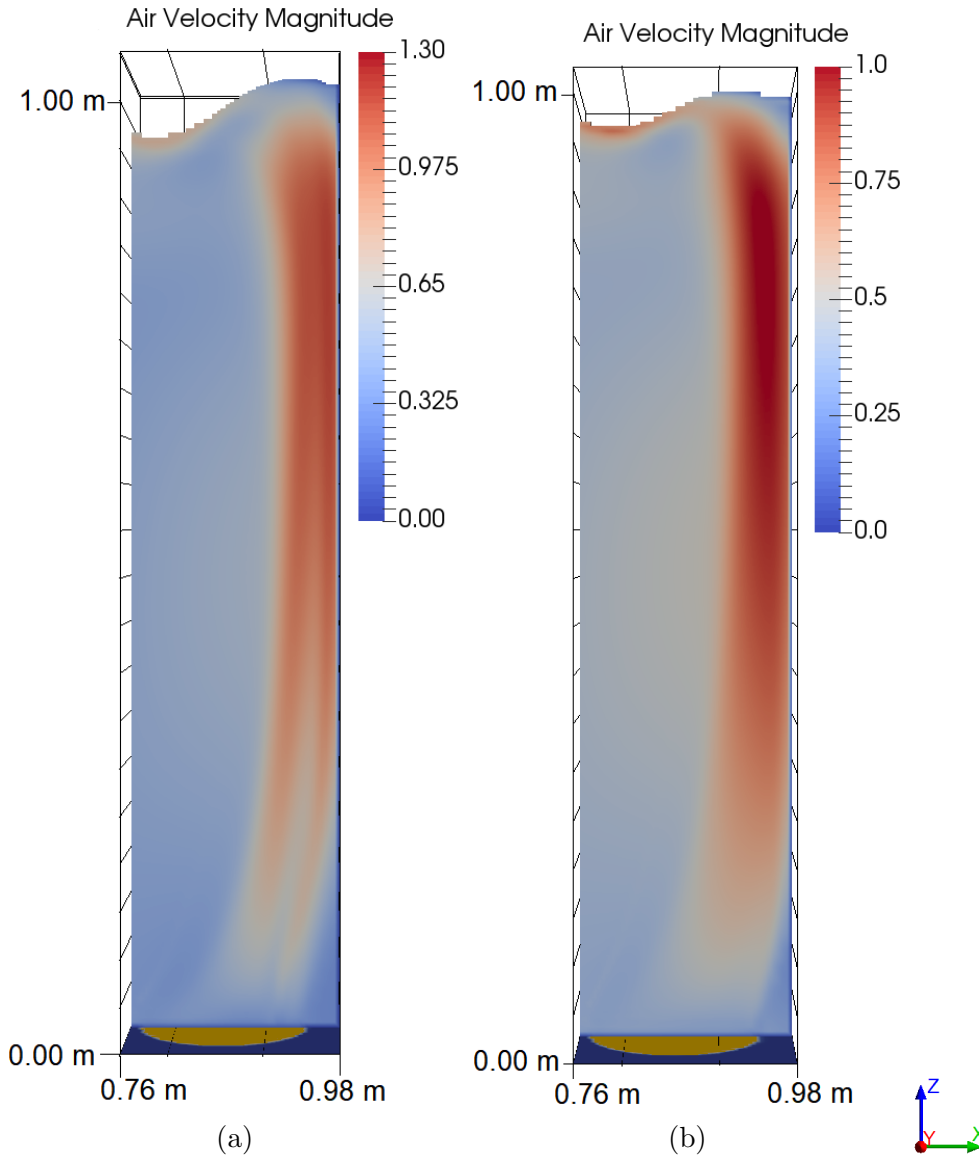


Figure 5.30: The air velocity magnitude (m/s) in the bubble plume region above the diffuser at a depth of $y = 12.8$ cm for a flow rate of: 0.6 L/s (a), and 0.3 L/s (b). The yellow circle at the base illustrates the location of the aerating diffuser.

If we consider the turbulence kinetic energy contours for the 0.6 L/s flow rate simulations in figure 5.31, it can be observed where the flow is most turbulent. Considering the turbulence kinetic energy contour plot in figure 5.31a, it is found that the turbulence kinetic energy is largest in the bubble plume and at the water surface. This is predictable as the bubble-water forces are all applied in the plume region which would create turbulent eddies in the flow. Additionally, with the full movement of fluid surface moving up and down, there are additional forces that are producing turbulent eddies. To further assess the turbulence in the reactor, the

turbulence kinetic energy intensity, k_{int} , has been calculated which is defined as,

$$k_{\text{int}} = \frac{k_{\text{water}}}{|\mathbf{u}_{\text{water}}|^2},$$

where k_{water} is the turbulence kinetic energy in the fluid and $\mathbf{u}_{\text{water}}$ is the water velocity. The turbulence kinetic energy intensity allows us to compare the magnitude of the turbulence kinetic energy compared with the fluid velocity. This allows us to find the regions in the reactor where the turbulence is dominant compared with the convective mixing. The results of this calculation are illustrated in figure 5.31b where the k_{int} value has been capped at 1. The region where the turbulence mixing is dominant is at the centre of the large vortex and the corners of the reactor. We have previously seen from figure 5.29a, that these are the slowest moving regions of the reactor and, therefore, it is predictable that the turbulence kinetic energy is dominant in these regions. The results imply that the main source of mixing is from the turbulence in these regions.

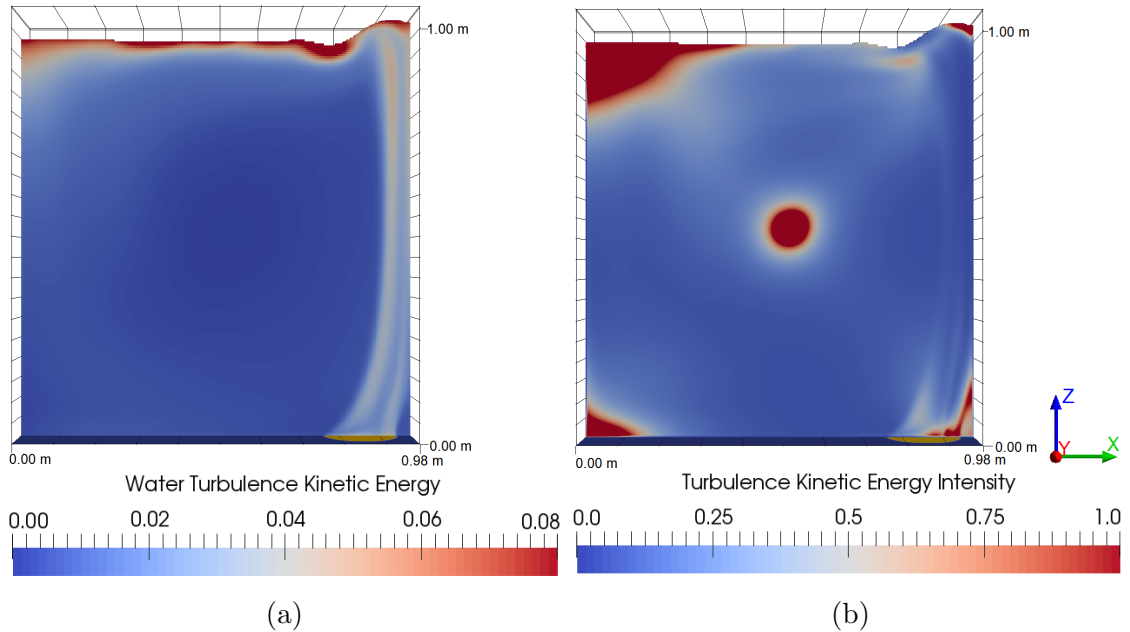


Figure 5.31: The water turbulence kinetic energy (m^2/s^2) (a) and turbulence kinetic intensity ($k_{\text{int}} = k_{\text{water}}/|\mathbf{u}_{\text{water}}|^2$) (b) at a depth of $y = 12.8$ cm for the 0.6 L/s flow rate results. The yellow circle at the base illustrates the location of the aerating diffuser.

Finally, the velocity profiles for flow rate 0.6 L/s along the width at a depth

of $y = 24.8$ cm are illustrated in figure 5.32 which are compared with another set of experimental data points. The 1/3 reactor has a maximum depth value of $y = 24.875$ cm and, therefore, the simulation profiles are right next to the symmetry wall in the simulation. This symmetry condition results in all the recorded y velocities equating to zero due to continuity; however, the y velocities in the experimental data are non-zero. This is a minor flaw in the 1/3 reactor geometry; nonetheless, the experimental recorded mean y velocities are close to 0 m/s which are small compared to the larger z velocities such that the predicted 0 m/s y velocities in the simulations are acceptable.

The x velocities for heights 43.5 and 53.5 cm follow the general experimental data profile and resides within the error spread of the data. For the z velocities, the simulation results matches almost perfectly with the experimental data at height 63.5 cm and very well at height 53.5 cm with only a slight over prediction of the velocity size near the left wall. The simulation calculates slightly higher velocities near each side wall for the height 43.5 cm profile compared with the experimental data. This difference could be a result of the symmetry wall condition as the simulation becomes pseudo two dimensional near the symmetry wall which, as seen in the 2D simulations in §5.4.1, results in larger predicted velocities due to the confinement. Finally, the velocity magnitudes profiles illustrate similar behaviour as the z velocity profiles when comparing with the experimental data. They match almost perfectly at a height of 63.5 cm and very well at a height 53.5 cm but with an over predication of the velocities at height 43.5 cm. Additionally, the experimental recorded velocities are a lot smaller at this depth and so the margin of error seems larger compared with figure 5.26 results. This causes the experimental data to look worse but they have similar standard deviation error spreads as all the other experimental points. If we assess the velocity magnitude contour vector plot at this depth in figure 5.29b, it can be seen that the rising bubble plume does not spread wide enough to reach this depth, which was seen in the rising z velocities in figure 5.28. The larger velocities at the top right of figure 5.29b indicates that the spreading

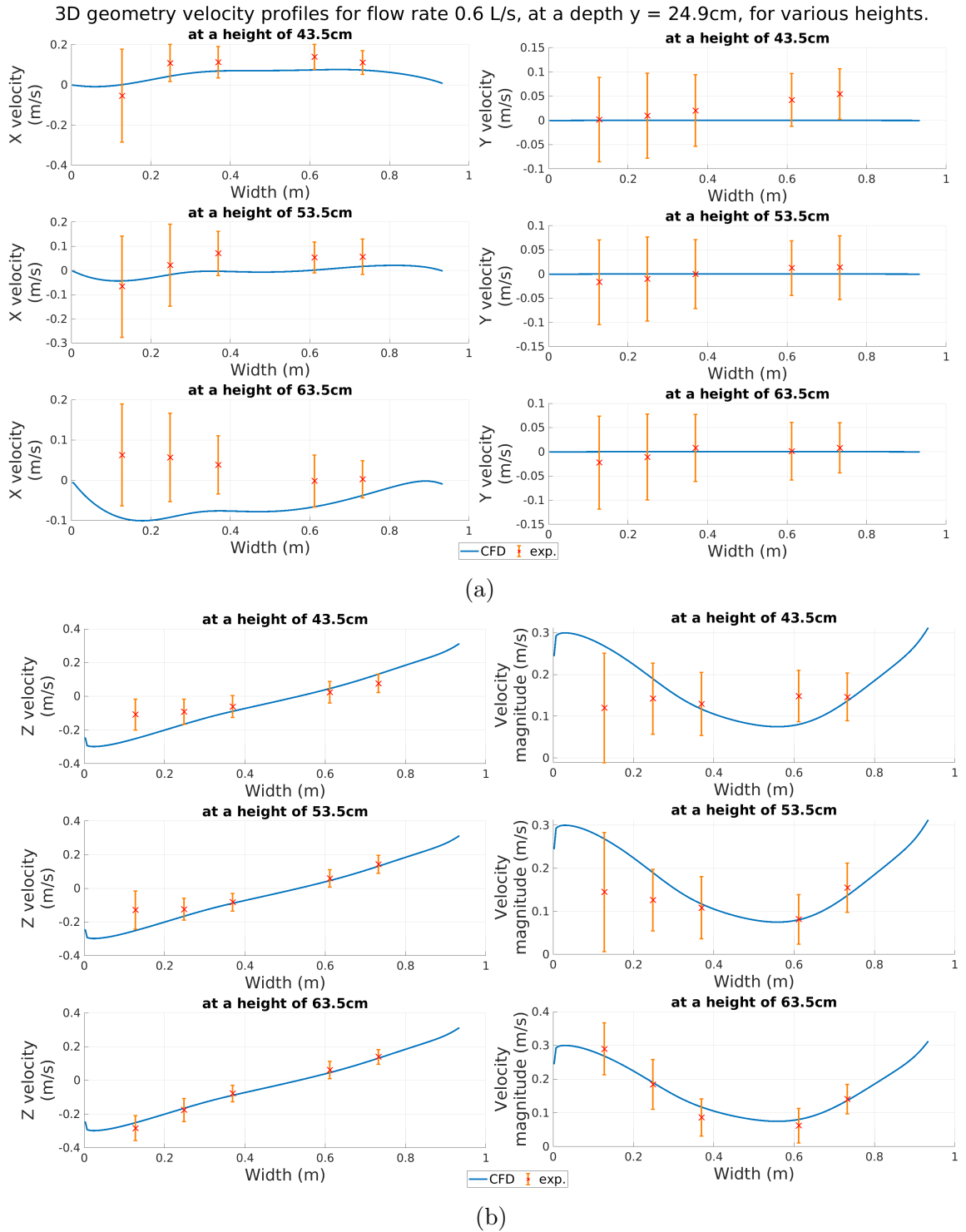


Figure 5.32: Comparison of the one third reactor simulation velocities against experimental data along width profiles at heights: 43.5, 54.5 64.5 cm, at a depth of 24.8 cm for an aeration flow rate of 0.6 L/s. The x and y velocities are shown in (a) and the z velocities and 3D velocity magnitudes are shown in (b).

of the fluid surface at the top of the bubble plume is the main driver of the fluid at this depth. As illustrated in figure 5.29, the velocities at this depth are overall

smaller compared with the $y = 12.8$ cm depth results which is expected as it is not directly in line with the aerating diffuser and, therefore, not as influenced by the rising bubble plume. However, the general flow field structure still follows the same rotational vortex with approximately the same centre location as was seen down the middle of the reactor.

The 0.3 L/s flow rate 3D results

The 0.3 L/s flow rate simulation will now be investigated and assessed against the experimental data and compared with the 0.6 L/s flow rate simulation results. The analysis and conclusions made for the 0.3 L/s results are very similar to those made for the 0.6 L/s simulation and, therefore, less details are provided to avoid repetition. Assessing the velocity profiles at a depth of $y = 12.8$ cm, as illustrated in figure 5.33, it is found that the simulations in general match well with the experimental data.

The x velocities suggest the vortex centre resides at the 53.5 cm height at a width of 0.52 m, based on minimum of the velocity magnitude, which is slightly to the left of the location in the 0.6 L/s results while the experimental data implies it is higher, similar to the case in the 0.6 L/s analysis. The y velocities agree well with the experimental data with the profiles passing very close to the mean experimental values. The z velocities and the velocity magnitude matches very well with the experimental data, especially at heights 53.5 and 63.5 cm. In general, the 0.3 L/s results match better with the experimental data compared with the 0.6 L/s results. It is difficult to identify where the bubble plume starts in the 0.3 L/s z fluid velocities due to the smooth profile. However, as illustrated in figure 5.28b, the bubble plume has a ellipsoidal profile near the side wall that is almost identical in shape and size as the 0.6 L/s bubble plume.

Investigating the 0.3 L/s velocity magnitude contour vector plots in figure 5.34a, it is found to have the familiar vortex flow field that was seen in the 0.6 L/s but at a slower velocity. One difference between the two simulations is that the water

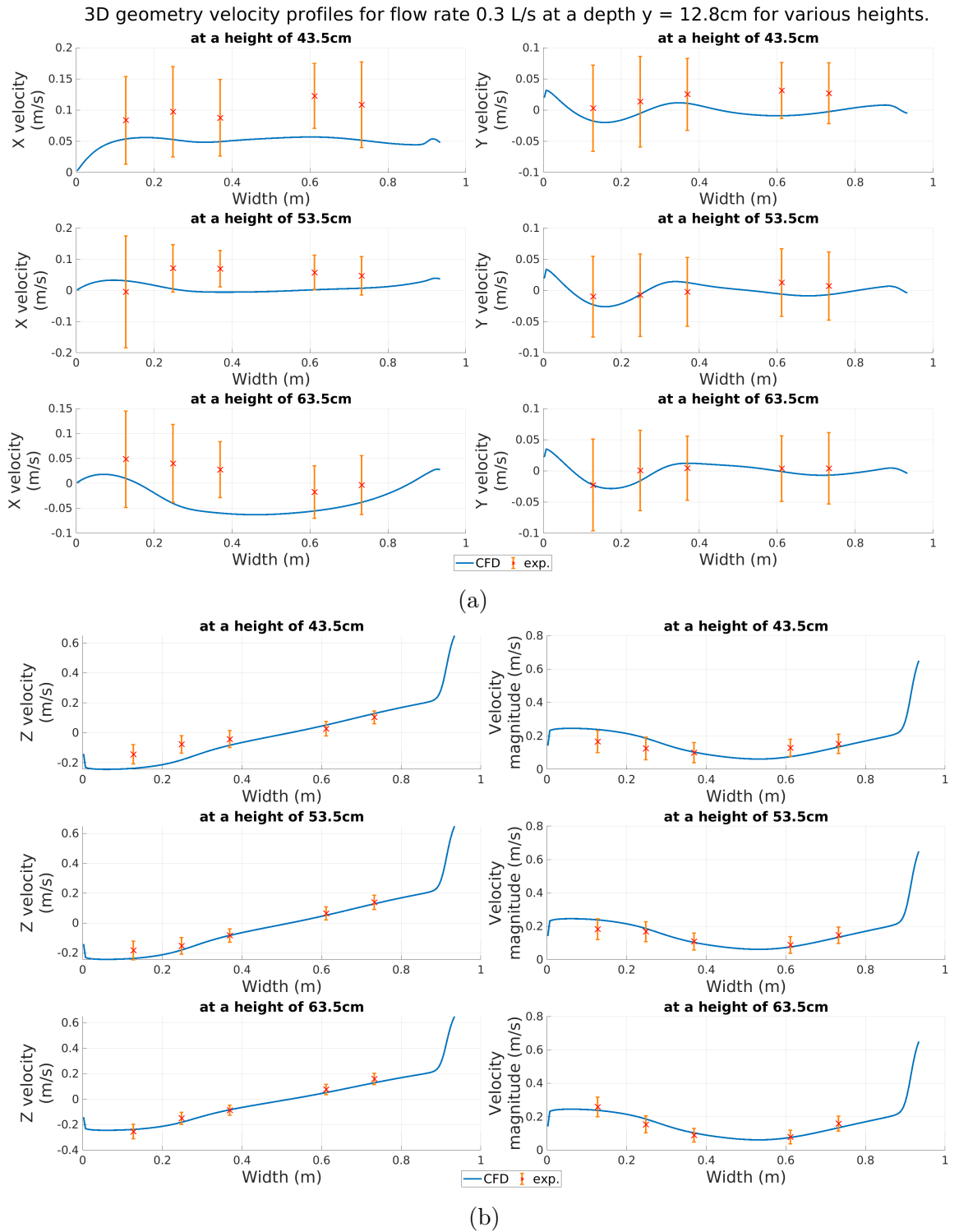


Figure 5.33: Comparison of the one third reactor simulation velocities against experimental data along width profiles at heights: 43.5, 54.5 64.5 cm, at a depth of 12.8 cm for an aeration flow rate of 0.3 L/s. The x and y velocities are shown in (a) and the z velocities and 3D velocity magnitudes are shown in (b).

velocities near the base of the bubble plume in the 0.3 L/s results have a smoother profile across the width compared with the 0.6 L/s case. If we consider the 0.6

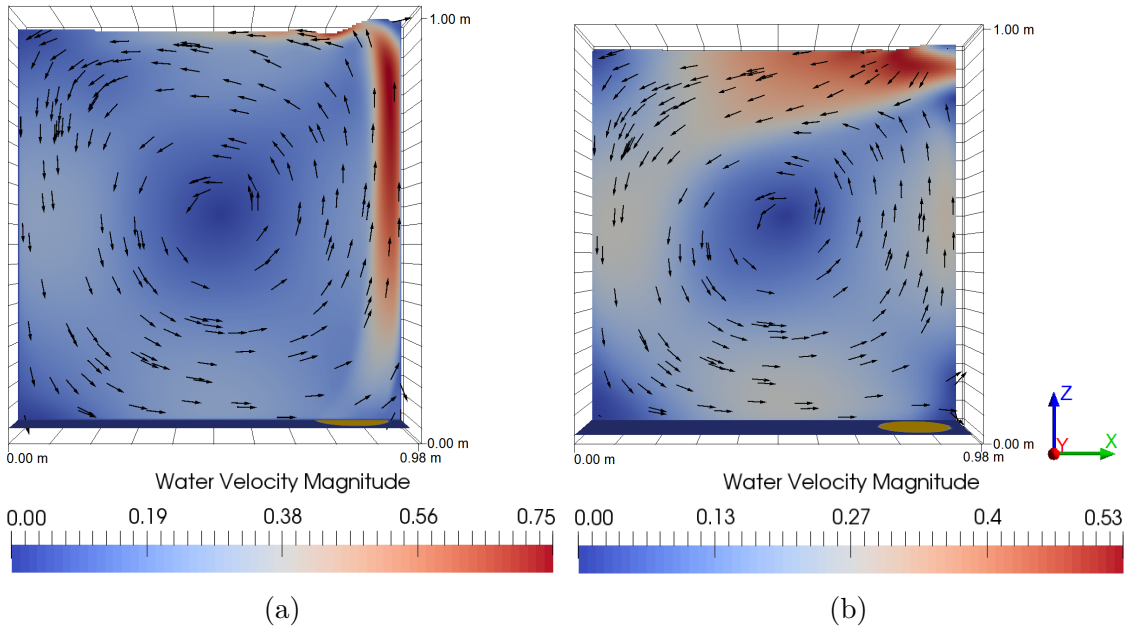


Figure 5.34: The water velocity magnitude (m/s) contour and normalised vector plot for flow rate 0.3 L/s at a depth of: $y = 12.8$ cm (a) and $y = 24.8$ cm (b). The yellow circle at the base illustrates the location of the aerating diffuser.

L/s air velocity profile in figure 5.30a, there are almost two plumes rising upwards from the base that re-combine near the top; while the 0.3 L/s air plume profile in figure 5.30b has only one single rising plume profile. This suggests the 0.3 L/s bubbles are grouping up into one swarm as they rise while the 0.6 L/s bubbles, due to the higher number of bubbles which creates more turbulence and instabilities in the rising plume, form two separate swarms that imitate two plumes.

Assessing the turbulence kinetic energy and intensity contour plots for the 0.3 L/s flow rate results in figure 5.35, it is observed that there is a similar contour profile to those seen in the 0.6 L/s results. The overall turbulence kinetic energy is less than then the 0.6 L/s results which is predictable as the velocities are slower. The majority of the turbulence kinetic energy is at the fluid surface and in the plume which is expected as these are the regions with the most chaotic and complex fluid structures due to the fluid surface and rising bubbles, respectively. Similarly, the turbulence kinetic energy intensity illustrates that the turbulent mixing dominates in the centre and corners of the reactor, as was the case for the 0.6 L/s flow rate simulation.

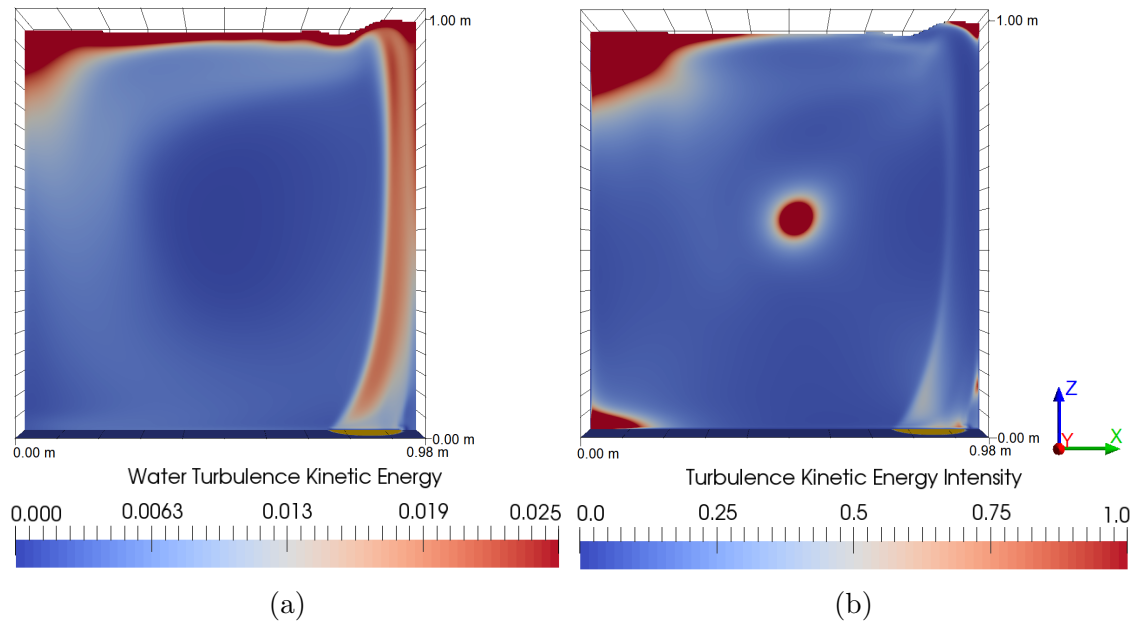


Figure 5.35: The water turbulence kinetic energy (a) and turbulence kinetic intensity ($k_{\text{int}} = k_{\text{water}}/|u_{\text{water}}|^2$) (b) at a depth of $y = 12.8$ cm for flow rate 0.3 L/s. The yellow circle at the base illustrates the location of the aerating diffuser.

Investigating the velocity profiles against the experimental data at a depth of $y = 24.8$ cm for the flow rate 0.3 L/s simulation produces the results illustrated in figure 5.36. The simulation also suffers from the symmetry wall condition problem, as described in the 0.6 L/s case, where the y velocities are all 0 m/s. Similarly, the x velocities are in the correct magnitude range but the location of the vortex differs from the experiments such that the sign values are off for the 63.5 cm height profiles. The standard deviation spread is smaller for the 0.3 L/s experimental data as the flow is slower and more stable such that the ADV measurements are more accurate at this flow rate. The z velocities and velocity magnitudes profiles match well with the experimental data, especially for the 63.5 cm height profiles, with only a slight over prediction of the velocities near the left wall at the 43.5 cm height.

Finally, a comparison of the velocity profile for the two flow rates at a depth of $y = 12.8$ cm was made, as illustrated in figure 5.37. In general, the velocities for all the plots are lower for the 0.3 L/s flow results. The x velocity profiles are very similar for both implying that they are both predicted similar vortex structures. Interestingly, the y velocities are similar with a periodic structure but are out of

3D geometry velocity profiles for flow rate 0.3 L/s, at a depth $y = 24.9\text{cm}$, for various heights.

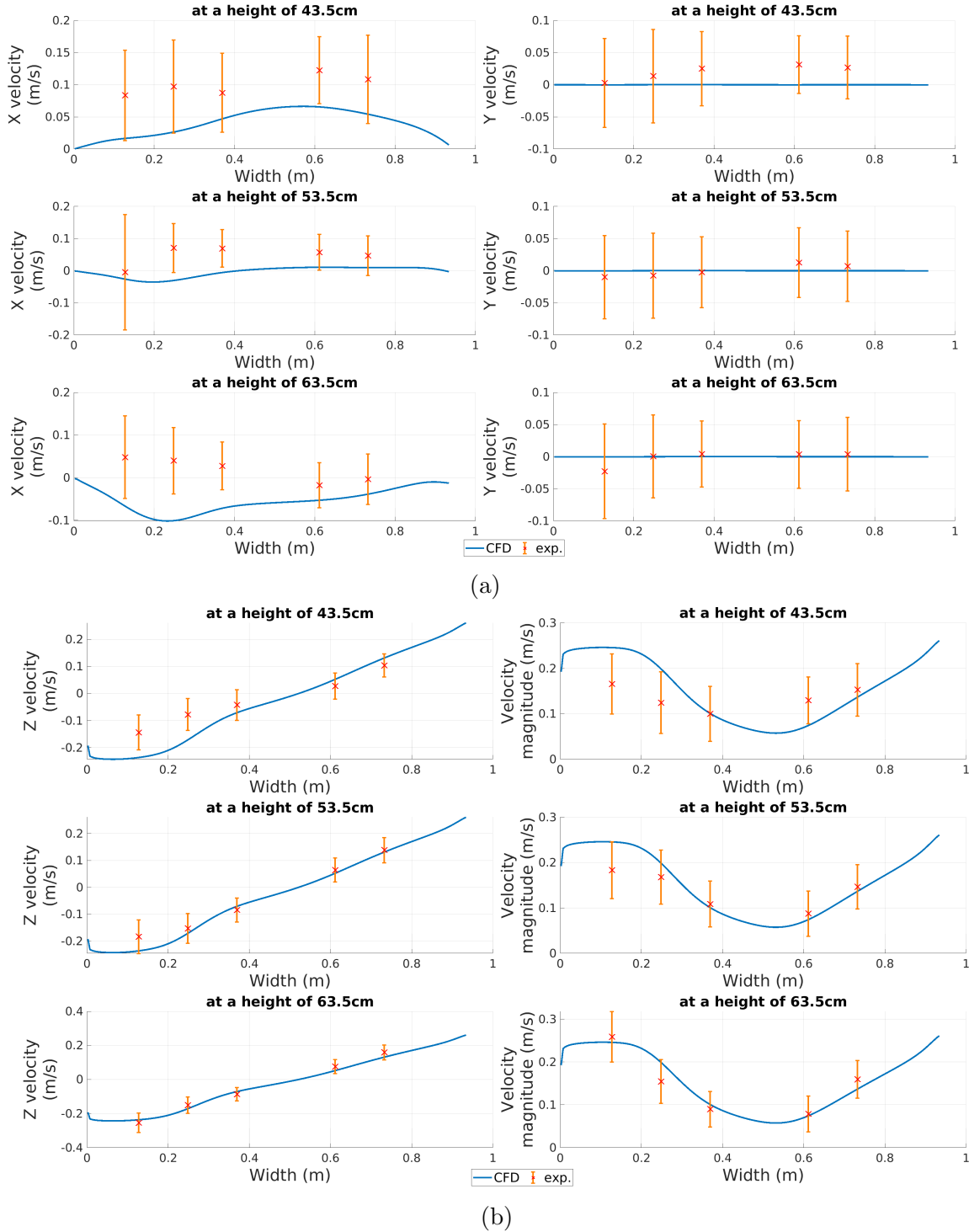


Figure 5.36: Comparison of the one third reactor simulation velocities against experimental data along width profiles at heights: 43.5, 54.5 64.5 cm, at a depth of 24.8 cm for an aeration flow rate of 0.3 L/s. The x and y velocities are shown in (a) and the z velocities and 3D velocity magnitudes are shown in (b).

phase with one another. This suggests that there might be oscillations in the y velocities over time that are longer than the 2 minutes such that, for our 2 minute

3D velocity profiles comparing flow rate 0.3 and 0.6 L/s, at a depth $y = 12.8\text{cm}$, for various heights.

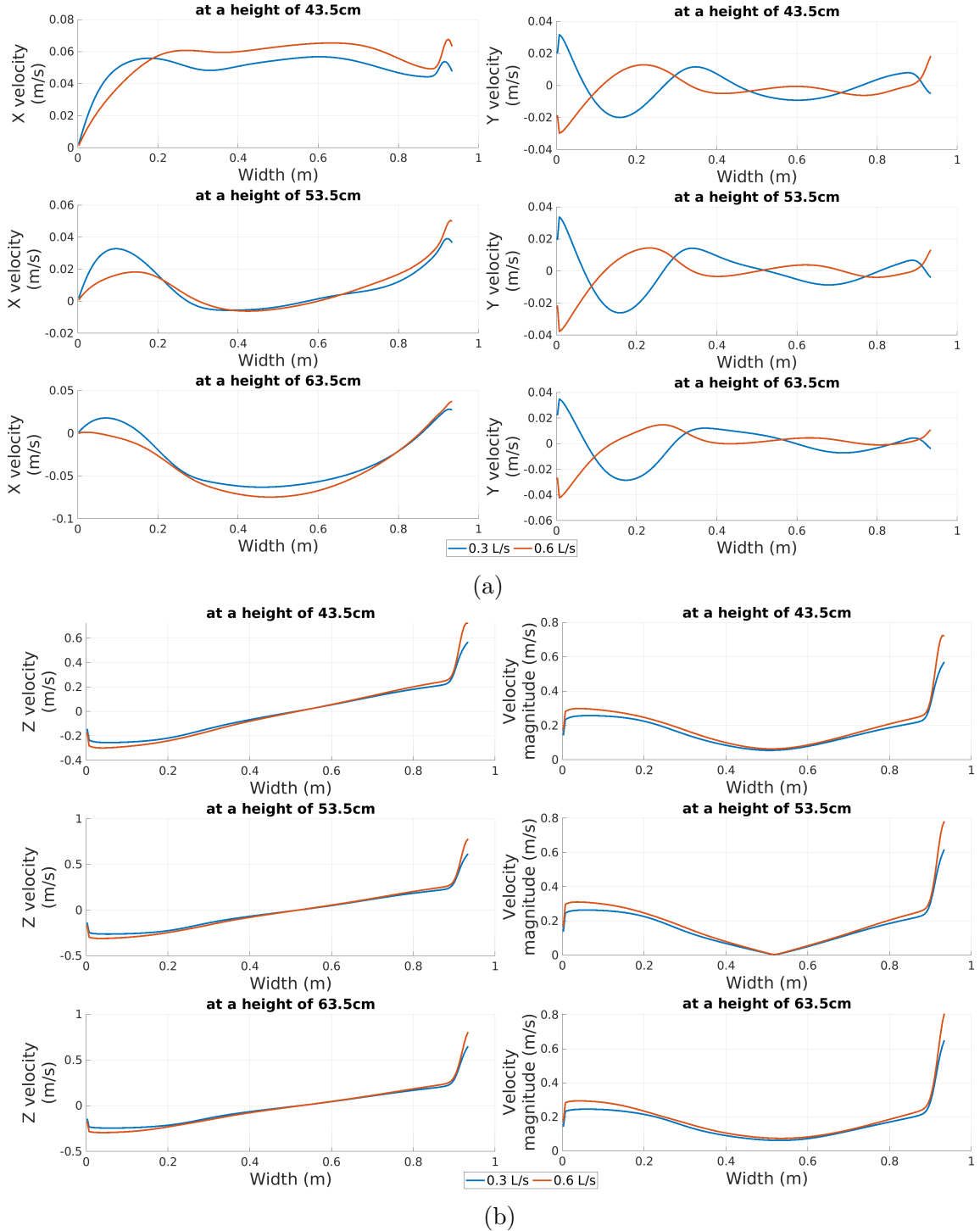


Figure 5.37: Comparison of the velocities for the aeration flow rates 0.3 and 0.6 L/s in the one third reactor simulation along width profiles at heights: 43.5, 54.5 64.5 cm, at a depth of 24.8 cm. The x and y velocities are shown in (a) and the z velocities and 3D velocity magnitudes are shown in (b).

averaging period, we only measured some of the oscillation period. Furthermore, this could explain the large standard deviation spread of the experimental y velocities

as these velocities are combined data from separate runs which could be picking up data from different periods of the oscillations. Surprisingly, besides near the bubble plume, the bulk fluid flow velocities are similar in magnitude for both flow rates. This implies that pumping twice as much air does not increase the convective mixing significantly in the reactor. If an operational aim for this reactor was to reduce the power consumption while still achieving the same mixing efficiency, these results would imply that the 0.3 L/s flow rate could be used in preference to the 0.6 L/s to save on operational costs with minimal changes to the mixing capabilities of the reactor. However, an aeration tank is used to both mix and provide a source of oxygen for the bacteria in the tank. A lower flow rate result could reduce the oxygen mass transfer and cause less oxygen to be available for the bacteria which could impede the biological performance. To investigate this, the coupling methodology would need to be implemented to assess the efficiency gain of using a 0.3 L/s over a 0.6 L/s flow rate.

5.4.3 Summary

A comparison of the 3D CFD results for a flow rate 0.6 and 0.3 L/s against experimental data has been made to validate the model. Additionally, an analysis of the generated flow field and bubble plume behaviour for both flow rates has been conducted and a comparison of the two flow rates with one another and with the 2D simulation has been undertaken. Overall, the 3D results for both flow rates match very well with the experimental data such that it reliably validates the CFD methodology and gives us confidence that the simulations are correctly predicting the hydrodynamics in the reactor. Therefore, these CFD simulation results for both flow rates can be used as the hydrodynamic flow field for the 3D coupled simulations to investigate the impact of the hydrodynamics on the biological processes in a later chapter.

5.5 Chapter summary

In this chapter, a comprehensive modelling study has been conducted to verify and validate the procedures for modelling an aeration tank in 2D and 3D. Through these studies, a CFD model has been created and validated for replicating the hydrodynamics observed in an aeration tank in 2D and 3D. The 2D simulations matched reasonably well with the experimental data such that practical verification studies can be conducted reliably, and the 3D simulations results matched very well with the experimental data for both flow rates considered, validating the modelling procedure. These results confirm that the simulations are reliably able to capture the key hydrodynamics in 3D and 2D that are observed in the aeration tank. This gives us confidence in the accuracy of the simulation results when the oxygen mass transfer is implemented and the impact of the hydrodynamics on the biological processes is investigated in the next chapter.

In order to show that the modelling procedure is suitable, a series of studies has been conducted as outlined below. In the first part of this chapter, the methodology for simulating the aeration tank in OpenFOAM has been described such that the procedure could be repeated. In the following section, the procedure for creating the 2D simulations has been defined and mesh and time independence studies has been completed to confirm the required mesh refinement and time needed to reach a steady state, respectively. The 2D mesh refinement study concluded that a hexahedron mesh with approximately 500 000 cells was refined enough and a run time of 160 seconds was found to be long enough to reach a steady-state. The 2D simulations have been used to conduct a comprehensive verification study on the impact of fine membrane inlet conditions, bubble size, and the bubble-water dynamic force models on the calculated results to assess their reliability in recreating the hydrodynamics in the aeration tank. Additionally, all these simulation included the free surface which, to our knowledge, has not been included in previous simulations of wastewater treatment aeration tanks.

A new method for modelling the fine membrane diffuser was outlined which, to our understanding, has not been proposed before. The inlet condition study found that 20 % of the full inlet surface area was the optimal area for replicating the holes in the diffuser membranes used in the aeration tank which was modelled using a volume fraction of 0.2 with the necessary horizontal inlet velocity to conserve the air flow rate. The free surface was found to have an impact on the calculated results and, therefore, it is important to include to accurately predict the hydrodynamics in the reactor. It was found that a bubble Sauter mean diameter of 2.5 mm matched best with the experimental data which agrees with the average bubble diameter range described in the manual for the membrane diffuser ([xylem, 2020](#)). A detailed study reviewing the various bubble force modelling choices for replicating the bubble-fluid interactions in a fine membrane diffuser driven aeration tank was conducted which, to our knowledge, has not been seen in previous work. The study of the bubble-water dynamic force models found that simulations with the virtual mass force, [Schiller and Naumann \(1935\)](#) drag model and the [Antal et al. \(1991\)](#) wall lubrication force model matched well with the experimental data, validating the modelling procedure. This procedure was then used for describing the bubble dynamics in future simulations with confidence due to these verification and validation studies.

In the next section, a time analysis and mesh independence study was conducted for the 3D 1/3 reactor geometry to confirm the necessary time conditions and mesh refinement. The simulations found periodicity after 160 seconds over a 120 second period such that a 120 second time averaged solution was computed after an initial 160 second had passed and used as the time averaged steady-state result which can then be compared with the measured experimental velocities. Additionally, a mesh refinement study found that we had mesh independence at 2.86 million cells for the 3D geometry.

In the final section, the 2D and 3D hydrodynamic results were compared with one another and the experimental data to assess their reliability of predicting the hydrodynamics in the aeration tank. A study comparing the 2D and 3D simulation

results was conducted and found that the 3D simulations matched better with the experimental data for both flow rates due to the additional dimension being modelled in the 3D simulation which allowed for additional dispersion of the fluid momentum and energy. An analysis of the generated hydrodynamics in the 3D simulations and a comparison of the results against experimental data for validation was completed. The 3D simulation results agreed well with the experimental data which validated the modelling procedure. Finally, a comparison was made between the results from the 0.3 and 0.6 L/s flow rate 3D simulations and it was found that the 0.3 L/s flow rate produced similar levels of mixing in the aeration tank as the 0.6 L/s flow rate which implied that the 0.3 L/s flow; implying the 0.6 L/s to save on operational costs with minimal changes to the mixing capabilities of the reactor. In the next chapter, a description of how to implement and couple the biokinetic models into these generated hydrodynamic flow fields will be defined.

Chapter 6

Coupling hydrodynamics, oxygen mass transfer and biokinetic models

A main focus of this work is to define a procedure for coupling biokinetic wastewater models with the hydrodynamics in OpenFOAM. The coupled model can provide more insight into the link between the hydrodynamics and the biological performance of the reactors in AS systems ([Rehman et al., 2017](#); [Sánchez et al., 2018](#)) and can, therefore, be used to investigate how the biological processes are impacted when accounting for the hydrodynamics.

In this chapter, a procedure for coupling the biokinetic wastewater models into the hydrodynamic simulations with a free surface in OpenFOAM has been defined. An oxygen mass transfer model has been incorporated into the hydrodynamic simulations and verified. This has been used to evaluate the oxygenation of the tank for different diffuser configurations and flow rates. A simple aeration biokinetic model has been defined and coupled into the CFD hydrodynamic solutions to investigate the influence of: diffuser configuration, aeration flow rates, and tank inlet and outlet locations on the biological processes in 2D and 3D to see if there are benefits of the

coupled model over the conventional uncoupled biokinetic models. Finally, the full ASM1 model has been coupled into the hydrodynamic simulations to investigate the influence of the mixing on the biological processes compared with well-mixed reactor.

6.1 Previous work at coupling CFD and biokinetic models

There has been development of single phase ([Littleton et al., 2007](#); [Coughtrie et al.; Meister et al., 2017](#)), two-phase ([Glover et al., 2006](#); [Brannock et al., 2010](#); [Le Moullec et al., 2011](#); [Rehman et al., 2017](#); [Sánchez et al., 2018](#)) and three-phase ([Lei and Ni, 2014](#); [Yang et al., 2016](#)) CFD models that have integrated with ASMs to describe a range of different AS systems. [Glover et al. \(2006\)](#) were the first to propose coupling the hydrodynamics and biokinetic models. They described the procedure for coupling and reviewed the feasibility and draw-backs of the coupled model for future applications. They defined the ASMs and the coupled models as the global and local approaches, respectively. A comparison between these two approaches was given for three different systems: a pilot scale oxidation ditch which was used to validate the two approaches; a rectangle aerated batch reactor which was used to study the behaviour of a perfectly mixed reactor; and a real scale oxidation ditch system. An oxidation ditch schematic is illustrated in figure [6.1a](#).

[Littleton et al. \(2007\)](#) coupled the ASM2 model ([Henze et al., 2007](#)), which is used to model phosphorus removal, to a three-dimensional CFD model that describes a full-scale oxidation ditch. The coupled model was used to analyse if anaerobic potassium-accumulating organisms and general heterotrophic bacteria can coexist in the same closed-loop reactor. They concluded that it is possible to have anaerobic pockets within an aerated closed-loop if the aeration is sparse enough, confirming that these two types of bacteria can coexist in the same reactor.

Brannock et al. (2010) developed a 3D coupled CFD and ASM1 model for a membrane bioreactor (MBR) which reduces waste using biological treatment and then separates the sludge and treated water using an ultra-filtration membrane, as illustrated in figure 6.1b. The CFD model was validated and used to optimise mixing in MBRs and to identify the implications of membrane configurations on energy consumption. The integrated ASM1 model was used to confirm mixing effectiveness by correlating between the coupled model results and a benchmark ASM1 model. However, large differences were found with results in the aerobic tanks which implied further work is need to accurately model the oxygen transfer.

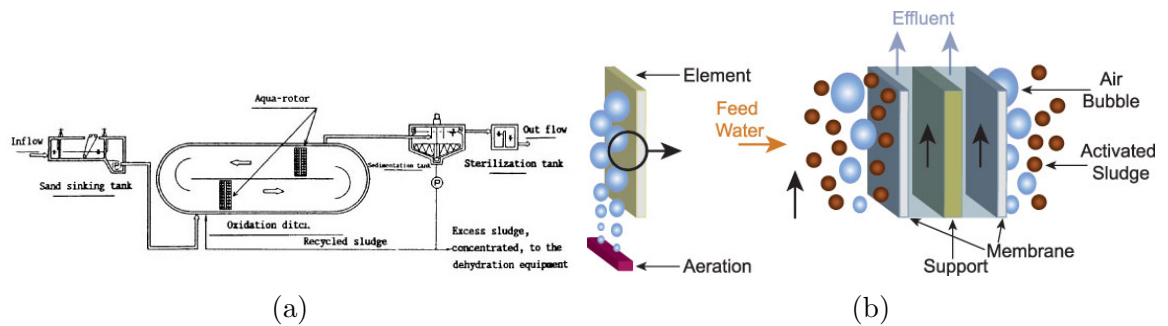


Figure 6.1: Schematic of an oxidation ditch (a) and an explanation of how MBRs work (b).

Le Moullec et al. (2010a) developed a two-phase coupled CFD and ASM1 model to investigate a long length gas-liquid pilot-lab scale reactor that contained an anoxic zone, aerobic zone and settler. The developed model could simulate the hydrodynamics, oxygen mass transfer and biological reactions in an AS pilot reactor and simulation results were compared to experimental data. The oxygen mass transfer was overestimated by the Higbie model (Higbie, 1935) compared to experimental values and so a larger bubble size was used to correct for this. It was found that the coupled model predicted some of the experimental parameter concentrations correctly while others, such as soluble ammonia concentrations, were predicted poorly. They concluded that, in a more rigorous CFD model, a third phase would be included to model flocs. Flocs are highly hydrated solids that are normally considered perfectly soluble in the liquid phase but could be modelled explicitly. Modelling flocs would require a new set of transfer and kinetic constants in the ASM1 model

to account for local affects.

[Le Moullec et al. \(2010b\)](#) also investigated another approach (the compartmental approach) proposed by [Rigopoulos and Jones \(2003\)](#) and [Guha et al. \(2006\)](#) to couple the biokinetics and hydrodynamics by comparing the reactor to a network of both structural and functional compartments. In the compartmental approach, a reactor is separated into a series of structural and functional compartments based on similar hydrodynamic structures in the flow field, as illustrated in figure 6.2. [Le Moullec et al. \(2010b\)](#) presented a compartmental methodology for the coupled model for the same pilot-lab scale bioreactor presented in [Le Moullec et al. \(2010a\)](#) for comparison. The compartments were determined from both the process knowledge and CFD results and it is assumed the biological concentrations in the ASMs are homogeneous in these compartments with a given tolerance. [Le Moullec et al.](#) concluded that the compartmental model can lose out on accuracy compared to the coupled model but, the approach is computationally quicker. The compartmental model can extract the necessary information from the CFD model to quickly calculate the biokinetic concentrations. However, it is important to note that [Le Moullec et al.](#) chose the compartments based on the hydrodynamic structures and not the characteristic reaction time suggested by [Guha et al.](#). Therefore, there is an element of their own judgement in the simulation setups which is not mathematically consistent and could impact on results. Also, the models are not easily repeatable for alternative systems. If the compartments were solved, based on the characteristic reaction time ([Guha et al., 2006](#)), it could be found that the computational expense of the simulation is the same or greater than the coupled CFD and biokinetic models.

[Coughtrie \(2016\)](#) developed a new model that coupled the hydrodynamics for a gas-mixed bioreactor to a nutrient based biokinetic and photosynthetic growth model for algae. The CFD model was taken from previous work ([Coughtrie et al., 2013](#)) that used a CFD model to investigate the accuracy of different turbulence models for predicting the experimental results in a gas-lifted AD with a central draft-tube,

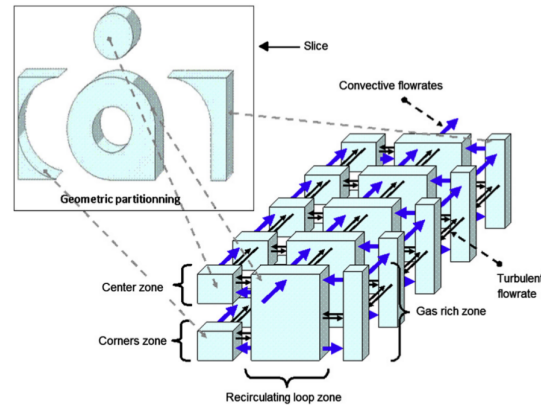


Figure 6.2: An image of the compartmental breakdown for [Le Moulec et al. \(2010b, 2011\)](#)

as illustrated in figure 6.3. Comparisons were made between the different turbulence models on their ability to predict velocities, separation, reattachment and overall flow-field. Additionally, a comparison study between the Euler-Lagrange multiphase and single phase models at predicting the solution was completed. The conclusion drawn were the transition-SST turbulence model provided the most accurate predictions while the RNG $k - \epsilon$ model was shown to be unsuitable for modelling the digester's low-Re number flow. It was found that the Eulerian-Lagrangian multiphase and single-phase model provided comparable solution predictions and, therefore, the single-phase model could be used with confidence to model the AD; providing a significant reduction in complexity and computational expense. The integrated biokinetic model is a combination of a nutrient limited growth model and a light limited photosynthetic growth model which describes the impact of the algae cells storage capabilities and light availability, respectively, on the absorption rate of nutrients for growth. The combined photosynthesis nutrient growth model was then integrated into the CFD model to form the photosynthesis nutrient and hydrodynamic model. The coupled model was compared and validated against time-dependent experimental data from the literature. Furthermore, [Coughtrie \(2016\)](#) looked at minimising the mesh quality while still containing the most important fluid features. Each mesh cell can be modelled as a continuous-stirred-tank that can utilise the tank in series method that assumes each cell is like a perfectly mixed micro-reactor with

flow leaving and entering from adjacent cells. This is similar to the compartmental method described by [Le Moullec et al. \(2010b\)](#). The coupled model predicted the biomass growth accurately for the first 7 days but then over-predicts the results once the external nitrogen was depleted. The coupled model showed improved biomass growth compared to the uncoupled model when increasing the reactor volume for all sizes.

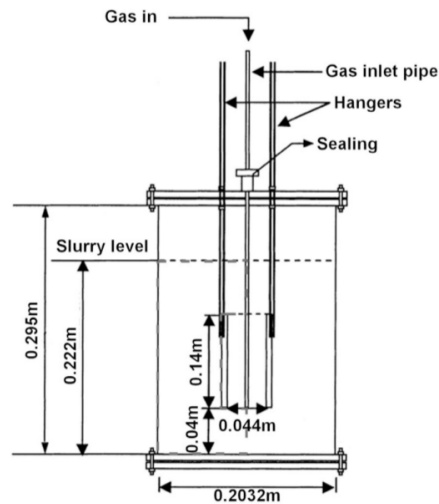


Figure 6.3: The bench scale AD geometry ([Coughtrie et al., 2013](#)).

[Yang et al. \(2016\)](#) developed and validated a coupled CFD and biokinetic model. This incorporated the oxygen mass transfer and sludge rheology for a lab-scale air-lift external circulated membrane bioreactor. The validated model was then used for optimisation studies of membrane configuration and aeration profiles to improve membrane scouring and nitrogen removal efficiency within the lab-scale reactor, respectively. A simplified 3 species ASM1 was used for the biokinetic model that describes nitrogen transformation ([Zhao et al., 1995](#)) and the Higbie model for oxygen mass transfer ([Higbie, 1935](#)). A cost-effective membrane scouring configuration and nitrogen removal rate was found using the coupled model by modifying the gas-liquid height and aeration intensity. However, further work would be required to evaluate if the results apply for large-scale MBRs.

6.1.1 Coupling biokinetic model in aeration tanks

The first attempt to couple the biokinetic and hydrodynamics in an aeration basin CFD simulation was conducted by [Gresch et al. \(2011\)](#); however, they only coupled a simple Monod hyperbolic term and did not model the mass transfer of oxygen into the fluid. Further coupling work with aeration was done by [Lei and Ni \(2014\)](#) in which they calibrated and validated a three-phase 3D coupled model to describe sewage water, air bubbles and activated sludge in a pilot-scale oxidation ditch, as illustrated in figure 6.4. The coupled model was used to investigate the effect of the pseudo-solid sludge phase on the oxygen mass transfer and biological processes by varying the activated sludge and other biological component concentrations in the wastewater. Modifications needed to be made to the oxygen transfer rate and the ASM1 parameters to accurately represent the transport of sludge in the oxidation ditch. The calibrated coupled model was used to gain insight into the behaviour of oxidation ditches. They recommended that the coupled model could be used as a design tool to find optimal arrangements of aeration zones in an oxidation ditch.

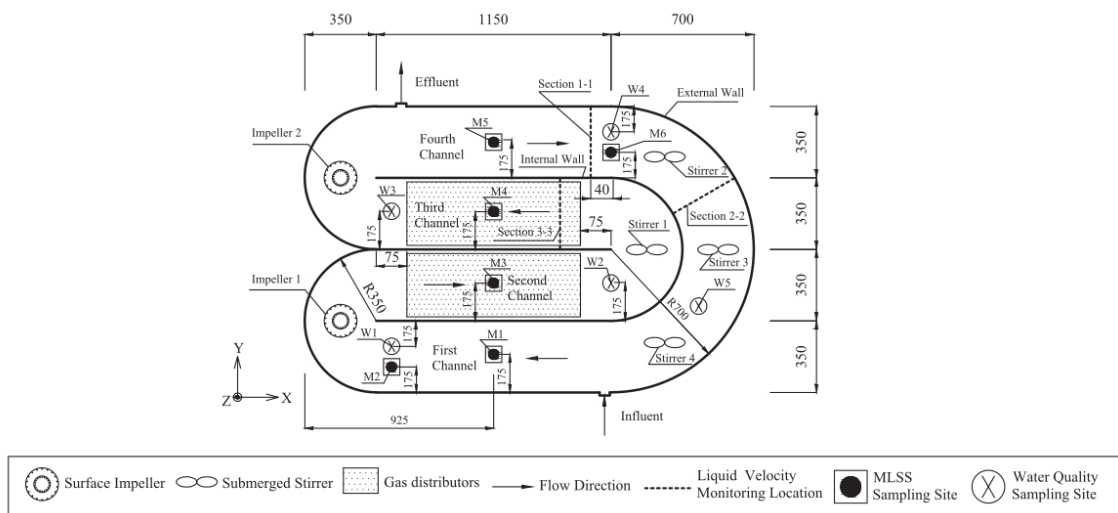


Figure 6.4: Schematic for the pilot-scale oxidation ditch modelled in [Lei and Ni \(2014\)](#).

[Rehman et al. \(2017\)](#) developed a coupled CFD model with the biokinetic ASM1 model to provide evidence that incomplete mixing in an aeration basin leads to inhomogeneity of the biokinetic component concentrations and demonstrated the

added value the coupled model can provide for process, analysis, and evaluation of full-scale systems. This was achieved by CFD modelling an aeration compartment of a full-scale plant and validating it experimentally. The hydrodynamic CFD model used the mixture model for modelling the two phases; the realizable $k - \epsilon$ turbulence model to close the RANS equations; and a bulk density model to simulate the wastewater properties. Acoustic Doppler current profiles were used to take velocity measurements to validate the the CFD model. The steady state solution was found for the CFD simulation and used for the coupled simulations and the Higbie model (Higbie, 1935) was used to calculate the mass transfer coefficient. The coupled simulations were run using a frozen steady state hydrodynamic solution from the CFD simulations. A range of constant influent conditions and air flow rates were simulated and compared with a traditional tank in series model. The coupled model predicted non-uniform concentrations in areas of poor mixing that had commonly been assumed as well-mixed and it was shown that the tank in series model would not capture the dynamic conditions seen in the CFD model. Additionally, they found local fluid density fluctuations can impact the hydrodynamics which then impedes the biological processes. The coupled model results illustrate the benefits of combining the two models to observe how the hydrodynamics affects the performance of the biological processes. However, the model included additional mechanical stirrers and did not look at the impact of the aeration only as the driving force for mixing (Amaral et al., 2018). Furthermore, the mixture model was used to model the two-phase interactions which might be applicable for this reactor. However, this does not allow direct modelling of the bubble-fluid interactions which is possible in the Eulerian-Eulerian formulation and is important for the fine membrane bubble driven aeration tanks.

Sánchez et al. (2018) created a coupled model and investigated how intermittent aeration can impact the biological processes. The CFD model used a two-phase Eulerian-Eulerian model to simulate the liquor and gas; the $k - \epsilon$ turbulence model for closure of the RANS equations; and the Higbie model (Higbie, 1935) for modelling

the mass transfer of the oxygen. A “frozen” steady state CFD simulation of the aerators on and off is found and the coupled transient simulation switches between the two steady-state flow field solutions when modelling the intermittent aeration. The evaluation found that a reduction in flow rate could increase the efficiency of the aeration systems with a reduced power consumption. However, the research only considers the aeration on and off and not how alternative configurations can impact the amount of oxygen available and they neglect the transient behaviour of their reactor in the hydrodynamic simulations. Additionally, they provide minimal information about the creation and validation of the hydrodynamic CFD simulation. A summary of the model choices for five papers that have followed similar procedures conducted in this thesis are presented in Table 6.1.

Paper	Wastewater Unit Process Modelled	Dim	Biokinetic Model	Multiphase Phases.	Turbulence Model	Mass Transfer Model	Bubble Force Interactions	Steady or Transient?
Gresch et al. (2011)	Full scale Aeration Tank	3D	Monod-type Kinetic	(Euler-Euler) Sewage – Air.	SST k – omega Model	-	>Drag >Buoyancy	CFD – Trans. Coup – Trans.
Lei & Nei. (2014)	Pilot-scale Oxidation Ditch	3D	ASM1	(Euler-Euler) Sludge – Sewage – Air.	K – epsilon Model	Higbie Model (- Bubbles); Kumar and Rao (- Surface Aeration).	>Drag >Buoyancy >Lift >Virtual Mass	CFD – Steady. Coup – Steady.
Karpinska & Bridgeman (2017)	Lab-scale Aeration Tank.	3D	-	(Euler-Euler) Water – Air.	SST k – omega Model	Higbie Model.	>Coalescence >Break up >Drag >Buoyancy	CFD – Trans.
Rehman et al. (2017)	Water Resource Recovery Facility	3D	ASM1	(Mixture) Sewage – Air.	Relizable K – epsilon Model	Higbie Model.	>Buoyancy	CFD – Steady. Coup – Trans.
Sanchez et al. (2018)	Full-scale Activated Sludge Reactor.	3D	ASM1	(Euler-Euler) Sewage – Air.	K – epsilon Model	Higbie Model.	>Buoyancy >Drag >Virtual Mass	CFD – Steady. Coup – Trans.

Table 6.1: Summary of key modelling choices used in [Gresch et al. \(2011\)](#); [Lei and Ni \(2014\)](#); [Karpinska and Bridgeman \(2017\)](#); [Rehman et al. \(2017\)](#); [Sánchez et al. \(2018\)](#), that have investigated wastewater aeration tanks using CFD with coupling of the oxygen mass transfer and ASMs.

In this chapter, a procedure for coupling the biokinetic equations into the hydrodynamics solutions in OpenFOAM will be outlined. The difficulties in coupling the two-phase CFD simulation results compared with single-phase results will be explained. The free surface has been included in the hydrodynamic simulations, which has been neglected in previous work, and needs careful consideration when coupling in the biokinetic models. The methods for achieving this will be outlined

and solutions to the difficulties that arose will be described. The oxygen mass transfer model will be defined and implemented to assess the oxygenation in the tank. The results from this will be used to derive global volumetric oxygen transfer rates and saturation concentrations in various tank configurations and an analysis of the results to derive what are the dependency of the calculated values. Finally, the ASMs will be coupled into the hydrodynamic simulation results and used to investigate how the hydrodynamics can impact the biological processes. These will be compared with the non-coupled ASM that have implemented the previous derived global volumetric oxygen transfer rates and saturation concentrations for each tank configuration to produce similar oxygenation rates in both models. As a result, a direct comparison of how the hydrodynamics impact the biological processes can be made which, to our knowledge, has not been implemented in previous work.

6.1.2 Coupling using Smooth Particle Hydrodynamics (SPH)

Another approach for coupling the hydrodynamics and biokinetic models is the meshless, Lagrangian, smoothed particle hydrodynamic (SPH) method. The SPH method was developed by [Gingold and Monaghan \(1977\)](#) and [Lucy \(1977\)](#) as a numerical technique to solve astrophysics hydrodynamic equations. SPH is a fully Lagrangian, meshless, CFD method that has been applied to a wide range of problems. The advantages of the SPH method is the ease of modelling advection due to the Lagrangian nature and ability to conveniently incorporate physical conservation laws. However, the SPH method is computationally more expensive than mesh-based CFD methods but, its simplicity and robustness in incorporating the biokinetic models makes it a viable application for modelling wastewater treatment.

[Meister et al. \(2015, 2017\)](#) proposed a 2D SPH model for simulating the wastewater hydraulics and biokinetic processes for a series of AS tanks. They outlined the methodology behind the model: each particle contains a set of variables whose value is a weighted sum of the surrounding particles and itself; and the Navier-

Stokes equation can be split into an ordinary differential equation for each particle and integrated in time. The ASM1 model is used as the biokinetic model which is coupled by treating each particle like a perfectly mixed micro-reactor which moves with the overall tank flow. Each reactor is independent of the surrounding particles unless near an inflow or outflow where the concentrations are averaged over the particles in the inflow or outflow area. The model was used to simulate both an anoxic and aerobic tank where air bubbles were modelled using four SPH particles to save on computational power. Figure 6.5 illustrates an overview of the ASP and an example of the SPH anoxic basin. The biokinetic compound concentrations were evaluated by segmenting particles into grids of constant size in the tank. The results were validated with reference data from the original ASM1 model and gave good agreement demonstrating its capabilities for modelling wastewater treatment processes. However, the model is unable to simulate growth and decay of biomass in the biokinetic model; or diffusion of concentrations within the Lagrangian framework. Additionally, it suffers from high computing requirements which is dependent on number of particles, this is a significant issue when extensions are made to 3D.

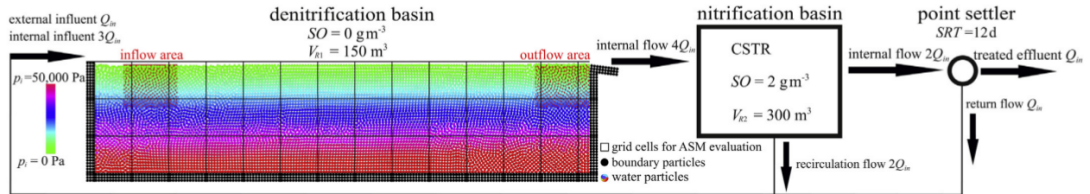


Figure 6.5: Overview of the ASP and SPH model for an anoxic basin Meister et al. (2017)

6.2 Proof of concept for coupling biokinetic models into CFD simulations

In §2.2, we defined a simple 2 species biokinetic model and extended the rate equations to account for the hydrodynamics and the local inlet and outlet, as defined in

equations (2.10) and (2.11). For ease of explanation, these are shown again below,

$$\frac{dX_B}{dt} + \nabla \cdot (\mathbf{u}X_B) - \nabla \cdot (\Gamma_{X_B} \nabla X_B) = \frac{\hat{\mu}S_s}{K_s + S_s} X_B - bX_B + \frac{Q_{in}}{V_{in}} X_{B_{in}} - \frac{Q_{out}}{V_{out}} X_B, \quad (6.1)$$

$$\frac{dS_s}{dt} + \nabla \cdot (\mathbf{u}S_s) - \nabla \cdot (\Gamma_{S_s} \nabla S_s) = -\frac{1}{Y} \frac{\hat{\mu}S_s}{K_s + S_s} X_B + \frac{Q_{in}}{V_{in}} S_{s_{in}} - \frac{Q_{out}}{V_{out}} S_s.$$

In this section, we will describe the process of how these transport equations are implemented and solved in a single-phase CFD simulation in ANSYS Fluent for proof of concept before we attempt to achieve the same for two-phase simulations in OpenFOAM. If we couple the transport equations straight into the CFD simulations then the biokinetic components are solved in each mesh cell along with the other CFD variables every iteration. To initially investigate the coupling procedure, the 2D SPH anoxic basin defined in Meister et al. (2017) and illustrated in figure 6.5 was replicated in ANSYS Fluent (Ansys, 2018) and the two-species biokinetic equations defined in equation (6.1) were coupled into it. The basin had a total fill volume of 152 m³ (14 m × 3.3 m × 3.3 m) and a 2D slice through the middle of the depth at 1.65 m with dimensions 14 m × 3.3 m was modelled, as illustrated in figure 6.6a. The SPH model in Meister et al. (2017) does not have conventional inlet and outlet surfaces as with normal CFD models but a region of cells in a zone that are designated the inlet and outlet zones, that have the inlet and outlet sources terms in the biokinetic transport equations applied in those cells, respectively. Additionally, the basin is mixed with a rotational mechanical stirrer (Meister et al., 2017) which is simulated by having zones within the domain that increase the momentum of the fluid as they enter, referred to as recirculation zones, which increases momentum towards and away from the outlet in the top and bottom zones, respectively. A mesh replicating the inlet, outlet and recirculation zones used in the SPH model was created in ANSYS ICEM (Ansys, 2018) and is illustrated in figure 6.6b.

Additionally, a mesh with an inlet and outlet surface was also simulated to compare the difference between the two inlet modelling approaches and their im-

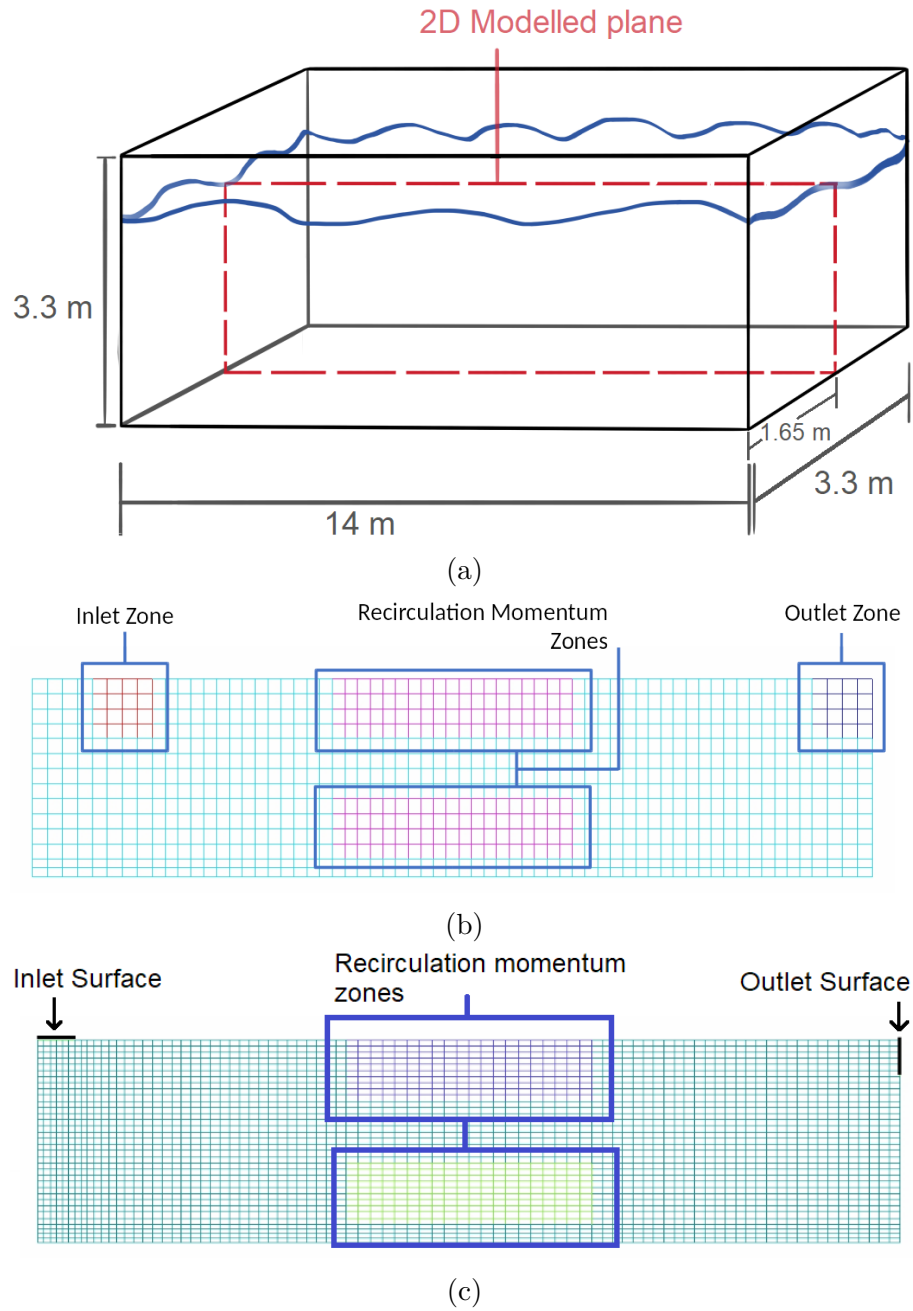


Figure 6.6: An illustration of the 2D anoxic reactor geometry being modelled (a) and the mesh for used for the simulations where the inlet and outlet as been modelled with zones (b) and as surfaces (c).

pact on the biological processes. In this case, the transport equations defined in equations (2.10) and (2.11) no longer have the inlet and outlet source terms but instead, the fluid entering through the inlet carries the biokinetic component concentrations which will leave with the fluid when they pass through the outlet. The outlet was defined as a pressure outlet and the inlet was defined with a volumetric flow rate of $Q = 0.0243 \text{ m}^3/\text{s}$, corresponding to a fill time of 2 hours, which is a

desired hydraulic retention time (HRT) of an anoxic basin [Meister et al. \(2017\)](#). An illustration of this mesh is presented in figure [6.6c](#) where the recirculation zones values are the same as defined in figure [6.6b](#).

The two reactor cases were transient and run for 24 hours with the coupled two species biokinetic transport equations. The hydrodynamics reached a steady-state flow field within a few minutes of the simulation run time. The velocity and vector profiles for the inlet zone and surface simulations are presented in figures [6.7a](#) and [6.7b](#), respectively. The flow field structure for both simulations are identical; however, the inlet zone has overall faster fluid velocities in the right vortex loop which is surprising as they are both being stirred in the same way. The difference is due to the presence of the outlet surface in the top right of figure [6.7b](#) as this allows fluid to leave after being driven across, so a large portion of the fluid momentum is removed. In the inlet zone simulation, due to the nature of the closed box setup, the infused fluid momentum cannot leave and can only be transferred to help further mix the reactor, resulting in larger velocities. Both simulations have a fast and slow moving vortex on the right and left of the reactor, respectively.

The initial and inlet values for the biokinetic concentrations, the values of the constants in the biokinetic transport equations, and the flow rate and volume values for the inlet zone simulation are defined in table [6.2](#). The contour plots of the biological concentrations after the 24 hours along with the velocity vector profiles are presented in figures [6.8a](#) and [6.8b](#) for the inlet zone and surface simulations, respectively.

As illustrated in figure [6.8](#), the different speeds of the two vortices are having an impact on the biological processes. The slower vortex to the left has a larger variation in concentrations compared with the faster vortex to the right where the concentrations are almost uniform. A key difference between the two inlet modelling approaches is the concentrations profiles near the inlets. The concentrations entering through the inlet surface have some momentum as they enter with the flow, as seen in figure [6.8b](#), which causes the newly entered concentrations to flow downwards

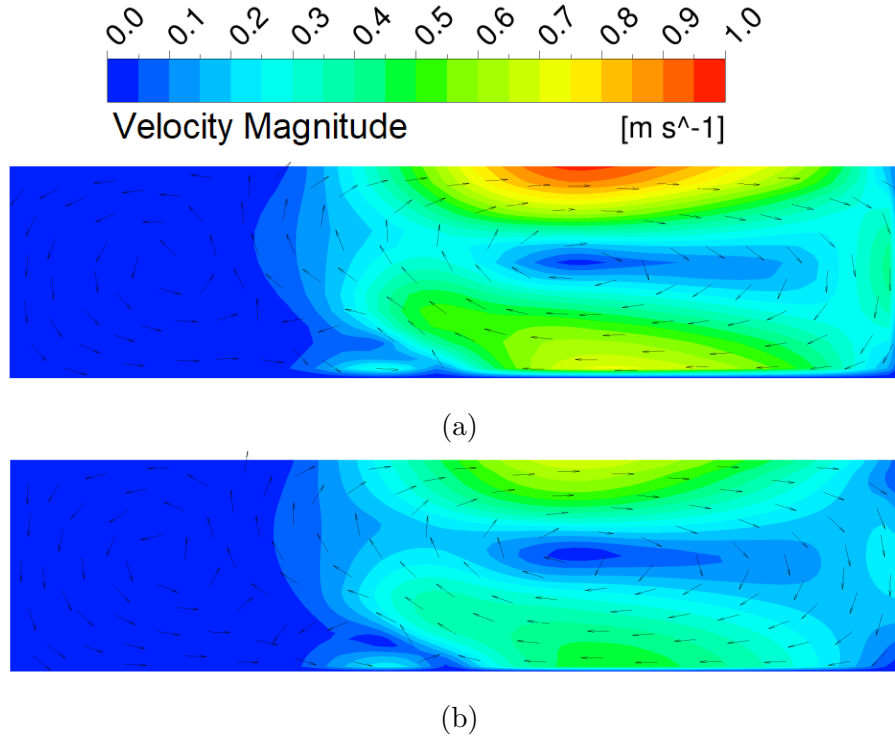


Figure 6.7: Velocity magnitude contour and normalised vector plots of the 2D anoxic basin for the inlet zone (a) and surface (b) simulations.

Parameters	Notation	Value	Units
Maximum specific growth rate	$\hat{\mu}$	6.94×10^{-5}	s^{-1}
Decay rate	b	2.31×10^{-6}	s^{-1}
Growth yield	Y	0.67	-
Diffusion coefficient of parameter i	Γ_i	1.0×10^{-5}	$\text{m}^2 \text{s}^{-1}$
Half velocity constant for S_s	K_s	20.0	mg/L
Inlet and outlet flow rate	Q_{in}, Q_{out}	0.0243	m^3/s
Inlet and outlet zone volume	V_{in}, V_{out}	117	m^3
Initial S_S tank concentration	$S_{S,initial}$	63	mg/L
Initial X_B tank concentration	$X_{B,initial}$	31	mg/L
S_S inlet concentration	$S_{S,inlet}$	15	mg/L
X_B inlet concentration	$X_{B,inlet}$	25	mg/L

Table 6.2: The initial and inlet concentrations, biokinetic transport equations constants, and inlet zone model values for the simulated 2D anoxic basin coupled model.

and then to the right which results in the new concentrations reaching the faster vortex to the right. In the inlet zone simulation, because the new concentrations enter with no initial momentum, they are unable to leave the slow moving vortex as easily which is why the concentrations are slightly lower in the right vortex of

figure 6.8a. This illustrates that the location chosen to input the concentrations into the reactor can significantly influence the biokinetics if the reactor is not well stirred. In summary, it has been shown that the hydrodynamics can impact the biological process in the reactor such that we do not get a uniform distribution of concentrations in the reactor which can also be captured in the CFD simulations.

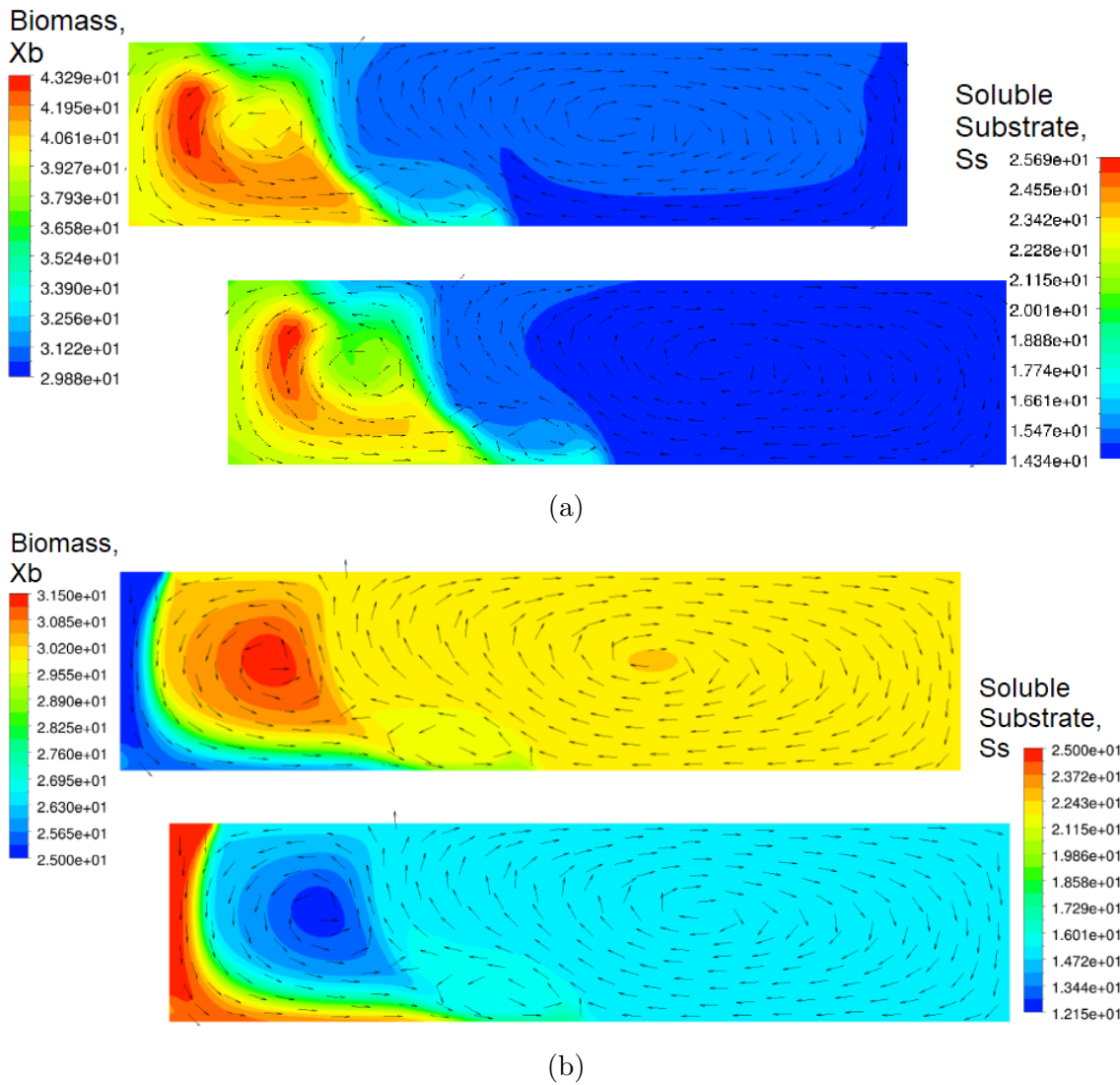


Figure 6.8: Contour plots with the normalised velocity vector maps of the biokinetic concentrations X_B and S_s (mg/L) in the anoxic basin after 24 hours for the inlet zone (a) and inlet surface (b) simulation.

Finally, an identical system was run in the ASIM5 software, as described in §2.1.3, that assumes the reactor is well-mixed such that the concentrations are uniform throughout the reactor. The results from this were compared with the average concentrations throughout the reactor for each biokinetic component from the two

CFD simulations over time. The average concentrations over time are presented in figure 6.9 and the final results after 24 hours are presented in table 6.3. It takes 10 to 15 hours for the S_S and X_B concentrations to reach a steady-state in all 3 models, respectively. The ASIM5 and inlet surface simulation match very well which implies that the inlet surface reactor is behaving as a well-mixed reactor while the difference seen in the inlet zone simulation implies the hydrodynamics in this reactor is having an effect on the biological processes such that the concentrations are not matching with the ASIM5 results, illustrating that the hydrodynamics can impact the biological processes.

These simulations were run as a proof of concept for coupling biokinetic equations into CFD simulations; however, these has been done using a simple, single phase, low resolution CFD simulation setup. The aeration tank we have modelled is two-phase which raises additional challenges in coupling the biokinetic equations, specifically that the air volume fraction acts as a source term for the soluble oxygen which needs to be modelled. Additionally, the biokinetic equations in these coupled simulations were solved at the same time as the hydrodynamic flow field. This was acceptable for these simulations due to the low mesh resolution. However, at higher mesh resolutions, this becomes computationally more expensive. The time scale required to solve the hydrodynamics is in seconds while the biokinetic equations are in hours and days. Therefore, there is a challenge in dealing with these two time scales effectively to reduce computational costs while retaining accuracy. In the next sections, we will discuss how this coupling is implemented in OpenFOAM and the challenges and solutions needed to deal with the computational complexities with coupling the hydrodynamics and biokinetics for two-phase solutions.

6.3 Solver setup - *scalarTransportFoam*

The hydrodynamic flow field has been solved in the aeration tank using the *reactingTwoPhaseEulerFoam* OpenFOAM solver (OpenFOAM, 2020), as described in

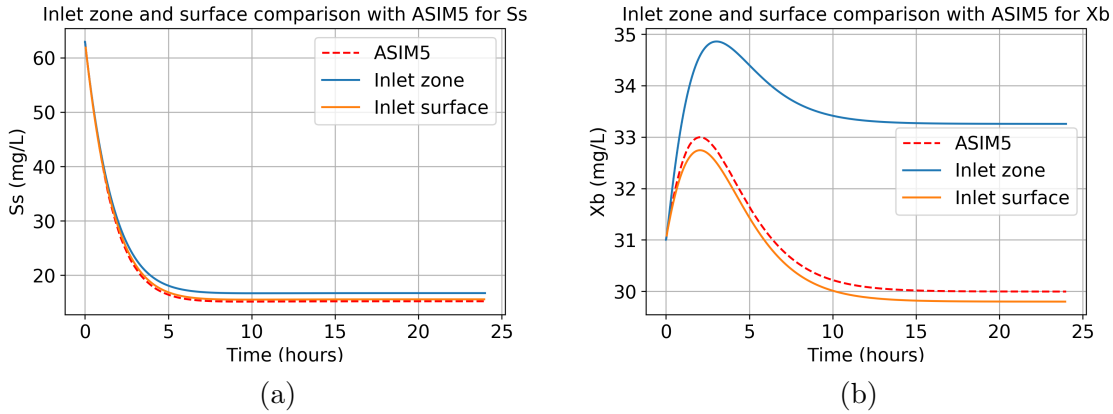


Figure 6.9: A comparison between the two coupled simulations and the ASIM5 software results for the average biokinetic concentrations S_S (a) and X_B (b) over a 24 hour period.

Software	Biokinetic component	Average reactor concentration (mg/L)	Standard deviation (mg/L)
ASIM5	X_B	29.91	-
ASIM5	S_S	15.37	-
Fluent, Inlet zone	X_B	33.17	4.17
Fluent, Inlet zone	S_S	16.64	3.30
Fluent, Inlet surface	X_B	29.63	1.14
Fluent, Inlet surface	S_S	15.92	2.77

Table 6.3: Final average biokinetic concentrations after 24 hours for the two coupled simulations along with the standard deviations of the averages to give an indication of the distribution of the concentrations in the reactor and the ASIM5 final results.

§5.1, and the steady-state or time averaged flow field has been found for the 2D and 3D results, respectively. The objective in this chapter is to couple the biological processes into these hydrodynamic fields. However, if the transport equations were to be coupled straight into the two phase solver, this would lead to extremely high computational times as the extra transport equations would be solved at the same time as the two-phase fluid equations. Furthermore, the time scales of the biological processes is in the hour to day scale while the hydrodynamics is in the scale of seconds. Therefore, solving both at the same time would be extremely computationally inefficient. The aeration tank flow field was found to have reached a

time averaged steady-state after 3 - 5 minutes such that we expect the hydrodynamic flow field to be relatively unchanged for the hours required for the biological processes to take place. As a result, we can take this solved flow field from the two-phase simulation and assume it is constant over the time period required for the biokinetics. Therefore, the Navier-Stokes equations no longer need to be solved and only the transport equations need to be calculated. This allows for a larger time step to be used for solving the transport equations which would not be possible with the Navier-Stokes equations as it would result in instabilities. Similarly to the *reactingTwoPhaseEulerFoam* solver described in §5.1, OpenFOAM has another solver called *scalarTransportFoam* (OpenFOAM, 2020) which allows for a static fluid velocity field to be imported in as the velocity field when solving of the biological scalar transport equations, as defined in equation (6.1).

To explain how the *scalarTransportFoam* solver works, we will consider the transport equation for concentration, C , defined below,

$$\frac{dC}{dt} + \nabla \cdot (\mathbf{u}C) - \nabla \cdot (\Gamma_C \nabla C) = S_{C, \text{source}} - S_{C, \text{sink}}. \quad (6.2)$$

The \mathbf{u} is the imported velocity field from the two-phase solver; Γ_C describes the rate of diffusion of the concentration in the fluid; and $S_{C, \text{source}}$ and $S_{C, \text{sink}}$ are the source and sink terms that describe how the concentrations are created or consumed, respectively, and are defined by the terms in the ASM rate equations. The geometry, mesh and velocity field are imported from the two-phase simulations into the *scalarTransportFoam* solver and the transport equations are solved in each cell of the domain for each time step to calculate how much of the concentrations are: created, consumed, diffused and convected with the flow field. A difficulty arises as the *scalarTransportFoam* solver is defined for a single phase flow field. The biological processes only convect with the liquid phase such that only the liquid phase velocity field is required from the Eulerian simulation. However, the simulations have included the free surface of the tank, which has been neglected in previous work,

and results in a region of cells in the domain having no water volume fraction. The water velocity field from the Eulerian formulation is tightly coupled with the air and water volume fraction which means the velocity field cannot be transferred directly across.

The results obtained from the Eulerian simulations for the water velocity field have non-zero values in cells where the water volume fraction is zero, as illustrated by figures 6.10a and 6.10c, which are non-physical. In the Eulerian simulations, the volume fraction is always accounted for in the formulation such that these non-physical values are suppressed and do not impact the physical solution. However, the water velocity field is the field imported into the single phase *scalarTransportFoam* solver. Once imported, the volume fraction is no longer accounted for and these non-physical values are not removed. Therefore, we have to replace these non-physical values with something physical. This is achieved by applying a volume fraction filter to the velocity field. A volume fraction filter value is defined, α_{filter} , such that if the air volume fraction in a cell is greater than this value, $\alpha_g > \alpha_{\text{filter}}$, then the water velocity in that cell is set to zero. An example of this is illustrated in figure 6.10b for an $\alpha_{\text{filter}} = 0.5$. As long as α_{filter} is smaller than 1 but larger than the α_g observed in the fluid, this will remove the non-physical water velocity values in the air layer at the top of the reactor. However, a decision is required for the choice of α_{filter} value which is not trivial as the choice can influence the rate of oxygen mass transfer near the surface. Additionally, consideration needs to be made for how the calculated water velocity field is imported; specifically if we account for the volume fraction and air velocity in the conversion of the two-phase water velocity to the single phase solver. These are issues that only arise due to modelling of the free surface in the hydrodynamic solutions which has been neglected in previous work and, therefore, did not have to consider these difficulties. The impact of these choices will be investigated, discussed, and assessed in later sections using the oxygen mass transfer model.

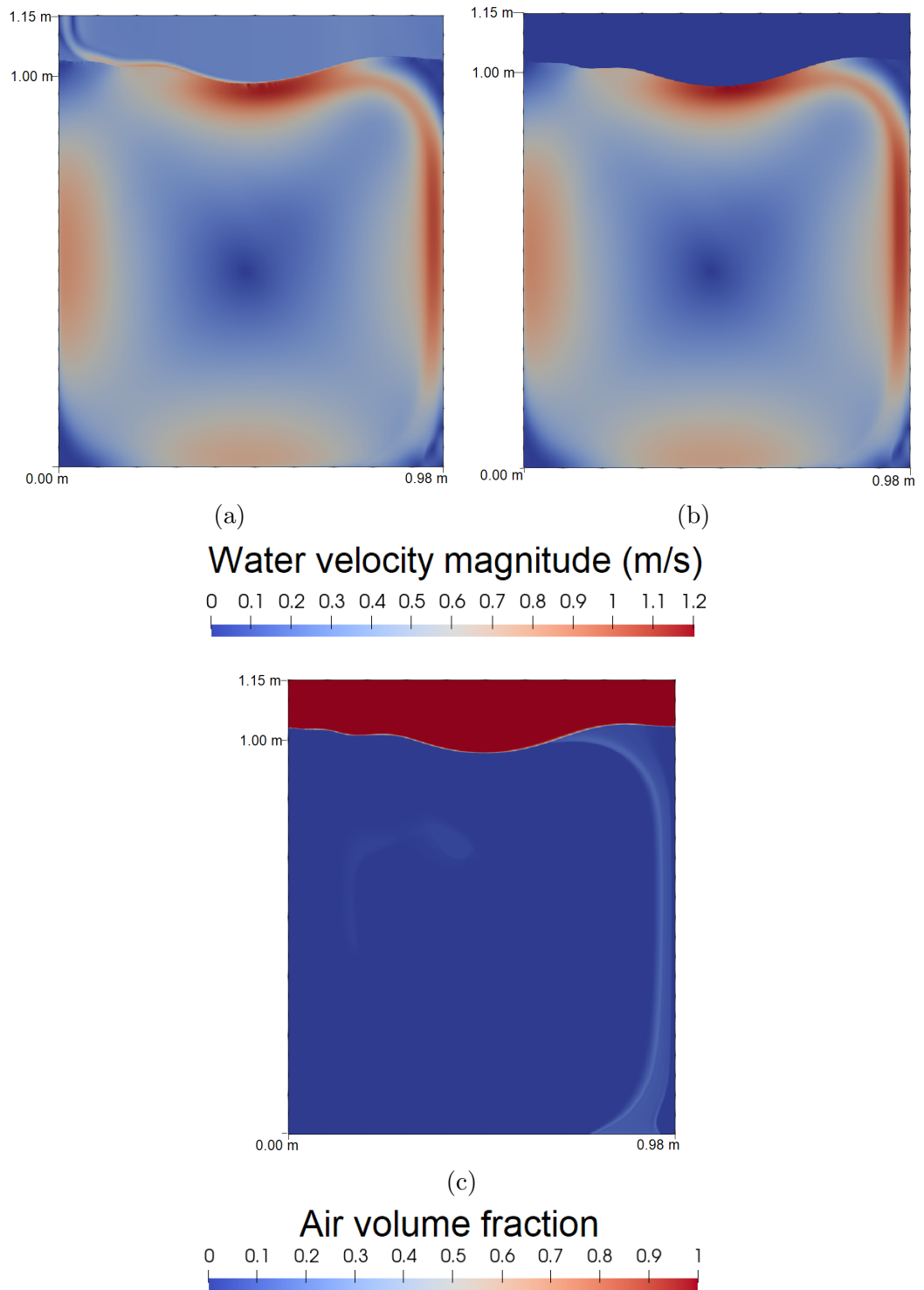


Figure 6.10: Contour plots of the Eulerian water velocity magnitude before, (a), and after, (b), the air volume fraction filter, $\alpha_{\text{filter}} = 0.5$, has been applied. This is to illustrate the removal of the non-physical non-zero fluid velocity above the fluid surface. Contour plot (c) is the air volume fraction profile in the reactor to show where the fluid surface lies for the 0.6 L/s 2D simulation.

6.3.1 Solution method, initial and boundary conditions

The *SIMPLE* algorithm is used to solve the transport equations in the *scalarTransportFoam* solver. The bounded first order implicit Euler method has been used for the discretisation of the time derivative. The Gaussian approach has been applied to calculate the face values for the other terms with the second order unbounded central differencing scheme for the interpolation of the Laplacian and gradient terms. The divergence formulation used the first order bounded upwind scheme which is less accurate than some of the second order formulations. However, the boundedness of this formulation was crucial for the stability of the transport equations. If we consider the ASM formulation in §2.1.1, a recurring term in the ASMs is the hyperbolic term,

$$\frac{C}{K + C}, \quad (6.3)$$

where K is constant. This term behaves well for concentrations above 0 and is stable in this region; however, issues arise if the concentration goes below 0. If we consider the illustration of the hyperbolic function in figure 6.11, if C goes below zero and $|C| \approx |K|$, the denominator of the function tends to zero which leads to the function diverging to $\pm\infty$.

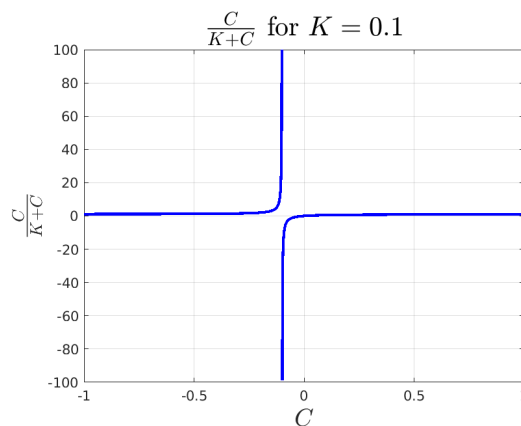


Figure 6.11: An illustration of the hyperbolic function when the concentration goes below zero.

The concentration going below zero initially is non-physical and the ASMs

terms should restrict the concentrations going below zero. However, when these are solved numerically for a given time step, the change in concentration can be large enough that it results in a non-physical negative concentrations. This can only be caused by sink terms in the transport equations, negative terms that act to reduce the concentration each time step, as those are the only ones that reduce the concentration. If we rearrange the transport equation in equation (6.2) such that we have, $dC/dt = f(S_{C \text{ source}}, S_{C \text{ sink}})$, it is clear that the convection or divergence term acts as a sink term in the equation. This makes sense as the flow field causes concentrations to move away from cells, acting to reduce the concentrations in cells. If an unbounded divergence scheme is used for convection term, this can result in the divergence term calculating negative concentrations which causes non-physical behaviour to occur. Therefore, the first order bounded upwind scheme is necessary as it is bounded and stops the concentrations from going below zero due to the convection term although it comes at a cost of reduced accuracy in the form of increased numerical diffusion. Additionally, after every iteration of the SIMPLE algorithm, the maximum function was applied to all the concentrations, $\max(C, 0)$, to restrict the concentrations from going below zero to improve stability. A tolerance requirement of 10^{-6} was applied to all the concentrations per time step with a maximum number of iterations set to 1000.

The solver requires the diffusivity coefficients, Γ_C , for each of the biological transport equation to be defined. There is no reference in the literature to the diffusivity values for the ASM biological components besides the soluble oxygen in water which has $\Gamma_{SO} = 2.143 \times 10^{-9}$ at $25^\circ C$ (Zedníková et al., 2018). Lei and Ni (2014) and Rehman et al. (2017) both neglected the diffusion terms by setting the coefficient to zero in their transport equations such that they assumed the diffusion term is negligible compared to the convection and source terms. Sánchez et al. (2018) stated that the diffusivity can be broken down into the laminar and turbulent components, $\Gamma_C = \Gamma_{C,lam} + \Gamma_{C,turb} = \Gamma_{C,lam} + \mu_t / \rho S_{ch}$, where the turbulent diffusivity component can be related to the turbulent viscosity, density and turbulent

Schmidt number, μ_t , ρ and S_{ch} , respectively. [Sánchez et al. \(2018\)](#) assumed that the laminar diffusivity of the biological concentrations is of the same order as the other molecular diffusivity value, for example Γ_{SO} . In comparison with the turbulent diffusivity, with a Schmidt number of 0.7 and μ_t of $O(10^{-3})$, the laminar diffusivity is significantly smaller than the turbulent diffusivity such that it can be neglected and only the turbulent diffusivity needs to be considered. In our aeration tank simulations, we have μ_t values in a range of $10^3 - 10^4$ and, if we assume a Schmidt value, $S_{ch} = 0.7$, which has been used for similar ASM coupled models ([Le Moullec et al., 2011](#); [Karpinska, 2013](#); [Sánchez et al., 2018](#)), this gives us a diffusivity values, $\Gamma_C = O(10^{-5})$ m²/s. This value is small compared with the convection terms such that neglecting the term, as done in [Lei and Ni \(2014\)](#) and [Rehman et al. \(2017\)](#), is a reasonable assumption. However, these simulations are running for hours in simulation time such that we have time scales in a range of $10^3 - 10^4$ s. If we account for these large time scales, then the diffusivity terms is no longer completely negligible. Additionally, if we consider that there can be closed vortices in the flow field, as we have seen previously, then without any diffusion term there is no path for the concentrations to reach these regions. Therefore, a constant diffusivity value, $\Gamma_C = 10^{-5}$ m²/s, has been used for all the concentration transport equations.

In general, the units for the biological parameters in the ASMs are in *COD/L*. The dimensions available in OpenFOAM are the 7 SI units which does not include the defined units for the biological parameters in the ASMs ([OpenFOAM, 2020](#)). However, the definition of the biological concentration units in the solver is not important but it is used to ensure the transport equations are dimensionally consistent. Therefore, we can choose any combination of dimensional units without loss of generality. Therefore, the dimensions have been defined as mol/m³. In this work, the units for the concentrations of all the ASM components will be referred to as mg/L for simplicity. Additionally, all physical constants and rates have been converted into their base units to avoid confusion or errors due to inconsistent dimensions.

The geometry and boundary conditions are transferred from the two-phase

solver simulation. Additionally, the air and water volume fraction and the air velocity field are also transferred over as these are required for the oxygen mass transfer model which is defined in §6.4. The necessary initial concentrations files for each transport equation are created for storing the results and the zero gradient condition applied on all the boundaries. An inlet and outlet zone can be created in the domain to allow for source and sink terms, respectively, for the concentrations, similarly to the inlet zone method described in §6.2; this will be further discussed in §6.6.

6.4 Oxygen mass transfer implementation

A key part of the aeration tank is to provide a source of soluble oxygen to the bacteria through the mass transfer of oxygen into the fluid along the surface of air bubbles as they rise through the tank. However, the Eulerian formulation does not model the air bubbles directly but captures the dynamics of the bubbles through the air volume fraction; therefore, the air volume fraction is required in the oxygen mass transfer model. The interfacial mass transfer rate of air into water, I_{So} , can be described by the formula previously presented in §4.7,

$$I_{So} = k_l a (S_{o,sat} - S_o),$$

where k_l is the local mass transfer rate coefficient, a is the interfacial surface area between the air and water, $S_{o,sat}$ describes the saturation value of the soluble oxygen and $(S_{o,sat} - S_o)$ describes the gradient between the current and maximum soluble oxygen concentration and is the driving term for the mass transfer. The interfacial area, a , can be calculated from the volume fraction by the formula,

$$a = \frac{6}{d_b} \frac{\alpha_g}{\alpha_l} \quad (6.4)$$

where d_b is the bubble diameter, and α_g and α_l are the volume fractions of the gas and liquid phases, respectively. The local mass transfer rate coefficient, k_l , can be

derived from the Higbie penetration theory (Higbie, 1935) such that,

$$k_l = 2\sqrt{\frac{D_{S_o} u_{\text{slip}}}{\pi d_b}},$$

where D_{S_o} is the diffusivity of oxygen into water and $u_{\text{slip}} = |\mathbf{u}_l - \mathbf{u}_g|$ is the magnitude of the slip velocity between the two phases. These formulation for the interfacial mass transfer have been implemented in similar two-phase wastewater models in Lei and Ni (2014) and Karpinska and Bridgeman (2017) Sánchez et al. (2018). The bubble diameters in the simulations are $d_b = 2.5$ mm, the diffusivity of oxygen in water is $D_{S_o} = 2.143 \times 10^{-9}$ m²/s at 25 °C (Zedníková et al., 2018) and a soluble oxygen saturation value of $S_{o,\text{sat}} = 10$ mg/L has been used (Wang et al., 1978). Summary of these parameter values are presented in table 6.4.

Parameters	Notation	Value	Units
Diffusivity of oxygen in water	D_{S_o}	2.143×10^{-9}	m ² s ⁻¹
Bubble diameter	d_b	2.5	mm
Soluble oxygen saturation value	$S_{o,\text{sat}}$	10	mg/L

Table 6.4: Parameters used for the oxygen mass transfer model for the modelled aeration tank.

Introducing this formula as a source term in the soluble oxygen transport equation allows us to model the mass transfer of oxygen into the fluid. Additionally, using this oxygen mass transport equation, we can investigate the effect of the modelling choices for the α_{filter} value and velocity field implementation on the rate of soluble oxygen into the tank. Through this it is possible to assess the best choices without needing to solve additional transport equations. These studies are conducted in the following sections.

6.4.1 Water velocity field implementation study

The transport equations require the water velocity field from the two-phase simulations. However, if we were to just import the base calculated velocity field, $\mathbf{u}_{\text{water}}$, we would not be considering the volume fraction in each cell, specifically how much of each cell contains water. If a cell contained 50 % water due to the air bubbles, then the presence of the air in the cell could impact on how the water and concentrations convect in and out of the cells. Therefore, if we were to implement the base water velocity field, $\mathbf{u}_{\text{water}}$, then there would be no consideration of the water to air ratio in each cell.

Two more water velocity fields have been calculated that account for the volume fraction values in each cell and an investigation of the impact of all the choices on the oxygen mass transfer model were conducted. Along with the base water velocity field, $\mathbf{u}_{\text{water}}$, a weighted water velocity field, $\mathbf{u}_{\text{weighted}}$, has been calculated that is the water velocity field multiplied by the water volume fraction in each cell, $\mathbf{u}_{\text{weighted}} = \alpha_{\text{water}}\mathbf{u}_{\text{water}}$. The third field considered is the mixture velocity field, $\mathbf{u}_{\text{mixture}}$, which is calculated by a volume fraction weighting of the water and air velocity fields, $\mathbf{u}_{\text{mixture}} = \alpha_{\text{water}}\mathbf{u}_{\text{water}} + \alpha_{\text{air}}\mathbf{u}_{\text{air}}$.

The oxygen mass transfer transport equation has been solved using all three of the water velocity field formulations from the 2D 0.6 L/s two-phase simulation with a volume fraction filter value, $\alpha_{\text{filter}} = 0.21$, as this was larger than any observed air volume fraction inside of the fluid flow. The average soluble oxygen value throughout the reactor was calculated over a 30 minute interval for each water velocity field; the results are presented in figure 6.12.

It is clear that the choice of velocity field can impact the rate of oxygen transfer into the reactor. This is expected as modifying the velocity field changes the convection term in the transport equation which is the dominant term for transporting the soluble oxygen throughout the reactor. The $\mathbf{u}_{\text{weighted}}$ field produced a significant faster rate and higher total amount of oxygen transfer compared with the other two

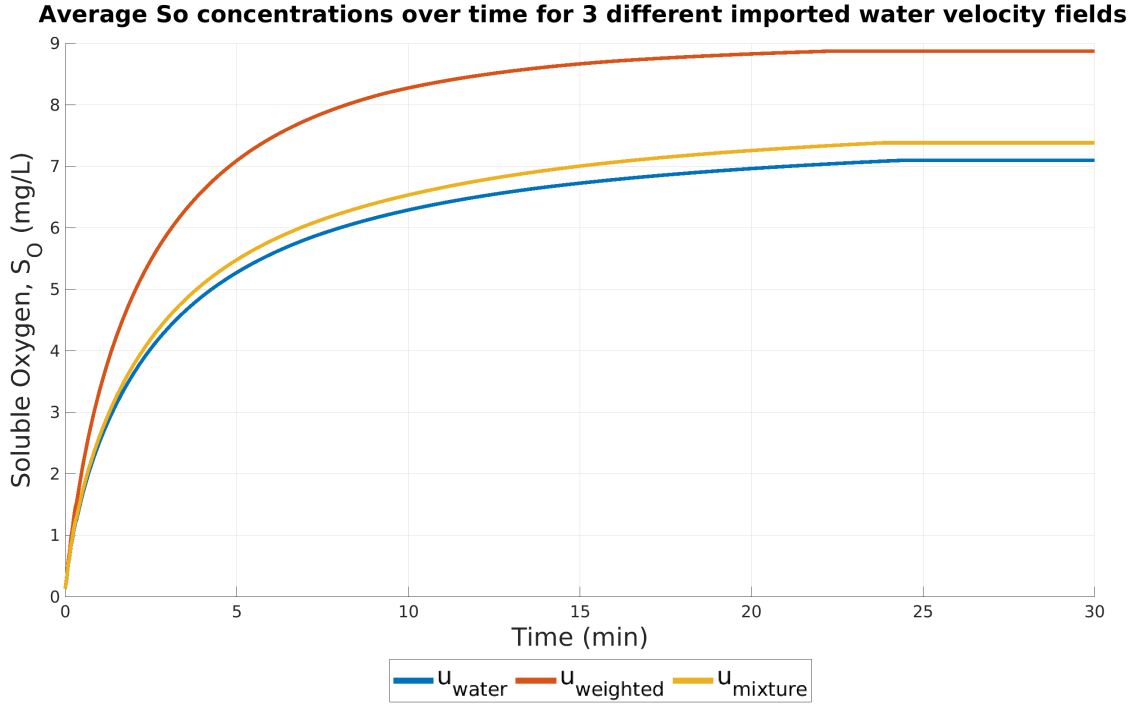


Figure 6.12: The average soluble oxygen in the reactor over time for three different water velocity fields from the two-phase simulations: the base water velocity field, $\mathbf{u}_{\text{water}}$; the water volume fraction weighted water velocity field, $\mathbf{u}_{\text{weighted}}$; and the combined water and air velocity field weighted by the water and air volume fraction, respectively, $\mathbf{u}_{\text{mixture}}$.

fields. This is because the weighting for the $\mathbf{u}_{\text{weighted}}$ field only reduces the velocity in cells where there is air volume fraction present which are also the only locations where the oxygen is transferred. Therefore, the fluid in the $\mathbf{u}_{\text{weighted}}$ field artificially spends a longer time in these cell with air and so more oxygen is transferred into the fluid before it moves away, resulting in higher average soluble oxygen values. In comparison, the $\mathbf{u}_{\text{water}}$ and $\mathbf{u}_{\text{mixture}}$ fields are much lower and similar in value which implies the velocity field is not changing much in the $\mathbf{u}_{\text{mixture}}$, although, we have accounted for the volume fraction in this formulation.

For choosing what velocity field to implement, the $\mathbf{u}_{\text{water}}$ field is acceptable; however, the $\mathbf{u}_{\text{mixture}}$ field takes into account the volume fraction of both phases and their contribution to the velocity field. Additionally, it follows the procedure of converting the two-phase simulation results to a single phase system. Therefore, the $\mathbf{u}_{\text{mixture}}$ velocity field has been used as the transferred velocity field for the transport equations for the future simulations.

6.4.2 Volume fraction filter study

As discussed previously in §6.3, because the free surface has been included in the hydrodynamic simulations, we need to apply a filter to remove the non-physical velocity values in the top air layer by choosing a volume fraction filter value, α_{filter} . In this study we will investigate how the value of α_{filter} impacts the oxygen transfer rate to verify the best value for filtering the velocities. The mixture velocity field from the 2D 0.6 L/s two-phase simulation has been used with filter volume fraction values: $\alpha_{\text{filter}} = 0.21, 0.5, 0.7, 0.9$ and 0.99 . The air volume fraction ranges from 0 - 0.2 in the reactor and, therefore, a filter value, $\alpha_{\text{filter}} = 0.21$, is the smallest value possible without affecting the velocities inside the fluid. Figure 6.13 illustrates how the average soluble oxygen changes with time for the 5 different filter values.

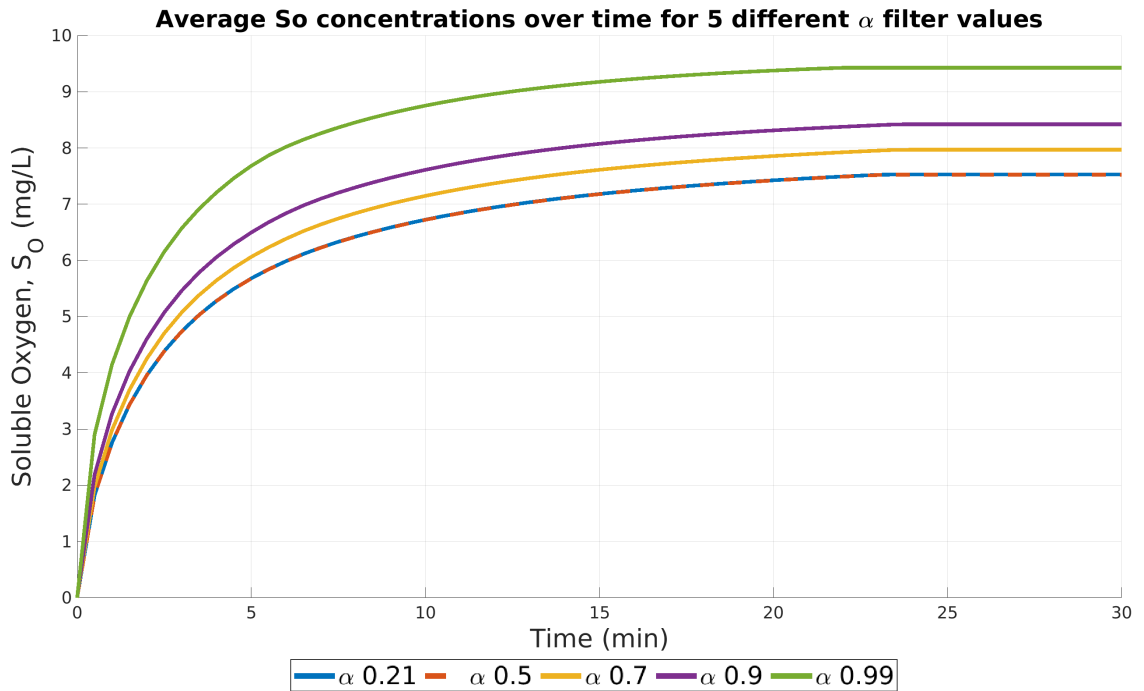


Figure 6.13: The average soluble oxygen over time in the reactor after applying 5 different α_{filter} values.

The filter values do not impact the results until the $\alpha_{\text{filter}} > 0.5$, at which point the average soluble oxygen increases significantly. The reason this occurs is that the interfacial area value, a , in the oxygen mass transfer model in equation (6.4) has an α_g/α_l term that diverges as $\alpha_g \gg \alpha_l$. Choosing an $\alpha_{\text{filter}} > 0.5$ results in

a region of cells at the fluid surface having significantly increased oxygen transfer rates due to this α_g/α_l term. Additionally, because the water velocity is faster near the fluid surface, the soluble oxygen gets mixed into the reactor more easily; causing the significant increase in total average soluble oxygen for these higher α_{filter} values. Another way to interpret the α_{filter} value is that it is the criteria for which we decide where the fluid surface ends and the air layer begins. The oxygen mass transfer model in §6.4 has been derived to model the transfer of oxygen due to rising bubbles through a fluid and not surface aeration from air entrainment at the surface. In this model, we have assumed that the surface aeration is small compared to the transfer due to rising bubbles such that its effects can be neglected. Therefore, an $\alpha_{\text{filter}} = 0.5$ is an appropriate value to use as this is the point where the water phase is no longer the continuous phase and we are no longer modelling bubbles in the fluid where the oxygen mass transfer model is valid. Additionally, we have shown that an $\alpha_{\text{filter}} < 0.5$ produces the same results as $\alpha_{\text{filter}} = 0.5$ such that we can choose this value without loss of generality. Therefore, an $\alpha_{\text{filter}} = 0.5$ has been chosen as the filter value to modify the two-phase velocity field for all future simulations.

6.4.3 Diffuser aeration rate study

Increasing the number of diffusers in the tank provides additional sources of momentum and aeration into the reactor which should improve the mixing and rate of oxygen transfer in the reactor, respectively. To investigate this, a series of 2D simulations were run with a range of different diffusers configurations and air flow rates to compare how they impact the flow field and oxygenation in the reactor in comparison with the one diffuser at flow rate 0.6 L/s. Two simulations with two diffusers running at each end of the tank were conducted with an air flow rate of 0.3 and 0.6 L/s each, for a total air flow rate of 0.6 and 1.2 L/s, respectively. Additionally, a simulation was run with four equally spread diffusers with an air flow rate of 0.15 L/s through each diffuser for a total air flow rate of 0.6 L/s. It is assumed that new diffuser configurations take the same amount of time to reach a steady-state

as the one diffuser simulation. A summary of the four setups being considered is described in table 6.5 and the average soluble oxygen in the tank over time for the four setups are presented in figure 6.14.

Cases	Description
1 diffuser, FR_{total} 0.6 L/s.	A 2D simulation of one diffuser running near the right side wall with an air flow rate of 0.6 L/s.
2 diffuser, FR_{total} 0.6 L/s.	A 2D simulation with two diffusers running, one next to the left side wall and the other next to the right side wall, with an air flow rate of 0.3 L/s for each diffuser, combining for a total air flow rate of 0.6 L/s.
2 diffuser, FR_{total} 1.2 L/s.	A 2D simulation with two diffusers running, one next to the left side wall and the other next to the right side wall, with an air flow rate of 0.6 L/s for each diffuser, combining for a total air flow rate of 1.2 L/s.
4 diffuser, FR_{total} 0.6 L/s.	A 2D simulation with four diffusers running, where each diffuser is equally spaced along the base of the reactor, with an air flow rate of 0.15 L/s for each diffuser, combining for a total air flow rate of 0.6 L/s.

Table 6.5: A description of the four diffuser setups considered in the study of the impact of different diffuser configurations on the oxygenation.

If we begin with comparing the results of the one and two diffuser setups that have a total flow rate of 0.6 and 1.2 L/s, respectively, in figure 6.14, it is clear that the rate of oxygen transfer increases when you double the amount of diffusers and air being pumped into the system. There is twice as much air being pumped into the system and, therefore, twice the amount of air available to transfer oxygen into the fluid. If we assess the hydrodynamic flow fields for the one and two diffuser setups in figures 6.15a and 6.15b, respectively, the two diffuser flow fields are very similar to the vortex velocity field in the one diffuser case but compressed into the right half of the reactor with a mirror plane placed down the middle of the reactor. This is not too surprising due to the symmetry in the reactor geometry with the two diffusers. Additionally, if we compare the volume fraction distribution in figure 6.16a for the

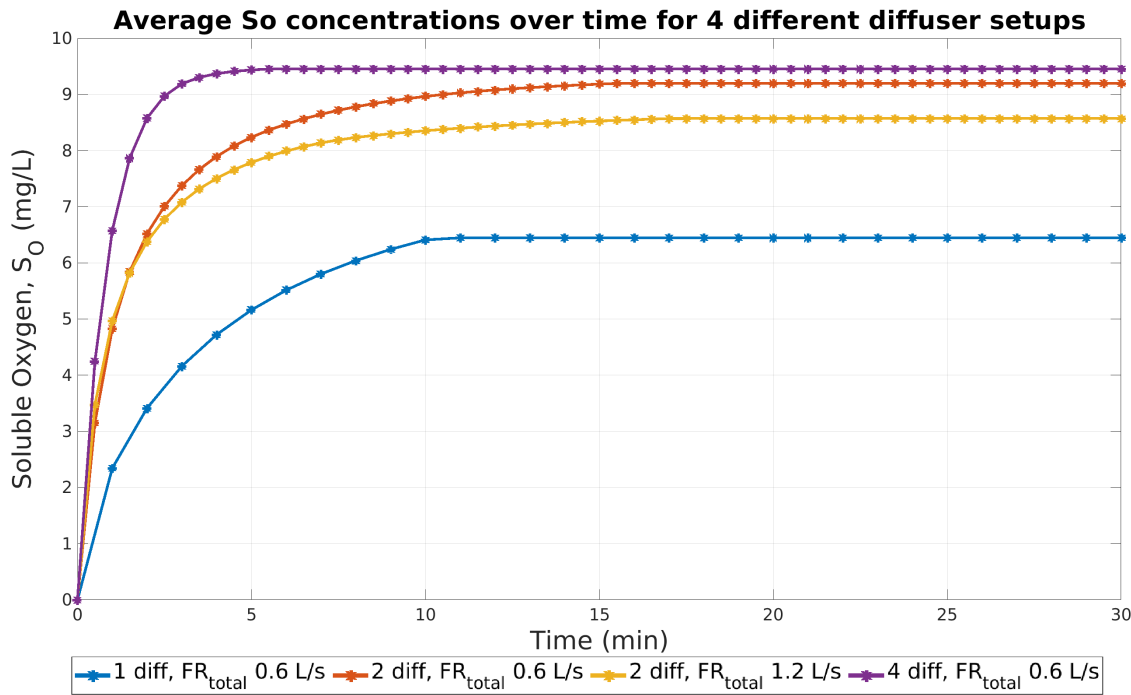


Figure 6.14: The average soluble oxygen in the reactor over time for 4 different diffuser configurations: 1 diffuser with a total flow rate of 0.6 L/s; 2 diffusers with a total flow rate of 0.6 L/s or 0.3 L/s each; 2 diffusers with a total flow rate of 1.2 L/s or 0.6 L/s each; 4 diffusers with a total flow rate of 0.6 L/s or 0.15 L/s each.

one and two diffuser setups, respectively, they both entrain a portion of air due to the vortices generated by the rising bubbles. In the case of the two diffusers, there are two regions of entrained air which are due to the two re-circulation vortices. These two vortices increase the hydrodynamic mixing in the reactor compared with the one diffuser which means the flow field convects more of the soluble oxygen around the reactor. This results in the two diffuser setup having a higher average soluble oxygen at the end of the 30 minutes.

Comparing the average soluble oxygen plots for the pair of two diffuser setups with total flow rate of 0.6 and 1.2 L/s in figure 6.14, it is found that the lower total flow rate setup results in more oxygen being transferred into the reactor after the full 30 minutes which is unexpected. If we analyse the oxygen transfer rates in the first 2 minutes, the gradient is larger for the total 1.2 L/s flow rate setup (this is clearer by the derived $k_l a$ in table 6.6) which implies that oxygen is being transferred faster in this setup than the 0.6 L/s setup. This is expected as there is twice as much air

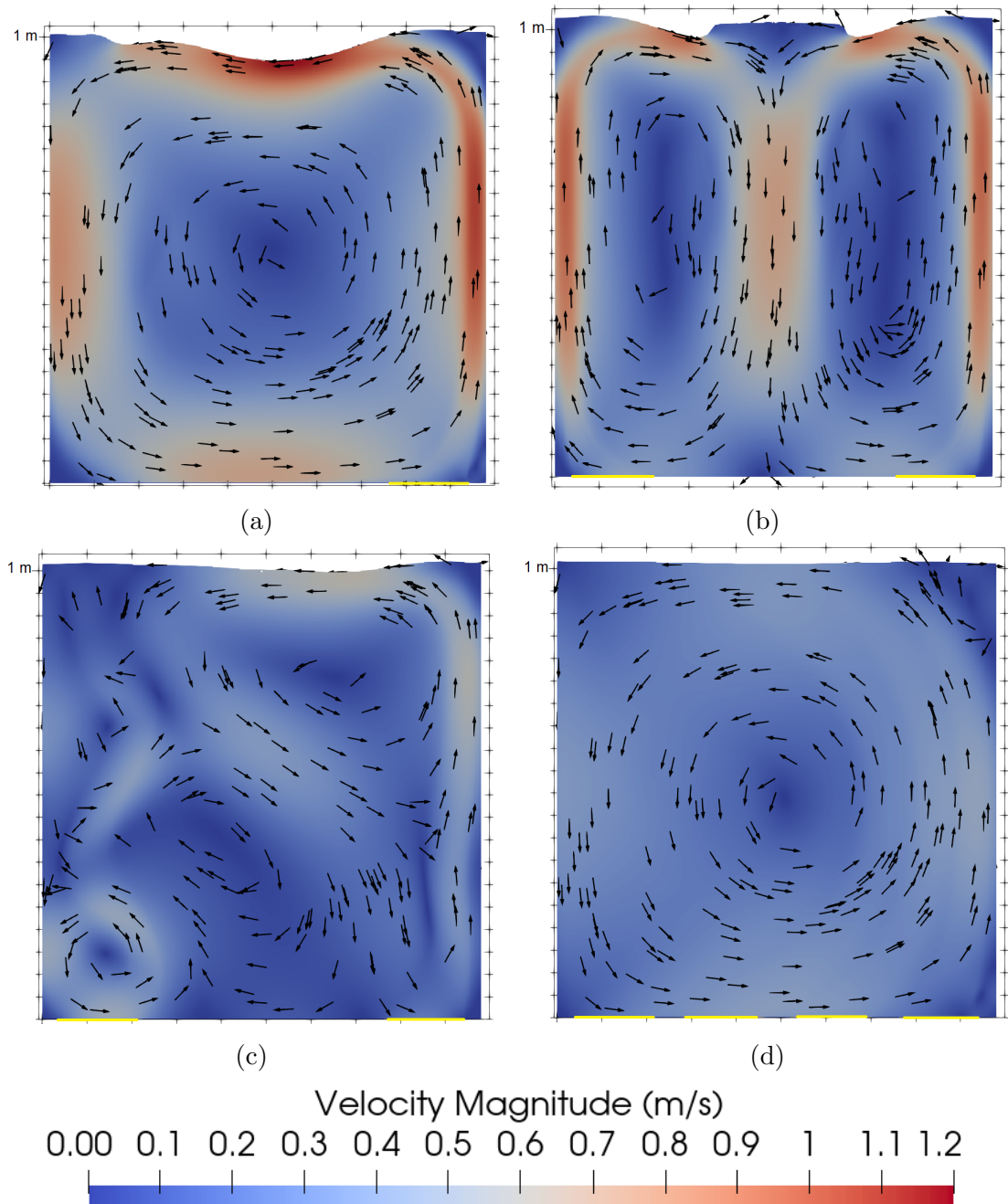


Figure 6.15: Velocity magnitude contour and normalised velocity vectors plots of the 2D simulation with: 1 diffuser with a total flow rate of 0.6 L/s (a); 2 diffusers with a total flow rate of 1.2 L/s or 0.6 L/s each (b); 2 diffusers with a total flow rate of 0.6 L/s or 0.3 L/s each (c); 4 diffusers with a total flow rate of 0.6 L/s or 0.15 L/s each (d). The yellow lines at the base indicates the locations of the aerating diffusers.

being pumped into the system per second for the 1.2 L/s setup. However, after two minutes, the amount of soluble oxygen in the 0.6 L/s setup passes the 1.2 L/s setup implying that the oxygen is now being transferred faster into this reactor setup with

the end result being that there is more soluble oxygen on average in the reactor with the lower aeration flow rate. This contradicts the expectation that pumping more air into reactor results in more soluble oxygen being transferred. The reason for this is that, after the initial 2 minutes, the convective flow field is now having a more dominant effect on increasing the overall soluble oxygen distribution in the reactor compared with just having more air per second pumped into the system. After two minutes, the regions in the reactor that have bubbles passing through them are reaching their soluble oxygen saturation value, $S_{o,sat}$; therefore, the driving term in the oxygen mass transfer model, $(S_{o,sat} - S_o)$, is no longer as large, resulting in a significant reduction in the rate of oxygen transfer. The only way to increase the amount of oxygen in the reactor is to convect the soluble oxygen away from bubbled regions to less aerated sections. This results in soluble oxygen being distributed throughout the reactor, reaching areas where there is no air present. Additionally, the convection moves the soluble oxygen away from the bubbled regions which results in a drop in the soluble oxygen, S_o , in those cells such that the driving term in the oxygen mass transfer model, $(S_{o,sat} - S_o)$, increases once again. This results in an a higher amount of soluble oxygen on average throughout the reactor.

This can be further assessed by comparing the velocity fields generated by the two setups in figures 6.15b and 6.15c. The lower flow rate setup has a more chaotic velocity field which is improving the overall mixing. There are approximately 5 non symmetrical vortices in figure 6.15c compared with the two in figure 6.15b. These extra vortices result in the soluble oxygen being disrupted more uniformly compared with the higher flow rate velocity fields. Therefore, when the convection begins to be the dominant process in increasing the average soluble oxygen throughout the reactor, the lower flow rate has a more optimal flow field for distributing the soluble oxygen such that the average soluble oxygen in the 0.6 L/s setup passes the higher flow rate case after 2 minutes in figure 6.14. The reason for the more chaotic flow field in figure 6.15c is that the reduced air flow rate results in lower bubble rise velocities and less air jet like behaviour; causing the bubbles to be more influenced by the

generated flow field. This is clear if we consider the volume fractions distributions in figures 6.16b and 6.16c. The higher flow rate setup results in the bubble plume being drawn towards the side walls and becoming thinner, like an air jet. In the lower flow rate setups in figure 6.16b, the plume is less influenced by the side walls due to the lower bubble rise velocities and maintains its bubble plume width substantially longer as it rises. Therefore, the rising bubble plume covers a larger region of the reactor which increases the spread of oxygen transfer from the air into the fluid. Additionally, the shifting left bubble plume in figure 6.16c is an illustration of how the plume is being influenced by the generated flow field which results in asymmetry and instabilities in the flow, creating more vortices and, overall, a more optimal flow field for mixing.

Finally, if we consider the oxygen transfer rate in the 4 diffuser setup in figure 6.14, we find this setup has the fastest oxygen transfer rate compared with the others setups even though the total flow rate is the same as, or lower, than the others. If we consider the velocity field in figure 6.15, it is very similar to the one diffuser case which is surprising as, with the symmetry in the four diffuser configuration, we would expect a flow field more similar to the 2 diffuser 1.2 L/s setup in figure 6.15b. Therefore, the large increase in the oxygen transfer rate is not a result of a more chaotic flow field with extra vortices, as was the case for the 2 diffuser 0.6 L/s setup. If we consider the volume fraction profile in figure 6.16d, the four bubble plumes are all drawn towards the right wall which is similar behaviour to the one diffuser setup and explains why the two setups have similar velocity fields. However, the four diffusers perform so much better than the one diffuser setup even though they have similar flow fields which is surprising as we have shown that the flow field can highly influence the rate of oxygen transfer through the whole reactor. However, when you consider the four diffuser bubble plume profiles in figure 6.16d, the bubbled air flows through more than half of the reactor and also passes right through the centre of the vortex loop where the fluid velocity is the slowest. This results in a large portion of the reactor having direct sources of soluble oxygen into

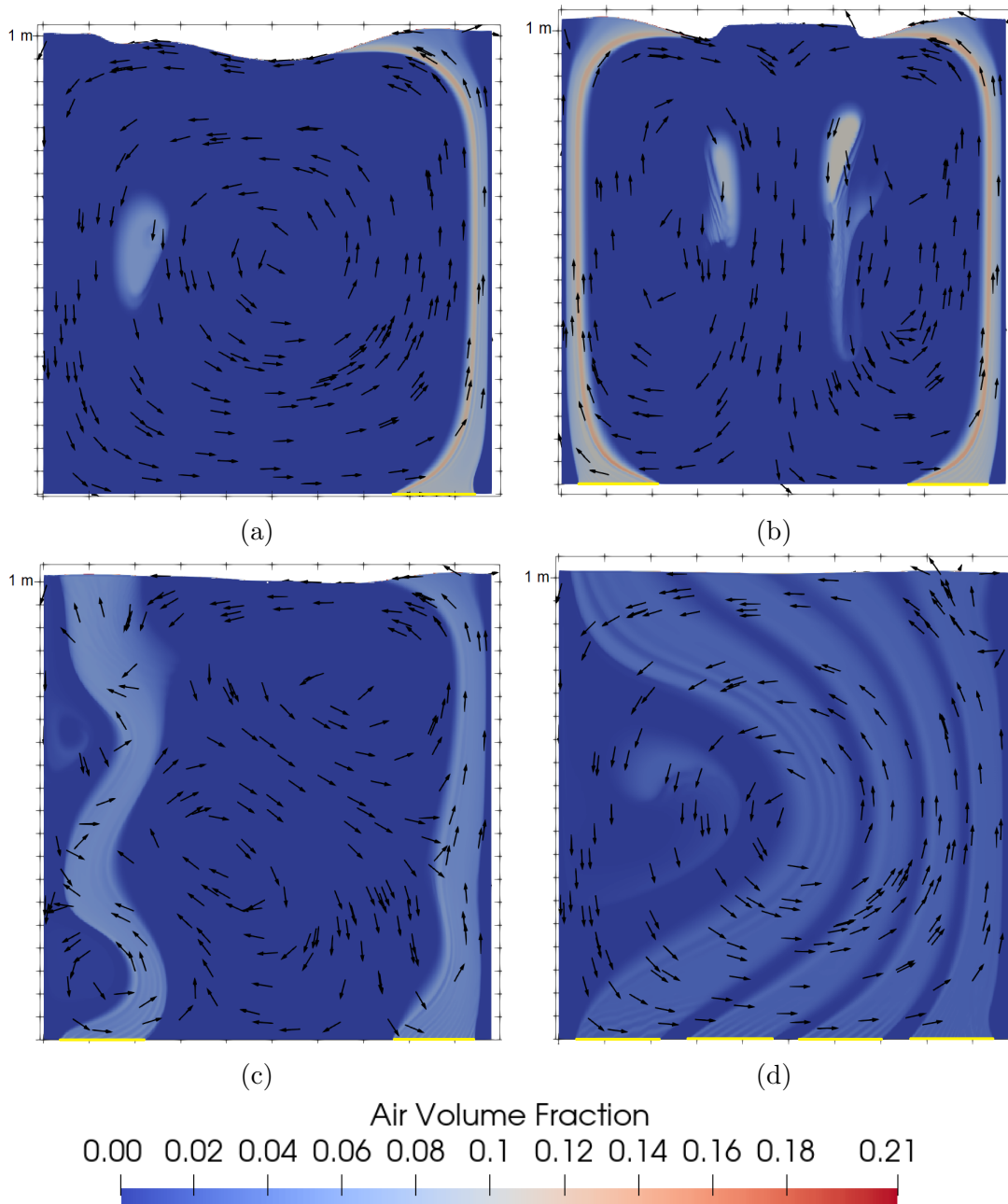


Figure 6.16: Air volume fraction contour and normalised velocity vectors plots of the 2D simulation with: 1 diffuser with a total flow rate of 0.6 L/s (a); 2 diffusers with a total flow rate of 1.2 L/s or 0.6 L/s each (b); 2 diffusers with a total flow rate of 0.6 L/s or 0.3 L/s each (c); 4 diffusers with a total flow rate of 0.6 L/s or 0.15 L/s each (d). The yellow lines at the base indicates the locations of the aerating diffusers.

the fluid due to air being present. Additionally, the slower velocities causes the fluid to spend a longer time in the regions where bubbles are present and, even though the numbers of bubbles are lower due to lower flow rate, the bubbles spend longer in the fluid which allows more time for the oxygen to transfer across. Overall, this

leads to a significant increase in the rate of oxygen transfer into the fluid.

We have not investigated how these diffuser setups affect the biological processes in the ASMs; however, this study has shown that the positioning of diffusers and aeration flow rate can significantly impact the rate of oxygen transfer into the reactor in non-trivial ways. This would, consequently, impact the biological performance of the reactor if the oxygen transfer was the rate limiting factor in the biological reactions. Additionally, we have shown a case where doubling the aeration flow rate reduces the average amount of soluble oxygen in the reactor which, in practice, would result in an increase in power consumption and reduced efficiency. Using the oxygen mass transfer transport equation, we have shown that consideration of the hydrodynamics can give us insight into how changes in reactor operation can both improve and reduce the oxygenation efficiency of the reactor which is important for the performance of the biological processes.

6.4.4 Deriving volumetric oxygen transfer coefficient, $k_l a$, from simulations

Every aeration tank with a specific diffuser configuration or aerating system will have their own defined global or volumetric oxygen transfer coefficient, $k_l a$, that could be determined experimentally. In the oxygen mass transfer simulations, the $k_l a$ is modelled using the Higbie penetration theory (Higbie, 1935) and volume fraction to compute the oxygen mass transfer on a local cell basis. The average soluble oxygen throughout the reactor over time is then computed, as illustrated in figure 6.14. It is possible from the average soluble oxygen data to derive a volumetric $k_l a$ and saturation value by fitting an exponential curve with the form derived in §4.7,

$$\begin{aligned}\frac{dS_o}{dt} &= \gamma(\alpha - S_o), \\ S_o(t) &= \alpha - (\alpha - \beta)e^{-\gamma t},\end{aligned}$$

where $\alpha = S_{o,sat}$ is the soluble oxygen saturation value; $\beta = S_{o,init}$ is the initial soluble oxygen value in the reactor; and $\gamma = k_l a$ is the volumetric oxygen transfer coefficient. In our simulations, the initial soluble oxygen value is zero, $\beta = 0$ mg/L, which simplifies the fitting function too,

$$S_o(t) = \alpha(1 - e^{-\gamma t}) = S_{o,sat}(1 - e^{-k_l a t}).$$

A curve fitting function in *MATLAB* was applied to the one diffuser 0.6 L/s average soluble oxygen profile in figure 6.14 which produces the curve fitted result in figure 6.17. The fitted exponential plot calculated a volumetric oxygen mass

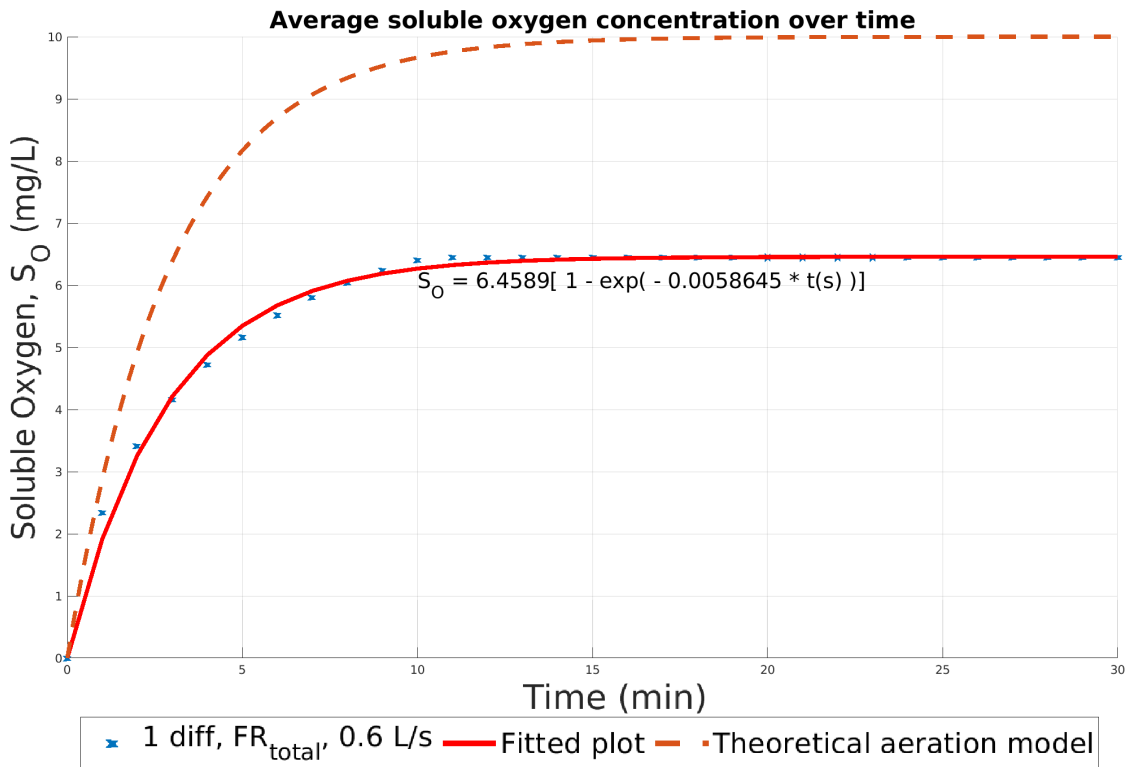


Figure 6.17: The average soluble oxygen in the reactor over time for the 1 diffuser at a flow rate of 0.6 L/s with a fitted exponential function to the data. Additionally, the profile from the theoretical model for the same diffuser configuration derived using data provided in the membrane diffuser manual (xylem, 2020), as described in §4.7.1.

transfer coefficient $k_l a = 5.865 \times 10^{-3} \text{ s}^{-1}$ and a soluble oxygen saturation value $S_{o,sat} = 6.46$ mg/L. If we compare this plot with the theoretical aeration model, as described in §4.7.1, for the same configuration that was derived from data provided

in the membrane diffuser manual (xylem, 2020), the theoretical model predicts a faster oxygen transfer rate as well as a higher saturation value. Moreover, the soluble oxygen concentrations does eventually reach the defined saturation value, $S_o = S_{o,sat} = 10$ mg/L. If we consider the formulation of the theoretical model, it assumes that oxygen is being transferred constantly everywhere, driven by the $(S_{o,sat} - S_o)$ term, such that, as long as the saturation concentration has not been reached, the oxygen continues to be transferred and the soluble oxygen concentration increases. In comparison with the simulation data, oxygen is only transferred where the air present which is not uniform throughout the reactor. Furthermore, the simulation does not reach the saturation value defined in the oxygen mass transfer model, $S_{o,sat} = 10$ mg/L.

The oxygen mass transfer model uses the same driving term, $(S_{o,sat} - S_o)$, in its formulation and has the same saturation value, $S_{o,sat} = 10$ mg/L, which implies the reactor would eventually reach the saturation value. The oxygen can only enter the fluid when it passes through regions where there is air; however, because the tank is not uniformly mixed, there are regions of the reactor where a path does not exist from areas with air to these regions for soluble oxygen to travel along. The only way for soluble oxygen to reach these regions is through diffusion which is very slow. As a result, the average soluble oxygen does not reach the defined $S_{o,sat}$, but a lower value of $S_{o,sat} = 6.46$ mg/L, implying a 65 % efficiency.

If we compare the calculated global oxygen transfer coefficient from the simulation, $k_l a = 5.865$ s⁻¹, to the derived theoretical value from §4.7.1, $k_l a = 5.654 \times 10^{-3}$ s⁻¹, we find the two $k_l a$ coefficients are almost identical. The theoretical $k_l a = 5.645 \times 10^{-3}$ s⁻¹ has been derived from an average SOTE for the membrane diffusers from the diffuser manual (xylem, 2020) which was obtained via aeration experiments. The matching of the global oxygen transfer coefficient from the simulation with the theoretical value verifies the oxygen transfer model and gives us confidence that the oxygen transfer model is giving us reasonable values for the aeration in the tank. Additionally, considering figure 6.17 again and taking into account

that the global oxygen transfer coefficients are almost identical for both plots, we can conclude that the difference between the two plots is due to the difference in the $S_{o,sat}$ value. The theoretical model had a defined saturation value $S_{o,sat} = 10$ mg/L which is approximately near the maximum amount of soluble oxygen than can be dissolved in water depending on the temperature of the wastewater (Wang et al., 1978), which we can conclude is too high for this diffuser setup.

To further assess the oxygen transfer model, fitted oxygenation curves were calculated for the three other diffuser setups studied in §6.4.3, as illustrated in figure 6.18, and the calculated global $k_l a$ are compared with the theoretical derived $k_l a$ values for each setup, as shown in table 6.6.

Diffuser configuration and total flow rate	Simulation derived global		Theoretical derived $k_l a$ ($\times 10^{-3}$ s $^{-1}$)
	$S_{o,sat}$ (mg/L)	$k_l a$ ($\times 10^{-3}$ s $^{-1}$)	
1 diffuser, FR _{total} 0.6 L/s	6.46	5.86	5.65
2 diffuser, FR _{total} 1.2 L/s	8.45	11.97	11.31
2 diffuser, FR _{total} 0.6 L/s	9.09	10.17	5.65
4 diffuser, FR _{total} 0.6 L/s	9.45	19.84	5.65

Table 6.6: The derived global $k_l a$ and $S_{o,sat}$ from the simulations and the theoretical derived $k_l a$ for four different diffuser setups, as previously studied in §6.4.3.

For the 1 and 2 diffuser setups with total flow rate 0.6 and 1.2 L/s, respectively, the simulation and theoretical derived $k_l a$ value are almost identical which further verifies the oxygen transfer model. However, this is not the case for the other two diffuser setups. The theoretical model does not account for spreading the same amount of air by having multiple diffusers such that the theoretical $k_l a$ for the 2 and 4 diffuser setups with total flow rate 0.6 and 0.6 L/s, respectively, is identical to the one diffuser case as the total flow rate has not changed. Additionally, it is important to note that the defined SOTE % from xylem (2020) used to calculate the theoretical $k_l a$ has not been derived for these lower flow rates per diffuser such that they are technically not valid. However, the simulation derived $k_l a$ are all of similar order to the theoretical values, reassuring us that the oxygen transfer

model is giving us reasonable oxygenation rates and values. If we compare all the simulation derived k_1a values for the diffuser setups, we can observe that multiplying the number of diffusers by some factor results in a similar multiple increase in the k_1a value. Additionally, increasing the flow rate also results in an increase in the k_1a value, but only a small increase; doubling the flow rate results in an approximate 10% increase in the transfer coefficient. It can be concluded that the k_1a transfer coefficient is very dependent on the spread of bubbles throughout the reactor, specifically the air volume distribution, and less dependent on the amount of air being pumped through the reactor per second. If we compare the derived $S_{o,sat}$ values, we observe an increase in $S_{o,sat}$ with number of diffusers but a decrease with an increase in flow rate. As discussed in §6.4.3, this is due to the difference in the generated hydrodynamic flow field, specifically that the 2 diffuser with total flow rate 0.6 L/s setup has a more optimal mixing flow field for distributing the soluble oxygen. Therefore, we can conclude that the derived $S_{o,sat}$ is dependent on the hydrodynamic flow field generated in the reactor.

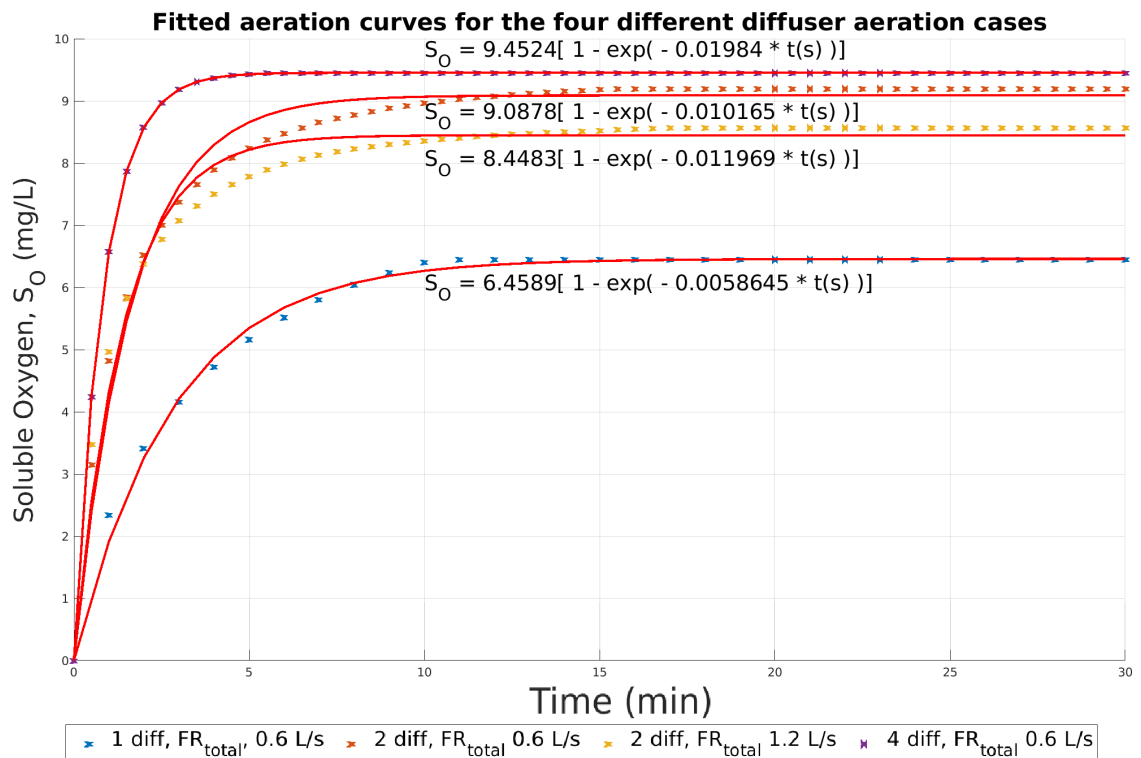


Figure 6.18: The average soluble oxygen over time for the four different diffuser setups from §6.4.3 with the fitted exponential aeration functions.

In summary, we have shown how to derive global $k_{l}a$ and $S_{o,sat}$ values from the simulations. An assessment of the derived $k_{l}a$ values against theoretical values from experimental data in the membrane diffuser manual (xylem, 2020) has verified the model and given us more confidence in the oxygen transfer model results. An analysis of the derived global $k_{l}a$ and $S_{o,sat}$ values for four different diffuser configurations has informed us that the $k_{l}a$ and $S_{o,sat}$ values are dependent on the air volume fraction or bubble distribution and generated convective flow field, respectively. Moreover, if a reactor was reaching a desired $k_{l}a$ values but not $S_{o,sat}$, this would be an indication that enough air is rising through the reactor to transfer the oxygen but the generated flow field is not distributing the soluble oxygen effectively enough. Therefore, an additional mechanical stirrer would be more ideal to improve the distribution of soluble oxygen compared with having an additional aerating diffuser as this would be more cost effective.

An important observation is that these derived oxygenation rates can give us insight into if a reactor is “well-mixed” or not. If the prescribed $S_{o,sat}$ in the oxygen transfer model is not reached in the simulations, then it would be expected that the tank is not well-mixed and, therefore, it would be expected that the biological process would be impacted. Alternatively, if the prescribed $S_{o,sat}$ is reached, then it is expected that the biological processes would not be impacted. As a result, this process of deriving an oxygenation curve could serve as an initial check to assess the hydrodynamic mixing, similar to a tracer model, before coupling the biological processes which are more computationally expensive. Finally, using the defined method to derive global $k_{l}a$ and $S_{o,sat}$ values from the simulations, we can derive global aeration rates for each simulated reactor that can be implemented into the ASMs (see equation (6.6) for an example) to allow us to directly compare the coupled and uncoupled ASMs to fully understand the effect of the hydrodynamics on the biological performances.

6.4.5 Reducing the resolution to improve simulation speed

The previous oxygen mass transfer studies have only been solving for one transport equation in 2D and for 30 minutes of real time which can be run on a single computing core over a 2 - 4 hour period. However, once the other biological processes are included from the ASMs, this will increase the number of equations being solved per iteration which will increase the computational demand of the simulations. Furthermore, these simulations will need to be run for 2 hours or more real time which further increases the computational demand; and this is all before we consider the extra demand from 3D simulations. Therefore, we need to find ways of reducing the computational demand to reduce the overall run time.

Mesh Number	Number of cells ($\times 10^5$)	Time step (s)	Courant number	
			Max.	Mean
#1	5.01	0.001	0.970	0.32
#2	4.03	0.001	0.866	0.287
#3	2.50	0.0012	0.818	0.271
#4	1.25	0.002	0.953	0.317
#5	0.63	0.0025	0.849	0.283

Table 6.7: The reduced mesh resolutions, chosen time steps and corresponding Courant numbers used in the reduced mesh resolution study.

One method is to reduce the mesh resolution for the transport simulations. The mesh resolution was produced and assessed to accurately resolve the hydrodynamic features generated by the aerating diffusers in chapter 5. A steady-state velocity field has been found with these meshes through the two-phase simulation and the resultant velocity field has been transferred over to the transport solver. However, the resolution required to resolve the hydrodynamics in the two-phase solve is not necessarily required for the transport solver. It may be possible to reduce the resolution and interpolate the refined velocity field onto these coarser meshes without impacting the transport equation solutions significantly which would provide a procedure to reduce the computational demand of the simulations. This procedure has

been applied previously in [Le Moullec et al. \(2011\)](#) and [Coughtrie \(2016\)](#). To investigate this, 2D simulations with the oxygen mass transport equation were solved for a series of uniformly reduced mesh resolutions. The time step used for each simulation was chosen such that the maximum Courant number was below 1.0 for each specific simulation to confirm that the difference in solutions was only due to the mesh resolutions and not the time step. Table 6.7 summarises the mesh resolution and time steps chosen for this study. A plot of the average soluble oxygen throughout the reactor for each mesh is presented in figure 6.19.

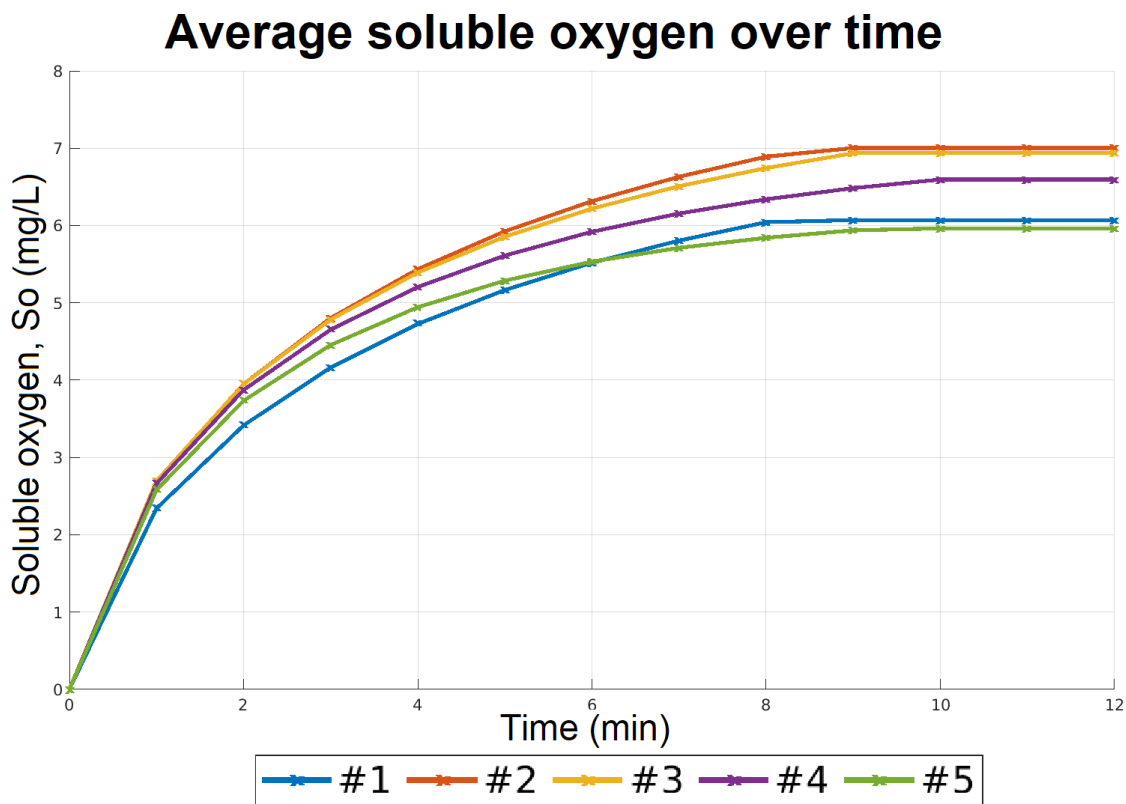


Figure 6.19: The average soluble oxygen in the system over time for the 5 different mesh resolution.

As illustrated in figure 6.19, the mesh resolution is impacting the simulation results. Mesh 2 and 3 result in a faster oxygen transfer initially and a higher saturation value at the end; implying the soluble oxygen is being stirred better for these mesh simulations. However, for mesh 4 and 5 the average soluble oxygen in the domain is less than mesh 2 and 3, specifically, mesh 5 matches the most with the original mesh 1. Considering how the velocity field is interpolated onto the coarser

meshes, the difference in the solutions is to be expected. While the general bulk velocity field will look the same, as illustrated in figure 6.20, the soluble oxygen is transferred on a local cell basis in the regions where the air is located. Reducing the mesh changes the local cell behaviour for both the velocity field and air volume fraction which are the driving forces for the oxygen mass transfer. Changing this can lead to soluble oxygen reaching or missing regions in the flow that was not the case at the previous resolutions.

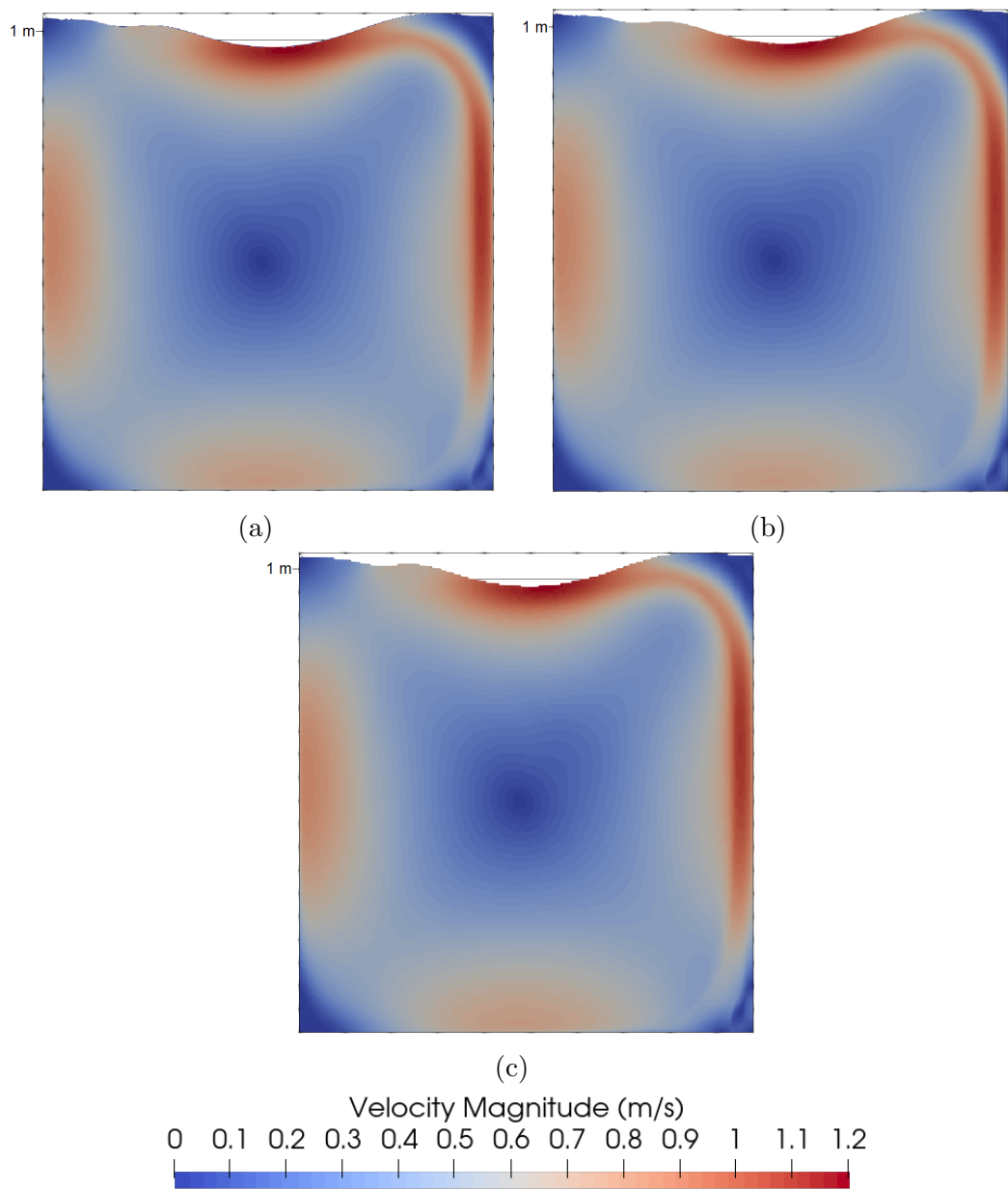


Figure 6.20: The velocity magnitude contour plots for mesh: #1 (a), #3 (b) #5 (c).

If we consider the soluble oxygen profiles after 2 minutes for mesh #1, 3 and 5, we can assess how the resolution changes are impacting the soluble oxygen transfer and mixing on a local scale. Comparing figure 6.21a and figure 6.21b, there is a higher maximum soluble oxygen in the domain and larger concentrations of soluble oxygen reach the slow moving corners in mesh #3 compared with mesh #1. Additionally, both have no soluble oxygen in the centre of the vortex loop. In comparison with figure 6.21c, higher concentrations of soluble oxygen reach the slow moving corners than mesh #1, similarly with mesh #3, but the maximum soluble oxygen in the domain is lower than in mesh #1. Additionally, there is more soluble oxygen near the centre of the vortex loop in mesh #5 compared with the other meshes.

Overall, the changes to the velocity field and volume fraction when interpolating onto a coarser mesh results in changes in the oxygen transfer rates. In general, reducing the mesh resolution artificially increases the mixing of the soluble oxygen. This is expected as, if we were to reduce the mesh to 1 cell, then we would no longer be considering the hydrodynamics and we would return to the normal biokinetic rate equations. The concentrations in the centre of the vortex for mesh #3 and #1 look the same with qualitatively implies the mesh #3 and #1 results are similar. From this study, any reduction in mesh resolution artificiality changes the mixing in the reactor which impacts the results. For the work in this thesis, the mesh resolution will be unchanged for future simulations. However, if the computational demand becomes too high, a mesh reduction will be applied and the effect of this on the simulation results will need to be considered in the analysis. From the results of this study, it is recommended to not go below half of the original mesh resolution to reduce the amount of artificial numerical diffusion.

6.5 Simple biokinetic aeration model (SBAM)

We will now begin coupling the biological process from the ASMs. However, initially, instead of coupling the full 12 transport equations from the ASM1 model, as defined

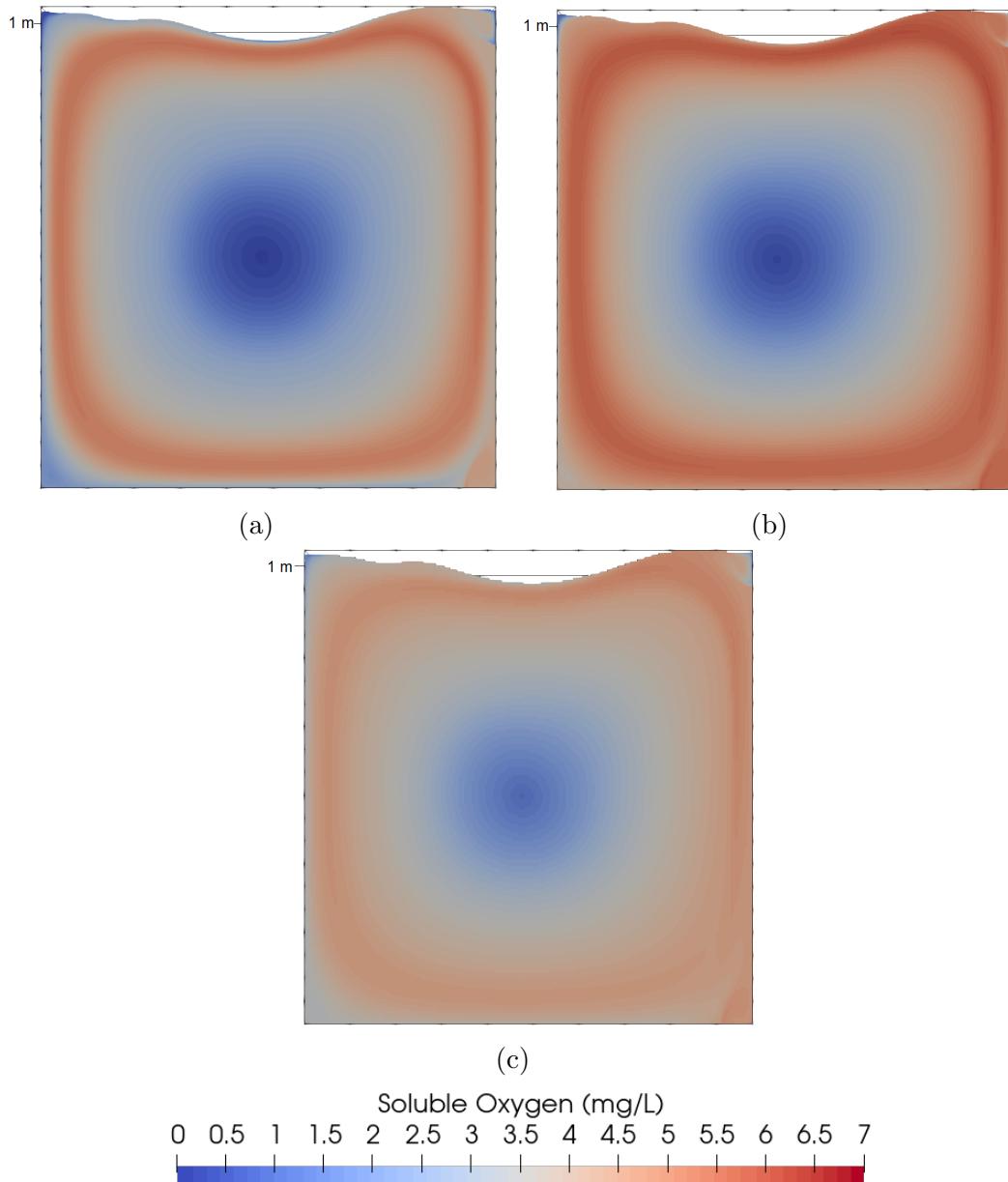


Figure 6.21: The soluble oxygen contour plots after 2 minutes for mesh: #1 (a), #3 (b) #5 (c).

in the matrix in figure 2.3, a three species AS model will be derived that includes the soluble oxygen and is an extension of two species AS model defined in §2.1.1. The three species AS model has been derived by only considering the aerobic growth and decay processes for the active heterotrophic biomass and the three biological components soluble oxygen, soluble substrate and active heterotrophic biomass (S_o , S_s and $X_{B,H}$, respectively) from the ASM1 matrix in figure 2.3. This leads to the simplified biokinetic aeration model (SBAM) which can be represented by the matrix

in figure 6.22, where $X_{B,H}$ is referred to as X_B as all the biomass is heterotrophic in this model. When we also consider the oxygen mass transfer term, we get the three

		Continuity			Process Rate, ρ_j [ML ⁻³ T ⁻¹]	
Component	\rightarrow	i	1	2		3
j	Process	\downarrow	X_B	S_S	S_O	
1	Growth		1	$-\frac{1}{Y}$	$-\frac{1-Y}{Y}$	$\mu \frac{S_S}{K_S + S_S} \frac{S_O}{K_O + S_O} X_B$
2	Decay		-1			bX_B
Observed Conversion Rates ML ⁻³ T ⁻¹		$r_i = \sum_j r_{ij} = \sum_j \nu_{ij} \rho_j$				Kinetic Parameters: Maximum specific growth rate: μ Half-velocity constant: $K_S K_O$ Specific decay rate: b
Stoichiometric Parameters: True growth yield: Y		Biomass [M(COD) L ⁻³]	Substrate [M(COD) L ⁻³]	Oxygen (negative COD) [M(-COD) L ⁻³]		

Figure 6.22: The matrix form of the SBAM model, a reduced 3 species version of the ASM1 matrix that includes soluble oxygen; A simplification of the matrix in Henze et al. (2007).

biokinetic rate equations below,

$$\begin{aligned}
 \frac{dS_o}{dt} &= k_l a (S_{o,sat} - S_o) - \hat{\mu} \frac{1-Y}{Y} \frac{S_s}{K_s + S_s} \frac{S_o}{K_o + S_o} X_B, \\
 \frac{dS_s}{dt} &= -\hat{\mu} \frac{1}{Y} \frac{S_s}{K_s + S_s} \frac{S_o}{K_o + S_o} X_B, \\
 \frac{dX_B}{dt} &= \hat{\mu} \frac{S_s}{K_s + S_s} \frac{S_o}{K_o + S_o} X_B - bX_B.
 \end{aligned} \tag{6.5}$$

which we will refer to as the uncoupled SBAM. If we convert the biokinetic equations into advection-diffusion transport equations and substitute the oxygen mass transfer model for $k_l a$ from §6.4, then we derive the coupled SBAM model,

$$\begin{aligned}
 \frac{dS_o}{dt} + \nabla \cdot (\mathbf{u}S_o) - \nabla \cdot (\Gamma_{S_o} \nabla S_o) &= 12 \frac{\alpha_g}{d_b \alpha_l} \sqrt{\frac{D_{S_o} u_{slip}}{\pi d_b}} (S_{o,sat} - S_o) \\
 &\quad - \hat{\mu} \frac{1-Y}{Y} \frac{S_s}{K_s + S_s} \frac{S_o}{K_o + S_o} X_B, \\
 \frac{dS_s}{dt} + \nabla \cdot (\mathbf{u}S_s) - \nabla \cdot (\Gamma_{S_s} \nabla S_s) &= -\hat{\mu} \frac{1}{Y} \frac{S_s}{K_s + S_s} \frac{S_o}{K_o + S_o} X_B, \\
 \frac{dX_B}{dt} + \nabla \cdot (\mathbf{u}X_B) - \nabla \cdot (\Gamma_{X_B} \nabla X_B) &= \hat{\mu} \frac{S_s}{K_s + S_s} \frac{S_o}{K_o + S_o} X_B - bX_B,
 \end{aligned} \tag{6.6}$$

where Y is the yield constant; K_s and K_o are the half-velocity constants for S_s and S_o , respectively; $\hat{\mu}$ and b are the growth and decay rate of the biomass and the other terms have been defined in sections 2.2 and 6.4. The values of the constants are derived from Henze et al. (2007) and are defined in table 6.8. The SBAM

Parameters	Notation	Value	Units
Maximum specific growth rate	$\hat{\mu}$	6.94×10^{-5}	s^{-1}
Decay rate	b	2.31×10^{-6}	s^{-1}
Growth yield	Y	0.67	-
Diffusion coefficient of parameter i	Γ_i	1.0×10^{-5}	m^2s^{-1}
Half velocity constant for S_o	K_o	0.20	mg/L
Half velocity constant for S_s	K_s	20.0	mg/L

Table 6.8: Constants for the SBAM model used in OpenFOAM.

model allows us to run investigations into how the hydrodynamics can impact the biological processes without the need to include all 13 transport equations from the ASM1 model which would significantly increase the required computational demand, allowing for more studies to be conducted.

6.5.1 Comparison of coupled and uncoupled SBAM model

In this section, the SBAM model will be coupled with the hydrodynamics to model a batch reactor and compared with the uncoupled SBAM to assess how the hydrodynamics impacts the biological processes. The 2D one diffuser 0.6 L/s reactor is being considered for the batch reactor. The equations described above in ?? are solved using the velocity field from the one diffuser 0.6 L/s simulation. The coupled SBAM will be compared with the uncoupled SBAM, described by equation (6.6) and solved in *MATLAB*, to assess the effect of the hydrodynamics on the biological rate reactions in the coupled model. The *ODE45* function in *MATLAB* was used, which is a numerical function provided by *Matlab* that uses the 4th order Runge Kutta numerical method, to solve the set of equations in the uncoupled SBAM. However, we still require a k_{la} and $S_{o,sat}$ for the source term in the oxygen equations. In this

Cases	Description
Coupled SBAM	Solving the SBAM with the effects of the hydrodynamics included by solving the transport equations in ?? for the 2D one diffuser 0.6 L/s simulated reactor.
Uncoupled SBAM	Solve the SBAM model as described in equation (6.6) with the $k_l a$ and $S_{o,sat}$ values derived from the 2D one diffuser 0.6 L/s simulation using the method described in §6.4.4

Table 6.9: A description of the two cases considered in this section.

case, we have implemented the derived values for $k_l a$ and $S_{o,sat}$ from the method described in §6.4.4 for the 2D one diffuser 0.6 L/s reactor. Therefore, we have the coupled SBAM that models the aeration locally and considers the hydrodynamics and the uncoupled model that has similar aeration rates but is applying that aeration uniformly throughout the reactor such that we do not need to consider the hydrodynamics. This means that when we compare the results of the two models, because the aeration rates are comparable we can fully analyse the effects of the hydrodynamics on the biological processes. A summary of the two cases considered are described in table 6.9.

The initial conditions for the concentrations in these simulation are summarised in table 6.10. The initial concentrations of S_s and X_B were chosen such that we see a drop in the soluble oxygen before reaching the soluble oxygen saturation value. This allows us to observe how the system behaves when there is not an abundance of soluble oxygen to get a better understanding of how limited soluble oxygen affects the system and to better assess the effect of the hydrodynamic flow field. The simulations are run for 8 hours and the average concentrations throughout the reactor is calculated at 5 minute intervals for the coupled model. The results for all three concentrations for both models are presented in figure 6.23. For the coupled SBAM results, the standard deviation for each data point was calculated and included on the plots as a shaded region to indicate the distribution of the concentrations in the

reactor at each data point.

Parameters	Notation	Value	Units
Initial S_S tank concentration	$S_{S,\text{initial}}$	400	mg/L
Initial X_B tank concentration	$X_{B,\text{initial}}$	200	mg/L
Initial S_o tank concentration	$S_{o,\text{initial}}$	0	mg/L

Table 6.10: The initial conditions for the coupled and uncoupled SBAM simulations.

Comparing the plots in table 6.10, there is a clear difference in the results indicating that the hydrodynamics is impacting the biological processes. If we first consider the soluble oxygen, in the coupled SBAM it reaches an average of around 4.5 mg/L after approximately 10 minutes and stays at this value for another 3 hours. Comparatively, the uncoupled SBAM reaches a higher concentration of around 5 mg/L after 15 minutes and then decreases slowly for approximately 3.5 hours as the system compensates for the increase in biomass from growth. It takes 3 hours for the coupled SBAM average S_o to begin to decrease due to higher biomass concentrations.

After 7 hours, the coupled SBAM model average S_o begins to increase once again as the S_s has decreased enough to significantly impact the growth of biomass which results in less soluble oxygen being consumed so the amount of soluble oxygen in the tank increases. For the uncoupled SBAM, it only takes 4 hours for the S_s to be depleted enough to impact the biomass growth. If we consider the standard deviation spread of the S_o for the coupled SBAM in figure 6.24, the concentration of soluble oxygen varies ± 0.5 mg/L throughout the 8 hour period. However, if we consider the S_o contour plot in figure 6.24a after 4 hours, the S_o is as low as 2.3 mg/L in some regions of the reactor. This variation is the main cause in the difference between the coupled and uncoupled SBAM results. In non-aerated regions of the tank, only the hydrodynamic flow field can convect the S_o to these regions. Therefore, there are areas in the tank where there is minimal S_o present for the biomass to consume and grow. This significantly reduces the rate of growth on

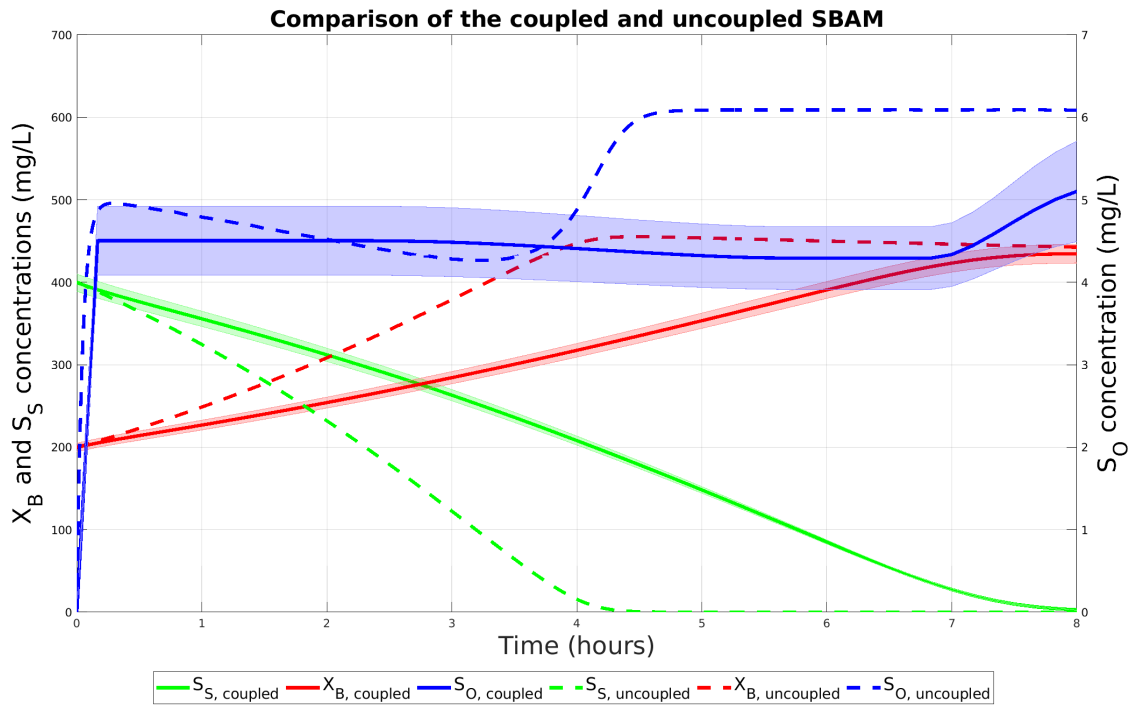


Figure 6.23: The average concentrations over time for the coupled and uncoupled SBAM in the 2D 0.6 L/s reactor. The shaded regions are the standard deviations from the averaging across the whole reactor in the simulation results for each concentration at each point to illustrate how much the concentrations vary in the reactor.

average throughout the reactor which results in this slower increase and decrease of the X_B and S_S concentrations, respectively. This is clearer from the variation in the contour plots in figures 6.24b and 6.24c. From the S_O contour plot in figure 6.24a, the soluble oxygen concentrations are lowest around the sides of the reactor. This impacts the rate of growth as biomass consumes less soluble substrate which results in the biomass and soluble substrate being largest and smallest, respectively, in these regions, as can be seen in figures 6.24b and 6.24c.

An unexpected result is that the middle of the reactor, which is the centre point of the vortex flow field, has the largest concentration of biomass even though this is a slower moving region of the reactor which S_O struggles to reach, indicated by the lower concentration of S_O in the centre of figure 6.24a. In this case, adequate soluble oxygen is reaching the centre of the reactor to not hinder the growth rates. Additionally, the slower moving flow field allows for the growth reactions to occur without being convected away and spread throughout the reactor. This results in

the highest and lowest concentrations of X_B and S_S occurring in the centre of the reactor, respectively.

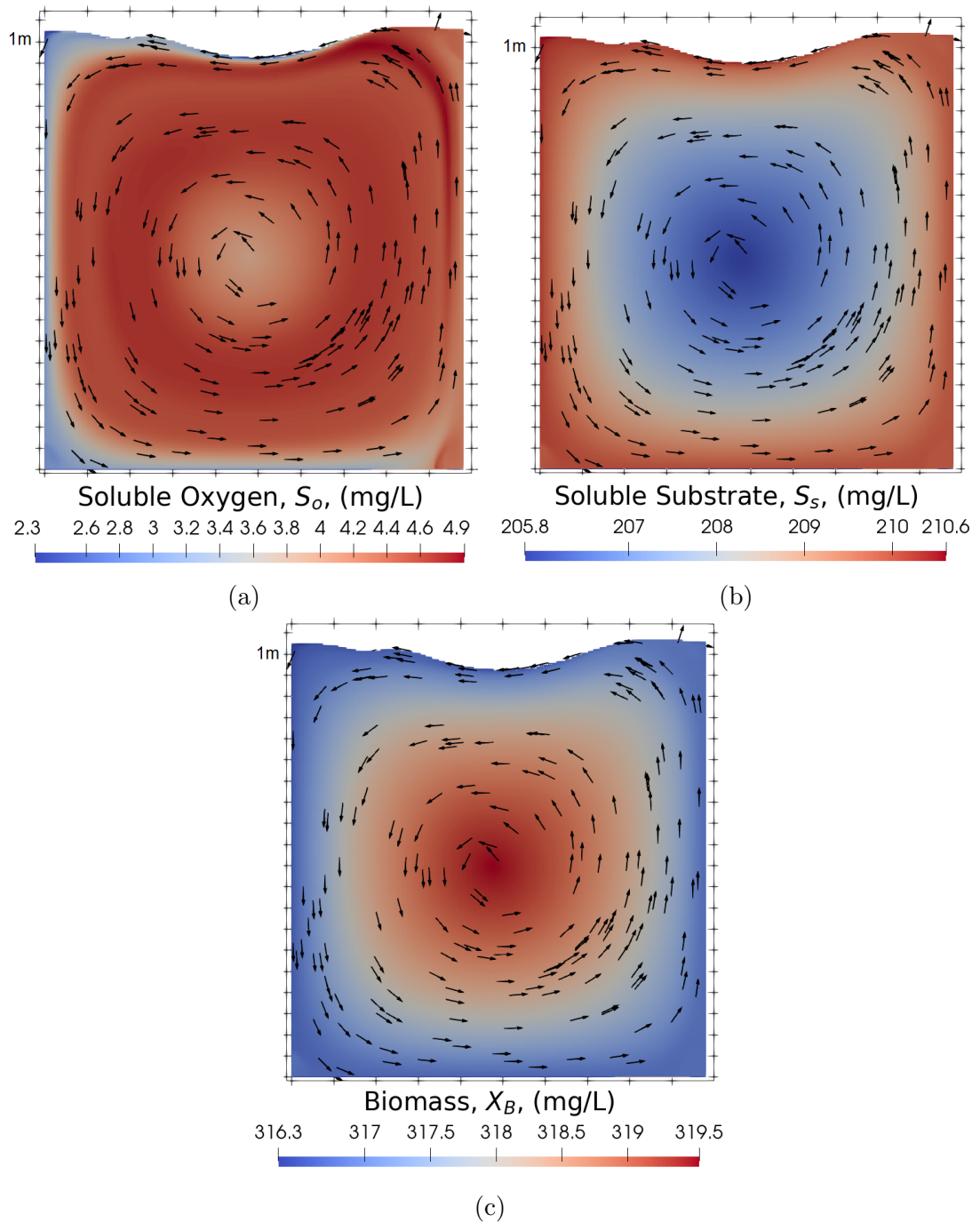


Figure 6.24: Contour plots of the coupled SBAM S_o (a), S_s (b) and X_B (c) concentrations in the reactor after 4 hours with normalised velocity vectors to understand how the concentrations are moving.

In summary, through the comparison of the coupled and uncoupled SBAM with similar aeration rates, we have illustrated the direct impact of the hydrodynamics

on the biological performances. In this modelled 2D reactor, including the effects of the hydrodynamics results in the reactor needing twice the amount of time to reach the maximum biomass concentrations. This emphasizes that neglecting the hydrodynamics can significantly change the expected result from the biokinetic models, reinforcing the importance of including the hydrodynamics in the models.

6.6 Inlet location case study

In the studies above, the simulations have been modelling a batch reactor which is the case for our experimental aeration tank. However, in a real aeration tank there is wastewater entering and leaving continuously, carrying biological concentrations during the operation of the reactor. In the ASMs, extra source terms, in the form $(Q/V)C$, are required in the rate equations to model the additional concentrations entering and leaving through the inlets and outlets, as shown in equations (2.1) and (2.2). In the rate equations, these terms assume the concentrations entering the tank are spread throughout the domain, or more specifically, that the mixing hydrodynamic flow field is such that the concentrations are instantaneous mixed uniformly throughout the reactor. However, we have already shown in §6.5.1 that the hydrodynamic field may not be uniformly mixing the concentrations. In this study, we will investigate the effect of including and changing the location of the inlet and outlet in the reactor on the biological processes.

The hydrodynamic simulations do not have an inlet and outlet and so the zone approach, as described in §6.2, has been used to model the inlet and outlet. To create the zones in OpenFOAM, the *topoSet* utility has been used to define and name the zoned regions inside of the domain. To apply the source terms to the transport equations, the *scalarSemiImplicitSource* source term function with the *specific* approach was implemented into the *fvOptions* utility which applies the extra source terms in the *topoSet* defined zones.

It is assumed that the flow rate at the inlet and outlet is slow such that their

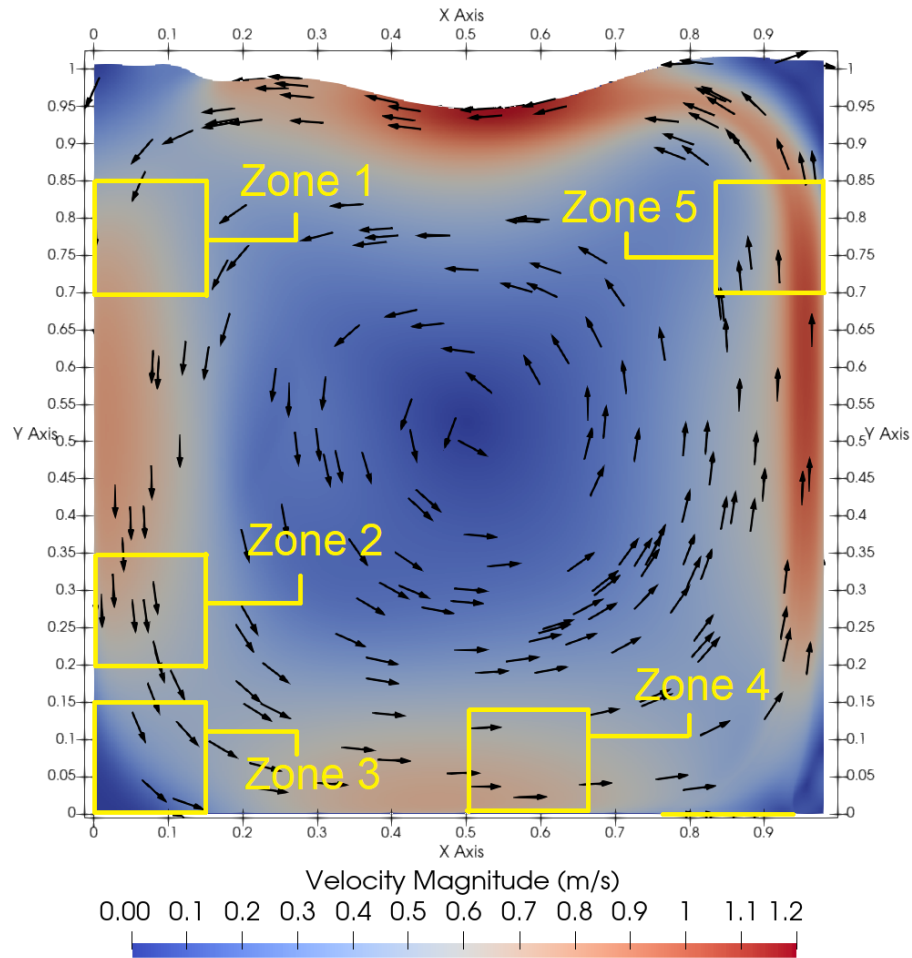


Figure 6.25: The velocity magnitude contour and normalised velocity vectors plot for the 2D one diffuser 0.6 L/s simulation with an illustration of the approximate zone locations for the inlet case study, where each zone has the same area. The yellow line at the base indicates the location of the aerating diffuser.

effects on the hydrodynamic flow field can be neglected. To assess this, if we consider that aeration tanks are designed to have a hydraulic retention time of 2 hours (Meister et al., 2017) then we can derive a flow rate, Q , for the 1/3 reactor. The 1/3 reactor has a volume of 0.237 m^3 which gives us a flow rate of $Q = 3.292 \times 10^{-5} \text{ m}^3/\text{s}$. If we assume we have a pipe connected to the tank with a radius of 2.5 cm and area of $1.95 \times 10^{-3} \text{ m}^2$ which is about 0.27 % of the side wall area, then the calculated inlet velocity is $v_{in} = 0.017 \text{ m/s}$, which is two magnitudes smaller than the velocities generated by the rising bubbles in figure 6.25. Therefore, our assumption to neglect the hydrodynamic effect of the inlet and outlet is reasonable. However, it is important to note that this assumption would not necessarily be valid for a

full-scale aeration tank. This is because the inlet velocity scales with the reactor volume but the flow field velocity in the tank is expected to be of the same order of magnitude as adding more diffusers to accommodate the bigger reactor does not increase the magnitudes of the velocities seen in the fluid. Therefore, this assumption would need to be re-assessed for modelling a full-scale reactor.

The SBAM has been implemented using the 2D 0.6 L/s flow rate simulation. The zones considered for the inlet and outlet are illustrated in figure 6.25 and the three cases simulated are described in table 6.11. The zones are all assumed to

Inlet case	Inlet location	Outlet location
#1	Zone 5	Zone 2
#2	Zone 5	Zone 4
#3	Zone 3	Zone 1

Table 6.11: Summary of the inlet and outlet locations for the three inlet cases considered.

have the same volume, $V_{\text{zone}} = 0.15 \times 0.15 \times 0.247 = 5.56 \times 10^{-3} \text{ m}^3$, where the zones extend the full depth of the 1/3 reactor to be consistent with the 2D nature of the simulations. The flow rate, $Q = 3.292 \times 10^{-5} \text{ m}^3/\text{s}$, as defined above is used for both the inlet and outlet to conserve continuity in the tank. The initial values in the tank for the S_S and X_B concentrations were defined as 25 and 1500 mg/L, respectively, and the inlet values of 750 and 25 mg/L, respectively. The large initial X_B and S_S inlet concentrations, which may be unrealistic, were chosen to speed up the biokinetic processes and allow us to observe the impact of the inlet location in a reasonable time period. A summary of all these values are presented in table 6.12. The coupled SBAM model with the values and parameters defined in table 6.8 were run for the three inlet zone cases over a 30 minute period to assess and compare the impact of the inlet and outlet locations.

The large S_S inlet concentration was chosen to observe the impact of the inlet zone location more clearly and, therefore, this concentration will be the focus in this

Parameters	Notation	Value	Units
Inlet and outlet flow rate	Q_{in}, Q_{out}	3.292×10^{-5}	m^3/s
Inlet and outlet zone volume	V_{in}, V_{out}	5.56×10^{-3}	m^3
Initial S_S tank concentration	$S_{S,initial}$	25	mg/L
Initial X_B tank concentration	$X_{B,initial}$	1500	mg/L
Initial S_o tank concentration	$S_{o,initial}$	0	mg/L
S_S inlet concentration	$S_{S,inlet}$	750	mg/L
X_B inlet concentration	$X_{B,inlet}$	25	mg/L
S_o inlet concentration	$S_{O,inlet}$	0	mg/L

Table 6.12: Summary of the initial and inlet conditions for the inlet case studies.

section. The average S_S concentration over the 30 minute period for each inlet case is presented in figure 6.26 along with the *Matlab ODE45* 4th order Runge Kutta method numerical method solution of the uncoupled SBAM with the same inlet conditions, designated the “Uncoupled inlet SBAM”. Additionally, the S_S contour profiles for each inlet case after 30 minutes is presented in figure 6.27.

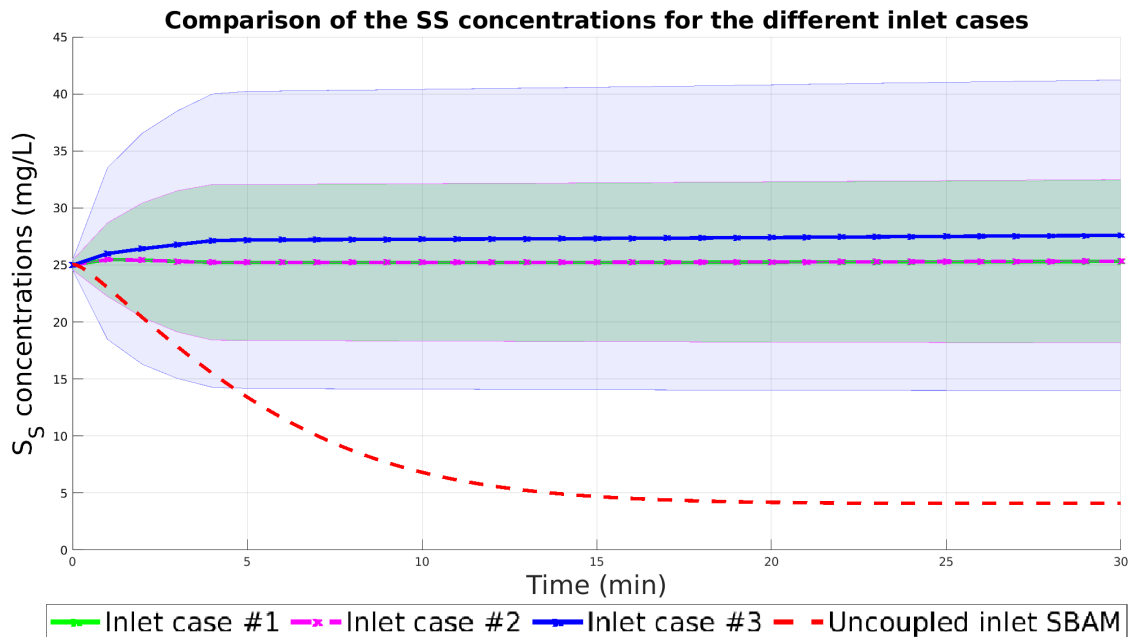


Figure 6.26: The average soluble substrate over time for the three inlet cases stated in table 6.11 and the uncoupled SBAM with the same conditions. The shaded regions are the standard deviations from the averaging across the whole reactor in the simulation results for each concentration at each point to illustrate how much the concentrations vary in the reactor.

Analysing figure 6.26, there is significant difference between the uncoupled and

coupled results which, from our previous analysis in §6.5.1, is expected due to the inclusion of the hydrodynamics. In the uncoupled SBAM, the inlet and outlet conditions are applied uniformly throughout the reactor such that it takes around 20 minutes for the S_S rate equations to reach an equilibrium. In comparison, the average S_S concentrations in the inlet cases see only a slight change from the initial concentrations and reach an equilibrium after around 5 minutes. However, from the standard deviation shaded region in figure 6.26, it is clear that the S_S concentration have a large variation in the tank. This is clearer when we consider the S_S contour profiles in figure 6.27.

The S_S concentrations vary from the 10 - 33 mg/L for the inlet case 1 and 2 in figures 6.27a and 6.27b and even more for inlet case 3. The hydrodynamics flow field dictates how the concentrations are distributed through the reactor. Furthermore, the effectiveness of the inlet and outlet locations are also dependent on the flow field as it defines where the concentrations enter, travel to, and if they can reach the outlet to leave. Therefore, choosing poor inlet and outlet locations can result in the concentrations not being distributed efficiently; obstructing the biological processes. This effect can be seen in the differences in the S_S concentrations in the inlet cases.

Inlet case 1 and 2 give almost identical results in the average and contour plots in figures 6.26 and 6.27, which is foreseeable as they both have the same inlet zone location and the zone locations for both cases where chosen in fast moving regions of the tank. In comparison, inlet case 3 had the inlet location in the bottom left corner which contained a small closed vortex. This results in S_S concentration being trapped and building up such that it rising above the 55 mg/L limit in figure 6.27 and rises up to 150 mg/L. This results in higher concentrations of S_S in the outer regions compared with the central areas which impacts the biological processes, illustrated by the differences in average S_S concentrations between the inlet cases in figure 6.26. The hydrodynamic closed vortex is partly due to the 2D nature of the simulations and not having an additional dimension to move along; however, we have shown that the choice of the inlet and outlet location can impact on the biological performance

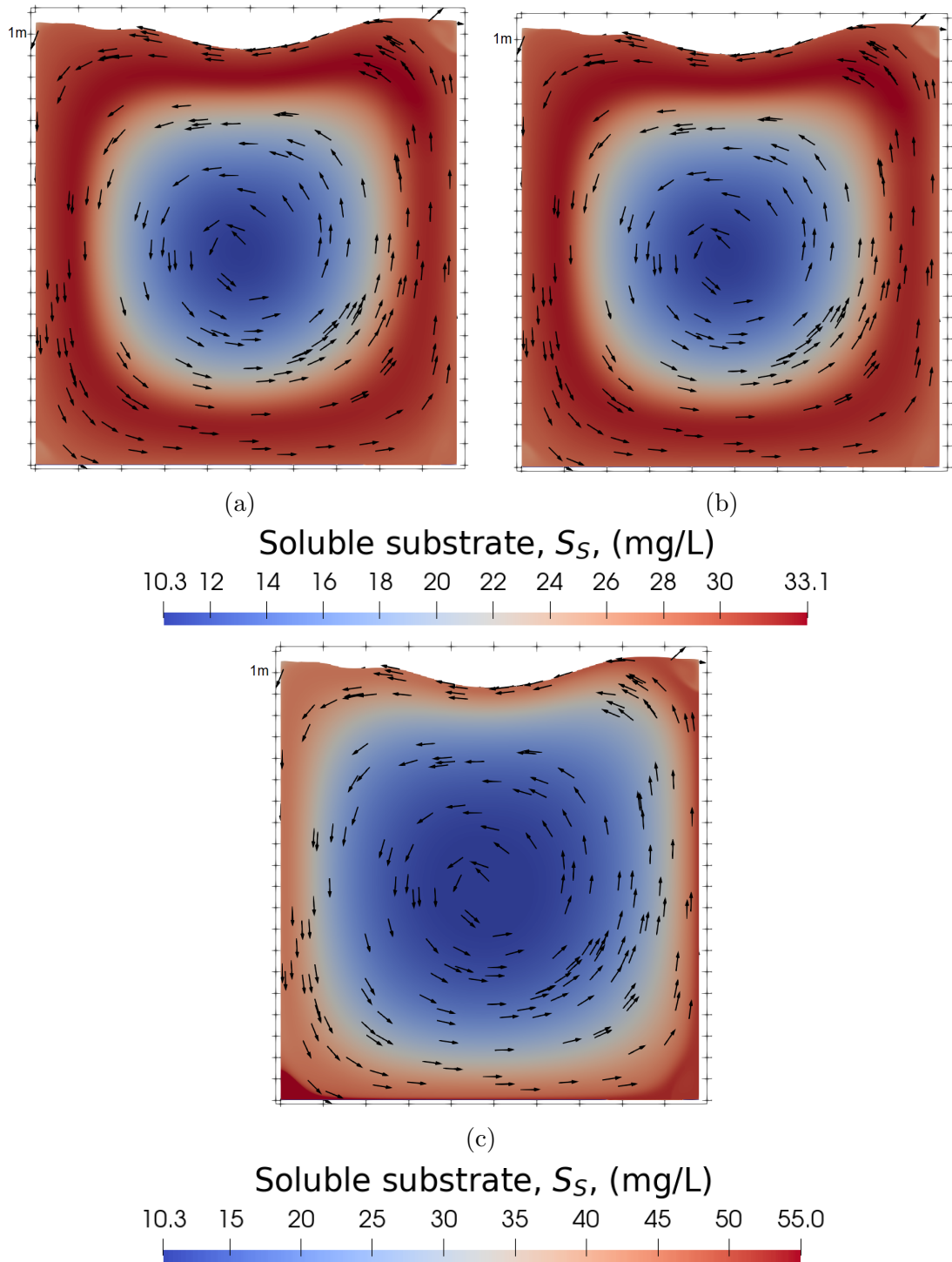


Figure 6.27: Contour and normalised velocity vector plots of the S_s concentrations for inlet case #1 (a), #2 (b) and #3 (c) in the reactor after 30 minutes. The (c) contour plot has been capped at 55 mg/L so that it is easy to observe the concentration distribution in the reactor. However, the maximum concentration reaches up to 150 mg/L.

of the reactor. In the the uncoupled SBAM model, the results do not change with the moving of the inlet and outlet locations as the model assumes the concentrations

enter and leave uniformly throughout the reactor and is only dependent on the rates of the in and outflow. It is only possible to investigate the impact of the inlet and outlet location by using a coupled model, emphasising another potential benefit of using the coupled model over non coupled ASMs.

6.7 Three dimensional flow rate study

In this section, the oxygen transfer and SBAM will be coupled with the 3D 1/3 reactor hydrodynamic velocity fields for the 0.3 and 0.6 L/s air flow rates in §5.4, as illustrated in figure 5.34 and figure 5.29, respectively. An analysis of the difference between the 2D and 3D solutions for the oxygenation of the reactor as well as the impact on the biological processes in the SBAM will be made. Additionally, the coupled results from the 0.3 and 0.6 L/s hydrodynamic solutions will be compared to observe how the flow rate impacts the biological solutions in 3D to evaluate the optimal flow rate for the aeration tank.

6.7.1 Oxygen mass transfer

To begin with, the oxygenation rates of the two 3D simulations will be compared. The parameters defined in table 6.4 are used for the oxygen transfer model. The average soluble oxygen throughout the reactor is calculated over a 30 minute period for both flow rate simulations and plotted in figure 6.28. Additionally, the curved fitted solutions are included for the simulations.

The 0.6 L/s flow rate reactor has a larger calculated global $k_{l}a$ value which implies the oxygen is transferring faster for this flow rate compared with the 0.3 L/s flow rate. From our analysis in §6.4.4, this suggests the 0.6 L/s flow field has a better air volume fraction distribution. Additionally, the calculated soluble oxygen saturation value, $S_{o,sat}$, is larger for the 0.6 L/s implying that the hydrodynamic flow field is better at mixing compared with the 0.3 L/s flow rate. However, the

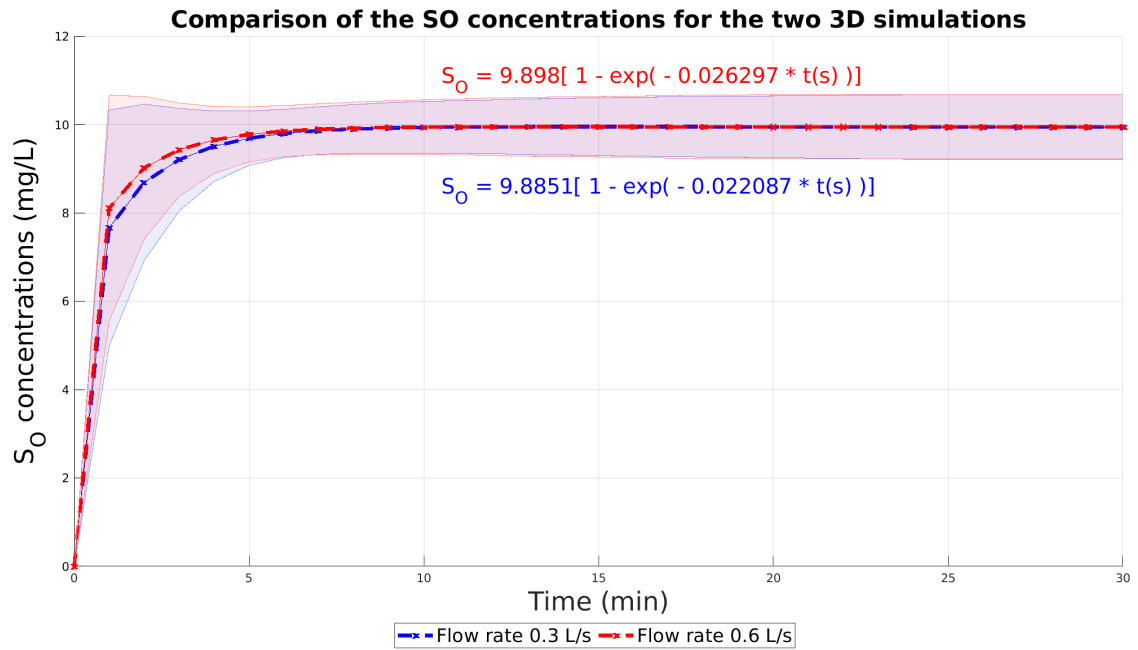


Figure 6.28: The average soluble oxygen over time for the 0.3 and 0.6 L/s 3D simulations and their curve fitted solutions. The shaded regions are the standard deviations from the averaging across the whole reactor in the simulation results for each concentration at each point to illustrate how much the concentrations vary in the reactor.

difference in these values are very small when we consider the plots in figure 6.28. The amount of air being pumped per second has doubled for a 20% increase in the rate of oxygen transfer coefficient and less than a 1% increase for the saturation value. For the additional power costs required to pump twice as much air, the increase in the amount of oxygen entering the reactor is minimal. Furthermore, both simulations have almost reached the 10 mg/L saturation value defined in the oxygen mass transfer model defined in §6.4. This suggests that both flow fields are very close to desired “well-mixed” reactor and, more specifically, the extra air being pumped in the 0.6 L/s is not achieving any additional benefits for the reactor operation. This is clearer when we consider the soluble oxygen disruptions throughout the reactor in figure 6.29.

The soluble oxygen profile for both flow rates in figure 6.29 are very similar, illustrating that the distribution of the soluble oxygen is almost the same for both flow rates. The 3D 1/3 reactor hydrodynamic flow field has a central vortex, similarly to what is seen in the 2D simulations, which results in a region of the reactor that is

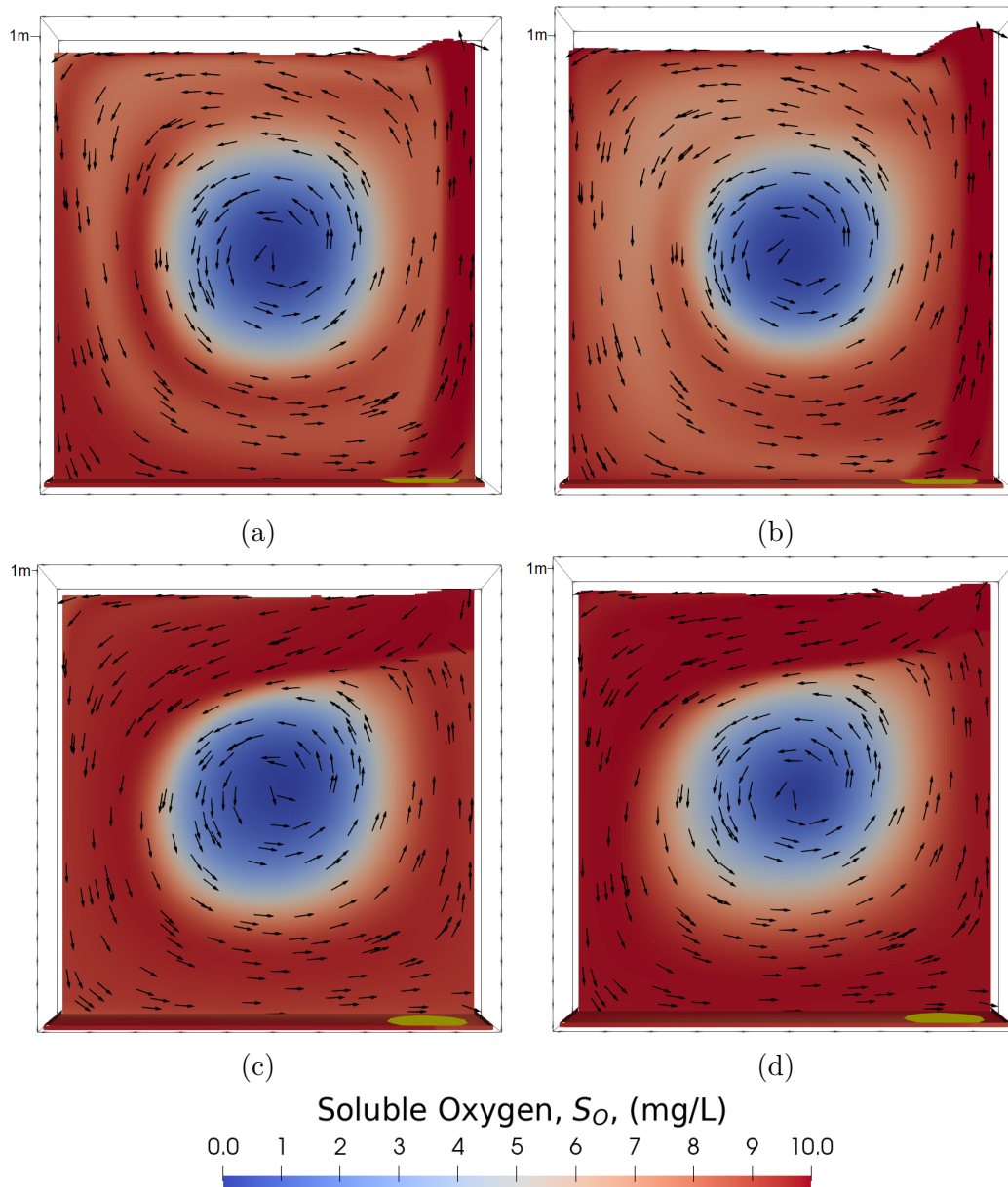


Figure 6.29: The soluble oxygen, S_o , contour plots and normalised velocity vectors after 1 minute for the 1/3 reactor at a depth of $y = 12.8$ cm at flow rate 0.3 L/s (a) and 0.6 L/s (b) and depth of $y = 24.8$ cm at flow rate 0.3 L/s (c) and 0.6 L/s (d). The yellow circle at the base illustrates the location of the aerating diffuser.

difficult for the transferred oxygen to reach via convection. This central region is the limiting factor for why the plots in figure 6.28 do not reach the 10 mg/L saturation instantly. The size of the central region that has less than 5 mg/L of soluble oxygen and is smaller in the 0.6 L/s flow rate simulation, figures 6.29b and 6.29d, compared with the the 0.3 L/s flow rate simulation,, figures 6.29a and 6.29c. This implies that the flow field generated in the 0.6 L/s is convecting the soluble oxygen to this central

region faster and is reason for the difference between the average soluble oxygen plots in figure 6.28. Another interesting feature is that there is more soluble oxygen at a depth of $y = 24.8$ cm near the far symmetry plane, figures 6.29c and 6.29d, compared with the central plane, figures 6.29a and 6.29b, for both flow rates. This is a result of the 3D flow field being compressed and becoming more 2D as it approaches the symmetry plane in the simulation; this results in a build up of soluble oxygen concentration. In the central plane, the soluble concentration has 3 directions to move causing more soluble oxygen travelling along depth or y axis and out of the plane, resulting in less observed soluble oxygen.

Comparing the 3D average soluble oxygen plots in figure 6.28 to the 2D plots in figure 6.17, it is clear that the 3D flow field is having a significant impact on the rate of oxygen transfer. As discussed previously, the $k_l a$ and $S_{o,sat}$ are dependent on the air volume fraction distribution and hydrodynamic flow field, respectively. Modelling an additional dimension, even though we have shown the velocities are small from experiments in this dimension, helps to spread the air volume fraction and convect the soluble oxygen to the non aerated regions. Furthermore, if we compare the 3D soluble oxygen profiles in figure 6.29 to the 2D ones in figure 6.21, the 3D simulations do not have dead zones in the corners of the reactor which, for the 2D simulations, can only be reached by the diffusion of the concentration which is extremely slow. These corner regions have another dimension to escape which results in a more uniform soluble oxygen distribution for the 3D simulation in figure 6.29.

The conclusion from this analysis is that the 3D 0.6 L/s flow field does not significantly improve the oxygenation of the reactor compared with the 0.3 L/s such that the 0.3 L/s flow rate could be run to save operational costs without hindering the oxygenation of the reactor. Additionally, from how fast the reactor is oxygenated from these oxygenation curves, it would be expected that the 3D reactor is well-mixed and that the coupled SBAM model will produce identical results as the uncoupled SBAM. To check this, we will couple the SBAM model into the 3D

hydrodynamic simulations.

6.7.2 Biological processes

In this section, the SBAM is implemented into a batch reactor using the flow fields from the two 3D simulations to assess and compare how the two different flow rates effect the biological processes. The parameters for the SBAM model are defined in table 6.8 and the same initial concentrations defined in table 6.10 was used. From the calculated oxygenation curves in figure 6.28, the tank is being well oxygenated which implies a good air distribution and mixing flow field and so we expect the coupled SBAM for the 3D reactor to be the same or very similar to the uncoupled SBAM. The simulations were run for 4 hours in real time and the average concentrations over time in the reactor were calculated for flow rate 0.3 L/s and 0.6 L/s which are presented in figures 6.30a and 6.30b with their corresponding uncoupled SBAM results, respectively.

Comparing the results in figure 6.30 to the 2D 0.6 L/s coupled SBAM results in figure 6.23, where the model took twice as long to consume all the soluble substrate than the uncoupled SBAM, there is almost no difference between the coupled and uncoupled SBAM concentrations for both flow rates in the 3D results, which was predicted. In the 3D reactor, the hydrodynamic flow field generated by the aerating diffuser is providing enough oxygen for the biological processes and mixing the concentrations such that they are uniformly distributed throughout the reactor for both flow rates. As a result, the uncoupled and coupled SBAM results are identical which implies that for this reactor, at these flow rates, the hydrodynamics can be neglected for modelling the biological processes. This is because when a reactor is stirred enough such that the hydrodynamics are not impacting the biological processes, the coupled and uncoupled SBAM produce identical results. If we compare the coupled SBAM results for both flow rates in figure 6.30, the average concentrations over time is almost identical for both reactors. This implies that the

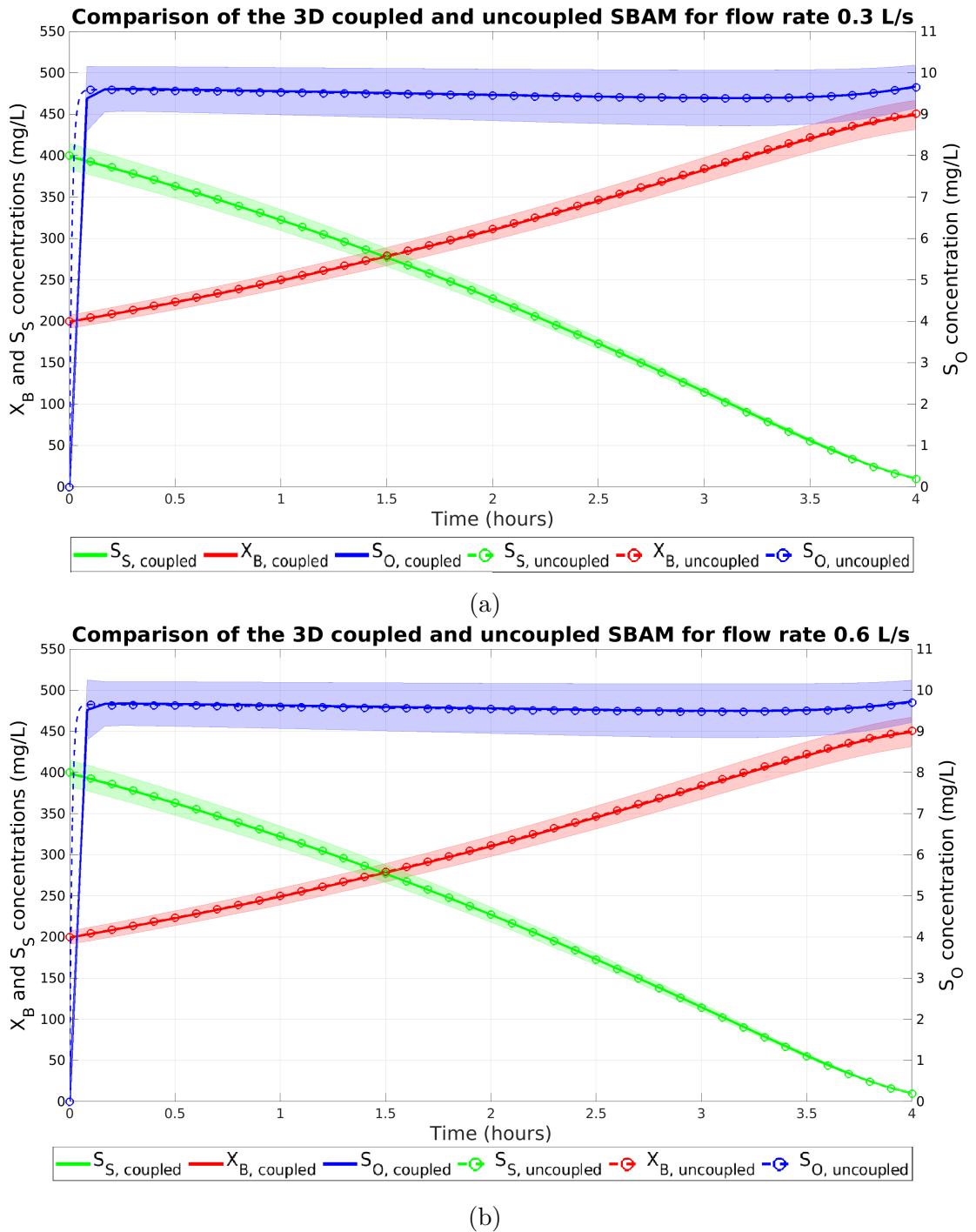


Figure 6.30: The average concentrations over time for the coupled and uncoupled SBAM in the 3D 0.3 L/s (a) and 0.6 L/s (b) reactor. The shaded regions are the standard deviations from the averaging across the whole reactor in the simulation results for each concentration at each point to illustrate how much the concentrations vary in the reactor.

additional air being pumped by the 0.6 L/s reactor compared with the 0.3 L/s reactor is providing no additional mixing or oxygen and is just consuming more power at no additional benefit to the biological process; which was also concluded from the

oxygen plots in figure 6.29. Therefore, for this reactor setup, the aeration rate of 0.3 L/s could be used over the 0.6 L/s with no impact on the biological processes; saving on operational costs.

It is important to note that, for these simulations, we have assumed a uniform initial concentration throughout the batch reactor. This is more likely to give a well-mixed solution due to the uniform spread of concentrations, especially because the oxygenation of the 3D aeration tank is very fast. In a real aeration tank, it would be expected to have a distribution in the tank. Additionally, the initial concentrations were taken from table 6.10 which were calculated such that the biological consumption rates could keep up with the oxygenation rates of the 2D modelled aeration tank. However, as the oxygenation in the 3D reactor is much faster, it is expected that the biological consumption rates cannot keep up with the oxygenation such that it was more likely to give a well-mixed result as seen. The initial concentrations were kept the same to allow a direct comparison between the 2D and 3D simulations results. A scenario could be created such that the biological consumption rates were comparable to the oxygenation rates; however, this could require concentrations that are extremely unrealistic to what could be seen in wastewater aeration tanks.

In summary, the 2D simulations can provide insight into how operational changes to the tank can influence the biological processes and, due to the lower computational demand, more computational simulations and investigations can be conducted for a given amount of time compared with the 3D simulations. However, if the reactor is only pseudo-2D, the 2D simulations will underestimate the full mixing capabilities and biological performance of a reactor design due to neglecting an additional dimension. Therefore, if a new reactor design is being investigated using the coupled model to assess the mixing capabilities and biological performance, then a full 3D simulation will be required to get an accurate representation of the reactors potential. Furthermore, we have verified the coupled SBAM model by showing that, in a well-mixed reactor, we get back to the uncoupled SBAM results. Finally, we have

shown that for this 3D reactor, having aeration flow rate above 0.3 L/s does not improve the mixing or biological performance of the reactor and would only increase the operational costs at no extra benefit.

6.8 Coupled ASM1 reactor

Finally, to complete the coupling procedure, the full ASM1 has been coupled into the simulations. The additional 10 transport equations, compared with the SBAM, significantly increase the computational demand. Therefore, the 2D 0.6 L/s simulation was considered for the flow field over the 3D simulations to save on computational power. Furthermore, of the 13 components included in the ASM1, the soluble inert organic matter, S_I , and the particulate inert organic matter, X_I , do not interact with the other components such that they have no impact on the biological process. Therefore, to further reduce the computational demand of the simulation, these components and transport equations have been neglected. The constants used in the ASM1 model are defined in table 6.13 (Henze et al., 2007).

An inlet and outlet was included in the simulations to model a continuous reactor. The locations of the inlet and outlet chosen for the continuous reactor are described by “inlet case #1” in table 6.11 and illustrated in figure 6.25 with the values for the inlet and outlet flow rates and volume defined in table 6.12.

The initial and inlet concentrations for the 11 components for the aeration tank were taken from the values used in Meister et al. (2017) for their modelled denitrification basin. The inlet concentration was a flow weighted average from the new activated sludge entering the tank and the returned activated sludge that has been recirculated back in. A summary of the initial and inlet concentrations are summarised in table 6.14.

The coupled simulations were run for 2 hours of simulation time. The main goal of an aeration tank in a wastewater treatment plant is to grow the heterotrophic

Parameters	Notation	Value	Units
Heterotrophic max. specific growth rate	$\hat{\mu}_H$	6.94×10^{-5}	s^{-1}
Heterotrophic decay rate	b_H	7.18×10^{-6}	s^{-1}
Heterotrophic growth yield	Y_H	0.67	-
Autotrophic max. specific growth rate	$\hat{\mu}_A$	9.26×10^{-6}	s^{-1}
Autotrophic decay rate	b_A	1.74×10^{-6}	s^{-1}
Autotrophic growth yield	Y_A	0.24	-
Half velocity constant for heterotrophic S_o	$K_{O,H}$	0.20	mg/L
Half velocity constant for autotrophic S_o	$K_{O,A}$	0.4	mg/L
Half velocity constant for S_s	K_S	20.0	mg/L
Half velocity constant for S_{NO}	K_{NO}	0.50	mg/L
Half velocity constant for S_{NH}	K_{NH}	1.0	mg/L
Half velocity constant for X_S	K_X	0.03	-
Fraction of biomass yielding particulates	f_p	0.08	-
Mass of COD in biomass	i_{XB}	0.086	-
Mass of COD in biomass products	i_{XP}	0.06	-
Correction factor for anoxic growth	η_g	0.8	-
Correction factor for anoxic hydrolysis	η_h	0.4	-
Ammonification rate	k_a	9.26×10^{-7}	L/mg s
Max specific hydrolysis rate	k_h	3.47×10^{-5}	s^{-1}
Diffusion coefficient of parameter i	Γ_i	1.0×10^{-5}	m^2/s

Table 6.13: Constants for the ASM1 implemented in the coupled OpenFOAM model.

biomass, X_{BH} , and to produce as much soluble nitrite and nitrates, S_{NO} , which comes partly through the consumption of ammonia, S_{NH} , such that, when the wastewater enters the anoxic chamber, there is enough S_{NO} for the anoxic growth of the heterotrophic biomass. Therefore, this section will focus on the: X_{BH} , S_S , S_{NO} and S_{NH} concentrations. The average concentration for each of these parameters in the reactor for the coupled ASM1 was calculated at 5 minute intervals. These were compared with the uncoupled or normal ASM1 results, calculated with the *ODE45* 4th order Runge Kutta numerical solver in *Matlab*, using the aeration rates derived in §6.4.4 for the 2D 0.6 L/s reactor. These results are plotted in figure 6.31.

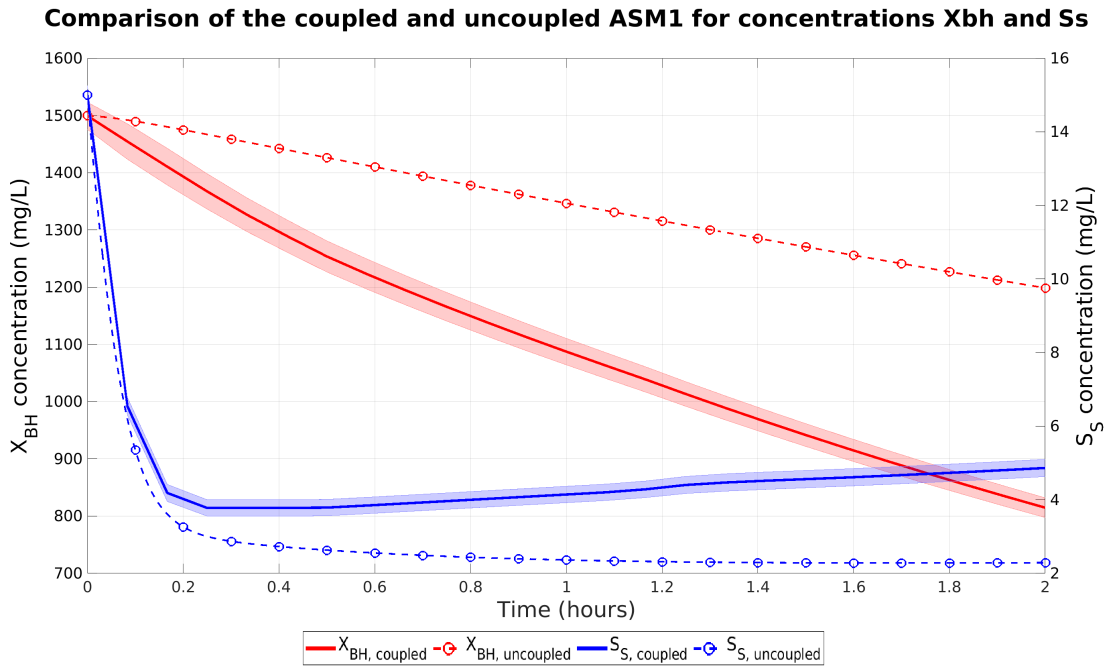
If we first consider the X_{BH} and S_S plots in figure 6.31a, it is clear that there

ASM1 component	Initial concentrations (mg/L)	Inlet concentrations (mg/L)
Soluble substrate, S_S	15	25
Slowly biodegradable matter, X_S	30	120
Heterotrophic biomass, $X_{B,H}$	1500	25
Autotrophic biomass, $X_{B,A}$	100	0
Particulate biomass, X_P	2000	200
Soluble Oxygen, S_O	0	0
Nitrate and nitrite, S_{NO}	5	0
Ammonia, S_{NH}	1	20
Soluble nitrogen, S_{ND}	0.5	1
Particulate nitrogen, X_{ND}	5	8
Alkalinity, S_{ALK}	4	5

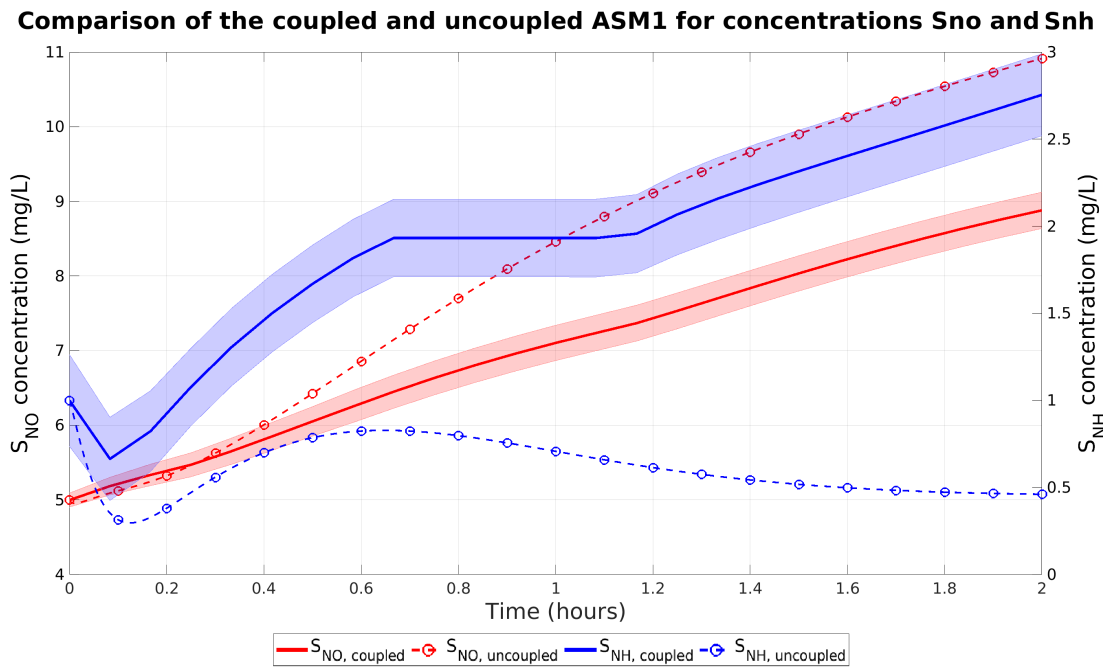
Table 6.14: The inlet and initial concentrations used for the coupled ASM1 model, derived from [Meister et al. \(2017\)](#).

is a difference between the coupled and uncoupled ASM1. This is predictable as we have previously shown in §6.5.1 that the 2D 0.6 L/s reactor is not well-mixed such that the coupled and uncoupled models are not identical using the SBAM. In the coupled results, the X_{BH} is decaying faster compared to the uncoupled model which, because the decay term is only dependent on the X_{BH} concentration, implies that the growth term for the X_{BH} is not as large in the coupled model. The X_{BH} growth term is dependent on the amount of S_S in the reactor which is low in concentration. However, it is lower in the uncoupled ASM1 yet the X_{BH} concentration decays slower in this model. This is a result of the hydrodynamic flow field not uniformly distributing the new S_S entering via the inlet throughout the reactor, as illustrated by figure 6.32, which leads to different growth rates of the X_{BH} that are not overall as high as having a well-mixed reactor. The contour plots for the other biological components have very similar distributions to the S_S plot in figure 6.32.

If we consider the S_{NO} and S_{NH} concentrations in figure 6.31b, there is significant difference between the coupled and uncoupled ASM1 results. The S_{NO} concentrations are lower in the coupled model which implies that the aeration basin is not working as efficiently to create the nitrates and nitrate required for the bio-



(a)



(b)

Figure 6.31: The average concentrations over time for the coupled and uncoupled ASM1 for the 2D simulations at 0.6 L/s for concentrations X_{BH} and S_S (a) and S_{NO} and S_{NH} (b). The shaded regions are the standard deviations from the averaging across the whole reactor in the simulation results for each concentration at each point to illustrate how much the concentrations vary in the reactor.

logical processes in the anoxic basin due to the hydrodynamics. In the uncoupled ASM1, the S_{NH} concentration has reached a steady state between the biological

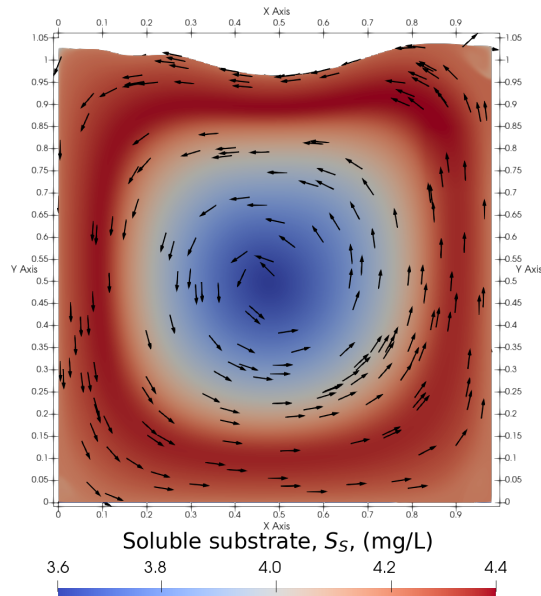


Figure 6.32: The soluble substrate, S_S , contour plots and normalised velocity vectors after 1 hour for the 2D 0.6 L/s reactor with the ASM1.

processes and the amount entering through the inlet by two hours which results in a lower amount of S_{NH} than what was initially in the reactor. However in the coupled reactor, the average S_{NH} concentration is always higher than the uncoupled results. After 0.7 hours, the S_{NH} concentrations reach a steady-state for around 0.5 hours where the consumption, creation and new S_{NH} concentration entering the reactor are in equilibrium. However, after 1.2 hours, one of the S_{NH} consumption processes must reach a critical limit such that it is not longer active, causing the S_{NH} to rise again. This would be caused by another component concentration becoming significantly low that results in the hyperbolic terms, as described in equation (6.3), in the processes rates being suppressed.

In summary, we have shown that inadequate mixing in an aeration tank can impact the biological processes. This causes reduced ammonification rates which results in higher ammonia concentrations remaining in the tank which is one of the main pollutants that is aimed to be removed during secondary treatment. Furthermore, this reduced mixing causes less S_{NO} available for the anoxic tank to utilise in the following process such that the inadequate mixing is impacting the biological performance in both the current and sequential tanks. This additional analysis is

only possible through the full coupling of the hydrodynamics and ASM1 which is not provided by the uncoupled ASM1.

6.9 Chapter summary

In this chapter, a description of the procedure for coupling biokinetic wastewater equations into hydrodynamic solutions with a free surface in OpenFOAM has been defined which has been used to create a coupled model. This coupled model has been used to show how the hydrodynamics can influence the oxygenation and biological processes in the aeration tank which would not be possible with the conventional uncoupled biokinetic models. To achieve this, a series of studies and investigations has been conducted which is discussed below. Additionally, it has been shown how studying the oxygenation of a tank setup first can give us insight into the mixing potential of the reactor, such that, it is possible to predict if the tank is already well-mixed without having to include the full biological processes, which could save on computational costs.

To begin with, an analysis of the methods for coupling the activated sludge model into CFD hydrodynamic simulations was made. A review of previous attempts and results from coupling the activated sludge models into different wastewater units was conducted. A simple reactor based on the modelled tank in [Meister et al. \(2017\)](#) was replicated in Ansys Fluent ([Ansys, 2018](#)) and a simple two species biokinetic model was coupled into the simulation to assess and confirm the coupling procedure. The methodology required to couple the activated sludge models into an OpenFOAM CFD simulations was described. Furthermore, the difficulties in coupling the two-phase CFD simulation results compared with single-phase results was explained, specifically the difficulties that arose from including the free surface that has been neglected in previous work, and solutions for overcoming these difficulties was outlined along with an assessment of the implications on the solutions. This allows for the coupling procedure to be replicated.

In the following section, a description of how to implement the oxygen mass transfer in the two-phase simulations was given. The results from the oxygen mass transfer model have been assessed and verified such that the oxygen mass transfer model can be used to derive the global $k_l a$ and $S_{o,sat}$ for the aeration tank. This process was used to compare and assess how the diffuser configurations and flow rates in the reactor can influence the oxygenation in the tank. It was found that increasing the number of diffusers aerating significantly increased the oxygenation of the reactor compared to increasing the flow rate such that, if aerating with fine membrane diffusers, having more diffusers and increased spreading is a better operational change than pumping more air into the system to improve aeration in the reactor. Furthermore, an analysis of the derived global $k_l a$ and $S_{o,sat}$ from these simulations found that the global $k_l a$ is dependent on the volume distribution in the tank while the $S_{o,sat}$ value is dependent on the hydrodynamic flow field generated by the aerating diffusers. Moreover, using these derived global aeration functions, it was proposed that these values can be implemented into the ASMs for the aeration to allow us to directly compare the coupled and uncoupled ASMs with similar aeration rates such that the impact of the hydrodynamics on the biological processes can be assessed. Additionally, a study of the effect of reducing the mesh resolution on the oxygenation was conducted and found that this added a significant amount of numerical diffusion that impacted the results. Therefore, it was not advised to do so unless the computational demand was too high at the original resolution.

The SBAM was defined as a simpler biokinetic aeration model that allowed us to investigate the impact of operational changes to the aeration tank on the biological processes without requiring the need to solve the full ASM1 model which would significantly increase the computational demand. A comparison of the coupled and uncoupled SBAM was conducted in a batch reactor to directly investigate the impact of the hydrodynamics on the biological processes. It was found that, in the 2D 0.6 L/s reactor, the hydrodynamics was not mixing enough such that the biological processes were requiring twice as long to maximise the biomass concentra-

tions compared with the uncoupled SBAM results. An investigation of the location of the inlet and outlet on the biological processes was conducted and found that if the locations were nearby a closed vortex loop in the reactor, this could adversely impact the biological processes because the incoming concentrations would become trapped and would not be distributed throughout the reactor. Coupled simulations were run with the hydrodynamic flow field results from the 3D 1/3 reactor for flow rate 0.3 and 0.6 L/s in a batch reactor and compared. Inclusion of the additional dimension significantly improved the mixing in the reactor as it removed the closed vortex loops that were seen in the 2D simulations. This resulted in both flow rates producing a well-mixed reactor such that the results for the coupled and uncoupled SBAM were identical. Therefore, having twice the aeration of 0.6 L/s compared with the 0.3 L/s added no additional benefit to the biological processes and would only be adding additional operational costs. As a result, the 0.3 L/s flow rate is a more adequate flow rate for this aeration tank. It was concluded that the 2D simulations can provide insight into how operational changes to the tank can influence the biological processes and, due to the lower computational demand, more simulations and investigations can be conducted for a given amount of time. However, the 2D simulations will underestimate the full mixing capabilities and biological performance of a reactor design compared with the 3D simulations due to neglecting of the additional dimension. Finally, the full ASM1 model was implemented into the 2D 0.6 L/s simulation and it was shown that inadequate mixing can reduce the amount of S_{NO} and S_{NH} produced and consumed, respectively, which decreases the effectiveness of the aeration tank which, as a result, can impact the performance of the following anoxic tank.

Chapter 7

Conclusions

The main aim of this thesis has been to define a framework for, and create, a validated coupled CFD model for a pilot-scale aeration tank. Through the work presented in this thesis, this aim has been achieved and the model has been utilised to analyse the influence of reactor operational changes on the wastewater biological processes. This thesis has defined a framework for developing a validated coupled model in detail which can be used and adapted by other CFD engineers to create their own validated coupled model. Experiments have been conducted in a pilot-scale aeration tank to record velocity measurements for validation purposes which is also available for other CFD engineers to use for validation of their own CFD models. A hydrodynamic two-phase CFD model has been verified and validated, following the steps in the defined framework, against experimental data which can be used by other CFD engineers for their work with confidence. Furthermore, the hydrodynamic CFD model includes the free-surface and its effects on the solution which has not been seen previously in literature; making this model unique for modelling aeration tanks. This CFD work has been completed in the open source CFD software *OpenFOAM* which makes the model more accessible. A procedure for coupling the biological equations with the hydrodynamic CFD simulations has been defined; this was not trivial due to the inclusion of the free-surface but detailed descriptions have been given on how to achieve this which can be repeated and adapted by other CFD

engineers for any biological AS model. The coupling methodology has been verified and a validated hydrodynamic and biological coupled CFD model, which includes the free-surface, has been created; achieving the main aim of this thesis. Finally, the coupled model has been used to assess how the operational features of the tank influences the biological processes, which is not be possible using the conventional ASMs, illustrating the key benefits of the coupled model. A summary of the key conclusions gained from this thesis is listed below.

- Through analysing experimental velocity results, it has been found that certain diffuser configurations produce pseudo 2D flow fields. This allows us to use 2D CFD simulation for initial verification checks, reducing the computational demand of the simulations for these studies.
- Through these 2D verification studies it has been concluded that, for modelling the aeration tank accurately, a bubble Sauter mean diameter of 2.5 mm; a volume fraction of 0.2 with the necessary inlet velocity to conserve the air flow rate at the inlet; the virtual mass force; the [Schiller and Naumann \(1935\)](#) drag model; and the [Antal et al. \(1991\)](#) wall lubrication force; produced results that best matched the experimental velocity measurements obtained.
- The free-surface has been included in the CFD simulations which has not been done in previous work and has been found to clearly influence the hydrodynamics and, therefore, the biological processes. As a result, the free-surface should be included in future CFD simulations of aeration tanks.
- It was found that two different air flow rates produced almost identical flow fields which implied that the lower flow rate could be used to save on operational costs with minimal impact on the mixing capabilities of the reactor.
- A hydrodynamic-oxygen coupled model has been created to assess how the diffuser configuration can influence the aeration rates in the tank. It has been found that doubling the number of aerating diffusers with the same air flow

rate could double the aeration rate while doubling the flow rate was found to have only an approximate 15% increase in the aeration rate. Therefore, having more diffusers is more efficient operational change compared to increasing the air flow rate.

- A method for calculating the global volumetric oxygen transfer rate and saturation concentration from the hydrodynamic-oxygen coupled CFD model was defined and it has been shown how each terms correlates with the local hydrodynamics in the tank such that, if experiments were conducted to calculate these values, the experimental results could be used to give insight into the hydrodynamic structures in the aeration tank.
- The coupled SBAM model has been used to investigate how operational changes can influence the biological processes and it has been shown that inadequate mixing can influence the biological processes, as expected, and that the location of the inlet and outlet in the aeration tank can influence the biological processes with the same hydrodynamic flow field.
- Finally, the full ASM1 model has been coupled into the hydrodynamic CFD model and it has been found that in adequate mixing results in much higher levels of soluble ammonia and, overall, reduced the efficiency of the aeration reactor.

A series of objectives had been set out at the beginning of this thesis. These objectives will be reviewed in the sequential sections to assess if they have been achieved fully or partially. Additionally, at the end of each objective review, where applicable, an assessment has been conducted on how the work could be extended.

Objective 1

The first objective was to “*investigate and confirm the methodology and procedure for coupling activated sludge models into CFD simulations*”. Through analysing previ-

ous literature and assessing the biokinetic models, the methodology and procedure for coupling the activated sludge models into CFD simulations has been defined, achieving this objective. Chapter 1 identified previous literature that has coupled biokinetic models into CFD simulations for wastewater treatment process which was further discussed in chapter 6 in more detail and confirmed that the methodology was possible. In chapter 2, the ASMs were analysed and a procedure for converting the biokinetic rate equations into transport equations has been defined. This provided a mathematical method to include the effect of the hydrodynamics in the biokinetic rate equations. As a result of this analysis, a methodology and procedure for coupling ASMs into CFD simulation was confirmed, achieving this objective.

Objective 2

The second objective was to “*design and manufacture a pilot-scale aeration tank to conduct experiments to obtain measurements for use in validation of the CFD simulations*”. As described in chapter 3, a pilot-scale aeration has been designed and manufactured. An ADV has been used to record velocity measurements for varying flow rates and diffuser configurations which has been compared with the CFD simulation for validation. As a result, the requirements for this objective have been met.

To achieve this objective, a perspex pilot-scale fine membrane diffuser aeration tank, based on a working pilot-scale aeration basin, was designed and manufactured. Velocity measurements in the tank were recorded using an ADV probe. An explanation of the ADV operation and procedure for recording measurements has been outlined in chapter 3; discussing the difficulties and solutions for measuring with an ADV in an aerated reactor. Using the defined procedure, velocity measurements at various points in the tank were recorded for a range of diffuser configurations and flow rates. A de-spiking algorithm for removing non-physical measurements from bubble interference has been defined which was evaluated and found to be correctly removing non-physical measurements. A summary of the potential errors and un-

certainties during the experiments has been discussed and found that they do not significantly impact on the accuracy of the measured data. The results for a series of diffuser configurations and flow rates were illustrated and an assessment of the accuracy of the data has been conducted. The results were found to be accurate; giving confidence in the measured velocities. Finally, certain data sets were found to show 2D, or pseudo 2D, behaviour in the measurements which implied that 2D simulations could be conducted and validated against these data sets.

As a result of meeting this objective, a series of velocity data sets has been obtained for a range of diffuser configurations which can be used to validate various hydrodynamic CFD simulations. However, this work could be taken further. While the total experimental recorded data set is large, a natural extension to this work would be to repeat the experimental procedure to record new measurements for existing or alternative diffuser configurations and flow rates. Furthermore, it would be of interest to conduct dissolved oxygen experiments to record the rate of oxygen mass transfer into the tank for different diffuser configuration and flow rates. If conducted, these results could be used to validate the oxygen mass transfer model implemented in the coupled model in chapter 6; however, due to equipment and time constraints, it was not possible to conduct these experiments as part of this research.

Objective 3

The third objective was to “*develop a CFD model to simulate the hydrodynamics within the pilot-scale aeration tank and assess the modelling approaches using the obtained experimental data to acquire a validated CFD model describing the aeration tank hydrodynamics*”. The potential numerical and CFD modelling choices for the aeration tank were defined in chapter 4 and an assessment of these choices against the experimental data was conducted in chapter 5. Through this assessment, a validated CFD simulation has been defined that was able to reliably replicate the hydrodynamic features observed in the pilot-scale aeration tank, achieving this ob-

jective.

To meet this objective, a series of steps needed to be conducted first. The purpose of chapter 4 was to outline: the fundamental governing equations, the CFD modelling choices, and the numerical methods adopted in the CFD simulations to replicate the multi-phase aeration tank. Models that mathematically replicate the bubble-fluid interactions in the tank were outlined. These procedures were implemented into the CFD models described in chapter 5 and comparisons of the modelling choices against the experimental velocity measurements were made to assess the models. The Eulerian-Eulerian approach has been used for simulating the air-water interactions and free surface which were solved in the CFD software OpenFOAM. Two-dimensional simulations were conducted to evaluate the air inlet conditions, bubble size and bubble-water forces on the hydrodynamics by comparing the results with the experimental velocity measurements. From these studies, the modelling choices that were found to produce results which best matched the experimental velocity measurements from these studies were: a bubble Sauter mean diameter of 2.5 mm; a volume fraction of 0.2 with the necessary inlet velocity to conserve the air flow rate at the inlet; the virtual mass force; the [Schiller and Naumann \(1935\)](#) drag model; and the [Antal et al. \(1991\)](#) wall lubrication force. Therefore, these modelling choices were adopted in the CFD simulations to replicate the aeration tank hydrodynamics. In addition, the hydrodynamic effects of the free surface has been modelled which is something that has not been considered in previous published work. The free surface was found to influence the calculated solutions and, therefore, is important to include to accurately predict the hydrodynamics in the tank. Using this modelling procedure, 2D and 3D hydrodynamic aeration tank simulations were conducted for different diffuser configurations and flow rates. These simulations were compared with the measured experimental velocities for validation and were found to match well with the experimental measurements; giving confidence in the reliability of the CFD model. A study comparing the 2D and 3D simulation results found that the 3D simulations perform better at matching

the experimental data for both chosen flow rates due to the additional dimension being modelled. Finally, a comparison was made between the results from the 3D 0.3 and 0.6 L/s flow rate simulations. It was found that both flow rates produced similar levels of mixing in the aeration tank; implying the 0.3 L/s flow rate could be used over the 0.6 L/s to save on operational costs with minimal impact on the mixing capabilities of the reactor. Through these studies and analysis, a validated hydrodynamic CFD model for the aeration tank has been developed that has been shown to produce reliable solutions, achieving the third objective.

The focus of the hydrodynamic modelling has been on a specific diffuser configuration at two different flow rates. There is additional experimental data available that could be used to further evaluate the CFD model for additional diffuser configurations to extend this work. However, these diffuser setups did not show 2D behaviour and would require 3D simulations which, consequently, would be computationally more expensive. The full 3D tank has not been modelled in this work due to the large computational costs. However, a full 3D tank simulation could be conducted and used to assess how representative the 1/3 simulations results are of the full tank hydrodynamics. The impact of different two-phase turbulence models have been studied before in previous work and, therefore, a turbulence model study was not considered in this thesis. However, a two-phase turbulence model study could be conducted and validated using the experimental velocity measurements and the findings could be compared with previous literature results. Additionally, an LES modelling approach for replicating the turbulence in the aeration tank, which to our knowledge has not be previously been studied, could be considered; however, this would be significantly computationally expensive.

Objective 4

The fourth objective was to “*modify the CFD model to allow for coupling of transport equations and analyse these changes to assess their impact on the solution to give confidence in the coupling procedure*”. This test case objective was to confirm

and give confidence that the coupling procedure produces appropriate results before coupling the biokinetic into the pilot-scale aeration tank hydrodynamic CFD simulations.

A simple CFD simulation of an aeration basin based on the work in [Meister et al. \(2017\)](#) was created in Ansys Fluent ([Ansys, 2018](#)) and a simple biokinetic model was coupled into the simulation. The tank was well-mixed and resulted in the coupled model producing identical results to the ASM which is expected and gave us confidence that the biokinetics had been successfully coupled into the CFD simulations; meeting this objective. However, while we had achieved the fourth objective, this was for a highly simplified single-phase test case with no aeration to focus on the coupling procedure rather than solution accuracy. Through the analysis of this test case, future issues were found for when the biokinetics are coupled into the two-phase hydrodynamic solutions in OpenFOAM; specifically, the large time step size difference required to resolve the hydrodynamics and biokinetic rates, and the difficulties that arise with including a free surface in the coupled model. These issues were discussed, assessed and solved in chapter 6.

Objective 5

The fifth objective was to “*couple the oxygen mass transfer model into the CFD simulations to model the oxygenation in the tank and investigate how different membrane diffuser configurations and flow rates can impact the oxygenation with a comparison of the results against the expected theoretical aeration to verify the oxygen transfer model; resulting in a verified coupled oxygen mass transfer and hydrodynamic CFD model*”. The challenges and solutions for implementing oxygen transfer model were outlined in chapter 6. Investigations of the impact of diffuser configuration and flow rates on the oxygenations have been conducted. These were compared with the expected theoretical aeration rates and found to match reasonably well which verified the oxygen mass transfer model; achieving the fifth objective.

In chapter 6, to help meet this objective, a procedure for coupling the oxygen mass transfer and biokinetic equations into the hydrodynamics in OpenFOAM was outlined. A process for transferring a two-phase hydrodynamic solution with a free surface into a single-phase solver in OpenFOAM has been defined which can be repeated by other CFD engineers. The difficulties in converting the two-phase solution to single-phase was outlined; specifically that the free surface has been included in the hydrodynamic simulations and, therefore, needs careful consideration. The modifications required for transferring the two-phase solution were assessed using the oxygen mass transfer model and it was found that the hydrodynamic structures in the fluid had been conserved; thus giving confidence that the hydrodynamic features are preserved in the coupled model. The implemented oxygen transfer model has been used to derive a global volumetric oxygen transfer rate and saturation concentration for various tank diffuser configurations and air flow rates. It was found that increasing the number of aerating diffusers significantly increased the oxygenation of the reactor compared to increasing the air flow rate. Therefore, having more diffusers is a more efficient operational change compared to pumping more air into the system to improve aeration in the reactor. Through analysis of the derived global volumetric oxygen transfer rate and saturation concentration, a relationship has been found for how these values depend on the local hydrodynamics in the tank such that, if these values were to be derived from experimental measurements, the calculated values can be used to give insight into the hydrodynamic structures of the reactor. These global volumetric oxygen transfer rates were compared with the theoretical aeration rates calculated in chapter 4 and were found to match reasonably well which verified the oxygen mass transfer model; giving confidence moving forwards with coupling the biokinetic equations. These investigations and studies helped achieve the fifth objective of the thesis. Additionally, these derived global volumetric oxygen transfer rate values can be used to replicate the oxygenation in the uncoupled ASMs for these reactors such that they can be directly compared with the coupled model to assess the effects of the hydrodynamics on the biological

processes.

The oxygenation from the free surface has been neglected in these simulations as it was assumed the mass transfer from the bubbles dominated the oxygenation. To extend this work, the surface aeration could be included to better represent the oxygenation of the tank and, with the inclusion of the free surface in these simulations, an investigation of how the free surface influences the surface aeration could be conducted. Additionally, the oxygen mass transfer model has only been verified by comparing with the derived theoretical aeration rates. If dissolved oxygen experiments were conducted to obtain dissolved oxygen measurements, as stated previously, for various diffuser configurations and flow rates, these measurements could be used to compare and validate the coupled oxygen transfer model in the coupled CFD simulations which would give more confidence and reliability in the predicted results.

Objective 6

The sixth objective was to “*implement the additional biokinetic transport equations to complete the coupled model and investigate the impact of the hydrodynamics and changes in the aeration tank operation on the biological processes*”; fulfilling the main aim defined for this thesis. ASMs have been implemented into the 2D and 3D hydrodynamic CFD simulations successfully which have been used to show that the hydrodynamics can influence the biological process when the tank is not well-stirred. Additionally, the model was used to investigate how the tank operation changes can influence the biological processes through changing the hydrodynamics which would not be captured if the hydrodynamics were not considered; showing the power of the coupled model.

In chapter 6, a simplified aeration ASM has been derived to investigate the effects of the hydrodynamics on the biological processes in a computationally efficient manner. It was found that the 2D reactor simulations did not mix the reactor

adequately enough which impeded on the biological processes; showing how the hydrodynamics can impact the biological processes. An investigation on the impact of the inlet and outlet locations on the biological processes has been conducted and it was found that these locations could influence the biological processes. These findings were only possible through the coupled model and shows how the model can give additional insight over the conventional ASMs. Coupled simulations were run with the 3D hydrodynamic results for flow rates 0.3 and 0.6 L/s in a batch reactor. It was found that these both resulted in a well-mixed reactor such that the coupled and uncoupled ASM were identical; therefore, there is no additional benefit for pumping at 0.6 L/s for this reactor. As a result, the 0.3 L/s flow rate can provide adequate mixing at reduced operational costs for this aeration tank setup which agreed with the results found in chapter 5. Finally, the full ASM1 has been coupled into the 2D reactor simulations and it has been shown that inadequate mixing can influence the biological processes in the full ASM1. Through these studies, the sixth objective of this thesis has been achieved and, along with the previous five objectives, the main aim of this thesis to generate a validated hydrodynamic and biokinetic coupled model and to show how it can be used to understand the influence of the hydrodynamics on the biological processes has been fulfilled.

In this thesis, a procedure has been defined for coupling biokinetic and hydrodynamic CFD simulations which can now be used to further investigate aeration tank features and designs. Water has been used extensively as the fluid in these studies as it best represented the fluid in the experimental aeration tank. However, to further extend this work, the fluid properties could be modified to better represent AS. The geometry used has been based on the pilot-scale aeration tank but this could be changed to better represent a segment of a full-scale aeration tank. Furthermore, the coupled model could then be used to optimise the reactor segment to find a more efficient energy balance between aeration and mixing. However, this would require creating a new mesh and re-running the hydrodynamic simulations. The 2D simulations found that the biological processes were impeded by lack of mixing.

To improve the mixing, rather than applying more air through the system, a mechanical helical agitator, as described in [Oates et al. \(2020\)](#), could be implemented to combine aeration and mechanical mixing. An optimisation study with the coupled model could then be conducted to find the an optimal energy balance between the two mixing methods which could operate at a lower cost compared to solely increasing aeration. Finally, the experimental pilot-scale aeration tank was based on a pilot-scale aeration basin with real wastewater pumping through it. It could be possible to obtain biological data from aeration basin to validate the biological components in the coupled ASM1 model.

7.1 Future project

In the sections above, descriptions have been given in how some of the work conducted in this thesis could be extended. The main extension for this work would be to conduct dissolved oxygen experiments for the diffuser configurations and flow rates considered in the hydrodynamic simulations completed in this thesis to obtain dissolved oxygen measurements for these setups. The measurements could then be used to compare with the coupled hydrodynamic and oxygen mass transfer model predictions to validate the oxygen transfer model; improving the confidence and reliability in the model. Below is a proposal that builds and combines all the work conducted in this thesis for a potential future research project.

Research is currently being conducted in showing how pumping hydrogen through ADs can interact with the organic matter in the slurry and help increase the yield of biogas or methane produced during the AD process. Similarly to an aeration tank, the hydrogen bubbles floating through the AD could provide all the mixing needed. However, it has been found that mechanical stirrers provide a more efficient process for mixing than rising bubbles through an AD. A question that arises from this is: does a limit exist to the amount of hydrogen gas that can be pumped into the AD such that increasing the amount of hydrogen gas does not increase the

yield of biogas from the reactor? and if so, at this limit is the tank stirred enough by the rising hydrogen bubbles to not impact the biological processes? If the tank is not stirred enough, then a combination of mechanical stirring and hydrogen gas bubbling through spargers could be found to increase the yield of biogas while not hindering the biological processes; potentially achieving the desired results at a lower operational cost. Additionally, the flow induced by the mechanical stirrer might increase the entrainment time of the hydrogen bubbles to allow for more hydrogen to transfer and increase the biogas yield. To investigate this, CFD simulations could be conducted that would combine the procedures defined for modelling gas bubbling through a reactor in chapter 5, to CFD models that describe mechanically stirred ADs, as defined in [Oates et al. \(2020\)](#), to produce a mechanically stirred and hydrogen gas bubbled AD hydrodynamic CFD model. This model could then be coupled with the AD biokinetic models, using the coupling methodology described in chapter 6, to investigate the biogas yield of this reactor. The aim of this would be to have a 3D CFD model that could evaluate the biogas production yield in a combined hydrogen gas bubbled and mechanical stirred AD.

Chapter 8

Appendix

8.1 Experimental Results

8.1.1 Configuration “c2” and “b2” combined results for flow rate 36 L/min

The “b2” and “c2” configuration was chosen to best represent an open bubble plume with minimal impact of the walls. However, in practice the symmetric open plume behaviour was not observed as the walls were still close enough to influence the flow field significantly and impeded on the plume. Therefore, even though the plume is in a symmetric configuration, it was unstable and periodic behaviour was observed where the plume would go from being in the centre to moving towards a side wall.

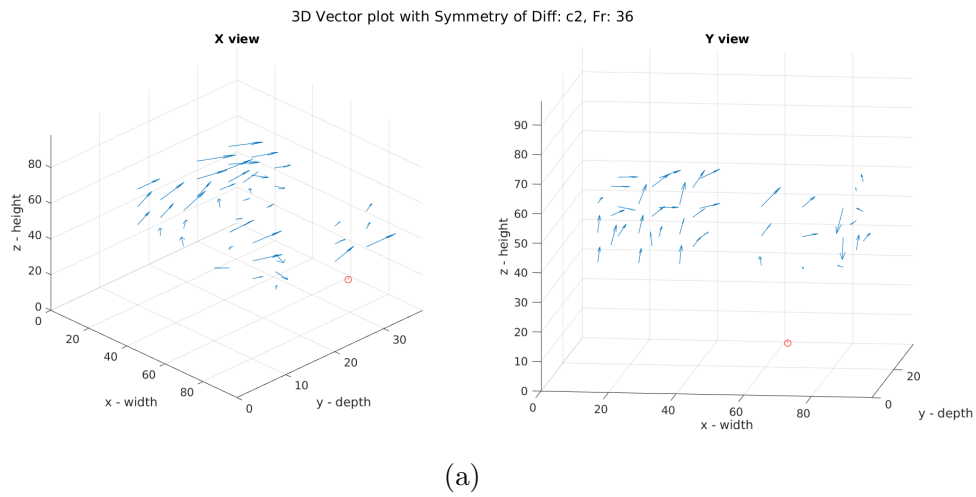
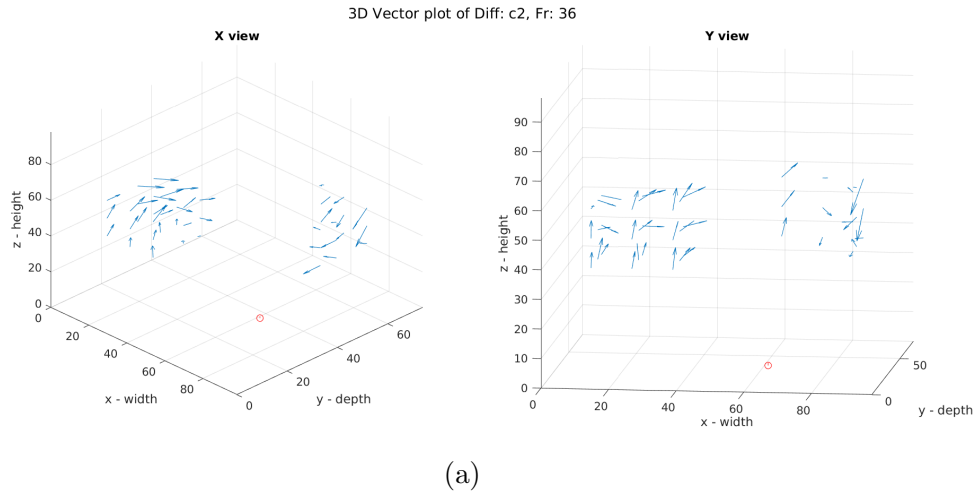


Figure 8.2: 3D vector plots of the diffuser configuration “c2” and “b2” combined at flow rate 36 L/min: without symmetry (a) and with symmetry (b). The red dot illustrates the centre locations of the aerating membrane diffusers.

Pt (ijk)	x (m)	y (m)	z (m)	u (m/s)	v (m/s)	w1 (m/s)	w2 (m/s)	u error (m/s)	v error (m/s)	w1 error (m/s)	w2 error (m/s)	w1 & w2 difference assessment
111	0.127	0.128	0.378	-0.003	0.03271	0.051629	0.05139	0.00076	0.00063	0.00105	0.00104	0.02702093
211	0.248	0.128	0.378	0.0113	-0.00583	0.067418	0.07035	0.00137	0.00253	0.00128	0.00097	0.34776846
311	0.369	0.128	0.378	0.0104	-0.00995	0.085927	0.08444	0.00223	0.00046	0.00038	0.00069	0.44698234
411	0.611	0.128	0.378	0.0082	-0.04397	0.060383	0.06097	0.00056	0.00099	0.00073	0.00073	0.09209499
511	0.732	0.128	0.378	-0.006	0.02991	-0.02496	-0.0251	0.00119	0.00049	0.00029	0.00029	0.05051375
611	0.853	0.128	0.378	-0.026	0.0132	0.000302	0.00024	0.00119	0.00123	0.00026	0.00026	0.02809824
112	0.127	0.128	0.478	-0.006	0.03955	0.057489	0.05741	0.00123	0.0004	0.00118	0.00118	0.00792047
212	0.248	0.128	0.478	0.0068	0.03155	0.065456	0.06566	0.00067	0.00022	0.00061	0.00066	0.0378676
312	0.369	0.128	0.478	0.0176	8.02E-06	0.071159	0.07076	0.00091	0.00064	0.00037	0.00035	0.12954448
412	0.611	0.128	0.478	0.0408	-0.01104	0.060379	0.06084	0.001	0.00144	0.00091	0.00094	0.05891812
512	0.732	0.128	0.478	0.0399	0.06271	-0.01492	-0.0148	0.00099	0.001	0.00089	0.00087	0.01580883
612	0.853	0.128	0.478	-0.015	0.03783	-0.11384	-0.1136	0.00187	0.00098	0.00064	0.00062	0.05214642
113	0.127	0.128	0.578	-0.001	0.05919	-0.0025	-0.0032	0.00128	0.00043	0.00131	0.0013	0.06593663
213	0.248	0.128	0.578	0.0106	0.05789	0.058287	0.0589	0.0016	0.00061	0.00117	0.00121	0.06063637
313	0.369	0.128	0.578	0.003	0.05628	0.071182	0.07167	0.00048	0.00101	0.00039	0.00034	0.16800457
413	0.611	0.128	0.578	0.0598	0.04031	0.065603	0.06586	0.00077	0.00145	0.00061	0.00063	0.04887087
513	0.732	0.128	0.578	0.0276	0.0653	0.01683	0.0171	0.00106	0.00037	0.00087	0.00081	0.03803637
613	0.853	0.128	0.578	-0.037	0.03514	-0.12821	-0.1282	0.00188	0.00107	0.00061	0.00058	0.01091405
121	0.127	0.249	0.378	0.0098	0.03342	0.072713	0.07279	0.00064	0.00071	0.00067	0.00066	0.01378287
221	0.248	0.249	0.378	-0.005	-0.00058	0.062932	0.06329	0.0008	0.00108	0.00067	0.00065	0.06351945
321	0.369	0.249	0.378	0.0408	-0.0338	0.059045	0.05944	0.00087	0.00083	0.00038	0.00035	0.12972956
621	0.853	0.249	0.378	-0.007	0.05247	0.041006	0.0405	0.00075	0.00088	0.00198	0.00199	0.02960866
122	0.127	0.249	0.478	0.0302	0.0672	-0.00602	-0.0063	0.00089	0.00113	0.0012	0.00118	0.02541968
222	0.248	0.249	0.478	0.0409	0.02455	0.034195	0.0338	0.00049	0.00125	0.00196	0.00188	0.02421396
322	0.369	0.249	0.478	0.0477	-0.00031	0.040653	0.04055	0.00016	0.00036	0.0005	0.00046	0.02525285
622	0.853	0.249	0.478	-0.037	0.04177	-0.03827	-0.0384	0.00036	0.00107	0.00062	0.00063	0.01797382
123	0.127	0.249	0.578	0.0451	0.0847	-0.04221	-0.0433	0.00157	0.00049	0.00081	0.00079	0.15358271
223	0.248	0.249	0.578	0.0477	0.06662	0.028283	0.02849	0.00059	0.00093	0.0006	0.00062	0.03956661
323	0.369	0.249	0.578	0.0377	0.02543	0.065191	0.06492	0.00099	0.00052	0.00061	0.00064	0.04486506
623	0.853	0.249	0.578	-0.008	0.01765	0.005483	0.00561	0.00101	0.00088	0.00038	0.00038	0.03978944
131	0.127	0.313	0.378	0.0146	0.05061	0.028507	0.02828	0.00057	0.00128	0.00052	0.00053	0.05116203
231	0.248	0.313	0.378	0.0145	-0.01007	0.051786	0.05161	0.00119	0.00095	0.00111	0.0011	0.01842
331	0.369	0.313	0.378	0.0458	-0.03671	0.044229	0.0443	0.00087	0.00075	0.00065	0.00064	0.01369213
631	0.853	0.313	0.378	0.0015	0.07678	-0.00129	-0.0017	0.00191	0.00267	0.0019	0.0019	0.02474692
132	0.127	0.313	0.478	0.0453	0.06492	-0.04566	-0.046	0.00079	0.00044	0.00063	0.00055	0.07233832
232	0.248	0.313	0.478	0.0695	0.01749	-0.0063	-0.0057	0.00035	0.00144	0.00066	0.00065	0.08620586
332	0.369	0.313	0.478	0.0786	-0.00349	0.024728	0.02465	0.00057	0.00079	0.00104	0.00103	0.01087387
632	0.853	0.313	0.478	-0.033	0.02255	0.003503	0.00341	0.0006	0.00175	0.00075	0.00077	0.01447745
133	0.127	0.313	0.578	0.0541	0.06974	-0.03132	-0.0321	0.00069	0.00086	0.00082	0.00085	0.10631848
233	0.248	0.313	0.578	0.0698	0.04309	0.014788	0.01469	0.00031	0.00146	0.00044	0.00048	0.0259978
333	0.369	0.313	0.578	0.0717	0.01495	0.036798	0.03673	0.00067	0.00107	0.00117	0.00116	0.00722391
633	0.853	0.313	0.578	-0.015	0.02062	0.023346	0.02353	0.00046	0.00088	0.00033	0.00035	0.06183653

Table 8.1: The ADV velocity results for diffuser configuration “c2” and “b2” combined data set for flow rate 36 L/min with the calculated standard errors for each component and an evaluation of the accuracy of each point by dividing the absolute difference in the calculated z velocities by the smallest standard deviation of the z velocity components to quantify the accuracy of the data. Green, yellow and red correspond to the magnitude of the z velocity difference being below 1, in between 1 and 2, and outside of 3 standard deviations.

8.1.2 Configuration “c2” and “b2” combined results for flow rate 18 L/min

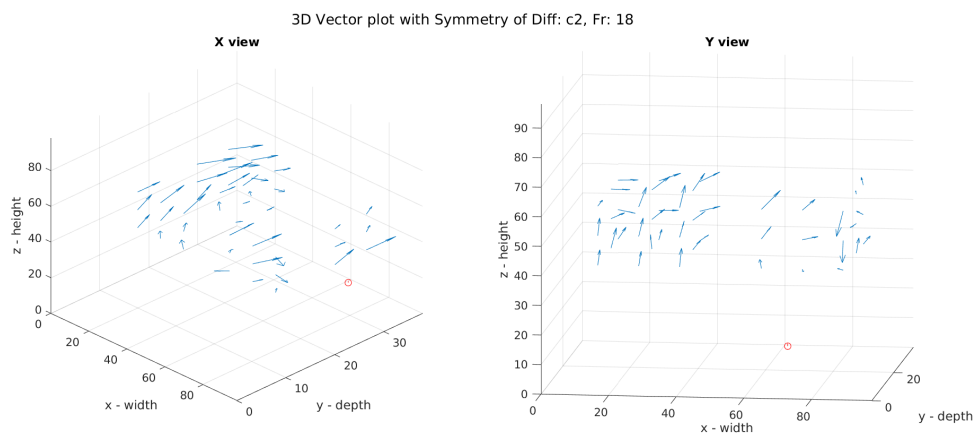
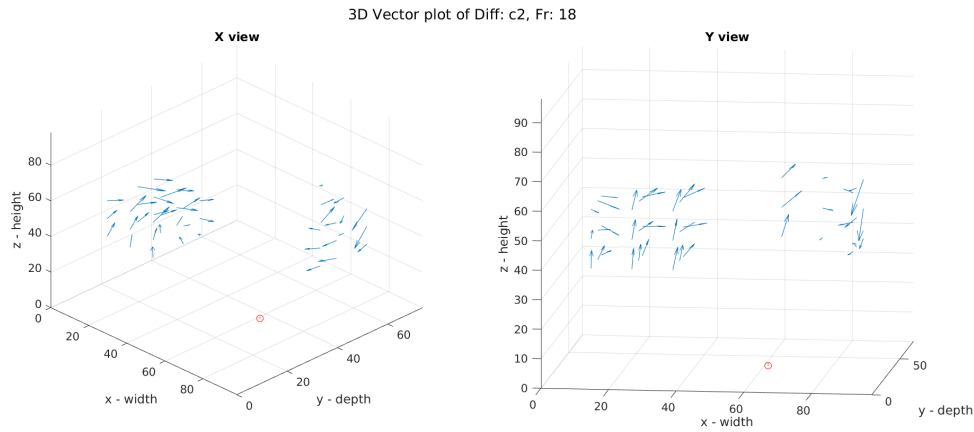


Figure 8.4: 3D vector plots of the diffuser configuration “c2” and “b2” combined at flow rate 18 L/min: without symmetry (a) and with symmetry (b). The red dot illustrates the centre locations of the aerating membrane diffusers.

Pt (ijk)	x (m)	y (m)	z (m)	u (m/s)	v (m/s)	w1 (m/s)	w2 (m/s)	u error (m/s)	v error (m/s)	w1 error (m/s)	w2 error (m/s)	w1 & w2 difference assessment
111	0.127	0.128	0.378	-0.0033	0.02928	0.045425	0.04529	0.000383	0.000573	0.0009938	0.00099	0.01544677
211	0.248	0.128	0.378	0.0037	0.00385	0.060163	0.06055	0.000531	0.000282	0.0006527	0.00063	0.07024246
311	0.369	0.128	0.378	0.01478	-0.01287	0.070256	0.07061	0.000469	0.000664	0.0004576	0.00047	0.08900843
411	0.611	0.128	0.378	0.01143	-0.03819	0.056068	0.0562	0.000777	0.00024	0.000358	0.00036	0.04178598
511	0.732	0.128	0.378	-0.0055	0.01398	-0.00384	-0.0043	0.000687	0.000395	0.0011648	0.00118	0.04296399
611	0.853	0.128	0.378	-0.0056	0.02702	-0.02345	-0.0238	0.001567	0.000318	0.0034959	0.00353	0.01109765
112	0.127	0.128	0.478	-0.0018	0.03495	0.016875	0.01648	0.000798	0.000294	0.0008426	0.00083	0.05530993
212	0.248	0.128	0.478	0.00499	0.02326	0.053139	0.05296	0.000553	0.000235	0.0005091	0.00051	0.04069196
312	0.369	0.128	0.478	0.01005	0.00531	0.062198	0.06204	0.00078	0.000535	0.0009409	0.00094	0.01983557
412	0.611	0.128	0.478	0.05008	-0.00673	0.047716	0.04768	0.000196	0.001061	0.0006544	0.00066	0.00654133
512	0.732	0.128	0.478	0.0332	0.03759	0.00331	0.00307	0.00143	0.000904	0.0007592	0.00076	0.0358426
612	0.853	0.128	0.478	-0.0056	0.03791	-0.08451	-0.0848	0.001393	0.000751	0.0003224	0.0003	0.10217329
113	0.127	0.128	0.578	0.01222	0.04838	-0.02163	-0.022	0.001445	0.000449	0.0024583	0.00245	0.01781956
213	0.248	0.128	0.578	0.00353	0.05266	0.045861	0.04599	0.000507	0.000776	0.0002236	0.00022	0.06901158
313	0.369	0.128	0.578	0.01361	0.04579	0.052452	0.05325	0.000587	0.000918	0.0003828	0.00041	0.24163017
413	0.611	0.128	0.578	0.0404	0.02892	0.048549	0.04847	0.000803	0.000986	0.0004954	0.00052	0.01949194
513	0.732	0.128	0.578	0.02074	0.04978	0.016438	0.01651	0.001021	0.000609	0.0005573	0.00054	0.01595468
613	0.853	0.128	0.578	-0.0262	0.03109	-0.0984	-0.098	0.0015	0.000776	0.0003262	0.00036	0.14408552
121	0.127	0.249	0.378	0.01212	0.03031	0.033921	0.034	0.000454	0.000753	0.0011114	0.00111	0.00850604
221	0.248	0.249	0.378	0.0066	-0.00774	0.049722	0.04985	0.000992	0.001972	0.0005559	0.00055	0.02631661
321	0.369	0.249	0.378	0.012	-0.02288	0.053621	0.05417	0.000408	0.000462	0.000261	0.00028	0.24406033
621	0.853	0.249	0.378	0.00139	0.06321	0.027487	0.02722	0.000359	0.000359	0.0003384	0.00032	0.09799774
122	0.127	0.249	0.478	0.02406	0.04811	-0.00885	-0.0092	0.000674	0.000302	0.0009157	0.0009	0.04395989
222	0.248	0.249	0.478	0.0317	0.03168	0.02148	0.02136	0.000224	0.000862	0.00048	0.00047	0.03016593
322	0.369	0.249	0.478	0.03917	-0.00632	0.030289	0.03011	0.000684	0.001017	0.0009246	0.00089	0.02292076
622	0.853	0.249	0.478	-0.0258	0.02852	-0.02233	-0.0226	0.000575	0.000827	0.0006622	0.00067	0.04083874
123	0.127	0.249	0.578	0.04497	0.06187	-0.03932	-0.0396	0.000797	0.000841	0.0005632	0.00057	0.0489082
223	0.248	0.249	0.578	0.0383	0.05953	0.025648	0.02537	0.000723	0.000604	0.0001793	0.00021	0.17909925
323	0.369	0.249	0.578	0.03343	0.03197	0.046878	0.04738	0.000654	0.000541	0.0002464	0.00027	0.23500116
623	0.853	0.249	0.578	-0.0156	0.0279	-0.00174	-0.0016	0.000557	0.000877	0.0006775	0.0007	0.03219089
131	0.127	0.313	0.378	0.0199	0.03638	0.00525	0.00498	0.001221	0.000626	0.001435	0.00144	0.02137604
231	0.248	0.313	0.378	0.01511	0.00889	0.046217	0.04599	0.000648	0.000347	0.0002632	0.00027	0.10127825
331	0.369	0.313	0.378	0.03319	-0.02585	0.045176	0.0456	0.000567	0.000971	0.0002463	0.00021	0.23262822
631	0.853	0.313	0.378	-0.0063	0.04285	0.000989	0.0009	0.001288	0.002875	0.0001734	0.00019	0.06245266
132	0.127	0.313	0.478	0.03927	0.03792	-0.03733	-0.0375	0.000405	0.000833	0.000256	0.0003	0.05359949
232	0.248	0.313	0.478	0.0547	0.03101	-0.00638	-0.0061	0.000561	0.001151	7.65E-05	0.00011	0.39738125
332	0.369	0.313	0.478	0.05994	0.00315	0.012487	0.01258	0.000588	0.000264	0.0005417	0.00054	0.01961357
632	0.853	0.313	0.478	-0.033	0.02841	-0.00264	-0.0029	0.000334	0.000745	0.0005749	0.0006	0.0315108
133	0.127	0.313	0.578	0.03584	0.03817	-0.01361	-0.0141	0.000228	0.000724	0.0004357	0.00046	0.13117806
233	0.248	0.313	0.578	0.05596	0.01728	0.011316	0.0114	0.000314	0.001733	0.0005606	0.00056	0.01746107
333	0.369	0.313	0.578	0.05375	0.00752	0.027429	0.02751	0.000378	0.000549	0.0002218	0.00024	0.04384717
633	0.853	0.313	0.578	-0.0207	0.0247	0.016748	0.01663	0.000989	0.000889	0.0010832	0.00109	0.0127553

Table 8.2: The ADV velocity results for diffuser configuration “c2” and “b2” combined data set for flow rate 18 L/min with the calculated standard errors for each component and an evaluation of the accuracy of each point by dividing the absolute difference in the calculated z velocities by the smallest standard deviation of the z velocity components to quantify the accuracy of the data. Green, yellow and red correspond to the magnitude of the z velocity difference being below 1, in between 1 and 2, and outside of 3 standard deviations.

8.1.3 Configuration “c1c2c3” results for flow rate 54 L/min

This configuration was chosen as a comparison with the “d1d2d3” and “a1a2a3” combined configuration. Similarly to the “b2” and “c2” configurations, the central symmetric plume was unstable. The occasional observed stable structure had the bubble plume shifting to the $x = 0.98$ back wall; behaving very similarly to the “d1d2d3” configuration. All the data was assessed to be good data as can be seen by all the green in table 8.3. Furthermore, the 3D vector plots for the configuration in figure 8.5 behaved similar to the “d1d2d3”, flow rate 54 L/min case in figure 3.15. This configuration showed the same recirculation in the centre but with a slight increase in velocity in the vertical direction due to reduced space from the shift of the diffusers away from the wall.

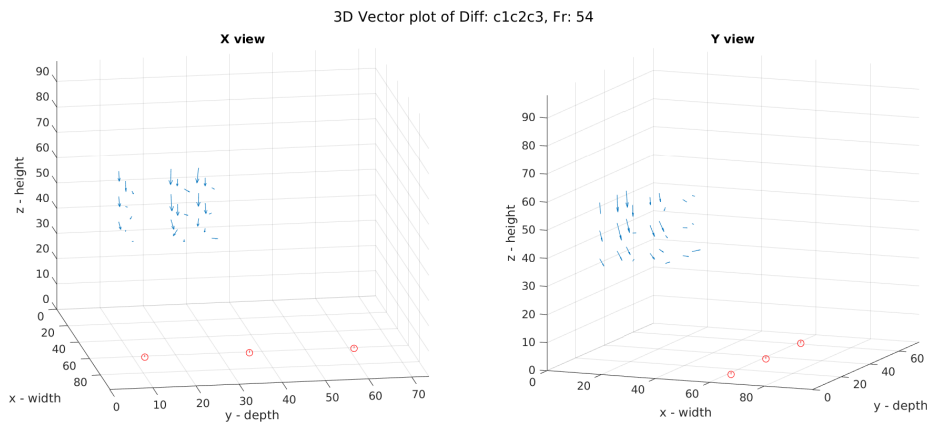


Figure 8.5: 3D vector plots of the diffuser configuration “c1c2c3” at flow rate 54 L/min.

Pt (ijk)	x (m)	y (m)	z (m)	u (m/s)	v (m/s)	w1 (m/s)	w2 (m/s)	u error (m/s)	v error (m/s)	w1 error (m/s)	w2 error (m/s)	w1 & w2 differenc e
111	0.127	0.128	0.378	0.044	0.013629	-0.047	-0.0474	0.0005	0.00091	0.00299	0.00297	0.0046666
211	0.248	0.128	0.378	0.025	0.011988	0.0229	0.02271	0.0017	0.0008	0.00037	0.00037	0.061563
311	0.369	0.128	0.378	0.062	-0.00542	0.0119	0.01178	0.00073	0.00078	0.00062	0.00063	0.0299135
112	0.127	0.128	0.478	0.04	-9.67E-05	-0.171	-0.1705	0.00119	0.00053	0.00329	0.00318	0.028364
212	0.248	0.128	0.478	0.035	0.001819	-0.056	-0.0565	0.00078	0.00083	0.00409	0.00408	0.0021737
312	0.369	0.128	0.478	0.027	-0.00584	-0.015	-0.0152	0.00062	0.00153	0.00108	0.00107	0.0131594
113	0.127	0.128	0.578	0.016	0.003493	-0.135	-0.1354	0.00138	0.00031	0.00042	0.00042	0.0452266
213	0.248	0.128	0.578	0.006	0.008057	-0.094	-0.0939	0.00076	0.0013	0.00328	0.00326	0.0100584
313	0.369	0.128	0.578	-0.016	0.003283	-0.037	-0.0373	0.00069	0.00089	0.00077	0.00077	0.0398754
121	0.127	0.249	0.378	0.053	0.013845	-0.109	-0.1087	0.0014	0.00027	0.00059	0.00066	0.1273219
221	0.248	0.249	0.378	0.059	-0.00827	-0.031	-0.0316	0.00144	0.00279	0.00195	0.00198	0.0570448
321	0.369	0.249	0.378	0.071	-0.0043	0.0076	0.00736	0.00081	0.00084	0.00107	0.00108	0.0214587
122	0.127	0.249	0.478	0.042	0.004661	-0.14	-0.1408	0.00126	0.00223	0.00434	0.00434	0.0304813
222	0.248	0.249	0.478	0.048	-0.0014	-0.108	-0.108	0.00103	0.00105	0.00134	0.00133	0.0198054
322	0.369	0.249	0.478	0.035	0.012978	-0.003	-0.0035	0.00061	0.00099	0.00038	0.00038	0.0767859
123	0.127	0.249	0.578	0.019	-0.00394	-0.185	-0.1849	0.00101	0.00044	0.00277	0.00276	0.000289
223	0.248	0.249	0.578	0.016	0.001929	-0.104	-0.1039	0.00075	0.00069	0.00211	0.00211	0.0032447
323	0.369	0.249	0.578	0.014	0.015328	-0.018	-0.018	0.00123	0.00192	0.00132	0.00133	0.0188654
131	0.127	0.313	0.378	0.049	-0.01133	-0.088	-0.0882	0.00075	0.00048	0.00187	0.00191	0.0074785
231	0.248	0.313	0.378	0.059	0.005462	-0.04	-0.0407	0.00038	0.00307	0.00096	0.00097	0.0275123
331	0.369	0.313	0.378	0.077	0.008758	0.0111	0.01099	0.00057	0.00262	0.00102	0.00102	0.0125802
132	0.127	0.313	0.478	0.036	-0.00722	-0.161	-0.1611	0.00081	0.00056	0.00097	0.00096	0.0057915
232	0.248	0.313	0.478	0.049	0.003013	-0.098	-0.0977	0.00083	0.00039	0.00163	0.00163	0.0118467
332	0.369	0.313	0.478	0.033	-0.00438	-0.012	-0.0125	0.00075	0.00131	0.0007	0.00073	0.056923
133	0.127	0.313	0.578	0.015	-0.01401	-0.17	-0.1705	0.00088	0.00033	0.00345	0.00344	0.0041382
233	0.248	0.313	0.578	0.015	-0.00108	-0.113	-0.1131	0.00034	0.00017	0.00093	0.00097	0.0157526
333	0.369	0.313	0.578	0.022	0.019772	-0.016	-0.016	0.00053	0.00038	0.00039	0.00039	0.0806941

Table 8.3: The ADV velocity results for diffuser configuration “c1c2c3” data set for flow rate 54 L/min with the calculated standard errors for each component and an evaluation of the accuracy of each point by dividing the absolute difference in the calculated z velocities by the smallest standard deviation of the z velocity components to quantify the accuracy of the data. Green, yellow and red correspond to the magnitude of the z velocity difference being below 1, in between 1 and 2, and outside of 3 standard deviations.

8.1.4 Configuration “d2” results for flow rate 36 L/min

This configuration is the closest case to the aeration rates in [Gresch et al. \(2011\)](#) with a structured flow field. The data in table 8.4 are all good with only one point in the reasonable criteria. The configuration behaved very similar to the “d1d2d3” case with the bubble plume flowing up along the side wall. The 3D vector plots in figure 8.6 had the largest velocities near the centre and decreased as you moved to smaller y values which is expected as you move away from the plane that is in line with the “d2” aerating diffuser. In comparison to the other configurations, there is not a clear re-circulation loop in the centre and the y velocity dominate more in this configuration.

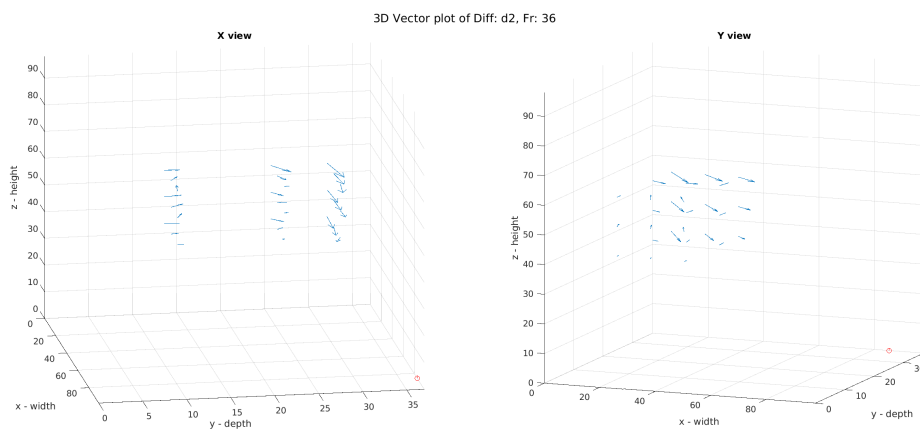


Figure 8.6: 3D vector plots of the diffuser configuration “d2” at flow rate 18 L/min.

Pt (ijk)	x (m)	y (m)	z (m)	u (m/s)	v (m/s)	w1 (m/s)	w2 (m/s)	u error (m/s)	v error (m/s)	w1 error (m/s)	w2 error (m/s)	w1 & w2 difference assessment
111	0.127	0.128	0.378	-0.031	0.0416	-0.01461	-0.0151	0.00032	0.00058	0.0003	0.0003	0.19283961
211	0.248	0.128	0.378	-0.018	0.0207	-0.00227	-0.00252	0.00034	0.0005	0.00062	0.00062	0.04685713
311	0.369	0.128	0.378	0.0064	0.0165	-0.0022	-0.00219	0.00061	0.00096	0.00059	0.00059	0.0022031
112	0.127	0.128	0.478	-0.033	0.0461	-0.00348	-0.00368	0.00077	0.00049	0.00046	0.00047	0.05229534
212	0.248	0.128	0.478	-0.028	0.0333	0.014811	0.01464	0.00083	0.00041	0.00022	0.00022	0.0920166
312	0.369	0.128	0.478	-0.021	0.0125	0.027958	0.02815	0.00113	0.00052	0.00042	0.00043	0.05356403
113	0.127	0.128	0.578	-0.012	0.0408	-0.00883	-0.00923	0.00069	0.00039	0.00101	0.00101	0.04557236
213	0.248	0.128	0.578	-0.015	0.0172	0.026052	0.02637	0.00086	0.00092	0.00041	0.00042	0.08841454
313	0.369	0.128	0.578	-0.026	-0.0014	0.039007	0.03928	0.0008	0.00039	0.00034	0.00034	0.09093481
121	0.127	0.249	0.378	0.0124	0.0334	-0.02401	-0.02419	0.00071	0.00038	0.00109	0.00108	0.01896601
221	0.248	0.249	0.378	0.02	0.0126	0.018842	0.01891	0.00119	0.00098	0.00038	0.00035	0.02383815
321	0.369	0.249	0.378	0.0399	-0.0042	0.022014	0.02202	0.00026	0.00073	0.00096	0.00096	0.00084756
122	0.127	0.249	0.478	0.0282	0.0306	-0.02537	-0.0256	0.00104	0.00095	0.00078	0.00074	0.03601915
222	0.248	0.249	0.478	0.0323	0.0224	0.010097	0.00966	0.0008	0.00072	0.00051	0.00054	0.10049174
322	0.369	0.249	0.478	0.0418	0.0088	0.018222	0.01792	0.00164	0.00122	0.00106	0.00106	0.03299397
123	0.127	0.249	0.578	0.058	0.0489	-0.04265	-0.04295	0.0007	0.00068	0.00037	0.00036	0.09526182
223	0.248	0.249	0.578	0.0779	0.0168	-0.0083	-0.00853	0.002	0.00104	0.00172	0.00173	0.01527023
323	0.369	0.249	0.578	0.0669	0.0073	0.023123	0.02298	0.00088	0.00092	0.00118	0.00118	0.01406826
131	0.127	0.313	0.378	0.0644	0.0122	-0.0811	-0.07808	0.00046	0.0009	0.00103	0.00107	0.33966197
231	0.248	0.313	0.378	0.0715	0.0017	-0.04873	-0.04845	0.00079	0.00091	0.00098	0.00099	0.03289221
331	0.369	0.313	0.378	0.0672	-0.013	-0.0117	-0.01152	0.00064	0.00134	0.00073	0.00072	0.02870892
132	0.127	0.313	0.478	0.0821	0.0223	-0.08442	-0.08289	0.00072	0.00083	0.00017	0.00013	1.3198324
232	0.248	0.313	0.478	0.0929	0.013	-0.05629	-0.0522	0.00128	0.00098	0.00119	0.00107	0.43925378
332	0.369	0.313	0.478	0.094	0.007	-0.02296	-0.02293	0.0015	0.00098	0.00103	0.00102	0.00359887
133	0.127	0.313	0.578	0.0998	0.0381	-0.09399	-0.09369	0.00072	0.00051	8.49E-05	0.00011	0.41545975
233	0.248	0.313	0.578	0.1273	0.0181	-0.0513	-0.05172	0.00168	0.001	0.00139	0.0014	0.0349122
333	0.369	0.313	0.578	0.1363	-0.0024	-0.0275	-0.02759	0.0005	0.00062	0.00036	0.00036	0.03038657

Table 8.4: The ADV velocity results for diffuser configuration “d2” data set for flow rate 36 L/min with the calculated standard errors for each component and an evaluation of the accuracy of each point by dividing the absolute difference in the calculated z velocities by the smallest standard deviation of the z velocity components to quantify the accuracy of the data. Green, yellow and red correspond to the magnitude of the z velocity difference being below 1, in between 1 and 2, and outside of 3 standard deviations.

8.2 2D assessment

8.2.1 Configuration “d1d2d3” and “a1a2a3” combined results for flow rate 108 L/min

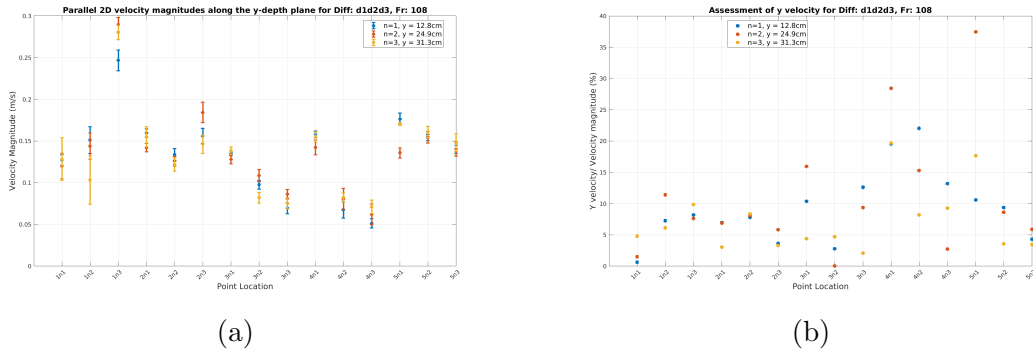


Figure 8.7: An assessment of the 2D behaviour of the “d1d2d3” and “a1a2a3” combined configuration at flow rate 108 L/min. A comparison of the velocity magnitude at points in parallel y planes (a) and the assessment of the y velocity compared with the velocity magnitude.

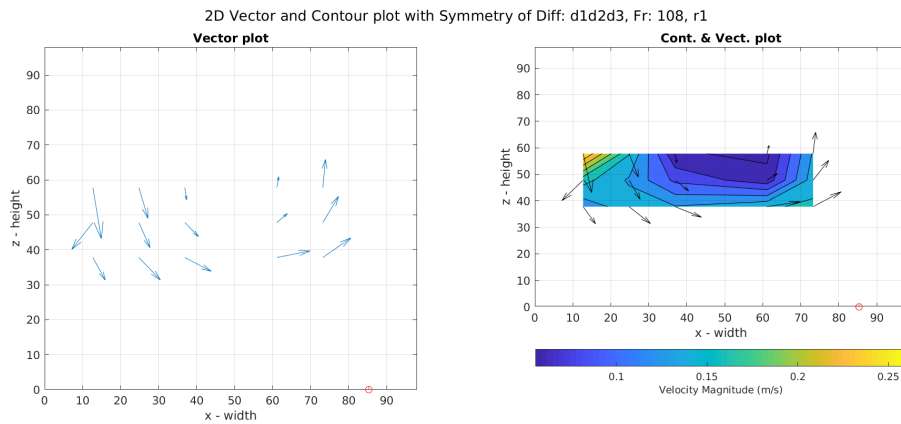


Figure 8.8: 2D vector and contour plots for the “d1d2d3” and “a1a2a3” combined configuration at flow rate 108 L/min along the row 1 diffusers or at $y = 12.8$ cm. The red dot illustrates the centre location of the aerating diffuser.

8.2.2 Configuration “c1c2c3” results for flow rate 54 L/min

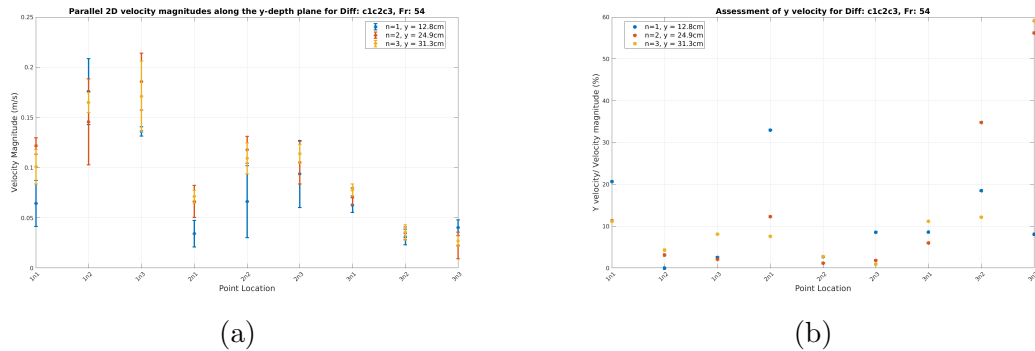


Figure 8.9: An assessment of the 2D behaviour of the “c1c2c3” configuration at flow rate 54 L/min. A comparison of the velocity magnitude at points in parallel y planes (a) and the assessment of the y velocity compared with the velocity magnitude.

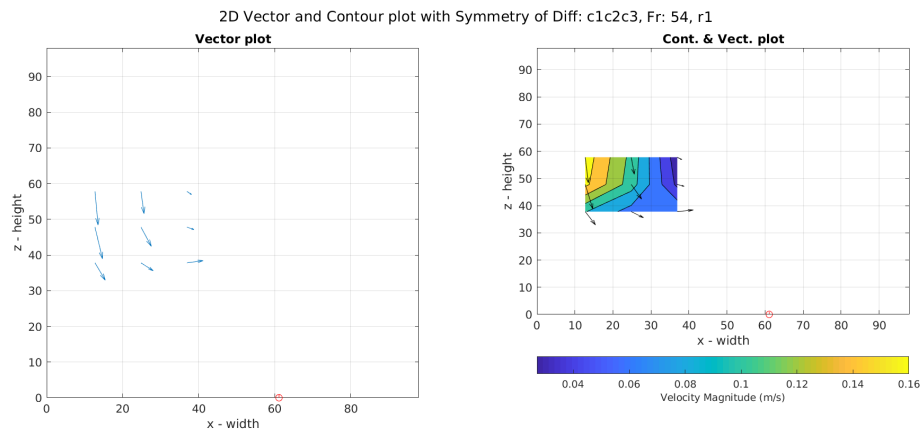


Figure 8.10: 2D vector and contour plots for the “c1c2c3” configuration at flow rate 54 L/min along the row 1 diffusers or at $y = 12.8\text{ cm}$. The red dot illustrates the centre location of the aerating diffuser.

8.3 Hydrodynamic modelling

Lift force model

The lift force aims to model the perpendicular force a bubble will experience as it travels through a shearing flow. Two simulations with the lift force were run that had a constant lift coefficient, $C_L = 0.1$, and the Tomiyama lift coefficient model which were compared with the results from the simulation without the lift force and the experimental data. These findings are presented in figure 5.17.

There is a sizeable difference between the simulations with and without the lift

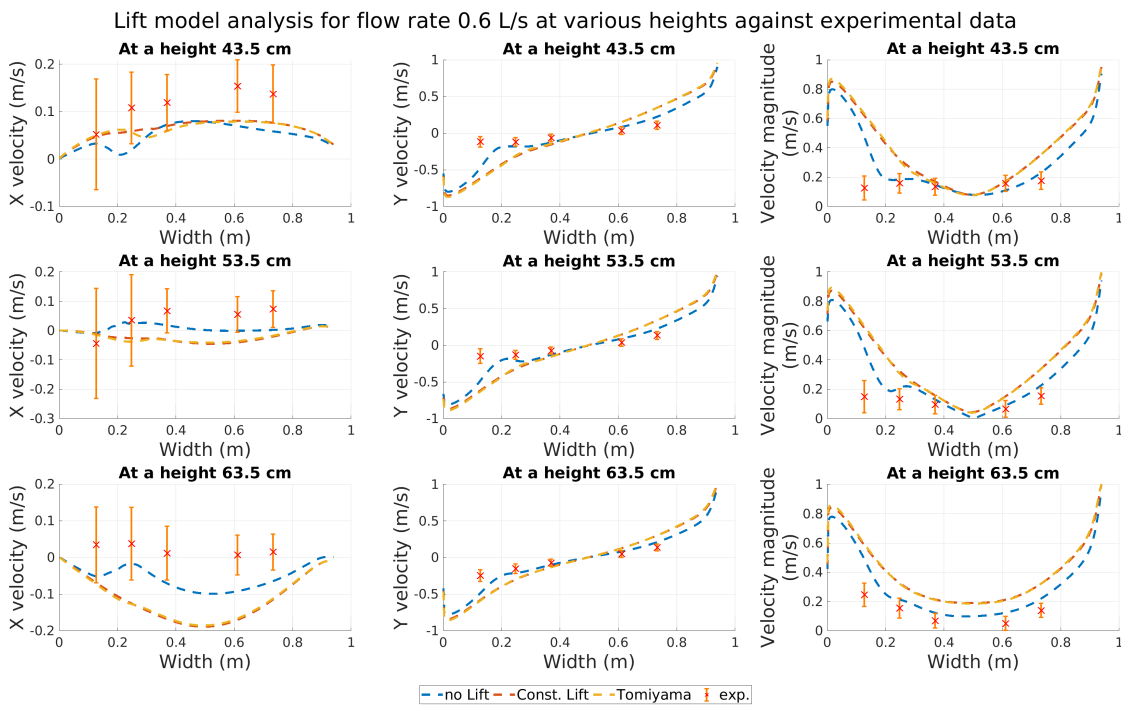


Figure 8.11: Analysis of lift force with constant coefficient and Tomiyama lift model against experimental data to assess the modelling choice.

model for all the plots which implies that the lift force has a strong influence on the solved hydrodynamics. The two lift models are almost identical which suggests that the Tomiyama lift coefficient formulation results in a similar value to the constant coefficient case, similar to what was found with the Tomiyama drag model. The lift models predict larger y velocities on either side of the tank compared with the non-lift simulation. Additionally, the lift models x velocities are more negative

at heights 53.5 and 63.5 cm compared with the non-lift simulation which implies the calculated centre of the vortex loop is lower in the tank. When comparing the results to the experimental data, the non-lift simulation matches the experimental data significantly better than the lift model cases. As a result, it is recommended to not include the lift model and future simulations will not include the lift model.

8.3.1 Turbulent dispersion model

Finally, we will briefly consider the turbulent dispersion model. The turbulent dispersion force models the influence of random turbulent eddies on the flow field from the bubbles which have been removed when deriving the RANS formulation. The [Burns et al. \(2004\)](#) model has been used, as described in §4.6, with a turbulent Prandtl number $\sigma_\alpha = 1.0$. However, the simulation computational cost increased significantly with this model and stability issues arose during run time. As a result, the simulation was only available to run for 120 seconds and was not able to reach the desired 160 seconds steady-state run time criteria. The results of the simulations are presented in figure 8.12.

There is significant difference between the two simulations for all plots. The large difference in the x velocities implies the vortex centre is calculated somewhere between 43.5 and 53.5 cm when using the turbulent dispersion model while the other simulation finds it somewhere between 53.5 and 63.5 cm. Additionally, the turbulent dispersion model predicts the largest peak of negative y velocities further away from the left side wall compared with the other simulations. When comparing with experimental data, the turbulent dispersion model matches significantly worse than the other simulation for all the plots. Overall, it is not recommended to use the turbulent dispersion model due to its computational cost and instability in the simulated results.

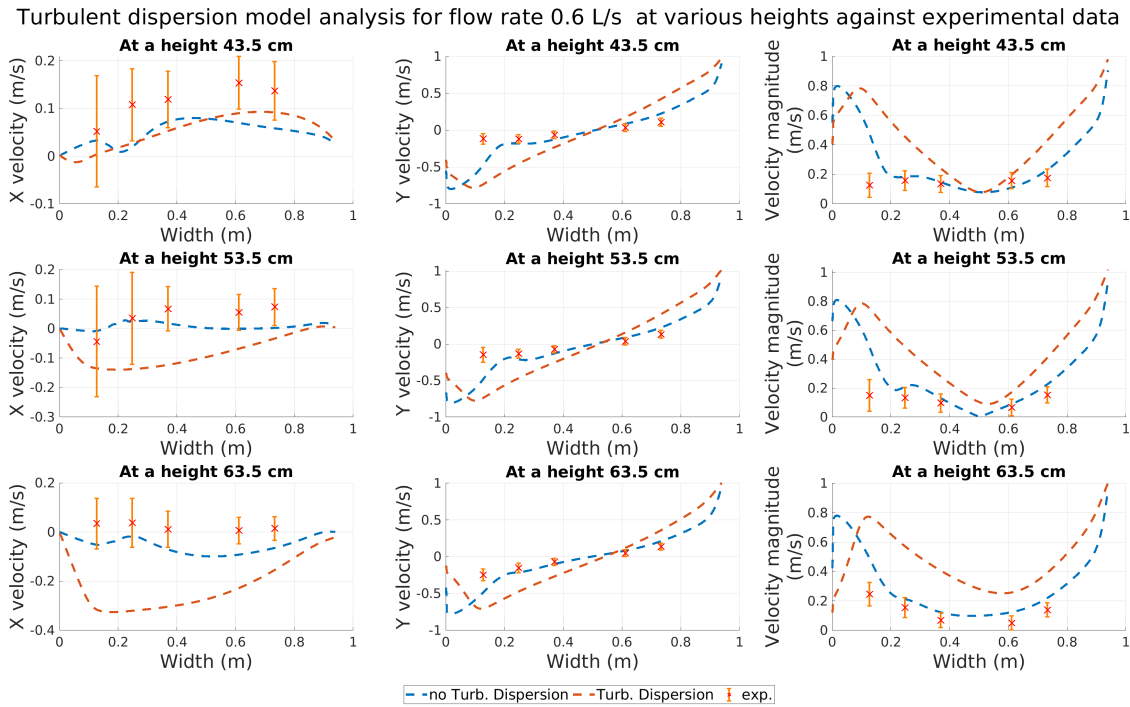


Figure 8.12: Analysis of the turbulent dispersion model against experimental data to assess the modelling choice.

8.4 Grid Convergence Index

The grid convergence index (GCI) is a statistical method used to determine the error associated with different mesh resolutions (Schwer, 2008). This method has been used to assess the mesh independence studies conducted in chapter 5 for the 2D and 3D meshes. The average velocity magnitude along the width profiles at heights 0.435, 0.535 and 0.635 m has been chosen as the quantity to analyse. Additionally, only meshes 1, 2 and 3 have been considered from the 2D and 3D mesh studies as mesh 3 was chosen as the designated mesh for both 2D and 3D studies. The GCI allows us to assess the solution for each mesh simulation and calculate a discretization error. The variable f_i denotes the designated quantity of interest for mesh i ; where larger i values refer to meshes with higher resolutions. The variable f_{ij} is defined as $f_{ij} = f_i - f_j$. The grid refinement ratio r_{ij} is the grid spacing ratio between increasing mesh resolutions. The value s is given by $s = \text{sign}(f_{12}/f_{23})$. The order of

convergence, p , is determined iteratively by solving the equation,

$$p = \frac{|\ln |f_{12}/f_{23}| + \ln((r_{23}^p - s)/(r_{12}^p - s))|}{\ln r_{23}}.$$

From p , the GCI can be calculated to estimate the amount of discretization error there is for the finest grid solution relative to the converged numerical solution. The formula for the GCI is given by,

$$GCI_{23} = F_s \frac{e_{23}}{r_{23}^p - 1}$$

where F_s is known as the safety factor and usually takes the value $F_s = 1.25$ based from applying GCI to many situations (Schwer, 2008), and $e_{ij} = |f_{ij}/f_i|$. Finally, the converged solution for the quantity being assessed can be estimated using the formula,

$$f_{23}^* = \frac{r_{23}^p f_3 - f_2}{r_{23}^p - 1}.$$

8.4.1 2D Simulations

For the 2D simulations, we will show the f_{ij} and r_{ij} calculations for the 3 mesh solutions at the 0.435 m height and then show the e_{ij} , GCI_{ij} and f_{ij}^* calculations along with the f_3 solution for mesh 3 for all 3 height profiles. The f_{ij} and r_{ij} are given in table 8.5. The values in table 8.5 can then be used to calculate e_{ij} ,

Mesh	1	2	3
Average Velocity Magnitude (m/s)	0.4534	0.4325	0.4416
f_{ij} (m/s)	-	0.0209	-0.0091
r_{ij}	-	2.069	1.9947

Table 8.5: The f_{ij} and r_{ij} calculations for the three meshes in the 2D mesh independence study for the 0.435 m height solutions. In this case, j corresponds to the column mesh number and $i = j - 1$.

GCI_{ij} and f_{ij}^* for 2D mesh 3. These are presented below in table 8.6 along with the corresponding average velocity magnitude for mesh 3. The maximum GCI value is

3.06 which implies that the discretization error is 3.06% for mesh 3.

Heights (m)	e_{32} (%)	GCI_{32} (%)	f_{32}^*	f_3
0.435	2.062	2.2445	0.4495	0.4416
0.535	2.244	2.691	0.4473	0.4378
0.635	2.212	3.0597	0.4524	0.4416

Table 8.6: The e_{ij} , GCI_{ij} and f_{ij}^* calculations for the three heights along with the average velocity magnitude, f_3 , for mesh 3.

8.4.2 3D Simulations

For the 3D simulations, we will show the f_{ij} and r_{ij} calculations for the 3 mesh solutions at the 0.435 m height and then show the e_{ij} , GCI_{ij} and f_{ij}^* calculations along with the f_3 solutions for mesh 3 for all 3 height profiles. The f_{ij} and r_{ij} are given in table 8.7. The values in table 8.7 can then be used to calculate e_{ij} ,

Mesh	1	2	3
Average Velocity Magnitude (m/s)	0.2002	0.1953	0.1897
f_{ij} (m/s)	-	0.0049	0.0056
r_{ij}	-	3.396	1.589

Table 8.7: The f_{ij} and r_{ij} calculations for the three meshes in the 3D mesh independence study for the 0.435 m height solutions. In this case, j corresponds to the column mesh number and $i = j - 1$.

GCI_{ij} and f_{ij}^* for 2D mesh 3. These are presented below in table 8.8 along with the corresponding average velocity magnitude for mesh 3. The maximum GCI value is 5.83 which implies that the discretization error is 5.83% for mesh 3.

Heights (m)	e_{32} (%)	GCI_{32} (%)	f_{32}^*	f_3
0.435	2.9441	3.9086	0.1838	0.1897
0.535	2.9051	4.0741	0.1713	0.1771
0.635	3.2802	5.8268	0.1733	0.1818

Table 8.8: The e_{ij} , GCI_{ij} and f_{ij}^* calculations for the three heights along with the average velocity magnitude, f_3 , for mesh 3.

Bibliography

- Amaral, A., Bellandi, G., Rehman, U., Neves, R., Amerlinck, Y., and Nopens, I. Mar. 2018. Towards improved accuracy in modeling aeration efficiency through understanding bubble size distribution dynamics. *Water Research*. **131**, pp. 346–355.
- Ansys. Fluent Theory Guide, Ansys, Inc. Last accessed on 22/10/2020 at:, 2018. URL <https://ansyshelp.ansys.com>.
- Antal, S., Lahey, R., and Flaherty, J. Sept. 1991. Analysis of phase distribution in fully developed laminar bubbly two-phase flow. *International Journal of Multiphase Flow*. **17**(5), pp. 635–652.
- ASCE. Measurements of Oxygen Transfer in Clean Water, 2007.
- Baltussen, M., Kuipers, J., and Deen, N. Feb. 2017. Direct numerical simulation of effective drag in dense gas–liquid–solid three-phase flows. *Chemical Engineering Science*. **158**, pp. 561–568.
- Besagni, G., Inzoli, F., and Ziegenhein, T. Mar. 2018. Two-Phase Bubble Columns: A Comprehensive Review. *ChemEngineering*. **2**(2), pp. 13.
- Bhuyar, L. B., Thakre, S. B., and Ingole, N. W. 2009. Design characteristics of curved blade aerator wrt aeration efficiency and overall oxygen transfer coefficient and comparison with CFD modeling. *International Journal of Engineering, Science and Technology*. **1**(1), pp. 1–15.

- Brannock, M., Leslie, G., Wang, Y., and Buetehorn, S. Jan. 2010. Optimising mixing and nutrient removal in membrane bioreactors: CFD modelling and experimental validation. *Desalination*. **250**(2), pp. 815–818.
- Burns, A. D., Frank, T., Hamill, I., and Shi, J.-M. The Favre Averaged Drag Model for Turbulent Dispersion in Eulerian Multi-Phase Flows. volume Paper No. 392, Yokohama, Japan, 2004.
- Capodaglio, A. and Olsson, G. Dec. 2019. Energy Issues in Sustainable Urban Wastewater Management: Use, Demand Reduction and Recovery in the Urban Water Cycle. *Sustainability*. **12**(1), pp. 266.
- Chen, P., Sanyal, J., and Dudukovic, M. Nov. 2004. CFD modeling of bubble columns flows: implementation of population balance. *Chemical Engineering Science*. **59**(22-23), pp. 5201–5207.
- Clift, R., Grace, J. R., and Weber, M. E. 1978. *Bubbles, drops, and particles*. Academic Press, New York.
- Colombo, M. and Fairweather, M. Dec. 2015. Multiphase turbulence in bubbly flows: RANS simulations. *International Journal of Multiphase Flow*. **77**, pp. 222–243.
- Coughtrie, A., Borman, D., Sleight, P., and Camargo-Valero, M. A coupled mixing and growth model for microalgae. *TBA*.
- Coughtrie, A., Borman, D., and Sleight, P. June 2013. Effects of turbulence modelling on prediction of flow characteristics in a bench-scale anaerobic gas-lift digester. *Bioresource Technology*. **138**, pp. 297–306.
- Coughtrie, A. R. 2016. *Coupling Hydrodynamic and Biological Process Models for Wastewater Treatment*. PhD thesis, University of Leeds.
- Davidson, M. R. Feb. 1990. Numerical calculations of two-phase flow in a liquid bath

- with bottom gas injection: The central plume. *Applied Mathematical Modelling*. **14**(2), pp. 67–76.
- Dhotre, M. T. and Smith, B. L. Dec. 2007. CFD simulation of large-scale bubble plumes: Comparisons against experiments. *Chemical Engineering Science*. **62**(23), pp. 6615–6630.
- Dhotre, M. T., Niceno, B., Smith, B. L., and Simiano, M. June 2009. Large-eddy simulation (LES) of the large scale bubble plume. *Chemical Engineering Science*. **64**(11), pp. 2692–2704.
- Fan, H., Qi, L., Liu, G., Zhang, Y., Fan, Q., and Wang, H. May 2017. Aeration optimization through operation at low dissolved oxygen concentrations: Evaluation of oxygen mass transfer dynamics in different activated sludge systems. *Journal of Environmental Sciences*. **55**, pp. 224–235.
- Garrido-Baserba, M., Sobhani, R., Asvapathanagul, P., McCarthy, G. W., Olson, B. H., Odize, V., Al-Omari, A., Murthy, S., Nifong, A., Godwin, J., Bott, C. B., Stenstrom, M. K., Shaw, A. R., and Rosso, D. Mar. 2017. Modelling the link amongst fine-pore diffuser fouling, oxygen transfer efficiency, and aeration energy intensity. *Water Research*. **111**, pp. 127–139.
- Gingold, R. A. and Monaghan, J. J. 1977. Smoothed particle hydrodynamics: theory and application to non-spherical stars. *Monthly notices of the royal astronomical society*. **181**(3), pp. 375–389.
- Glover, G. C., Printemps, C., Essemiani, K., and Meinhold, J. Feb. 2006. Modelling of wastewater treatment plants - how far shall we go with sophisticated modelling tools? *Water Science and Technology*. **53**(3), pp. 79–89.
- Goring, D. G. and Nikora, V. I. Jan. 2002. Despiking Acoustic Doppler Velocimeter Data. *Journal of Hydraulic Engineering*. **128**(1), pp. 117–126.
- Gosman, A. D., Lekakou, C., Politis, S., Issa, R. I., and Looney, M. K. Dec. 1992.

- Multidimensional modeling of turbulent two-phase flows in stirred vessels. *AIChE Journal*. **38**(12), pp. 1946–1956.
- Grace, J., Wairegi, T., and Nguyen, T. 1976. Shapes and velocities of single drops and bubbles moving freely through immiscible liquids. *Trans Inst Chem Eng*. **54**(3), pp. 167–173.
- Grant, S. B., Saphores, J.-D., Feldman, D. L., Hamilton, A. J., Fletcher, T. D., Cook, P. L. M., Stewardson, M., Sanders, B. F., Levin, L. A., Ambrose, R. F., Deletic, A., Brown, R., Jiang, S. C., Rosso, D., Cooper, W. J., and Marusic, I. Aug. 2012. Taking the "Waste" Out of "Wastewater" for Human Water Security and Ecosystem Sustainability. *Science*. **337**(6095), pp. 681–686.
- Gresch, M., Armbruster, M., Braun, D., and Gujer, W. Jan. 2011. Effects of aeration patterns on the flow field in wastewater aeration tanks. *Water Research*. **45**(2), pp. 810–818.
- Griborio, A., McCorquodale, J. A., and Rodriguez, J. A. Oct. 2014. CFD Modeling of Primary Clarifiers: The State-of-the-Art. *Proceedings of the Water Environment Federation*. **2014**(8), pp. 1926–1949.
- Guha, D., Dudukovic, M. P., Ramachandran, P. A., Mehta, S., and Alvare, J. May 2006. CFD-based compartmental modeling of single phase stirred-tank reactors. *AIChE Journal*. **52**(5), pp. 1836–1846.
- Haberman, W. and Morton, R. 1953. An Experimental Investigation of the Drag and Shape of Air Bubbles Rising in Various Liquids. pp. 59.
- Henze, M., Leslie, G. J. C. P., Gujer, W., Marais, G. V. R., and Matsuo, T. Jan. 1987. A general Model for Single-Sludge Wastewater Treatment Systems. *Water Research*. **21**(5), pp. 505–515.
- Henze, M., Harremoes, P., Jansen, J. I. C., and Arvin, E. Sept. 2001. *Wastewater Treatment: Biological and Chemical Processes*. Springer Science & Business Media.

- Henze, M., Gujer, W., Mino, T., and Van Loosdrecht, M., editors. 2007. *Activated sludge models ASM1, ASM2, ASM2d and ASM3*. Number 9 in Scientific and technical report / IWA. IWA Publ, London, reprinted edition.
- Higbie, R. 1935. The Rate of Absorption of a Pure Gas into a Still Liquid during Short Periods of Exposure. *Trans. AIChE.* **31**, pp. 365–389.
- Horan, N. J. 1989. *Biological Wastewater Treatment Systems: Theory and Operation*. John Wiley & Sons, University of Leeds, Leeds, UK.
- Jeppsson, U. 1996. *Modelling aspects of wastewater treatment processes*. PhD thesis, Lund Institute of Technology.
- Jeppsson, U., Pons, M.-N., Nopens, I., Alex, J., Copp, J. B., Gernaey, K. V., Rosén, C., Steyer, J.-P., and Vanrolleghem, P. A. 2007. Benchmark simulation model no 2: general protocol and exploratory case studies. *Water Science and Technology.* **56**(8), pp. 67–78.
- Kariyama, I. D., Zhai, X., and Wu, B. Oct. 2018. Influence of mixing on anaerobic digestion efficiency in stirred tank digesters: A review. *Water Research.* **143**, pp. 503–517.
- Karpinska, A. M. 2013. *New Design Tools for Activated Sludge Process*. PhD thesis, University of Porto, FEUP.
- Karpinska, A. M. and Bridgeman, J. Jan. 2016. CFD-aided modelling of activated sludge systems – A critical review. *Water Research.* **88**, pp. 861–879.
- Karpinska, A. M. and Bridgeman, J. Jan. 2017. Towards a robust CFD model for aeration tanks for sewage treatment – a lab-scale study. *Engineering Applications of Computational Fluid Mechanics.* **11**(1), pp. 371–395.
- Kim, M. I., Sin Kim, O., Lee, D. H., and Done Kim, S. Dec. 2007. Numerical and experimental investigations of gas–liquid dispersion in an ejector. *Chemical Engineering Science.* **62**(24), pp. 7133–7139.

- Le Moullec, Y., Gentric, C., Potier, O., and Leclerc, J. Jan. 2010a. CFD simulation of the hydrodynamics and reactions in an activated sludge channel reactor of wastewater treatment. *Chemical Engineering Science*. **65**(1), pp. 492–498.
- Le Moullec, Y., Gentric, C., Potier, O., and Leclerc, J. Jan. 2010b. Comparison of systemic, compartmental and CFD modelling approaches: Application to the simulation of a biological reactor of wastewater treatment. *Chemical Engineering Science*. **65**(1), pp. 343–350.
- Le Moullec, Y., Potier, O., Gentric, C., and Leclerc, J. May 2011. Activated sludge pilot plant: Comparison between experimental and predicted concentration profiles using three different modelling approaches. *Water Research*. **45**(10), pp. 3085–3097.
- Lee, I., Lim, H., Jung, B., Colosimo, M. F., and Kim, H. Dec. 2015. Evaluation of aeration energy saving in two modified activated sludge processes. *Chemosphere*. **140**, pp. 72–78.
- Lei, L. and Ni, J. Apr. 2014. Three-dimensional three-phase model for simulation of hydrodynamics, oxygen mass transfer, carbon oxidation, nitrification and denitrification in an oxidation ditch. *Water Research*. **53**, pp. 200–214.
- Leu, S.-Y., Rosso, D., Larson, L. E., and Stenstrom, M. K. Dec. 2009. Real-Time Aeration Efficiency Monitoring in the Activated Sludge Process and Methods to Reduce Energy Consumption and Operating Costs. *Water Environment Research*. **81**(12), pp. 2471–2481.
- Li, L., Liu, Z., Li, B., Matsuura, H., and Tsukihashi, F. 2015. Water Model and CFD-PBM Coupled Model of Gas-Liquid-Slag Three-Phase Flow in Ladle Metallurgy. *ISIJ International*. **55**(7), pp. 1337–1346.
- Littleton, H. X., Daigger, G. T., and Strom, P. F. June 2007. Application of Computational Fluid Dynamics to Closed-Loop Bioreactors: II. Simulation of

-
- Biological Phosphorus Removal Using Computational Fluid Dynamics. *Water Environment Research*. **79**(6), pp. 613–624.
- Lubchenko, N., Magolan, B., Sugrue, R., and Baglietto, E. Jan. 2018. A more fundamental wall lubrication force from turbulent dispersion regularization for multiphase CFD applications. *International Journal of Multiphase Flow*. **98**, pp. 36–44.
- Lucy, L. B. 1977. A numerical approach to the testing of the fission hypothesis. *The astronomical journal*. **82**, pp. 1013–1024.
- Ma, T., Ziegenhein, T., Lucas, D., and Fröhlich, J. Apr. 2016. Large eddy simulations of the gas–liquid flow in a rectangular bubble column. *Nuclear Engineering and Design*. **299**, pp. 146–153.
- McNamara, B. F., Layne, J., Hyre, M., Kinnear, D. J., and Bott, C. B. Jan. 2012. Evaluation of Three Full-scale Grit Removal Processes using CFD Modeling. *Proceedings of the Water Environment Federation*. **2012**(9), pp. 6008–6030.
- Meister, M., Bergmeister, C., Winkler, D., and Rauch, W. Activated sludge modelling with smoothed particle hydrodynamics. In *Proceedings of the 36th IAHR World Congress*, 2015.
- Meister, M., Winkler, D., Rezavand, M., and Rauch, W. Apr. 2017. Integrating hydrodynamics and biokinetics in wastewater treatment modelling by using smoothed particle hydrodynamics. *Computers & Chemical Engineering*. **99**, pp. 1–12.
- Menter, F. R. Aug. 1994. Two-equation eddy-viscosity turbulence models for engineering applications. *AIAA Journal*. **32**(8), pp. 1598–1605.
- Monod, J. 1949. The growth of bacterial cultures. *Annual Reviews in Microbiology*. **3**(1), pp. 371–394.

- Mori, N., Suzuki, T., and Kakuno, S. Jan. 2007. Noise of Acoustic Doppler Velocimeter Data in Bubbly Flows. *Journal of Engineering Mechanics*. **133**(1), pp. 122–125.
- Oates, A., Neuner, T., Meister, M., Borman, D., Camargo-Valero, M., Sleigh, A., and Fischer, P. Oct. 2020. Modelling Mechanically Induced Non-Newtonian Flows to Improve the Energy Efficiency of Anaerobic Digesters. *Water*. **12**(11), pp. 2995.
- OpenFOAM. OpenFOAM v4 User Guide, OpenFOAM. Last accessed on 09/04/2021 at:, 2020. URL <http://www.openfoam.org/>.
- Orhon, D., Babuna, F. G., and Karahan, O. Feb. 2009. *Industrial Wastewater Treatment by Activated Sludge*. IWA Publishing.
- Ovezea, A. Jan. 2009. Saving energy: Using fine bubble diffusers. *Filtration & Separation*. **46**(1), pp. 24–27.
- Ozturk, M. C., Martin Serrat, F., and Teymour, F. Jan. 2016. Optimization of aeration profiles in the activated sludge process. *Chemical Engineering Science*. **139**, pp. 1–14.
- Park, S. H., Park, C., Lee, J., and Lee, B. June 2017. A Simple Parameterization for the Rising Velocity of Bubbles in a Liquid Pool. *Nuclear Engineering and Technology*. **49**(4), pp. 692–699.
- POST. 2007. POSTNOTE: Energy and Sewage. *POST: Parliamentary Office of Science and Technology*. (282).
- Potter, M. C., Wiggert, D. C., and Ramadan, B. H. 2016. *Mechanics of fluids*. Nelson Education.
- Rehman, U., Audenaert, W., Amerlinck, Y., Maere, T., Arnaldos, M., and Nopens, I. Oct. 2017. How well-mixed is well mixed? Hydrodynamic-biokinetic model

- integration in an aerated tank of a full-scale water resource recovery facility. *Water Science and Technology*. **76**(8), pp. 1950–1965.
- Rigopoulos, S. and Jones, A. July 2003. A hybrid CFD—reaction engineering framework for multiphase reactor modelling: basic concept and application to bubble column reactors. *Chemical Engineering Science*. **58**(14), pp. 3077–3089.
- Roghair, I., Lau, Y., Deen, N., Slagter, H., Baltussen, M., Van Sint Annaland, M., and Kuipers, J. July 2011. On the drag force of bubbles in bubble swarms at intermediate and high Reynolds numbers. *Chemical Engineering Science*. **66**(14), pp. 3204–3211.
- Roman, M.-D. and Mure, M.-V. 2015. Process Optimization of Aeration in the Biological Treatment using Fine Bubble Diffusers. pp. 4.
- Rosso, D., Iranpour, R., and Stenstrom, M. K. May 2005. Fifteen Years of Offgas Transfer Efficiency Measurements on Fine-Pore Aerators: Key Role of Sludge Age and Normalized Air Flux. *Water Environment Research*. **77**(3), pp. 266–273.
- Rosso, D., Stenstrom, M. K., and Larson, L. E. Apr. 2008. Aeration of large-scale municipal wastewater treatment plants: state of the art. *Water Science & Technology*. **57**(7), pp. 973.
- Rusche, H. 2002. *Computational Fluid Dynamics of Dispersed Two-Phase Flows at High Phase Fractions*. PhD thesis.
- Rzehak, R. and Krepper, E. May 2013a. Bubble-induced turbulence: Comparison of CFD models. *Nuclear Engineering and Design*. **258**, pp. 57–65.
- Rzehak, R. and Krepper, E. Oct. 2013b. CFD modeling of bubble-induced turbulence. *International Journal of Multiphase Flow*. **55**, pp. 138–155.
- Samstag, R. W., Ducoste, J. J., Griborio, A., Nopens, I., Batstone, D. J., Wicks, J. D., Saunders, S., Wicklein, E. A., Kenny, G., and Laurent, J. Aug. 2016. CFD

-
- for wastewater treatment: an overview. *Water Science and Technology*. **74**(3), pp. 549–563.
- Schiller, L. and Naumann, A. 1935. A drag coefficient correlation. *Zeitschrift des Vereins Deutscher Ingenieure*. **77**, pp. 318–320.
- Schwer, L. E. 2008. IS YOUR MESH REFINED ENOUGH? Estimating Discretization Error using GCI. . *LS*. pp. 10.
- Shaver, D. and Podowski, M. Modeling of Interfacial Forces for Bubbly Flows in Subcooled Boiling Conditions. Center for Multiphase Research, Rensselaer Polytechnic Institute, 110 8th St., Troy, NY, 2015.
- Shih, T.-H., Liou, W. W., Shabbir, A., Yang, Z., and Zhu, J. 1995. A new k- ϵ eddy viscosity model for high reynolds number turbulent flows. *Computers Fluids*. **24** (3), pp. 227–238.
- Smith, B. Oct. 1998. On the modelling of bubble plumes in a liquid pool. *Applied Mathematical Modelling*. **22**(10), pp. 773–797.
- Spellman, F. R. and Drinan, J. 2003. *Wastewater Treatment Plant Operations Made Easy: A Practical Guide for Licensure*. DEStech Publications, Inc.
- Sánchez, F., Rey, H., Viedma, A., Nicolás-Pérez, F., Kaiser, A., and Martínez, M. Aug. 2018. CFD simulation of fluid dynamic and biokinetic processes within activated sludge reactors under intermittent aeration regime. *Water Research*. **139**, pp. 47–57.
- Terashima, M., So, M., Goel, R., and Yasui, H. Aug. 2016. Determination of diffuser bubble size in computational fluid dynamics models to predict oxygen transfer in spiral roll aeration tanks. *Journal of Water Process Engineering*. **12**, pp. 120–126.
- Thomas, R. E., Schindfessel, L., McLelland, S. J., Creëlle, S., and De Mulder, T. July 2017. Bias in mean velocities and noise in variances and covariances measured

- using a multistatic acoustic profiler: the Nortek Vectrino Profiler. *Measurement Science and Technology*. **28**(7), pp. 075302.
- Tomiyaama, A., Tamai, H., Zun, I., and Hosokawa, S. 2002. Transverse migration of single bubbles in simple shear flows. *Chemical Engineering Science*. pp. 10.
- Turovskiy, I. S. and Mathai, P. K. Aug. 2006. *Wastewater Sludge Processing*. John Wiley & Sons.
- Versteeg, H. K. and Malalasekera, W. 2007. *An introduction to computational fluid dynamics: the finite volume method*. Pearson Education Ltd, Harlow, England ; New York, 2nd ed edition.
- Vik, C. B., Solsvik, J., Hillestad, M., and Jakobsen, H. A. Feb. 2018. A multifluid-PBE model for simulation of mass transfer limited processes operated in bubble columns. *Computers & Chemical Engineering*. **110**, pp. 115–139.
- Wahl, T. L. June 2003. Discussion of “Despiking Acoustic Doppler Velocimeter Data” by Derek G. Goring and Vladimir I. Nikora. *Journal of Hydraulic Engineering*. **129**(6), pp. 484–487.
- Wallis, G. B. Oct. 1974. The terminal speed of single drops or bubbles in an infinite medium. *International Journal of Multiphase Flow*. **1**(4), pp. 491–511.
- Wang, L. K., Vielkind, D., and Wang, M. H. July 1978. Mathematical models of dissolved oxygen concentration in fresh water. *Ecological Modelling*. **5**(2), pp. 115–123.
- Wang, L. K., Pereira, N. C., and Hung, Y.-T. May 2009. *Biological Treatment Processes*. Springer Science & Business Media.
- Wang, Q. and Yao, W. July 2016. Computation and validation of the interphase force models for bubbly flow. *International Journal of Heat and Mass Transfer*. **98**, pp. 799–813.
- WEP. 2002. *Activated Sludge*. Water Environment Federation.

- Wilcox, D. C. 1993. *Turbulence modeling for CFD*. DCW Industries, Inc, La C nada, CA.
- Xu, N., Fan, L., Pang, H., and Shi, H. Aug. 2010. Feasibility study and CFD-aided design for a new type oxidation ditch based on airlift circulation. *The Canadian Journal of Chemical Engineering*. pp. n/a–n/a.
- xylem. Aeration Products, for energy efficient biological treatment, 2020. URL <https://www.xylem.com/siteassets/brand/sanitaire/sanitaire-resources/aeration-products-for-energy-efficient-biological-treatment.pdf>.
- Yang, M., Wei, Y., Zheng, X., Wang, F., Yuan, X., Liu, J., Luo, N., Xu, R., Yu, D., and Fan, Y. Nov. 2016. CFD simulation and optimization of membrane scouring and nitrogen removal for an airlift external circulation membrane bioreactor. *Bioresource Technology*. **219**, pp. 566–575.
- Zedn kov, M., Orvalho, S., Fialov, M., and Ruzicka, M. May 2018. Measurement of Volumetric Mass Transfer Coefficient in Bubble Columns. *ChemEngineering*. **2**(2), pp. 19.
- Zhao, H., Isaacs, S., Soeberg, H., and Jumme, M. 1995. An analysis of nitrogen removal and control strategies in an alternating activated sludge process. **29**(2), pp. 534–544.
- Zimmerman, W. B., Tesar, V., Butler, S., and Bandulasena, H. C. 2008. Microbubble generation. *Recent patents on Engineering*. **2**(1), pp. 1–8.
- Zimmerman, W. B., Hewakandamby, B. N., Tesař, V., Bandulasena, H. H., and Omotowa, O. A. Sept. 2009. On the design and simulation of an airlift loop bioreactor with microbubble generation by fluidic oscillation. *Food and Bioprocesses Processing*. **87**(3), pp. 215–227.